

Single-Particle Investigations of Plasmonic Nanoantennas for Energy Conversion

Dissertation to obtain
the doctoral degree of natural sciences (Dr. rer. nat.)



at the Faculty of Physics of the
Ludwig-Maximilians-Universität in Munich

submitted by
Simone Vera Ezendam
from Oss (NL)

Munich, 3rd of April, 2023

First Referee: Prof. Dr. Emiliano Cortés
Second Referee: Prof. Dr. Ralf Jungmann
Chairman: Prof. Dr. Lode Pollet
Assessor: Prof. Dr. Monika Aidelsburger
Day of oral examination: 17th of May, 2023

Abstract

Solar energy is a promising solution to the world's energy problems, and photovoltaic cells have made significant progress in converting sunlight into electricity. However, the intermittency of sunlight limits the usability of photovoltaic technology. Plasmonic nanoparticles have emerged as promising candidates for efficient solar energy conversion and storage. These metallic nanoparticles have unique optical properties that can be tuned by varying their size, shape, and composition. Through the investigation of the behavior of individual nanoparticles by single-particle techniques, this thesis aims to optimize their design and improve their efficiency, ultimately leading to more effective solar energy conversion and storage technologies.

We employ single-molecule localization microscopy to study plasmon-enhanced catalysis with super-resolution, revealing the mechanism driving the chemical transformation. This single-particle approach allows for precise investigation of the behavior of individual nanoparticles with subparticle and single-molecule turnover frequencies. We propose a design strategy for optimizing catalysts by maximizing the plasmonic field enhancement, which can lead to increased turnover rates at low irradiances.

Next, we examine the latest developments in hybrid plasmonic photocatalysis for solar fuel production, highlighting the importance of quantifying the role of temperature in the enhancement mechanism. We introduce a photothermal model for bimetallic core-shell nanoparticles and verify it with anti-Stokes thermometry, a single-particle technique that allows us to study the link between nanoparticle structure and heat generation. We show that geometry plays a crucial role since the addition of a catalytic shell over a plasmonic core strongly reduces the photothermal response, while the inclusion of the catalytic material in the form of satellites around the plasmonic core keeps the photothermal properties almost unaffected.

Finally, we broaden the focus to ensembles of nanoparticles in the last chapter, demonstrating the applicability and accuracy of anti-Stokes thermometry for investigating the photothermal properties of plasmonic ensembles. The knowledge gained from previous single-particle investigations provides a solid foundation for understanding the behavior of these larger-scale systems. Through comparison with quadriwave shearing interferometry we validate the reliability of this ensemble-based approach.

This thesis contributes to the advancement of plasmonic nanoantennas for energy conversion by providing valuable insight into the underlying physical properties. The knowledge gained from this work will not only guide the design of more efficient and sustainable energy conversion technologies but also broaden our understanding of plasmonic materials and their diverse applications. By integrating plasmonic photocatalysis, single-molecule localization microscopy, and photothermal characterization techniques, we aim to facilitate future research in areas such as photothermal therapy and solar energy conversion, ultimately contributing to create novel nanomaterials with improved functionality and performance.

Zusammenfassung

Solarenergie ist eine vielversprechende Lösung für die Energieprobleme der Welt und photovoltaische Zellen haben signifikante Fortschritte bei der Umwandlung von Sonnenlicht in Elektrizität gemacht. Die Unbeständigkeit des Sonnenlichts beschränkt jedoch die Nutzbarkeit der photovoltaischen Technologie. Plasmonische Nanopartikel haben sich als vielversprechende Kandidaten für effiziente solare Energieumwandlung und -speicherung herausgestellt. Diese metallischen Nanopartikel besitzen einzigartige optische Eigenschaften, die durch Variation ihrer Größe, Form und Zusammensetzung eingestellt werden können. Durch die Untersuchung des Verhaltens einzelner Nanopartikel mittels Einzelpartikeltechniken zielt diese Arbeit darauf ab, ihr Design zu optimieren und ihre Effizienz zu verbessern, was letztendlich zu effektiveren Technologien zur solaren Energieumwandlung und -speicherung führt.

Wir setzen die Einzelmolekül-Lokalisationsmikroskopie ein, um die plasmonenverstärkte Katalyse mit hoher Auflösung zu untersuchen, wobei wir feststellen, dass die Verstärkung der untersuchten Reaktion hauptsächlich auf die Photoanregung des Reaktionsmoleküls zurückzuführen ist. Dieser Ansatz auf Einzelpartikelebene erlaubt eine präzise Untersuchung des Verhaltens einzelner Nanopartikel. Wir schlagen eine Designstrategie zur Optimierung von Katalysatoren vor, die darauf abzielt, die plasmonische Feldverstärkung zu maximieren, was zu höheren Umsatzraten bei niedrigen Bestrahlungsstärken führen kann.

Als nächstes untersuchen wir die neuesten Entwicklungen in der hybriden plasmonischen Photokatalyse für die Produktion von Solartreibstoffen und betonen die Bedeutung der Quantifizierung der Rolle der Temperatur im Verstärkungsmechanismus. Wir stellen ein photothermales Modell für bimetallische Kern-Schale-Nanopartikel vor und verifizieren es durch Anti-Stokes-Thermometrie, eine Einzelpartikeltechnik, die es uns ermöglicht, den Zusammenhang zwischen Nanopartikelstruktur und Wärmeerzeugung zu untersuchen. Wir zeigen, dass die Geometrie eine entscheidende Rolle spielt, da die Zugabe einer Schale die photothermale Antwort stark reduziert, während die Einbeziehung von Satelliten die photothermischen Eigenschaften fast unverändert lässt.

Schließlich erweitern wir den Fokus auf Ensembles von Nanopartikeln und demonstrieren die Anwendbarkeit und Genauigkeit der Anti-Stokes-Thermometrie für die Untersuchung der photothermalen Eigenschaften von plasmonischen Ensembles. Dieses Kapitel baut auf das aus den vorherigen Einzelpartikeluntersuchungen gewonnene Wissen auf. Wir validieren die Zuverlässigkeit dieses ensemble-basierten Ansatzes durch den Vergleich mit Quadriwave-Scherinterferometrie.

Diese Arbeit trägt zur Weiterentwicklung von plasmonischen Nanoantennen zur Energieumwandlung bei, indem wertvolle Einblicke in die zugrunde liegenden Mechanismen gegeben werden. Das aus dieser Arbeit gewonnene Wissen wird nicht nur die Gestaltung effizienterer und nachhaltigerer Technologien zur Energieumwandlung leiten, sondern auch unser Verständnis von plasmonischen Materialien und ihren vielfältigen Anwendungen erweitern. Durch die Integration von plasmonischer Photokatalyse, Einzelmolekül-Lokalisationsmikroskopie und photothermalen Charakterisierungstechniken zielen wir darauf ab, künftige Forschung in Bereichen wie photothermalen Therapie und solare Energieumwandlung zu erleichtern, und letztendlich dazu beizutragen, neue Nanomaterialien mit verbesserter Funktionalität und Leistung zu schaffen.

Contents

Abstract	iii
Zusammenfassung	v
1 Introduction	1
2 Fundamentals	5
2.1 A short history of <i>Plasmonics</i>	6
2.2 A theoretical description of plasmonic nanoparticles	10
2.2.1 Solving Maxwell's Equations for spherical nanoparticles	10
2.2.2 A simplification for small spherical nanoparticles	13
2.2.3 Beyond spherical particles	16
2.2.4 Near fields	16
2.2.5 Plasmon Decay	17
2.3 A phenomenological summary	18
2.4 Plasmonic nanoantennas for energy conversion	21
2.4.1 Photovoltaic	21
2.4.2 Photothermal	22
2.4.3 Photocatalytic	23
3 Single particle studies	29
3.1 Limitations of ensemble measurements	30
3.2 Fabrication of single particle arrays	30
3.2.1 The assembly of colloidal nanoparticles	30
3.2.2 Nano lithography	35
3.3 An overview of relevant single particle techniques	36
3.3.1 Dark-field scattering	36
3.3.2 Surface enhanced Raman scattering	39
3.3.3 Photoluminescence spectroscopy	41
3.3.4 Electron microscopy	43
3.3.5 Single-molecule localization microscopy	45
4 Spatial distributions in plasmon-assisted catalysis	51
4.1 Gaining mechanistic insight	52
4.2 Designing a plasmonic model nanoreactor	53
4.3 Ordered arrays of individual plasmonic nanoreactors	55
4.4 In operando single-molecule plasmonic catalysis	56
4.4.1 Probing the reactant accessibility to the gold surface	58
4.4.2 The effect of photo-exciting the reactant	59
4.4.3 Spatial distributions of reactivity	60
4.4.4 The effect of the plasmon resonance	61
4.5 Conclusions	64

5	Hybrid plasmonic catalysis	67
5.1	Hybrid plasmonic nanomaterials for solar fuels	68
5.1.1	Properties of hybrid plasmonic nanomaterials.	69
5.1.2	Plasmon-assisted reactions towards solar fuel generation.	73
5.1.3	Performance metrics	74
5.1.4	State of the art of hybrid plasmonic catalysis	76
5.1.5	Challenges in hybrid plasmonic catalysis	80
5.2	Single particle thermometry in bimetallic plasmonic nanostructures	83
5.2.1	Theoretical estimations in core shell nanoparticles	84
5.2.2	Antistokes thermometry on single core shell nanoparticles	90
5.2.3	Core satellite nanoparticles	94
5.2.4	Predictions for other metal-metal hybrids	96
5.3	Conclusions	97
6	Beyond single particles	99
6.1	Scaling up plasmonics	100
6.2	Collective effects	100
6.2.1	Near-field coupling	101
6.2.2	Plasmonic surface lattice resonances	102
6.2.3	Collective heating	102
6.3	Metasurfaces for energy conversion	103
6.4	Anti-Stokes thermometry for plasmonic ensembles	105
6.4.1	From one nanoparticle to plasmonic ensembles	105
6.4.2	Optimizing sample and setup	107
6.4.3	Photothermal properties of arrays of gold nanodisks	108
6.4.4	Comparison with wavefront imaging	109
6.5	Conclusions	111
7	Conclusions and Outlook	113
	Appendix	114
A	Supplemental material associated with Chapter 4	118
B	Supplemental material associated with Chapter 5	133
C	Supplemental material associated with Chapter 6	145
D	Supplemental material associated with Chapter 7	149
E	Personal contributions	153
	Bibliography	155
	List of Abbreviations & List of Figures	184
	Acknowledgements	190

Energy conversion and the 21st century

Figure 1.1 - Fossil fuels

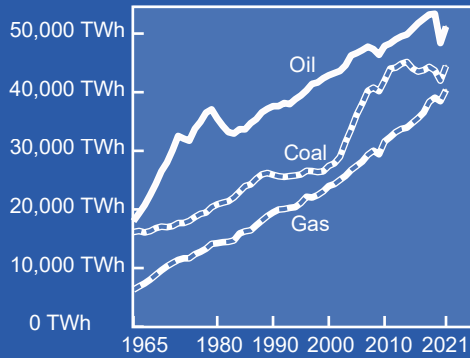


Figure 1.2 - Global warming

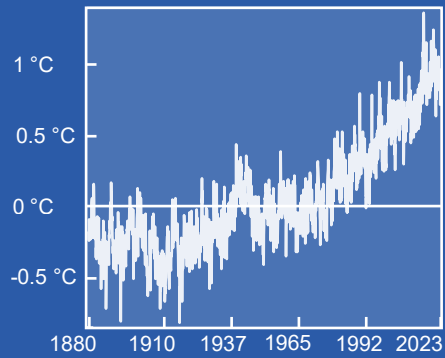


Figure 1.3 - Continuing increase of energy demands

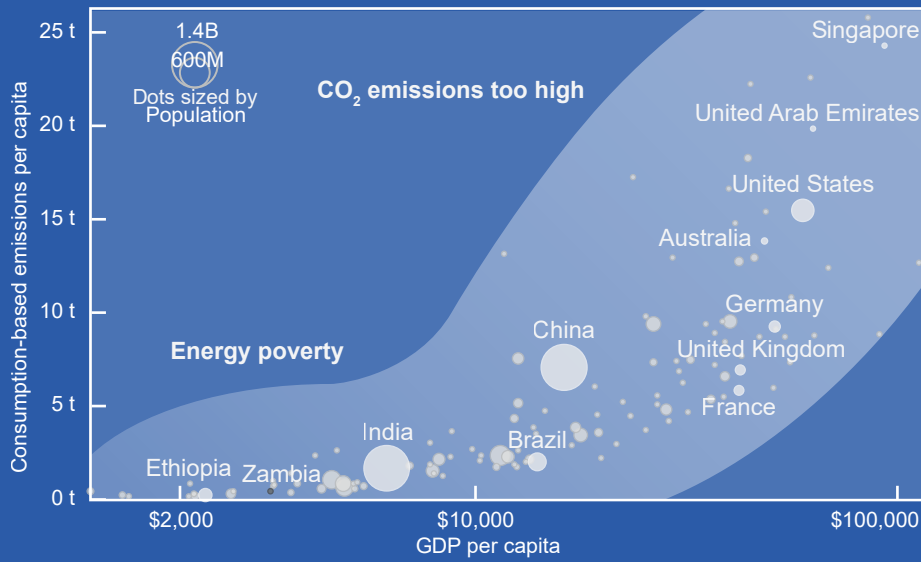
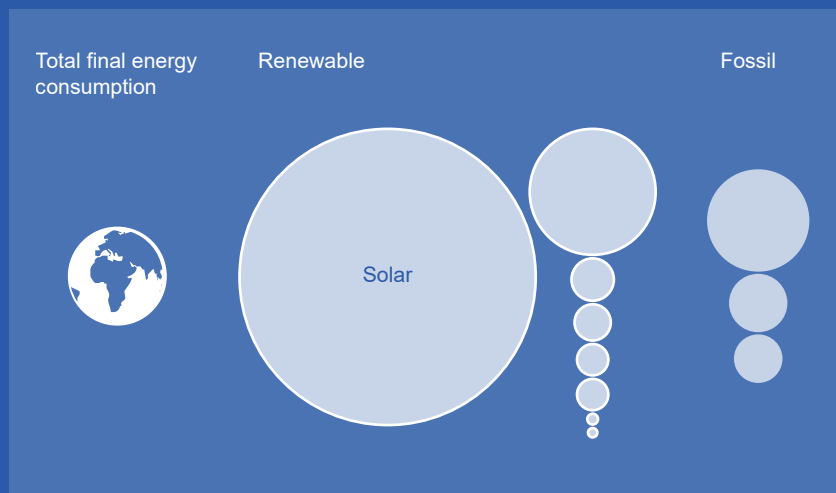


Figure 1.4 - 30 years of energy



1

Introduction

“The world is facing a double energy crisis. The majority of our energy production still results in the emission of greenhouse gases, and hundreds of millions of people still do not have adequate access to energy.”¹

Emission pathways to limit global warming to increases between 1.5°C and 2.0°C require steep reductions in global net emissions, reaching 25–45% in 2030 (compared to 2010 levels), with net-zero emissions by 2050–2070.⁸ On a per-capita basis, global emissions therefore need to go down to 2.5–3.3 tCO₂ per capita in 2030^{9,10} or less.^{11–13} While the the combustion of fossil fuels (Figure 1.1) keeps in increasing, so does the world’s average temperature (Figure 1.2). As long as we are emitting greenhouse gases their concentration in the atmosphere increases. The concentration of greenhouse gases in the atmosphere needs to stabilize and to achieve this the world’s greenhouse gas emissions have to decline towards net-zero. To bring emissions down towards net-zero will be one of the world’s biggest challenges in the years ahead. But the world’s energy problem is actually even larger than that, because the world has not one, but two energy problems.

Figure 1.3 shows the per capita CO₂ emissions on the vertical axis against the average income in that country on the horizontal axis. In countries where people have an average income between \$15,000 and \$20,000, per capita CO₂ emissions are close to the global average (4.8 tonnes CO₂ per year). In every country where people’s

Figure 1. **(1.1)** Increasing fossil fuel consumption since 1965. Source: BP Statistical Review of Global Energy. Adapted from Ref.² **(1.2)** Global warming: The monthly combined land-surface air and sea-surface water temperature anomaly is given as the deviation from the 1951–1980 mean. Source: National Aeronautics and Space Administration (NASA), Goddard Institute for Space Studies (GISS). Adapted from Ref.³ **(1.3)** CO₂ emissions against GDP in 2020. Adapted from Ref.,⁴ original data from Ref.^{5,6} **(1.4)** The area of the circles represents reasonably assured recoverable energy reserves from both finite and renewable resources over the next 30 years. These areas can be compared with total demand (earth image) over that same period. Adapted from Ref.⁷

average income is above \$25,000 the average emissions per capita are higher than the global average. High-income countries are home to only 16% of the world's population, yet they are responsible for almost half (46%) of the world's emissions.¹⁴ This is the first energy problem. The second problem is energy poverty. The reason that the emissions of low-income countries are low is the lack of access to modern energy. The lack of access to modern energy subjects people to a life in poverty. Relying on solid energy sources, such as wood, for cooking and heating is linked to high indoor air pollution, and no electricity means no refrigeration of food and no light at night. For the poorer three-quarters of the world, income growth means catching up with the living conditions of the richer world, but unless there are cheap alternatives to fossil fuels it also means catching up with the high emissions of the richer world. We want global incomes and living standards to increase. Doing so while limiting climate change is one of the greatest challenges of this century.

One promising solution to both of the world's energy problems is to harness the energy of the sun. The amount of solar energy that reaches the Earth's surface is about 5,000 times greater than the world's total energy use. Even when accounting for the land area that can reasonably be used, solar energy has the potential to cover 100 % of the global energy demand many times over (Figure 1.4). One way to capture solar energy is through photovoltaic cells, which convert sunlight directly into electricity. Photovoltaic technology has improved significantly in recent years, with increased efficiency and decreased costs. However, the usability of photovoltaic technology is limited by the intermittency of sunlight. Therefore, to fully realize the potential of solar energy, we need to develop technologies that can efficiently convert and store solar energy for use during periods of low sunlight.

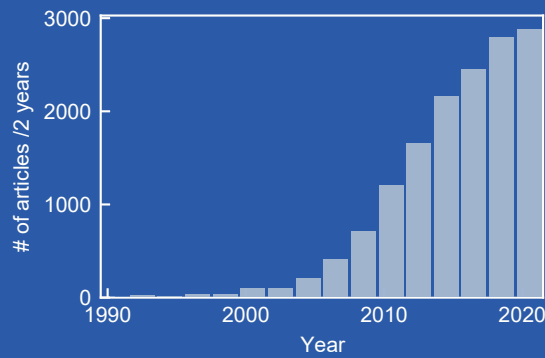
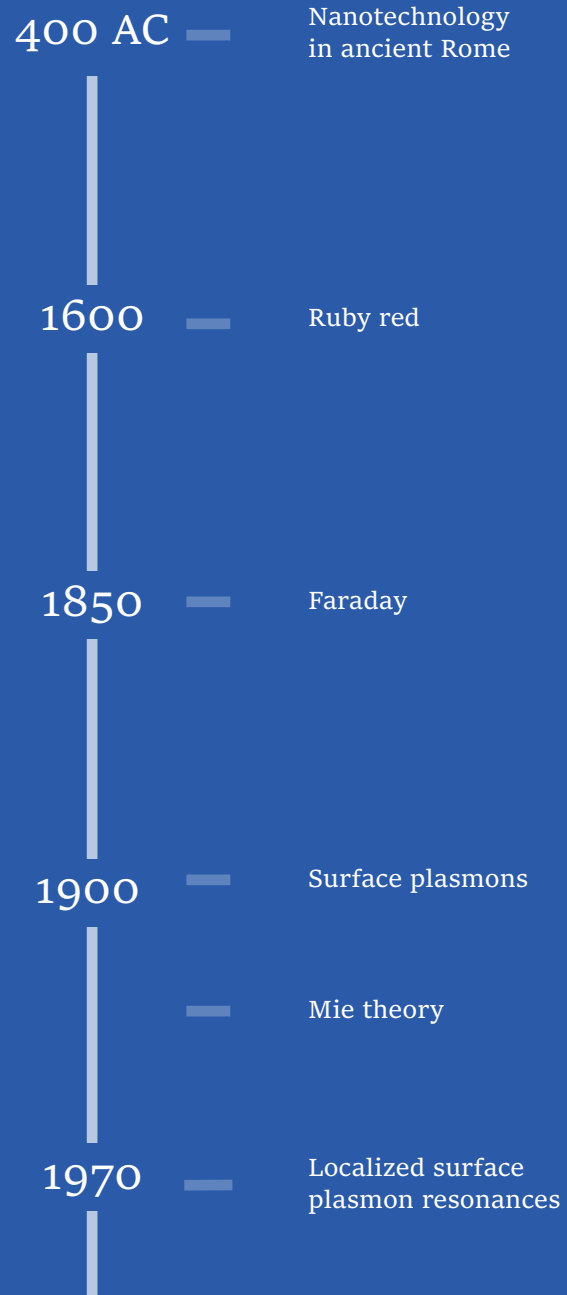
Plasmonic nanoparticles have proven to be promising candidates for such solar energy conversion processes. Plasmonic nanoparticles are metallic nanoparticles with surprising optical properties. They interact strongly with light and can absorb and concentrate light very efficiently. By tuning the material, size, shape, and composition of these nanoparticles, their properties can be tuned. As such, they have been shown to be beneficial in enhancing photovoltaic systems, but they can also act as photocatalysts. Recently, a plasmonic photocatalyst exceeded, for the first time, a photon-to-H₂ conversion efficiency of 15%.¹⁵

However, a deeper understanding of the mechanisms behind the enhancement of plasmonic nanoparticles is necessary to fully realize their potential. Single particle studies are needed to investigate the properties of individual nanoparticles, as these properties can differ from those of an ensemble of nanoparticles. By understanding the behavior of individual nanoparticles, we can optimize their design and improve their efficiency, ultimately leading to more effective solar energy conversion and storage technologies.

As the title suggests, this thesis delves into the realm of plasmonic nanoparticles for energy conversion, with a particular focus on studying them at the single particle level. In Chapter 2, we introduce the basics of plasmonic nanoparticles, including their optical properties. Then, in Chapter 3, we take a deeper dive into single particle-based methods to gain a more comprehensive understanding of these particles. Based on this foundation, we explore three systems in the subsequent chapters. Chapter 4 provides a detailed analysis of a plasmon-assisted reaction on a single metal nanoparticle, where we investigate the catalytic activity with subparticle resolution. Here, we examine the crucial contributions from hot electrons, near-fields, and temperature to gain mechanistic insight. In Chapter 5, we explore hybrid systems that combine a plasmonic metal with another catalytic component, thereby increasing the reactivity and moving closer to industrial applications. This investigation leads us to examine the performance of a hybrid system and analyze the synergy between the components. Finally, in Chapter 6, we broaden our focus and investigate ensembles of nanoparticles. This exploration is critical to understanding how these systems would perform at a scaled-up level. In this chapter, we analyze the collective properties of nanoparticle ensembles.

Overall, this thesis provides a comprehensive investigation of plasmonic nanoparticles for energy conversion, from the fundamental understanding of their properties to the practical applications of these materials. The results presented here highlight the need for a deeper understanding of the enhancement mechanisms, which can be achieved through single-particle studies, to develop efficient and effective energy conversion systems.

Plasmonics



2

Fundamentals

Plasmonic nanoparticles have unique optical properties that make them promising for energy conversion applications. This chapter provides an overview of their potential for photocatalytic, photovoltaic, and photothermal applications. The history of the field, theoretical and physical principles, and current state of the art are summarized. Plasmonic nanoparticles can interact with light in ways that are not achievable with conventional materials, leading to enhanced light absorption, scattering, and local field enhancement. Theoretical and physical principles that govern their behavior are explained, and current research trends, challenges, and opportunities are discussed. The aim is to provide a solid foundation for further investigation of the potential of plasmonic nanoparticles for energy conversion applications.

Figure 2.0 - The rise of Plasmonics. Top: A condensed version of the history of Plasmonics from Figure 2.1. Bottom: Number of published articles that include "localized/localised surface plasmon", "LSPR". Data from [Web of Science](#).

2.1 A short history of *Plasmonics*

The term *Plasmonics* was coined by Mark Brongersma and Harry Atwater in 1999.¹⁶ As can be seen in Figure 2.0, the number of articles investigating this class of materials has grown tremendously in the last two decades. Today, Plasmonics is a well-established research field that covers various aspects of surface plasmons for a variety of technologies, ranging from sensing and medical applications to different forms of energy conversion, such as photothermal, photovoltaic, and photocatalytic applications. However, the earliest findings of plasmonic materials date back more than a thousand years,^{17,18} although at that time humankind did not yet have the tools to investigate the nanoscale and therefore did not understand the physical properties associated with them. In the following, I will present a short journey through the history of *Plasmonics*, illustrated in Figure 2.1, which is a condensed version of what can be found in reviews of Brongersma,¹⁶ Hayashi *et al.*¹⁹ and Garcia *et al.*²⁰

Nanotechnology in ancient Rome. The Lycurgus cup shown in Figure 2.1 is probably the most famous example of the use of surface plasmons in ancient times. This late Roman artifact dates back to the 4th century AD and is the oldest known dichroic glass.^{17,18} It displays two distinct colors. Under direct light, it looks green, while when lit from the back, it appears red-purple. The origin of this is the presence plasmonic of metal nanoparticles. The synthesis of colloidal metal nanoparticles requires a large number of factors to be controlled, and it is clear that, at the time, the colouring of glass using gold and silver was far from routine. The inability to control the colorant process meant that relatively few glasses of this type were produced, and even fewer survived.¹⁷ This outstanding example of ancient nanotechnology is displayed in the British Museum. The craft then appears to have been lost and it was not until the 16th and 17th century in Europe, that the production of glass colored with gold nanoparticles became more routine. However, the underlying mechanism was still unknown.

Ruby red. Despite not being given that name until more than a century later, Michael Faraday's research is considered to represent the beginning of the research field we now call *Plasmonics*. He conducted systematic studies on light-matter interactions back in the 1850s.²¹ He fabricated and studied gold colloidal particles, looking closely at their distinctive ruby-red hues. A glass flask with gold nanoparticles created by Faraday himself, more than 150 years old, is still on display at the Faraday Museum. By the way cones of light travelled through dilute dispersions of gold nanoparticles, he knew that the color originated from minute particles even though they were too small to be observed with any technique at the time. At the beginning of the 20th century, the works of James Clerk Maxwell Garnett and Gustav Mie shed light on the physical origins of the bright colors of small metal nanoparticles; we will discuss Mie theory in 2.2.

Figure 2.1 History of Plasmonics. Photographs of the Lycurgus Cup adapted with permission from Ref.²² Copyright The Trustees of the British Museum (CC BY-NC-SA 4.0). Photograph of a ruby red glass adapted with permission from Ref.²³ Copyright The Corning Museum of Glass (CC BY-NC-SA 4.0). Print of Faraday lecturing, taken from the Illustrated London News; 1856.

A short history of Plasmonics

1600



In the 16th and 17th century in Europe, the production of glass colored with gold nanoparticles became more routine. Alchemists made „Gold Ruby“ and „Cranberry“ glasses. However, the underlying mechanism was still unknown.

400 AC



The Lycurgus cup is the oldest known dichroic glass. Under direct light, it looks green, while when lit from the back, it appears red-purple. This is due to the presence plasmonic **metal nanoparticles**.

1850



X. THE BAKERIAN LECTURE. - *Experimental Relations of Gold (and other Metals) to Light*. By MICHAEL FARADAY.

In the 1850s, Faraday fabricated and studied gold colloidal particles, looking closely at their distinctive ruby red hues. He was the first to understand that the color originated from minute particles even though they were too small to be observed with any technique at the time.

Surface Plasmons. To introduce the term "plasmons" we have to make a small detour; we will get back to metal nanoparticles in the 1970s. At the beginning of the 20th century, around the same time as the work of Maxwell Garnett and Mie on the optical properties of metal nanoparticles, Robert W. Wood perceived some unexplained features in optical reflection measurements he performed on metallic gratings. Over the course of the next decades, this was explained by propagating collective oscillations of free electrons at the interface between a metal and a dielectric material. These oscillations were later called "surface plasmons", and they have many applications, as they allow the confinement of light into subwavelength scales. We will not go into more detail on these surface plasmons in this thesis, and the interested reader is referred to the book by Stefan A. Maier.²⁴ Instead, we reconnect with our metal nanoparticles.

Collective oscillations in metal nanoparticles In 1970, Uwe Kreibig and Peter Zacharias analyzed the electronic and optical response of gold and silver nanoparticles.²⁵ In this work, for the first time, the optical properties of metal nanoparticles were described in the context of "*localized surface plasmon*" excitations. In contrast to the previously described surface plasmons that propagate along the surface, localized surface plasmons are a result of the confinement of a surface plasmon in a nanoparticle of size comparable to or smaller than the wavelength of light used to excite the plasmon. At the plasmon resonance frequency, the nanoparticle interacts very strongly with light. The distinct colors in ruby red or the Lycurgus cup are striking consequences of this, and they are a result of the fact that for noble metal nanoparticles the resonances lie at visible wavelengths.

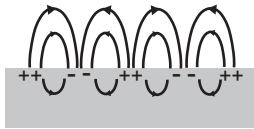
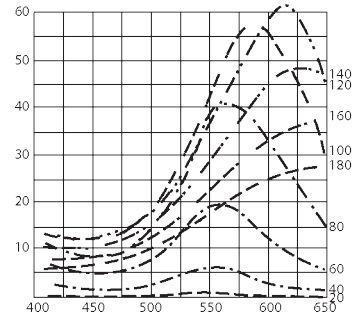
A plethora of resonances and applications. The optical properties of plasmonic nanoparticles are highly dependent on their size, shape, and composition, and can be tuned by controlling these parameters. The figure on the right shows exemplary colorful dispersions of different metal nanoparticles from our lab (synthesized by Matias Herran and Seunghoon Lee) in water. Apart from enhanced absorption and scattering at the plasmon resonances, which are the origin of the bright colors of the nanoparticles, localized plasmon resonances also result in high light intensities in confined regions close to the metal surface, an increase in temperature, and the generation of high-energy charge carriers. As a result, plasmonic nanoparticles have a wide range of potential applications, including sensing, imaging, and catalysis. In the following, we will present an overview of the theory behind the properties of localized plasmon resonances. A summary of these properties is presented on a phenomenological level in Section 2.3.

Figure 2.2 History of Plasmonics. Figure from Gustav Mie adapted with permission from Ref.²⁶ Photograph of dispersions of colloidal metal nanoparticles in water. From left to right: platinum (diameter around 5 nm), gold-platinum core-shell (diameter around 30 nm), gold (diameter around 20 nm), silver (diameter around 20 nm), silver prisms (edge length around 35 nm).

1900

XLII. *On a Remarkable Case of Uneven Distribution of Light in a Diffraction Grating Spectrum.* By R.W. WOOD, 1902

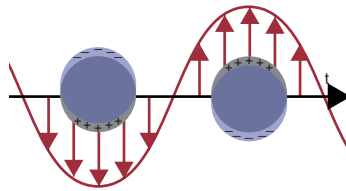
In 1902 Wood perceived some unexplained features in optical reflection measurements he performed on metallic gratings.



Over the next decades, this was explained by propagating collective oscillations of free electrons. These oscillations were later called **surface plasmons**.

At the beginning of the 20th century, Mie shed light on the physical origins of the bright colors of small metal nanoparticles. He solved Maxwell's Equations for gold nanoparticles and was able to explain and predict the color depending on nanoparticle size.

1970



In 1970, Kreibig and Zacharias discovered that the optical properties of metal nanoparticles can be described in the context of **localized surface plasmon resonances**.

2023

Numerous applications, from sensing, cancer treatments, to catalysis



2.2 A theoretical description of plasmonic nanoparticles

Now that we have an overview of the origins of the field of Plasmonics, let us dive into the physics of these striking optical properties. In this section, we will take a look at the theoretical description of localized surface plasmon resonances. A phenomenological summary of the most prominent plasmonic effects that are established here can be found in Section 2.3, after which we will also see how they can be exploited for energy conversion.

2.2.1 Solving Maxwell's Equations for spherical nanoparticles

In 1908, Gustav Mie published what is now known as *Mie theory*.²⁶ Mie provided a rigorous (but complicated) solution to the problem of scattering of light by spherical particles. It is not actually a theory; it is the analytical solutions of Maxwell's equations (2.1) for the absorption and scattering of light by a spherical particle.

Using Mie theory, the scattering from spherical particles of any size and at any wavelength can be calculated. So, let us start with Maxwell's equations named after James Clerk Maxwell. Maxwell took a set of known experimental laws (Faraday's Law and Ampere's Law) and unified them into a set of four elegant equations:

$$\nabla \cdot \mathbf{D} = \rho_{ext} \quad (2.1a)$$

$$\nabla \cdot \mathbf{B} = 0 \quad (2.1b)$$

$$\nabla \times \mathbf{E} = -\frac{\partial \mathbf{B}}{\partial t} \quad (2.1c)$$

$$\nabla \times \mathbf{H} = \mathbf{J}_{ext} + \frac{\partial \mathbf{D}}{\partial t} \quad (2.1d)$$

Where \mathbf{D} (the dielectric displacement), \mathbf{E} (the electric field), \mathbf{H} (the magnetic field), and \mathbf{B} (the magnetic induction or magnetic flux density) are the four macroscopic fields and ρ_{ext} and J_{ext} are the external charge and current densities. These equations describe how electric and magnetic field propagate, interact, and how they are influenced by objects. Just like the law of gravity, Maxwell's Equations are laws that govern our world. To solve Maxwell's equations for the scattering of a spherical particle, Mie followed the following approach.

1. Define the scattering problem in spherical coordinates
2. Express wave functions by a serial expansion of spherical harmonics
3. Implement electromagnetic boundary conditions at the sphere surface

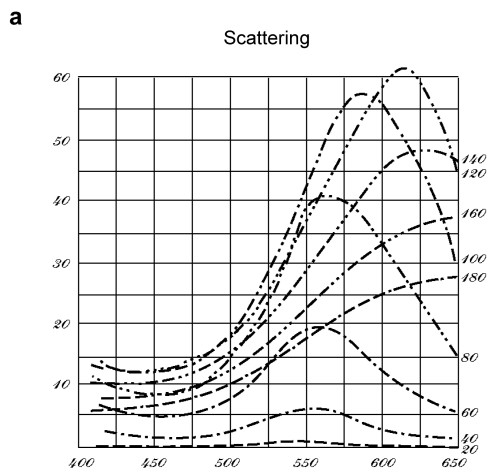


Fig. 14. Ausstrahlung kolloidaler Goldlösungen.

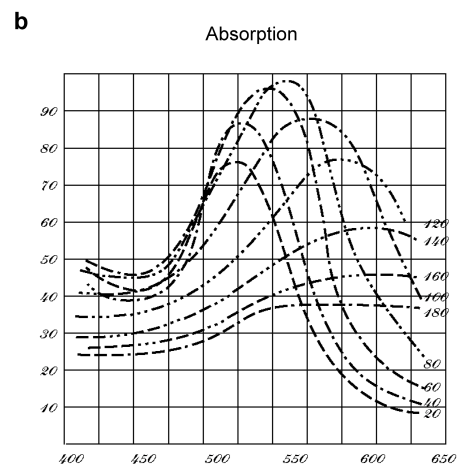


Fig. 25. Absorption kolloidaler Goldlösungen.

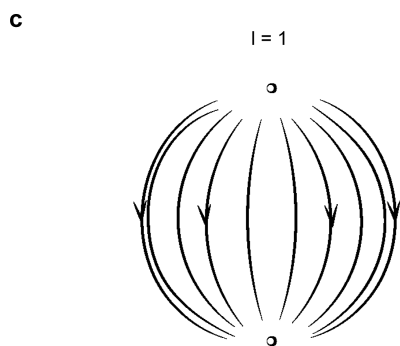


Fig. 3. Erste elektrische Partialschwingung

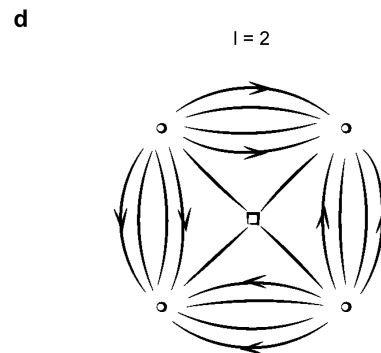


Fig. 5. Zweite elektrische Partialschwingung

Figure 2.2: **Mie theory - adapted from the original manuscript.** Scattering (**a**) and absorption (**b**) of colloidal gold solutions as calculated by Gustav Mie. It shows the size dependencies, with particle diameters ranging from 20 nm to 180 nm. (**c**) The electric Mie dipole resonance. (**d**) The electric Mie quadrupole resonance. Adapted with permission from Ref.²⁶

Details of the derivation can be found in Gustav Mie's original German manuscript.²⁶ It can be shown that the scattering efficiency Q_{scat} and the absorption efficiency Q_{abs} of spherical particles are given by:¹⁹

$$Q_{ext} = \frac{2}{((2\pi/\lambda)\sqrt{\epsilon_m}R)^2} \sum_{l=1}^{\infty} (2l+1) \text{Re}(a_l + b_l), \quad (2.2a)$$

$$Q_{scat} = \frac{2}{((2\pi/\lambda)\sqrt{\epsilon_m}R)^2} \sum_{l=1}^{\infty} (2l+1)(|a_l|^2 + |b_l|^2) \quad (2.2b)$$

$$Q_{abs} = Q_{ext} - Q_{scat} \quad (2.2c)$$

In this set of equations, R is the radius of the sphere, λ is the wavelength of the incident light and ϵ_m is the dielectric constant of the medium surrounding the sphere. a_l and b_l are the electric and magnetic Mie coefficients and expressed in terms of spherical Bessel and Hankel functions. The contributions in these sums, indexed by l , correspond to the orders of a multipole expansion with $l = 1$ being the dipole term, $l = 2$ being the quadrupole term, and so forth. From the efficiencies, the optical cross sections are calculated by simply multiplying with the geometrical cross section (πr^2 for spherical particles). From Equations 2.2 one can see that both the radius of the particle as well as its environment influence the resonance. As R increases, the peaks shift to longer wavelengths. Additionally, the relative contributions of Q_{scat} and Q_{abs} change. As R decreases, the relative contribution of Q_{abs} increases. In his seminal paper, Mie performed calculations for colloidal gold solutions of different-sized gold nanoparticles. His results are shown in Figure 2.2a-b. Figure 2.2c-d shows the electric modes for different orders.

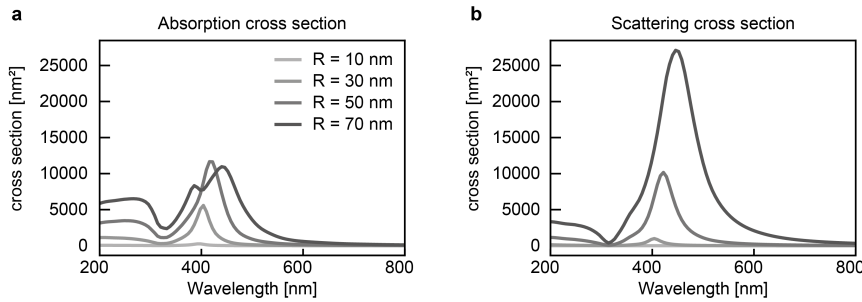


Figure 2.3: **Mie theory - calculations.** Silver nanospheres in water calculated using <https://nanocomposix.com/pages/mie-theory-calculator>.

Mie theory involves rather complex mathematics and physics, but there are several tools now available to calculate the optical properties of spherical nanoparticles in seconds. Figure 2.3 shows exemplary calculations for silver nanoparticles in water. Again, we see that the absorption dominates for small particles. With increasing size, the relative contribution of the scattering increases, until the scattering clearly dominates. Lastly, it is worth noting that for larger particles higher-order modes appear. For small particles much smaller than the wavelength of light, the spectra look much simpler and can be approximated by dipoles. We will further study this limit in the next section.

2.2.2 A simplification for small spherical nanoparticles

Mie's calculations work for spherical particles of any size, but the solution is rather complicated. For sufficiently small nanoparticles, much smaller than the wavelength of light, a quasistatic approximation of Maxwell's Equations can be used. In this case, the phase of the harmonically oscillating electromagnetic field can be assumed to be constant over the particle volume. This means that the field can be considered to be spatially uniform, apart from a time varying factor ($\mathbf{E}_0 e^{i\mathbf{k}\cdot\mathbf{r}-i\omega t} \approx \mathbf{E}_0 e^{-i\omega t}$). We can then solve the simplified problem of a particle in an electrostatic field and add the harmonic time dependence later. For this, we will follow the description from the book of Stefan A. Maier.²⁴

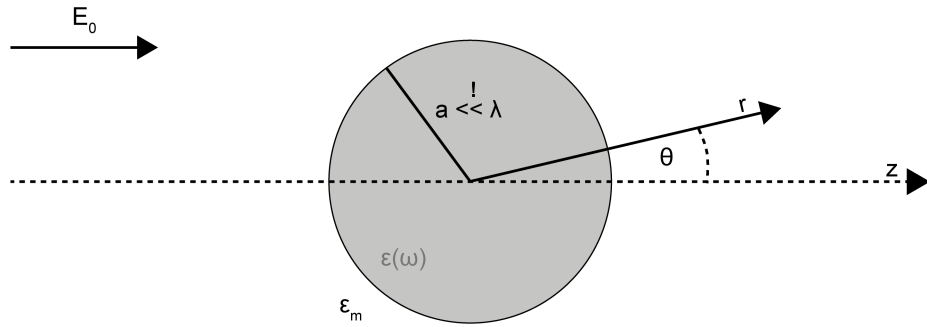


Figure 2.4: **Quasistatic approximation.** A homogenous, isotropic sphere of radius a - much smaller than the wavelength of light - in a uniform, static electric Field $\mathbf{E} = E_0 \hat{\mathbf{z}}$. At sufficient distance from the sphere, the field lines are parallel to the z -direction. The surrounding medium is isotropic and non-absorbing with the dielectric constant ϵ_m and we describe the dielectric response of the sphere by the complex number ϵ . θ is the angle between the position vector \mathbf{r} and the z -axis.

In this electrostatic approach, we are interested in a solution of the *Laplace equation* for the potential:

$$\nabla^2 \phi = 0 \quad (2.3)$$

From the potential ϕ , we will then be able to calculate the electric field $\mathbf{E} = -\nabla \phi$.

The geometry of our system is shown in Figure 2.4: A homogeneous isotropic sphere of radius a is placed in a uniform, static electric Field $\mathbf{E} = E_0 \hat{\mathbf{z}}$. At a sufficient distance from the sphere, the field lines are parallel to the z -direction. The surrounding medium is isotropic and non-absorbing with the dielectric constant ϵ_m and we describe the dielectric response of the sphere by the complex number ϵ (technically, it is described by the dielectric function $\epsilon(\omega)$). θ is the angle between the position vector \mathbf{r} and the z -axis.

This system has azimuthal symmetry and the general solution of Equation 2.3 is:²⁴

$$\phi(r, \theta) = \sum_{l=0}^{\infty} [A_l r^l + B_l r^{-(l+1)}] P_l(\cos(\theta)). \quad (2.4)$$

Here, $P_l(\cos(\theta))$ are the Legendre Polynomial of order l . We require that the potentials remain finite at the origin:

$$\phi_{in}(r, \theta) = \sum_{l=0}^{\infty} A_{l,in} r^l P_l(\cos(\theta)) \quad (2.5a)$$

$$\phi_{out}(r, \theta) = \sum_{l=0}^{\infty} [A_{l,out} r^l + B_{l,out} r^{-(l+1)}] P_l(\cos(\theta)). \quad (2.5b)$$

The coefficient $A_{l,in}$, $A_{l,out}$ and $B_{l,out}$ can now be determined from the boundary conditions at $r \rightarrow \infty$ and $r = a$.

At $r \rightarrow \infty$ we require the electric field to be $-E_0 z = -E_0 r \cos\theta$, which results in $A_{1,out} = -E_0$ and $A_{l,out} = 0$ for $l \neq 1$. At $r = a$ we require the equality of tangential and normal components of the electric field:

$$-\frac{1}{a} \frac{\partial \phi_{in}}{\partial \theta} \Big|_{r=a} = -\frac{1}{a} \frac{\partial \phi_{out}}{\partial \theta} \Big|_{r=a} \quad (2.6a)$$

$$-\epsilon_0 \epsilon \frac{\partial \phi_{in}}{\partial r} \Big|_{r=a} = -\frac{1}{a} \frac{\partial \phi_{out}}{\partial r} \Big|_{r=a} \quad (2.6b)$$

The application of the boundary conditions in Equation 2.6 ultimately leads to:²⁴

$$\phi_{in} = -\frac{3\epsilon_m}{\epsilon + 2\epsilon_m} E_0 r \cos\theta \quad (2.7a)$$

$$\phi_{out} = -E_0 r \cos\theta + \frac{\epsilon - \epsilon_m}{\epsilon + 2\epsilon_m} E_0 a^3 \frac{\cos\theta}{r^2}. \quad (2.7b)$$

If we take a closer look at Equation 2.7b we can rewrite it by introducing the dipole moment $\mathbf{p} = 4\pi\epsilon_0\epsilon_m a^3 \frac{\epsilon - \epsilon_m}{\epsilon + 2\epsilon_m} \mathbf{E}_0$:

$$\phi_{out} = -E_0 r \cos\theta + \frac{\mathbf{p} \cdot \mathbf{r}}{4\pi\epsilon_0\epsilon_m r^3} \quad (2.8)$$

From this we can see that the application of a field to a nanoparticle induces a dipole moment. If we further introduce the polarizability α , defined as $\mathbf{p} = \epsilon_0\epsilon_m \alpha \mathbf{E}_0$, we finally arrive at:

$$\alpha = 4\pi a^3 \frac{\epsilon - \epsilon_m}{\epsilon + 2\epsilon_m} \quad (2.9)$$

It is apparent that the polarizability experiences a resonant enhancement under the condition that $|\epsilon + 2\epsilon_m|$ is minimized. Based on the classic Drude model, $\epsilon(\omega)$ is a complex term whose real ($Re[\epsilon(\omega)]$) and imaginary ($Im[\epsilon(\omega)]$) parts can be estimated as a function of the excitation wavelength, the plasma frequency of the bulky metal, and the collision frequency of the free electron gas²⁴

For the case of a small or slowly-varying $Im[\epsilon]$ around the resonance, Equation 2.9 simplifies to

$$Re[\epsilon(\omega)] = -2\epsilon_m \quad (2.10)$$

This relationship is also called the Fröhlich condition and the associated mode (in an oscillating field) the *dipole surface plasmon* of the metal nanoparticle. The same relation can also be recovered by taking only into account the first mode in Mie theory. For coinage metals, the resonance condition is satisfied under visible-light excitation.

The electric field can be evaluated from the potentials ($\mathbf{E} = -\nabla\phi$). The resonance in α also implies a resonant enhancement of both the internal and dipolar fields. Apart from the large cross-sections we already saw in Mie theory, this field-enhancement at the plasmon resonance is the basis for many applications related to catalysis or sensing, some of which we will discuss in more detail throughout this thesis.

Let us return to the absorption and scattering properties that we discussed in Mie theory, now in the quasi-static approximation.

From α the corresponding cross section for scattering and absorption C_{scat} and C_{abs} can be calculated to²⁷

$$C_{scat} = \frac{k^4}{6\pi} |\alpha|^2 = \frac{8\pi}{3} k^4 a^6 \left| \frac{\epsilon - \epsilon_m}{\epsilon + 2\epsilon_m} \right|^2 \quad (2.11a)$$

$$C_{abs} = k \text{Im}[\alpha] = 4\pi k a^3 \text{Im} \left[\frac{\epsilon - \epsilon_m}{\epsilon + 2\epsilon_m} \right] \quad (2.11b)$$

Again, we see that both the absorption and scattering are resonantly enhanced at the dipole particle plasmon resonance. The plasmonic structure collects photons over a region larger than its physical size (as an antenna does) and concentrates that energy in a much smaller volume. Notably, the absorption cross section scales with a^3 while the scattering cross section scales with a^6 . As in Mie theory, we see that while absorption is dominant for very small nanoparticles, the relative contribution of the scattering to the extinction increases with increasing size. To summarize, in the quasistatic approximation we can think of localized surface plasmon resonances as resonances in the polarizability of the electron cloud. The electric field exerts a force on the electrons, polarizing the electron cloud. This picture is illustrated in Figure 2.5.

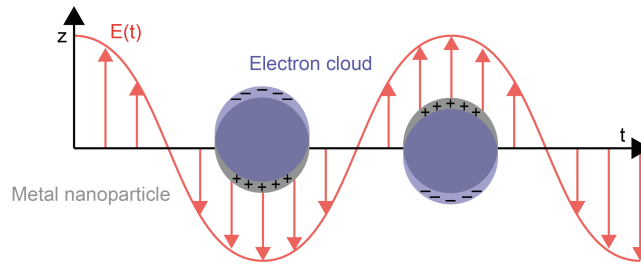


Figure 2.5: **A small nanoparticle in an oscillating electric field.** The electric field exerts a force on the electron cloud. The polarization is maximized at the localized surface plasmon resonance.

2.2.3 Beyond spherical particles

In the last decades, the synthesis of colloidal nanoparticles has been extended beyond spherical gold nanoparticles to both other metals but also more complex geometries. A few examples will be presented in Chapter 3. While spherical geometries have been treated by Mie-theory or in the quasi-static approximation, more complex geometries do not have analytical solutions to Maxwell's equations, and we have to resort to numerical methods. Finite-Difference Time-Domain (FDTD) simulations are a commonly used numerical method to model and solve Maxwell's equations, which govern the behavior of electromagnetic waves. The FDTD method discretizes both time and space and advances the electromagnetic fields over small time steps, computing the fields at each spatial point. The fields are then updated at each time step using the finite-difference approximation of Maxwell's equations. This process is repeated over many time steps to obtain a complete simulation of the electromagnetic fields.

2.2.4 Near fields

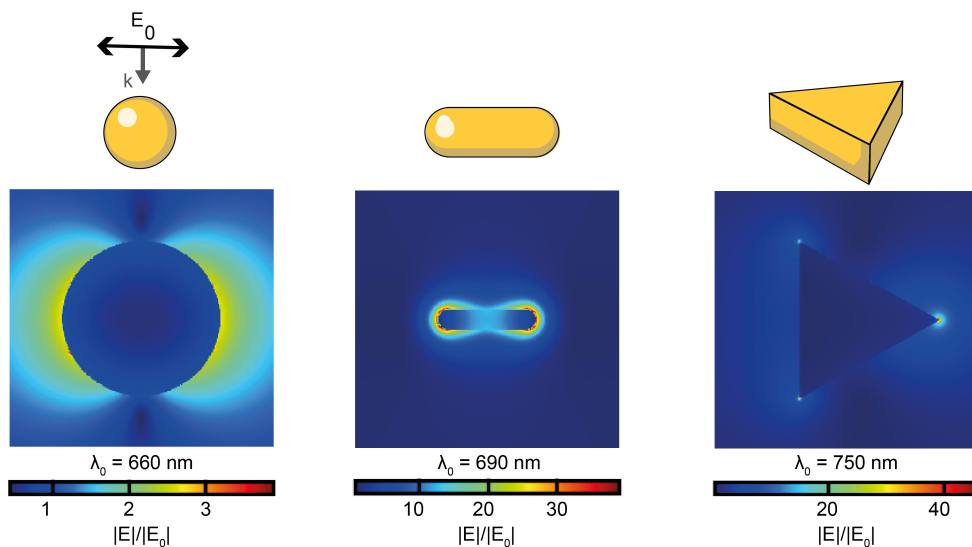


Figure 2.6: **Near fields.** Electric field distribution for gold nanoparticles with different geometries excited with linearly polarized light in free space. From left to right: Gold sphere, radius 90 nm; Gold rod, length: 76 nm radius 8 nm; Gold triangle, side length 105 nm. Adapted with permission from Ref.²⁸

In the framework of Mie theory, it is also possible to calculate the fields in the vicinity of the particle surface (near field).¹⁹ The near field refers to a distance of a few nanometers from the metallic structure, generally much smaller than the wavelength of light. The far-field and near-field resonances correlate quite well, although the positions and shapes of the peaks are slightly different.¹⁹ Again, beyond spherical particles, the near fields are calculated using simulations. Some illustrative examples are shown Figure 2.6. In the near-field region, the plasmon resonances are highly confined. Depending on the geometry, the fields near the particle surface can exhibit complex spatial patterns and can form *hotspots* where the intensity reaches values that are many orders of magnitude larger than the incident fields. This so-called *field enhancement* and can be utilized for surface-enhanced spectroscopy and sensing, among others.

2.2.5 Plasmon Decay

The plasmon resonance is damped by two competing processes that depend on the size and shape of the nanoparticle, as well as the refractive index of the surrounding medium. One is a radiative decay into photons, dominating for larger particles. The second is a non-radiative process due to absorption. The non-radiative decay is due to the creation of electron-hole pairs via either intraband excitations with the conduction band or interband transitions, which for noble metal particles are from lower-lying d-bands to the sp conduction band. Damping is often characterized by the "line width" of the plasmon resonance, which is a measure of how "sharp" or "narrow" the resonance peak is. A smaller linewidth corresponds to a more efficient trapping of energy in the plasmon mode and a longer plasmon lifetime.

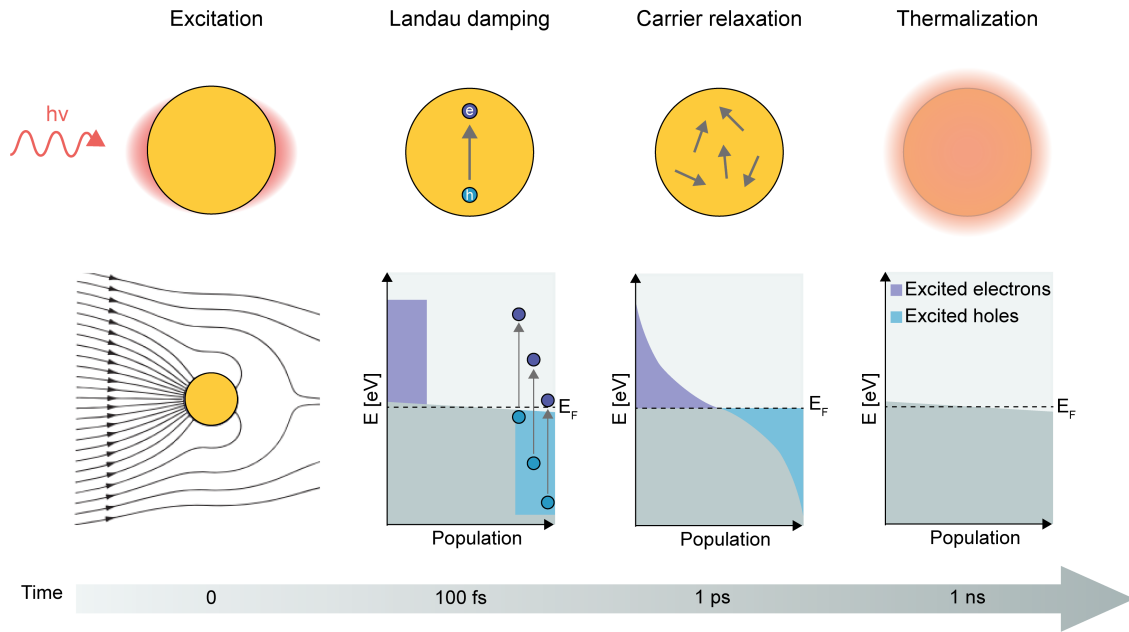


Figure 2.7: **Plasmon Decay.** Photoexcitation and subsequent relaxation processes following the illumination of a metal nanoparticle with characteristic timescales. The large optical cross section of the plasmonic nanoparticle leads to a large absorption of light and high local fields. In the first ~ 1 -100 fs localized surface plasmons dephase, and excited electron-hole pairs are produced by Landau damping and other photon-electron interactions. Hot electrons are represented by the purple areas above the Fermi energy E_F and hot holes distributions are represented by the blue area below E_F . Subsequently, the hot carriers will redistribute their energy by electron-electron scattering processes (100 fs - 1 ps) and electron-phonon scattering (1 ps - 10 ps). Finally, on a timescale of 100 ps to 10 ns, via phonon-phonon interactions. Adapted from Ref.,²⁹ the bottom left is adapted from Ref.³⁰

Shorter lifetimes due to faster dephasing result in a broadening of the plasmon resonance, and the line width of the plasmon resonance Γ is characterized by the time constant T_2 . The line width of the plasmon resonance then reads

$$\Gamma = \frac{2\hbar}{T_2} \quad (2.12)$$

The strength of a plasmon resonance can also be expressed using the notion of a *quality factor* $Q = E_{res}/\Gamma$.

The decay dynamics are well described by different processes that occur on different time scales, illustrated in Figure 2.7: At the very beginning, localized surface plasmons dephase, and excited electron–hole pairs are produced by Landau damping and other photon–electron interactions. During this short period, the excited electron–hole pairs described by a highly non-thermal distribution decay either through the re-emission of photons or the multiplication of carriers via electron–electron interactions (< 100 fs). Subsequently, the relaxation from this non-Fermi to a quasi-Fermi electron distribution through *electron-electron (e-e) scattering* (100 fs - 1 ps) and *electron-phonon (e-ph) scattering* (1 – 10ps), Ultimately, on a relatively long timescale, thermal energy is released into the environment, through *phonon-phonon (ph-ph) scattering* ($< (100$ ps - 10 ns)).^{31,32} For very small particles, where the bulk electron mean path is larger than the particle diameter, the dephasing of the coherent oscillation is further increased due to elastic scattering at the particle surface. This process is called chemical interface damping (not shown).

To summarize, the effects induced by the excitation and relaxation of localized surface plasmons can be favourably listed as electromagnetic near-field enhancement, charge-carrier excitation and local heating effects. In the following section we will summarize the learnings from the entire theoretical Section 2.2.

2.3 A phenomenological summary

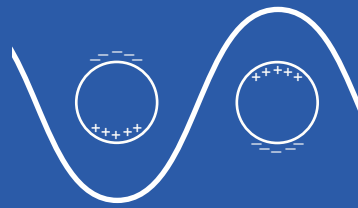
While Section 2.2 provided a theoretical and physical picture of localized surface plasmon resonances and their effects, this section is a phenomenological summary, illustrated on the right.

Localized surface plasmon resonances (LSPRs), are a phenomenon that occurs in small metallic particles when they are exposed to light. When light hits the surface of the particle, it excites the electrons in the metal, causing them to oscillate. There is a resonance frequency at which the particle interacts strongly with the light. This is the localized surface plasmon resonance.

The excitation of LSPRs, has multiple effects

1. In the vicinity of the nanoparticle, the intensity of light can be orders of magnitude higher than the incident intensity. Additionally, the field is confined in nanometer-sized volumes. By changing the geometry or combining particles with small interparticle distances, the magnitude of these so-called "**hot spot**" can be increased, resulting in very **high fields**. In this sense, plasmonic nanoparticles act as concentrators of light, which can be exploited in photovoltaics, sensing, or catalysis.
2. The excitation of localized surface plasmon resonances results in the generation of high-energy charge carriers, so called "**hot electrons**" or "hot holes". These charge carriers can be extracted for a variety of applications, such as photovoltaics or photocatalysis.
3. The oscillation of electrons in the nanoparticle ultimately generates **heat**. Again, there are numerous photothermal applications, ranging from cancer therapies to catalysis.

Localized surface plasmon resonances explained



Resonant interaction with light

Localized surface plasmon resonances are a phenomenon that occurs in small metallic particles when they are exposed to light. The electrons in the metal oscillate. On resonance, the particle interacts strongly with light, leading to an increased absorption



Light concentration

The resonance can cause an enhancement of the electric field near the surface of the particle. In nanosized regions the intensity of light is many times larger than the incident light.



Excited electrons

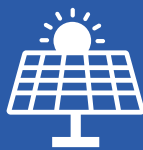
The increased absorption results in the generation of high energy charge carriers that can be extracted.



Temperature increase

When light is absorbed, it is ultimately converted into heat, causing the temperature of the particle and its surroundings to increase.

Applications



Photovoltaics



Diagnostics & Photothermal therapies



Photo & Thermal catalysis



Solar fuels

In essence, the unique ability of metal nanoparticles to strongly interact with light is attributed to their localized surface plasmon resonances. With significant potential for both medical and energy conversion applications, it is critical to explore the various ways in which this strong optical response can be tuned across the electromagnetic spectrum. Before delving into the current understanding and the state-of-the-art in Section 2.4, let us take a closer look at the properties and parameters that affect the resonances.

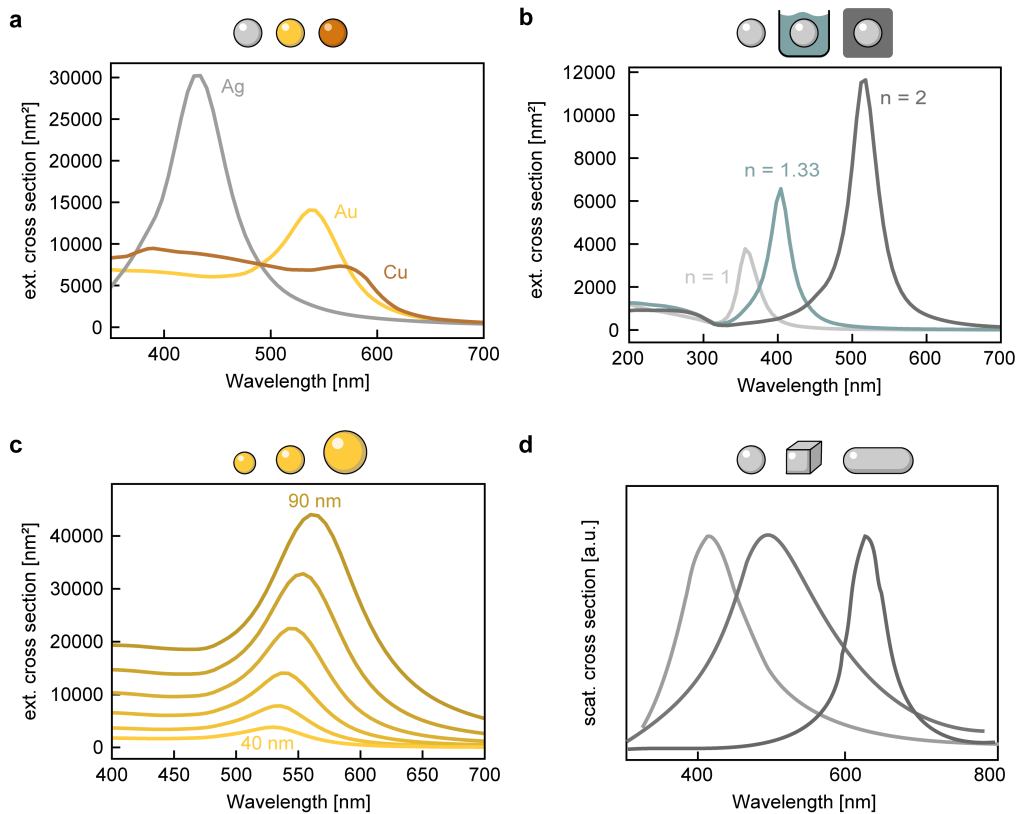


Figure 2.8: **Tunability of the resonances.** (a) Mie theory calculation of the extinction cross section of spherical nanoparticles (radius 60 nm) made of silver, gold and copper in water. (b) Mie theory calculation of the extinction cross section of spherical silver nanoparticles (radius 30 nm) embedded in different media ($n = 1$ is vacuum or air, $n = 1.33$ is water, $n = 2$ is silicon nitride). (c) Mie theory calculation of the extinction cross section of spherical gold nanoparticles of different sizes in water. (d) Illustration of the shape dependence of the normalized scattering cross section in Ag nanoparticles. d is adapted with permission from Ref. ²⁸

Material. Most importantly, the resonant wavelength of a metallic nanoparticle is influenced by the choice of material. Some common materials used in plasmonics include gold, silver and copper, and aluminum. Figure 2.8a shows the extinction cross section of spherical nanoparticles (radius 60 nm) made of different materials in water.

Medium. The plasmonic properties of the metal structure are also affected by the dielectric constant of the surrounding medium. This is illustrated in Figure 2.8b, for the same silver nanoparticle of radius 30 nm embedded in different media.

Size. Apart from the material and medium, the plasmonic characteristics of a metal nanostructure are influenced by its size. A metal structure can sustain localized surface plasmon resonances when its size is comparable to or smaller than the wavelength of the incident light. With increasing size, the resonance position redshifts, as can be seen in Figure 2.8c.

Shape. The resonance can be tuned by changing the shape from a spherical nanoparticle to more complex geometries, as shown in Figure 2.8d.

Coupling. When multiple metal structures are brought into close proximity, their plasmons can couple to form new plasmon modes with unique properties.

2.4 Plasmonic nanoantennas for energy conversion

The unique optical properties make plasmonic nanoparticles promising candidates for energy conversion applications. Generally, these processes include the conversion of light into electrical energy (photovoltaic), thermal energy (photothermal), and chemical energy (photocatalytic). In the following, we will present an overview of our current understanding of how plasmonic nanoparticles can contribute in these three areas, with a focus on photocatalytic applications.

2.4.1 Photovoltaic

This paragraph is only a brief introduction to plasmonic nanoparticles in photovoltaic applications, as photovoltaics is not a topic in this thesis. Photovoltaic systems that employ plasmonic nanoparticles can improve the efficiency of solar cells in two main ways. First, in a direct plasmonic solar cell, plasmons are used as the active photovoltaic material, relying on the hot carrier generation. Second, in a plasmon-enhanced solar cell, plasmonic enhancement is achieved through various mechanisms, including far-field scattering, near-field enhancement, and charge carrier transfer. Far-field scattering increases the absorption efficiency by decreasing reflections at the surface and by increasing the length of the optical paths of incident photons in the absorbing medium.³³ This is illustrated in Figure 2.9a. Plasmonic nanomaterials can also confine electromagnetic waves at the metal-dielectric interface and produce high intensity near-fields, again resulting in increased absorption,³³ as illustrated in Figure 2.9b. In addition, high-energy charge carriers generated by plasmon excitation can be injected into a nearby semiconductor.³³ For more information on this topic, the interested reader is referred to the review by Jang *et al.*³³

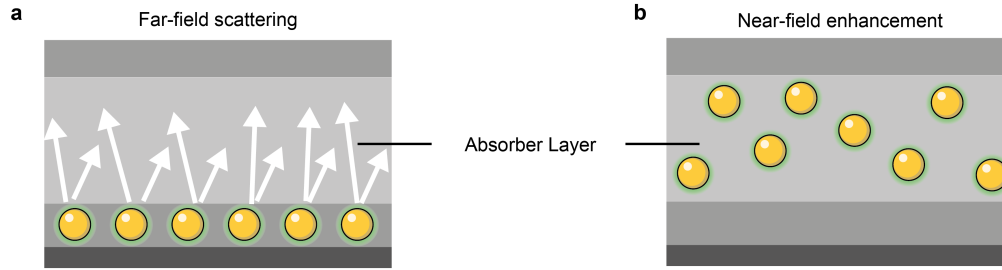


Figure 2.9: **Plasmonic nanoparticles for photovoltaics.** (a) Far-field scattering increases the absorption efficiency by decreasing reflections at the surface and by increasing the length of the optical paths of the incident photons in the absorbing medium. (b) Plasmonic nanomaterials can also confine electromagnetic waves at the metal-dielectric interface and produce high-intensity near-fields, again resulting in an increased absorption. Inspired by Ref.³⁴

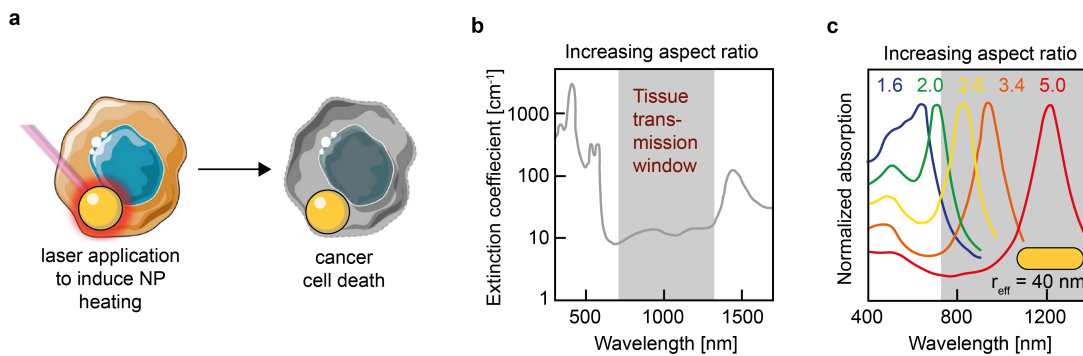


Figure 2.10: **Photothermal therapy.** (a) Photothermal therapy involves the delivery of nanoparticles into tumors, followed by laser irradiation to induce nanoparticle heating leading to cancer cell death. (b) Extinction coefficient of oxygenated blood as a representative tissue. (c) The absorption cross section of gold nanorods with varying aspect ratios with a fixed effective radius of 40 nm. (a) Adapted with permission from Ref.³⁵ (b) Adapted with permission from Ref.³⁶ (c) Adapted with permission from Ref.³⁷

2.4.2 Photothermal

We have already seen in a previous sections that with plasmon excitation, heating is unavoidable. These inherent losses were long considered detrimental, but in recent years, a number of photothermal applications have emerged. The field that exploits the heat generation of plasmon excitation is called *Thermoplasmonics*. Applications include protein denaturation, photothermal cancer therapy, drug and gene delivery, heat-assisted magnetic recording, photoacoustic imaging, plasmonic-induced nanochemistry, photothermal imaging, solar steam generation generation, and single living cell experiments³⁸ and to the interested reader I recommend the book by Guillaume Baffou from 2017,³⁸ or the more recent reviews.^{39,40} An example of plasmonic nanoparticles exploited for photothermal treatments is shown in Figure 2.10. Photothermal therapy involves the delivery of nanoparticles into tumors, followed by laser irradiation to induce nanoparticle heating leading to cancer cell death. Light absorption by healthy tissues needs to be avoided by employing wavelengths where biological tissues have a low extinction coefficient. This is illustrated in Figure 2.10b, where the

extinction coefficient of oxygenated blood (on a log scale) versus wavelength is shown. The biological window ranges from around 700 to 1400 (the water absorption bands are not considered here).³⁶ Thus, it is desirable to synthesize nanoparticles with light absorption in the near-infrared (IR) window. With the absorption wavelength tunable from visible to IR, plasmonic nanorods are suitable candidates for bioapplications. As shown in Figure 2.10c, increasing the aspect ratio of the gold nanorods gradually shifts the longitudinal absorption peak.³⁷

2.4.3 Photocatalytic

This section is based in part on our recent review on hybrid plasmonic catalysts, which we will discuss in more detail in Chapter 5. For millions of years, nature has used the sun as its primary energy source by photosynthesis during which sunlight is used to split water and produce energy-rich chemical compounds from CO₂. Inspired by this, artificial photosynthesis has become one of the most important research fields in the past decade. It consists mainly of two types of processes: one is water splitting into hydrogen (H₂) and oxygen (O₂) or the H₂ production from H₂-containing compounds, and the other is the reduction of CO₂ into fuels and chemicals, such as carbon monoxide, hydrocarbons, and oxygenates. These products are generally termed solar fuels. In artificial photosynthesis, the first step is to harvest and concentrate the solar energy in molecular-sized regions. Plasmonic nanoparticles are promising materials to perform these tasks, due to their exceptional absorption and their ability to control light and heat at the nanoscale.^{24,41–43} Therefore, plasmon-assisted catalysis is a young but growing field. For the interested reader I recommend the following reviews,^{44–46} perspectives^{47–49} and book⁵⁰ covering different topics of the area. Some of these resources focus on the theoretical aspects and the working mechanisms of plasmonic photocatalysis.^{51–53} Others discuss reactions driven by a particular plasmon-induced phenomenon, such as hot carrier generation,⁵⁴ photothermal effects⁵⁵ or both.⁵⁶ Furthermore, Devasia *et al.* focus on the possibility of controlling reaction pathways with plasmonic systems.⁵⁷ Finally, some reviews focus on particular reactions, such as the applications of plasmonic catalysts to organic transformations⁵⁸ or the CO₂ reduction reaction (CO₂RR).⁵⁹ It should be noted that in the field, two types of plasmon-assisted reactions are grouped under the term "plasmon-assisted catalysis": photocatalytic processes (typically thermodynamically favorable, $\Delta G < 0$, with G the Gibbs free energy) and photosynthetic processes (thermodynamically unfavorable, $\Delta G > 0$). For simplicity, from now on they will be referred to as photocatalytic. Among the large list of recently demonstrated plasmon-assisted reactions, Table 2.1 shows a few particularly relevant reactions towards the generation of solar fuels: H₂ generation reactions and CO₂ reduction reactions.

Hydrogen generation

Because hydrogen can be burned with no greenhouse emissions, it is a promising candidate to replace fossil fuels. Hydrogen has a high gravimetric energy density of 33.3 kW h kg⁻¹, which is almost three times higher than that of gasoline (12.4 kW h kg⁻¹).^{61,62} It is stable and can be liquefied, stored, or transported through

Reaction	Fuel
H₂ production	
$\text{NH}_3\text{BH}_3 + 3 \text{H}_2\text{O} \longrightarrow \text{NH}_4\text{B}(\text{OH}) + 3 \text{H}_2$ (Ammonia borane hydrolytic dehydrogenation)	Hydrogen
$\text{NaBH}_4 + 4 \text{H}_2\text{O} \longrightarrow \text{NaB}(\text{OH})_4 + 4 \text{H}_2$ (Sodium borohydride hydrolytic dehydrogenation)	Hydrogen
$\text{HCOOH} \longrightarrow \text{CO}_2 + \text{H}_2$ (Formic acid dehydrogenation)	Hydrogen
$2 \text{H}_2\text{O} + 4 \text{e}^- \longrightarrow 2 \text{O}_2 + \text{H}_2$ (Water splitting)	Hydrogen
CO₂ reduction	
$\text{CO}_2 + 2 \text{H}^+ + 2 \text{e}^- \longrightarrow \text{CO} + \text{H}_2\text{O}$	Carbon monoxide
$\text{CO}_2 + 2 \text{H}^+ + 2 \text{e}^- \longrightarrow \text{HCOOH}$	Formic acid
$\text{CO}_2 + 4 \text{H}^+ + 4 \text{e}^- \longrightarrow \text{HCHO} + \text{H}_2\text{O}$	Formaldehyde
$\text{CO}_2 + 6 \text{H}^+ + 6 \text{e}^- \longrightarrow \text{CH}_3\text{OH} + \text{H}_2\text{O}$	Methanol
$\text{CO}_2 + 8 \text{H}^+ + 8 \text{e}^- \longrightarrow \text{CH}_4 + 2 \text{H}_2\text{O}$	Methane
$2 \text{CO}_2 + 12 \text{H}^+ + 12 \text{e}^- \longrightarrow \text{C}_2\text{H}_5\text{OH} + 3 \text{H}_2\text{O}$	Ethanol

Table 2.1: Reactions towards solar fuel production. Adapted with permission from Ezendam *et al.*⁶⁰

pipelines. However, the majority of hydrogen is still produced from fossil fuels, resulting in excessive carbon emissions.⁶³ For hydrogen to become a sustainable fuel, it must be produced from renewable energy sources.

Photocatalytic hydrogen sources can be grouped into: 1. *water*. Solar hydrogen production via water splitting is especially attractive, since both water and sunlight are abundant. Materials for photocatalytic water splitting are either investigated towards their performance of full water splitting, where H₂ and O₂ evolution should occur in a stoichiometric 2:1 ratio, or by using a sacrificial hole acceptor, for only the hydrogen evolution reaction (HER). This simplifies research and prevents charge recombination. However, this sacrificial agent should also be cheap and abundant, as otherwise this could become a new bottleneck for the reaction to be scaled up. 2. *other hydrogen containing compounds*. While hydrogen has a high energy content per mass, its energy content per volume is poor. This makes storing enough hydrogen, e.g. on-board of means of transport, difficult. A possible solution is chemical storage in compounds with a higher storage density. This has resulted in compounds with a high hydrogen content, such as formic acid (HCOOH),⁶⁴ ammonia borane (NH₃BH₃)⁶⁵ or sodium borohydride (NaBH₄)⁶⁶ gaining attention, especially for mobile and portable applications.

Carbon dioxide reduction

Carbon dioxide (CO₂) is one of the main greenhouse gases that contributes to climate change.⁶⁷ CO₂ conversion can have the two-fold benefit of decreasing its atmospheric concentration while also producing fuels. Compared to hydrogen production, reactions for CO₂ conversion are much more complex, as a variety of reaction pathways coexist. Possible products include carbon monoxide (CO), formic acid (HCOOH), methane (CH₄), methanol (CH₃OH), ethane (C₂H₆), propane (C₃H₈), ethanol (CH₃CH₂OH), among others. These products require a different number of charge transfers, as shown in Table 2.1, and contain a different number of carbon atoms. Products with two or more carbon atoms, the so-called C2+ products, are desirable but difficult to produce.

Several steps can be involved, leading to the possibility of branching reaction pathways and various products being produced simultaneously. Therefore, a suitable large-scale photocatalyst for CO₂ reduction should not only present high efficiency but also high selectivity to one product.

One of the first plasmonic catalysis examples of CO₂ reduction was reported by Yu *et al.*⁶⁸ and is illustrated in Figure 2.11. Here, a colloidal suspension of 12 nm gold nanoparticles was employed to reduce CO₂. The nanoparticles promoted both the formation of CH₄ (Figure 2.11a) and C₂H₆ (Figure 2.11b), depending on both the wavelength and the photon flux. One of the most striking features of this report was the tunability of the reaction pathway, as it was dependent on both the energy of the photons and photon flux. This shows not only that plasmonic catalysts allow the use of visible light to drive kinetically challenging, multielectron reactions, but that they also enable control of mechanistic pathways and selectivity by appropriate choice of the light excitation characteristics.

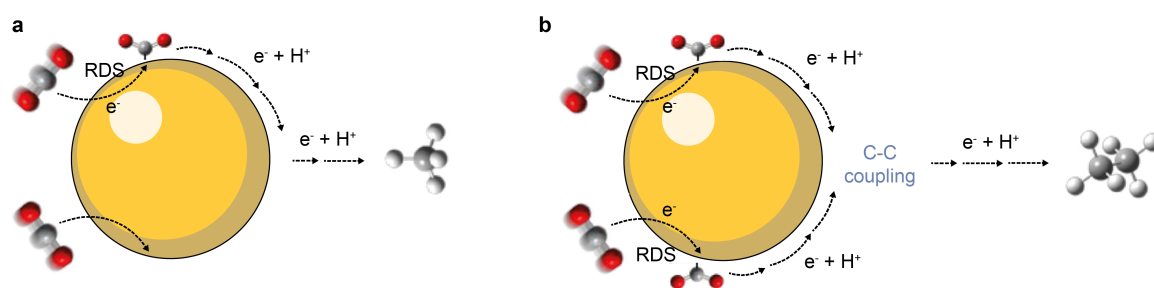


Figure 2.11: **Plasmonic nanoparticles for CO₂ reduction.** Schematic representation showing how light excitation influences hydrocarbon product selectivity. (a) the plasmonic excitation of AuNPs causes a hot electron to be transferred to adsorbed CO₂ to form a radical ion intermediate, CO₂^{•-} (or its hydrogenated form). After this rate-determining step (RDS for C1 generation), the formed CO₂^{•-} (or its hydrogenated form) proceeds through a cascade of hot-electron- and proton-transfer steps to result in CH₄ generation. (c) When the hot-electron-transfer rate is large (e.g., at high light intensity under interband excitation), more than one electron transfer can take place within the surface residence time of adsorbed CO₂, resulting in the simultaneous activation of two CO₂ adsorbates (RDS for C2 generation). The formed CO₂^{•-} intermediate pair can undergo C–C coupling. Subsequent transfer of a series of hot electrons and protons results in the formation of C₂H₆. Adapted with permission from Ref.⁶⁸

Other reactions

Apart from the generation of solar fuels, plasmonic catalysts have shown great promise in a wide range of commercially relevant reactions that typically require harsh conditions. In this way, plasmon-assisted catalysis could assist in carbonizing the chemical industry. For example, plasmonic gold nanoparticles have been used as efficient catalysts for the hydrogenation of nitrobenzene to aniline,⁶⁹ an essential precursor in the production of dyes and pharmaceuticals. Similarly, plasmonic palladium nanoparticles have been used as catalysts for the Suzuki-Miyaura cross-coupling reaction,⁷⁰ which is widely used in the pharmaceutical industry to synthesize biaryl compounds. Plasmonic nickel nanoparticles have been used as catalysts for the dehydrogenation of alkanes to produce alkenes,⁷¹ which are important intermediates in the production of

polymers and other chemicals. Furthermore, plasmonic materials have been used to catalyze the photodegradation of pollutants such as dyes and organic contaminants in water,⁷² which is an important application in environmental remediation. These examples demonstrate the potential of plasmon-assisted catalysis to revolutionize the chemical industry by making chemical reactions more efficient and environmentally friendly.

Challenges and mechanisms in plasmon-assisted catalysis

One of the biggest challenges facing plasmon-assisted catalysis is the price of synthesizing and manufacturing plasmonic materials for large-scale industrial applications. Even though laboratory-scale research has shown encouraging results, plasmon-assisted catalysis's scalability continues to be a significant obstacle. However, attempts to scale up the technology are limited by the relatively poor plasmonic efficiency. To solve these issues, scalable and affordable plasmonic material synthesis techniques must be created, and the design of plasmonic materials and catalytic reaction conditions must be optimized for greater efficacy and selectivity. To optimize plasmonic catalysts for future applications, a more in-depth understanding of the enhancement mechanisms is necessary.

The picture of localized surface plasmons drawn in Section 2.3, shows three main effects of localized surface plasmon excitation, namely near-field enhancement, hot-electron generation, and heat. All three effects can be exploited for catalysis. We have seen in Section 2.2.5 that these three effects occur on different timescales after excitation. However, under continuous-wave excitation, these three main effects occur simultaneously. This makes them difficult to disentangle. Additionally, this picture is oversimplified when it comes to plasmon-assisted catalysis. When a molecule is adsorbed on the catalyst surface, several mechanisms can affect a possible reaction. They are summarized in Figure 2.12. We will first discuss the three main charge excitation mechanisms that have been proposed throughout the literature:⁷³ The first, shown in Figure 2.12a, is *indirect hot-electron transfer mechanism*. Here, hot electrons are generated in the metal via non-radiative decay of a localized surface plasmon and then transferred to the molecule. The second, shown in Figure 2.12b, is *direct intramolecular excitation mechanism*. The localized surface plasmon induces direct excitation from the occupied state to the unoccupied state of the adsorbate. And the third is *direct hot-electron transfer mechanism*. Here, electrons are resonantly transferred from the metal to the molecule through interfacial electronic transitions; this mechanism is sometimes called plasmon-induced resonance energy transfer⁷⁴ (similar to Förster resonant energy transfer known as FRET). In addition, far-field scattering and near-field enhancement can enhance the absorption of nearby molecules. Finally, an increase in temperature that inevitably results from the plasmon decay can accelerate reactions; this mode of enhancement does not differ from thermal catalysis. The rate of (photo)catalytic reactions depends exponentially on the temperature via the Arrhenius relation. For this reason, even small uncertainties in the determination of the temperature of the catalytic active sites can result in large over- or underestimations of the reaction rate enhancement due to nonthermal plasmonic effects.

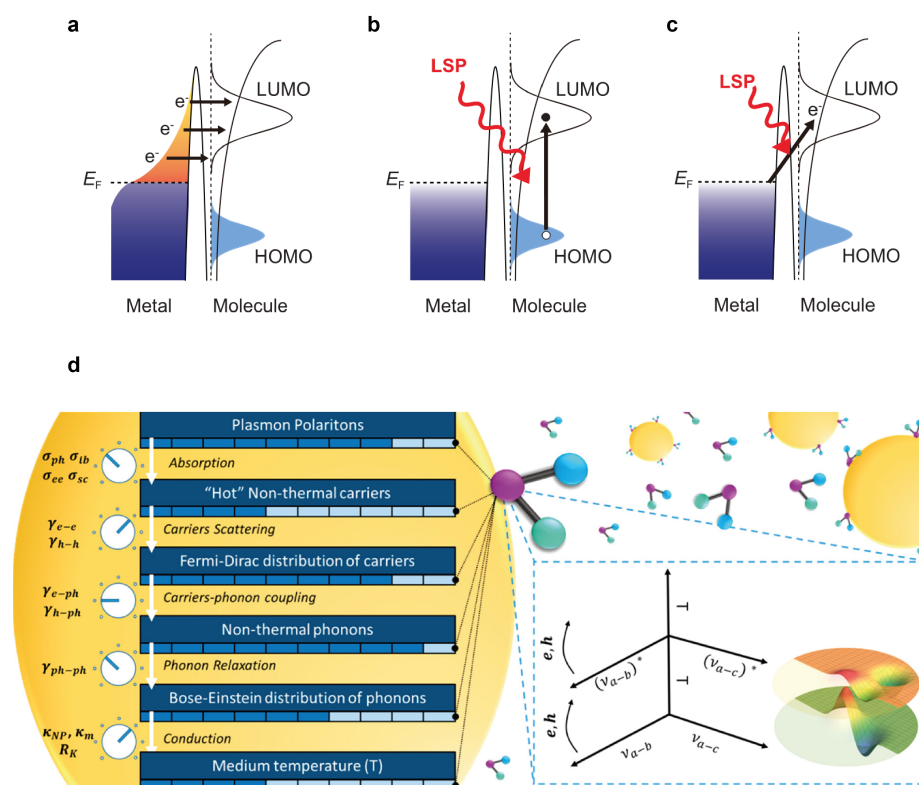
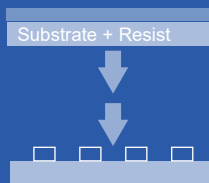


Figure 2.12: **Excitation mechanisms for plasmon-induced chemical reactions.** (a) Indirect hot-electron transfer mechanism. Hot electrons (e^-) generated via nonradiative decay of a localized surface plasmon transferred to the molecule. (b) Direct intramolecular excitation mechanism. The localized surface plasmon induces direct excitation from the occupied state to the unoccupied state of the adsorbate. (c) Direct charge transfer mechanism. The electrons are resonantly transferred from the metal to the molecule. (d) Manipulating the coupling constants between photons, electrons, and phonons allows one to tune the relative weight and energy distribution of each plasmon-derived phenomenon. This can alter the reaction pathway by selecting different channels to travel along the potential energy surface. This is highlighted in the inset as a new coordinate system of the potential energy surface for a plasmonic photocatalytic reaction. The excited electronic state may possess a lower activation barrier for the generation of products (linked to efficiency) as well as new valleys (linked to selectivity). (a-c) From Ref.,⁷³ reprinted with permission from AAAS. (d) Adapted with permission from Ref.⁷⁵

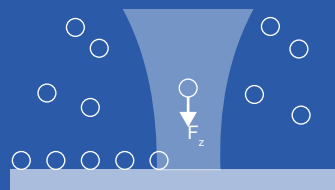
All of these mechanisms can be used to alter the reaction pathways, illustrated in Figure 2.12d. Manipulating the coupling constants between photons, electrons, and phonons allows one to tune the relative weight and energy distribution of each plasmon-derived phenomenon. This can alter the reaction pathway by selecting different channels to travel along the potential energy surface. The excited electronic state may possess a lower activation barrier for the generation of products, as well as new valleys.⁷⁵ In this way, reactions can be accelerated, the selectivity toward a desired product can be improved, and new, otherwise thermodynamically hindered, products can be generated. However, it is difficult to disentangle the contributions of the various mechanisms at play. Single-particle studies have emerged as a powerful tool for addressing this issue, providing a way to investigate individual nanoparticles. In the following chapter, we will address this in more detail, starting with the limitations of ensemble measurements.

Fabrication of single-particle arrays

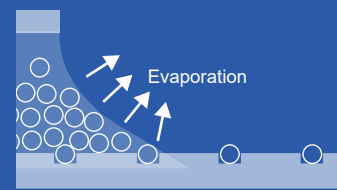
Electron beam lithography



Optical printing

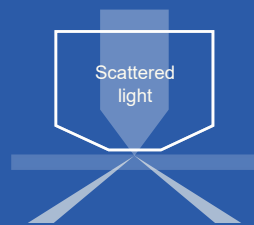


Capillary assisted assembly

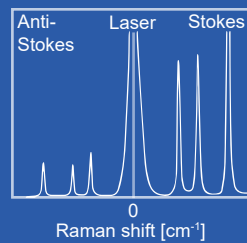


Single-particle techniques for energy conversion

Dark-field scattering



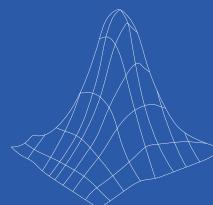
Surface enhanced Raman scattering



Photoluminescence spectroscopy



Super resolution microscopy



3

Single particle studies

This chapter focuses on the fabrication techniques for single particle arrays and summarizes the techniques for studying plasmonic nanoparticles for energy conversion. The first section discusses the limitations of ensemble measurements and the advantages of single-particle techniques. The second section gives an overview of fabrication methods for single-particle arrays. Finally, the third section summarizes various single-particle techniques, such as dark-field microscopy, electron microscopy, and single-molecule microscopy, as well as spectroscopic techniques. This chapter provides a comprehensive understanding of single-particle techniques for optimizing plasmonic nanoparticles in energy conversion applications.

3.1 Limitations of ensemble measurements

When trying to establish structure-property correlations of any (nano)material, ensemble averaging can be a serious obstacle. This is because heterogeneity in size, shape, nanostructure, and chemical composition is a general feature among particles at the nanometer and atomic level. Even across a single plasmonic nanoparticle, properties such as the catalytic activity can be non-uniform because of the existence of active surface sites and electric-field distributions, among others. Since many parameters directly influence performance for a variety of applications, their heterogeneity hinders the formation of a more in-depth understanding. To find an answer to the ensemble averaging problem, the field of "*Single-particle plasmonics*" has emerged over the past decade. Methods based on atomic force microscopy (AFM), dark-field spectroscopy, Raman spectroscopy, electron microscopy, and super-resolution fluorescence microscopy have made significant progress and revealed fascinating insights. Throughout this thesis, we study the optical, catalytic, and photothermal properties of different plasmonic nanoparticles at the single-particle level. This chapter will first provide an overview of the single-particle fabrication techniques that facilitate these studies (Section 3.2), followed by an overview of single-particle techniques in Section 3.3.

3.2 Fabrication of single particle arrays

Since Faraday's pioneering experiments in the 1800s (see Section 2.2), a wide variety of protocols have been developed to synthesize metallic particles of various shapes and sizes with high yields. However, only in the past two decades have these methods been refined to generate high-quality colloidal samples with good control over the average size and shape. Moreover, the rapid development of nanofabrication facilities has led to new methods for fabricating nanosized metal structures using lithographic techniques. This section will give a brief overview of the fabrication of metal particle arrays using wet-chemical and lithographic methods. This section is not intended to describe all the methods available for the preparation of metal particles. Instead, the aim of this section is to provide a brief overview. There are a number of high-quality review papers that provide a more in-depth explanation on both wet-chemistry⁷⁶⁻⁷⁹ and lithographic techniques.²⁸

3.2.1 The assembly of colloidal nanoparticles

Colloidal synthesis Colloidal metal nanoparticles can be synthesized using a variety of methods, for example, laser ablation, electrochemical reduction, and chemical reduction. The wet-chemical synthesis of metal particles is based on the reduction of metal ions in solution. When a specific shape of metal particles is required, chemicals that act as "shape directing" agents are often added to the solution. These protocols have been empirically developed, and there is still no clear picture of how shape control works. However, the field has advanced significantly in the last two decades, and a wide range of metal particle shapes can now be synthesized with high yields⁷⁶⁻⁷⁹. There are various shapes that can be achieved in colloidal metal nanoparticles, such as

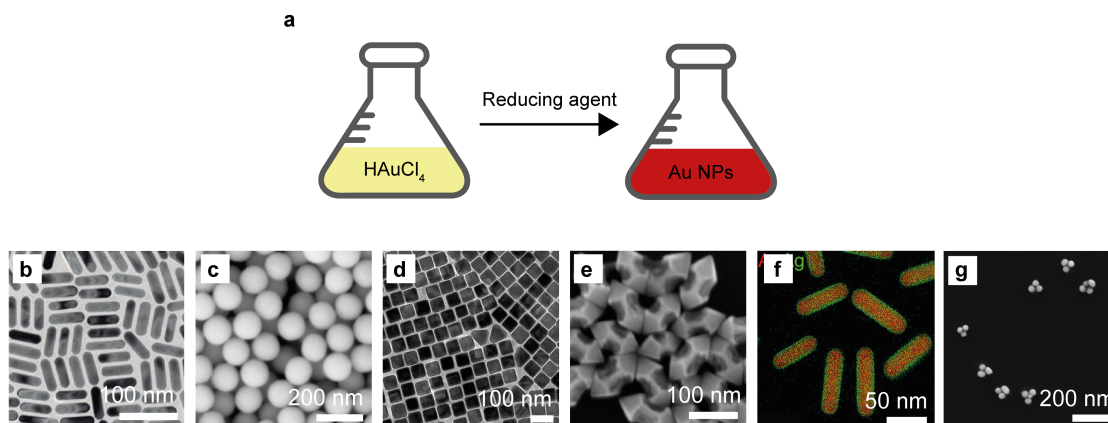


Figure 3.1: **Colloidal synthesis.** (a) exemplary illustration of a chemical synthesis of metal nanoparticles by the reduction of metal ions in solution. To control the size, shape and chemical composition, the concentration of precursors, temperature, surfactants and reaction time are controlled. (b-g) An exemplary selection of electron microscopy images of possible metal nanoparticles. (b) Gold nanorods, adapted from Ref.⁸⁰ (c) Superspherical gold nanospheres, adapted from Ref.⁸¹ (d) Silver nanocubes, adapted from Ref.,⁸² (e) Gold nanoarrows, adapted from Ref.⁸³ (f) Elemental mapping of gold nanorods (red) with a silver shell (green), adapted from Ref.⁸⁴ (g) gold nanoparticle trimers, adapted from Ref.⁸⁵

spheres, rods, cubes, triangles, stars, and many more. The shape of the nanoparticles can be controlled by various factors, such as the synthesis method, the concentration of the precursors, the temperature, the surfactants used, and the reaction time. Figure 3.1 shows an exemplary selection of possible structures. Although colloidal chemistry offers methods for producing a wide range of nanoparticles with various sizes, shapes, material compositions, and surface functionalities, their controlled deposition and assembly on arbitrary positions of substrates to enable single-particle investigations continues to be a significant challenge. In the following, we will discuss two techniques that allow the controlled positioning of colloidal particles with high precision.

Optical printing In 2010, the groups of Norbert Scherer at the University of Chicago⁸⁹ and Jochen Feldmann⁹⁰ at the Ludwig-Maximilians-Universität of Munich demonstrated almost simultaneously the optical printing of single spherical gold nanoparticles. In the following, I will provide a brief overview of the method and the current state-of-the-art, based on a recent review by Violi *et al.*⁹¹

An overview of the optical printing process is shown in Figure 3.2. A colloidal suspension of nanoparticles with a specific net electric charge is brought into contact with a substrate with the same charge sign. In this way, electrostatic repulsion prevents the nanoparticles from spontaneously depositing on the substrate. The fundamental objective of optical printing is to use optical forces on the nanoparticles to break through this repulsion barrier at precise points on the substrate, where the nanoparticles are deposited. A laser beam that is precisely focused onto the substrate is employed to accomplish this. The process can be summarized in three steps:

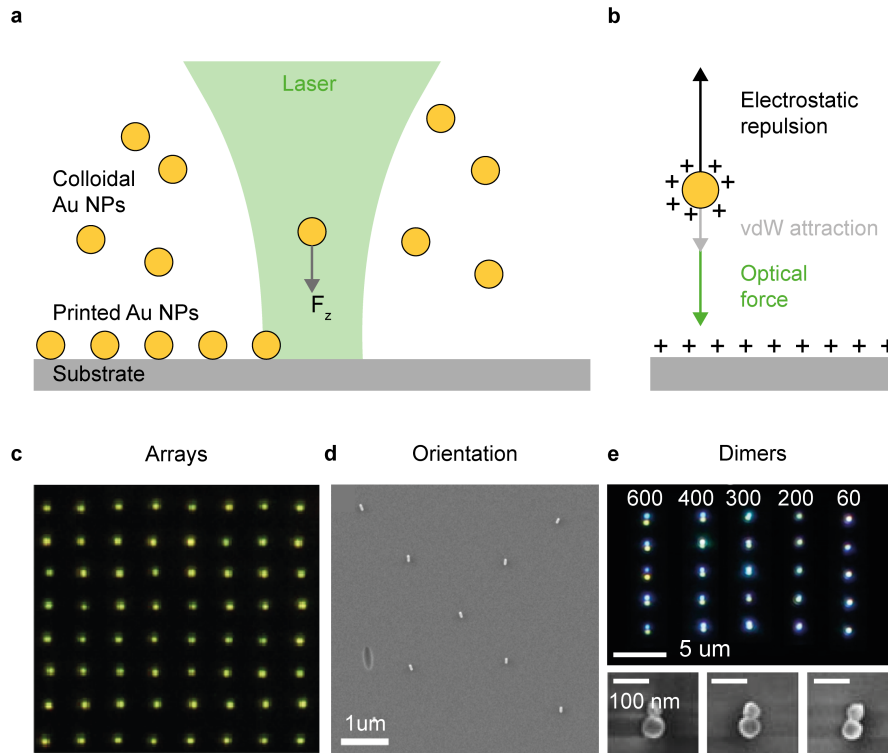


Figure 3.2: **Optical printing of colloidal nanoparticles.** (a) Scheme of optical printing of colloidal nanoparticles. In the solution on top of the substrate the nanoparticles are in Brownian motion. A laser is focused onto the sample. When a particle enters the beam, the optical forces print it onto the substrate. After printing, the sample is advanced to the next desired position. (b) The substrate and the particles have the same surface charge to avoid a spontaneous deposition. If the optical forces are high enough to overcome the electrostatic potential barrier, the particle is printed onto the substrate and held in place by the attractive van der Waals forces. (c) A dark field image of a printed array of gold nanospheres. (d) Unisotropic nanoparticles can be printed with a controlled orientation. (e) Multiple particles can be arranged in close proximity. c is adapted from Ref.⁸⁶ d is adapted from Ref.,⁸⁷ e is adapted from Ref.⁸⁸

1. A nanoparticle is in free diffusive Brownian motion until it randomly reaches the capture volume of the excitation beam.
2. Once inside the capture volume, optical forces drive the nanoparticle toward the substrate.
3. At distances between the nanoparticle and the substrate on the order of a few tens of nanometers, other forces become relevant. These are the electrostatic repulsion and the van der Waals attraction, as described by DLVO (Derjaguin-Landau-Verwey-Overbeek) Theory. Electrostatic repulsion dominates for larger distances, whereas van der Waals attraction dominates for small distances. The addition of both results in the formation of a potential barrier. If the optical forces are large enough to overcome this barrier, the nanoparticle will be printed onto the substrate and adheres through van der Waals forces.

This methodology has been applied to print more complex geometries, two of which

are shown in Figure 3.2. First, it is possible to print gold nanorods with polarization control by employing linearly polarized lasers. An example is shown in Figure 3.2. A linearly polarized 1064 nm focused laser beam was used to trap and orient nanorods with longitudinal plasmon resonance at 724 nm. Then, a co-aligned linearly polarized 532 nm laser was switched on to print the nanorod on the substrate. The authors found that the highest orientational control was achieved if the trapping and printing lasers were polarized perpendicularly to each other.⁸⁷ The second example shows dark-field and scanning-electron-microscopy (SEM) images of Ag-Au heterodimers printed with a set distance of 60 nm, equal to the diameter of both particles. The nanoparticles were printed on-resonance using wavelengths of 405 and 532 nm for silver and gold nanoparticles, respectively. This not only allowed the particle to be printed at arbitrary distances, but also the orientation of the dimer was well controlled.⁸⁸

Currently, the lateral printing accuracy is comparable to the diameter of the nanoparticles,⁸⁶ a higher precision could be achieved, for example, by using an optical tweezer to controllably position the particle in the focus of the printing beam, or by engineering more complex optical profiles. To make this technique applicable to industrial fabrication, for which large substrate areas are required, the speed of printing needs to be greatly increased. Instead of trading off speed for accuracy, another possibility is to parallelize the process. By using multiple laser beams, or, as shown by Nedev *et al.*, by using a spatial light modulator, to create a pattern of multiple laser foci, several nanoparticles can be printed simultaneously.⁹²

Template-assisted self-assembly Template-assisted assembly is an umbrella term for techniques that employ a nanostructured template to assemble colloidal nanoparticles. Forces guiding the assembly can be, for example, capillary forces, electrostatic forces, and gravitational forces.^{85,94–99} The template is often a replica of a nanostructured silicon master, where the master is fabricated using nanolithography (Section 3.2.2). The master can then be reused hundreds of times to create the same replica.⁸⁵ Template-assisted assembly has a number of advantages compared to nanolithography. First, it reduces the long writing times associated with large-scale patterning. Second, the crystallinity of nanolithographically fabricated structures is typically polycrystalline, whereas that of colloidal nanoparticles is often monocrystalline. Last, it also allows for the assembly of certain 3D geometries that cannot be fabricated using nanolithography, such as spheres.

In the following, I will focus on the assembly using capillary forces, as used later in Chapter 4. Capillary assembly is essentially a controlled dewetting process in which the meniscus of an evaporating droplet containing particles is moved over a predefined topographical template. Capillary forces at the meniscus act as the driving force to assemble the particles into the predefined sites, i.e., two-dimensional (2D) arrays of “traps”. Above a critical contact angle value, the horizontal force exerted by the liquid meniscus becomes high enough to prevent particles from depositing on a flat substrate, leading to selective immobilization of the particles inside the nanostructured traps (3.3b). A more in-depth discussion can be found in Ref.⁹⁸ In addition to nanoparticle concentration and surface functionalization, evaporation speed and contact angle must also be controlled. To this end, a setup as illustrated in Figure 3.3a can be used.

Using capillary-assisted particle assembly, a variety of geometries have been real-

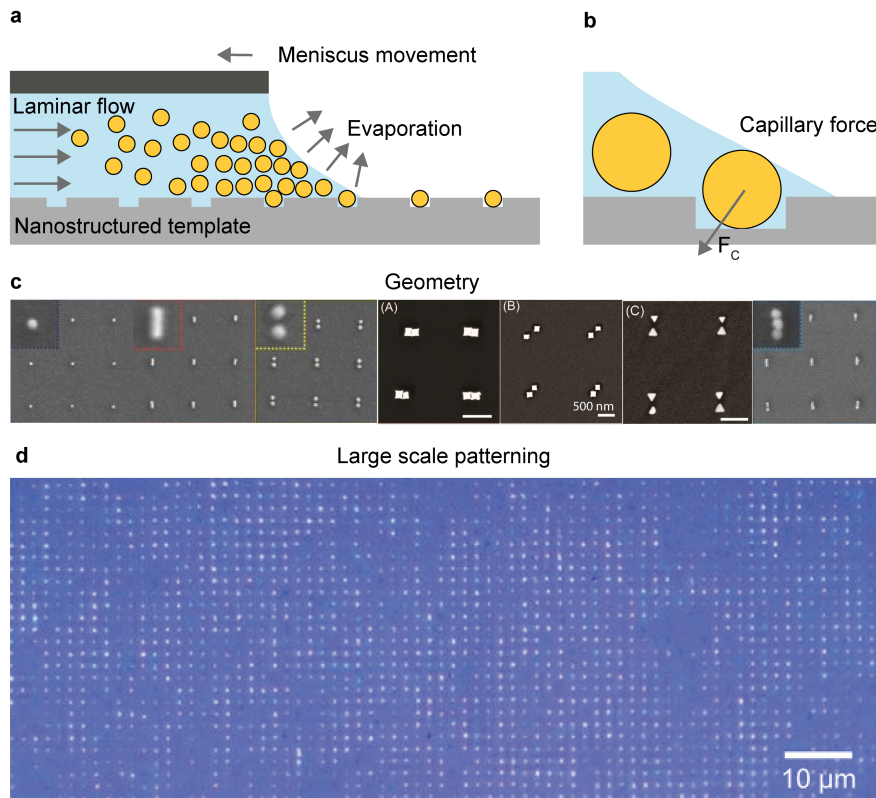


Figure 3.3: **Template-assisted self-assembly** (a) Schematic illustration of a setup for template-assisted self-assembly. It shows a setup using capillary forces, similar to what was used in Chapter 4. Essential elements are an evaporation-induced flow field, the local trapping capillary force (F_c), the creation of a dense, stable particle suspension at the evaporating front (the accumulation zone), the nanostructured template, and the controlled movement of the meniscus. (b) Zoom in of (a) in the printing region. The capillary force pushes the nanoparticle back, where it falls into a hole in the nanostructured template. (c) Scanning electron images of nanoparticles assembled with capillary forces. Possible structures include (from left to right) nanospheres, nanorods, spherical dimers, cube dimers edge-to-edge, corner-to-corner; bowties, trimers. (d) Template-assisted self-assembly facilitates fast large scale patterning (arrays of sizes on the order of cm^2) (c) adapted from Refs.^{93,94} (d) adapted from Ref.⁸⁵

ized. This includes, for example, spheres, rods, sphere dimers, dimers made of triangles (bowties), as well as cubes with both face-to-face and edge-to-edge alignment (Figure 3.3c). In many cases, the nanoparticles are assembled into predefined trenches on a poly(methylsiloxane) (PDMS) stamp that is a replica of a silicon master. For the further applicability of this method, the assembled nanoparticles have to be transferred onto substrates in a free-standing form, increasing their accessibility. This is often done by simply bringing the PDMS stamp into contact with the desired substrate, followed by releasing the stamp. However, this technique suffers from poor printing yields. This limitation can be overcome by using polymethylmethacrylate (PMMA) instead of PDMS. Instead of mechanically removing the stamp after printing, PMMA can be dissolved in acetone, leaving only the nanoparticles adsorbed on the substrate and improving the printing yield to around 98%.⁸⁵ In this way, capillary-force based assembly can be used to produce large-scale free-standing arrays of nanoparticles (Fig-

ure 3.3d).

3.2.2 Nano lithography

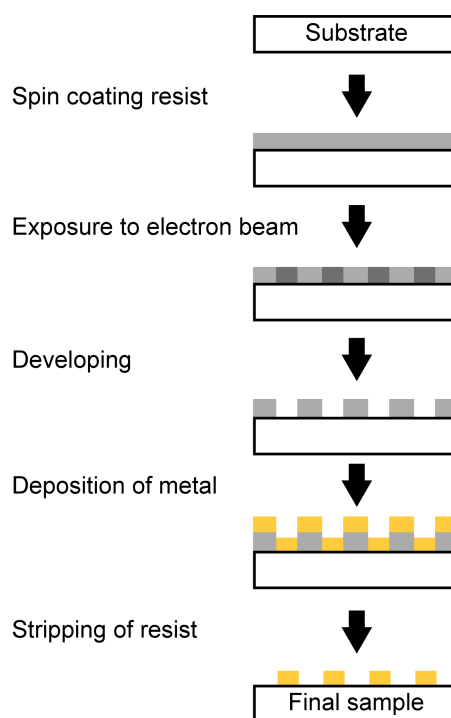


Figure 3.4: **Electron beam lithography.** Electron beam lithography is the most commonly employed nano lithography tool. This illustration shows the most essential steps when employing a positive electron beam resist.

Top-down fabrication strategies generally result in well-ordered and highly periodic plasmonic arrays. They can be prepared with high reproducibility and structural homogeneity. There are several top-down fabrication techniques, such as electron beam lithography (EBL), reactive ion etching (RIE), focused ion beam (FIB), and nanoimprint lithography (NIL), among others. EBL is one of the most common nanofabrication methods that employ a focused beam of electrons to create periodic plasmonic nanostructures. In the following, we will briefly describe the process. In EBL, the substrate is usually made of glass or silicon. Here, glass is the obvious choice for optical transmission measurements. The most important steps of the fabrication process are shown in Figure 3.4a. First, the substrate is coated with electron-sensitive resist via spin coating. The resist undergoes chemical changes upon exposure to the electron beam. In a so-called "positive resist", the electron beam breaks polymer backbone bonds and turns the exposed polymer into fragments of lower molecular weight. During the second step, called "development", a solvent developer selectively washes away the lower molecular weight fragments and leaves the unexposed portion of the resist

film intact. The desired material is then added onto the substrate via thin-film deposition techniques, such as thermal evaporation. The residual resist, which is also covered by the deposited material, is subsequently dissolved, leaving behind the desired pattern. A crucial requirement is that the deposited film is not continuous over the patterned and nonpatterned regions, which is achieved by a sufficient height difference between the resist and the deposited material. The high lateral resolution of EBL relies on the use of the electron beam for exposure, which can be focused down to a few nanometers and is limited by the beam column rather than the wavelength of the electrons. On the downside, the equipment is expensive and each pattern must be written individually; thus, the fabrication of large-scale substrates is both costly and time-consuming. Additionally, it is not possible to use lithographic techniques to fabricate certain three-dimensional structures, such as spheres or concave cubes.

3.3 An overview of relevant single particle techniques

This section provides a brief overview of single-particle techniques used to study plasmonic nanoantennas for energy conversion. The following is not a comprehensive list; instead, the focus is on the most relevant techniques for the following chapters of this thesis. We will discuss both spectroscopic and microscopic techniques. For experimental details, please refer to Appendix 7.

3.3.1 Dark-field scattering

Dark-field scattering is the most widely used optical tool for single-nanoparticle investigation. Dark-field refers to the fact that, in contrast to regular bright-field illumination, the background appears dark. This is because the signal does not include the unscattered beam. In Dark-field, the particle is illuminated with a hollow cone of light. This is achieved by using a condenser with two numerical apertures (NAs) NA_{con}^{out} and NA_{con}^{in} . The scattered light from the particle is collected by an objective with a lower NA ($NA_{obj} < NA_{con}^{in}$). In this way, the incident illumination is not collected and only the light scattered by the particle reaches the detector. If we recall that the scattering of plasmonic nanoparticles shows distinct resonances that depend on the material, size, geometry and its surroundings (Chapter 2.3), it becomes clear that the scattering signal carries a lot of information. In this way, it can be used to optically characterize samples and also to monitor refractive-index changes in the surroundings. This has applications for sensing, catalysis, and nanothermometry.

Dark-field microscopy can be achieved in reflection or transmission. In reflection, excitation and collection occur through the same objective, and the condenser is integrated into the collection objective. The transmission configuration is shown in Figure 3.5a. The condenser lens focuses the light onto the sample. Typically, immersion oil ensures refractive index matching of the space between the condenser and the substrate. The objective lens collects the scattered light. In both reflection and transmission configurations, the collected light is collimated in the back focal plane of the objective and sent either to a camera for dark-field microscopy or spatially

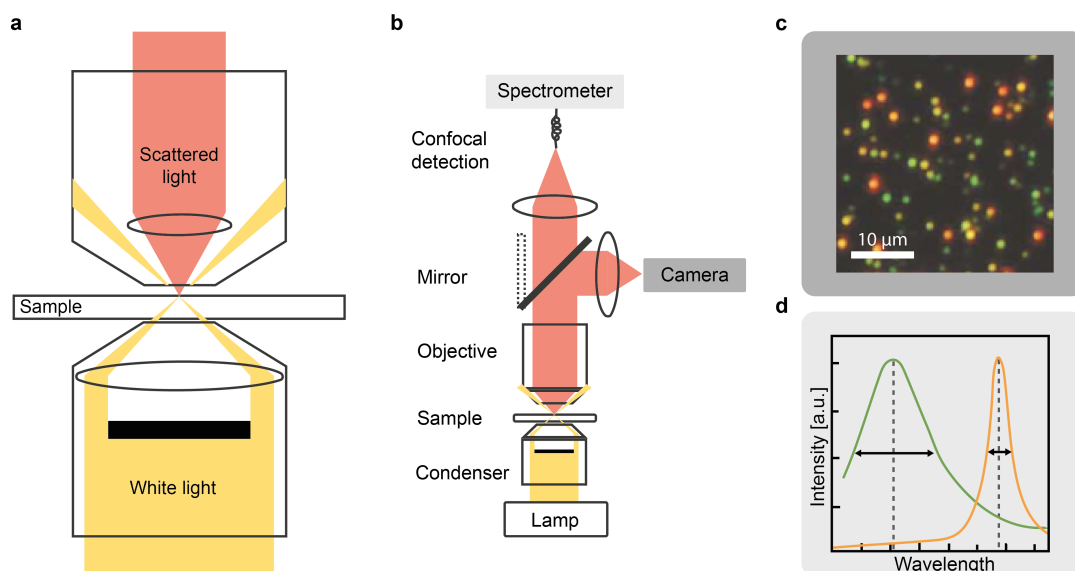


Figure 3.5: **Working principle of a dark field scattering setup.** (a) Illustration of the illumination and collection in the transmission configuration. The light is incident on the sample at a high angle and not collected through the collection objective. Only the light scattered by the sample is detected. (b) The scattered light can be sent either to a camera for imaging, or light is filtered through a pinhole for confocal detection and sent to a spectrometer. (c) Exemplary true color dark field image of gold nanorods (red) and gold nanospheres (green) on a substrate. (d) The scattering of the gold nanospheres and gold nanorods. (c) and (d) are adapted from Ref.¹⁰⁰

filtered through a pinhole and coupled to a spectrometer for dark-field spectroscopy (Figure 3.5b). In Figure 3.5c we see an exemplary true color dark field image of plasmonic nanoparticles on a substrate. The scattering shows distinct colors, namely red (gold nanorods) and green (gold nanospheres).¹⁰⁰ The scattering spectra of two exemplary nanoparticles are shown in Figure 3.5d, where a difference in the peak position (dashed lines) and the line width (arrows) can be seen.¹⁰⁰ In ensemble measurements, the line width is usually masked by inhomogeneous broadening effects due to morphology dispersions. Although dark-field scattering is a powerful technique to determine resonance positions and linewidth, the quantitative determination of the scattering cross-section is more difficult, as the amplitudes change drastically with excitation and collection angles.¹⁰¹

While throughout this work we will use dark-field scattering for the characterization of nanoantennas only, it has also been employed to track chemical reactions and to gain a more fundamental understanding of plasmonic nanoparticles. Three examples are shown in Figure 3.6.

First, in Figure 3.6a the heterogeneity of seemingly identical gold dimers is revealed.¹⁰² The SEM image on the left shows two gold dimers. Figure 3.6a also shows representative dark-field scattering spectra of seven individual dimers. Although the dimers look similar under SEM, none of the spectra look exactly alike. The dashed line shows the average position of the longitudinal mode, as extracted from 46 dimers. The histogram of the position of the longitudinal mode illustrates the broad distribution

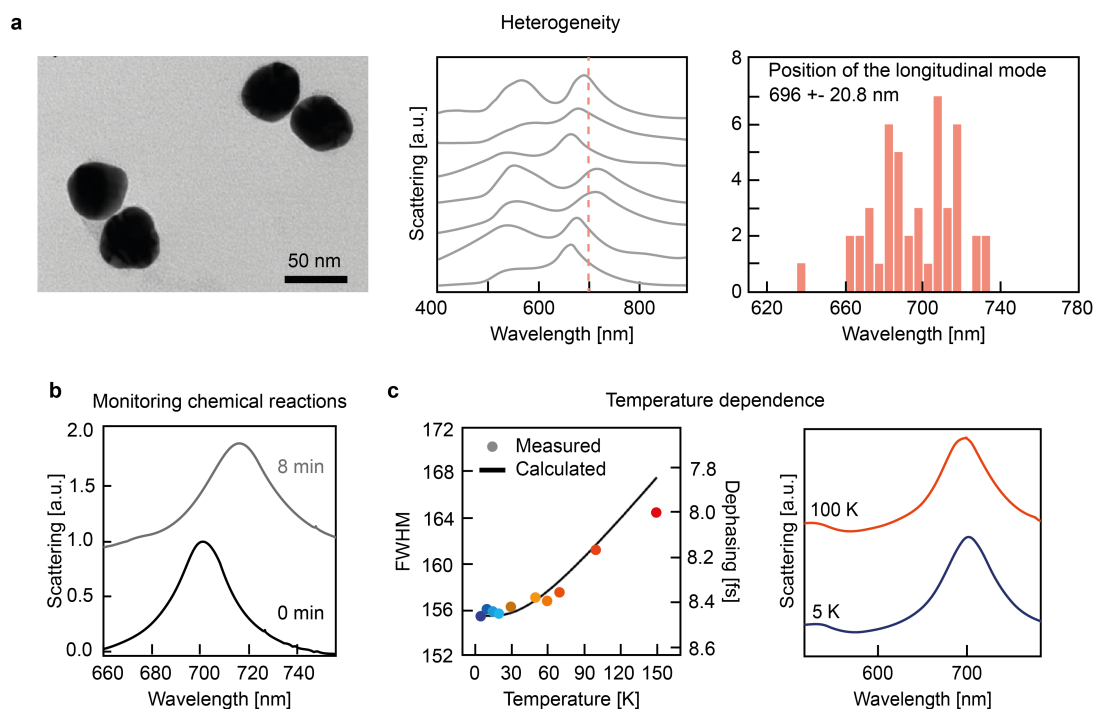


Figure 3.6: **Single particle darkfield measurements.** (a) The heterogeneity of plasmonic nanoparticles. From left to right: SEM image, dark-field scattering spectra, histogram of the position of the longitudinal mode. (b) Monitoring chemical reactions. Shown here is the changing scattering spectrum during the growth of gold nanorods by reduction of AuCl_4^- (c) Temperature dependence of plasmon dephasing. Left shows the FWHM against temperature and the calculated dephasing time, following the same trend. Right shows exemplary scattering spectra for 5 K and 100 K from which the FWHM was extracted. (a) adapted from Ref.,¹⁰² Copyright American Chemical Society 2019. (b) Adapted from Ref.,¹⁰³ Copyright Springer Nature 2008. (c) adapted from Ref.,¹⁰⁴ copyright De Gruyter 2020

of the peak position (696 ± 20.8 nm). Figure 3.6b shows how the resonance position extracted from the dark-field scattering spectra of the nanoparticles can be used to gain information about catalysis.¹⁰³ Here, the monitored reaction is the growth of gold nanorods from the reduction of AuCl_4^- . Within 8 minutes, the aspect ratio of the rod changed from 2.87 to 3.01, corresponding to a redshift in the dark-field scattering spectrum. From this, the authors were able to determine that this corresponds to an addition of ~ 100 gold atoms per second. The final example shown in Figure 3.6c shows the temperature dependent full-width-half-maximum (FWHM) of the dark-field scattering spectra of a single Au nanowire on top of an Au film.¹⁰⁴ The authors found that the FWHM increased by 5.8% when the temperature increased from 5 to 150 K. exemplary spectra for 5 K and 100 K are shown on the right. This temperature-dependent study allows for further insight into the damping processes of plasmonic nanoparticles. Similar to Figure 3.6b, dark field scattering can also be used to monitor changes in the refractive index in the surroundings of the nanoparticle due to plasmonic heating. Overall, Dark-field is a very versatile method and is easy to use. However, its limitation is that the scattered intensity scales as the squared volume of the nanoparticles. Therefore, for small particles, dark-field scattering is

easily overwhelmed by signals from dielectric impurities, substrate roughness, or even thermodynamic fluctuations of the medium. Its application to small objects requires very clean substrates, as background scattering starts to obscure the measurements. The size limit is around a few tens of nanometers (~ 30 nm for gold nanospheres) under standard conditions.¹⁰⁵

3.3.2 Surface enhanced Raman scattering

Surface-enhanced Raman scattering (SERS) is a spectroscopic technique that uses nanostructured metal surfaces or metal nanoparticles to enhance the Raman scattering signal from molecules.^{106–109} Raman scattering is named after C.V. Raman, an Indian physicist who discovered the effect in 1928.¹¹⁰ When light is scattered by a molecule, a small fraction of the scattered photons changes their energy. The frequency shift from the excitation frequency is related to the vibrational energy levels of the molecule. This is illustrated in Figure 3.7a. Because each molecule has a unique vibrational fingerprint, Raman scattering provides information about the chemical composition of a sample. However, Raman spectroscopy has a low sensitivity as a result of the very low cross-section of typical molecules. That is why an enhancement is needed.

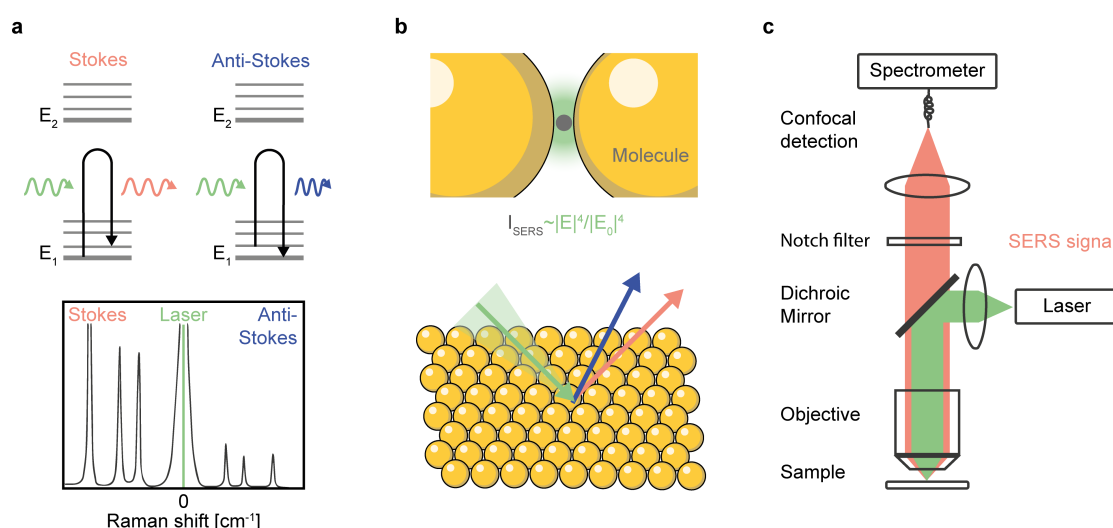


Figure 3.7: **Surface enhanced Raman scattering.** (a) Raman scattering is inelastic light scattering with a molecule. The Raman spectrum on the bottom is a plot of the intensity of the scattered light as a function of frequency. The peaks in the spectrum correspond to the vibrational modes of the molecules. (b) Surface-Enhanced Raman Scattering is a variation of Raman scattering that enhances the Raman signal by several orders of magnitude. The signal scales to the power of four with the local fields that can be enhanced through plasmonics. (c) Illustration of a setup to measure Raman signal. A single wavelength is used to excite the sample.

The enhancement effect of SERS is due to several factors. The first is the strong electromagnetic field near the resonantly excited nanoparticle, which in turn enhances the Raman scattering signal from nearby molecules (Figure 3.7b). The SERS enhancement is often approximated by averaging $|E|^4 / |E_0|^4$, where E_0 is the incident (laser) field amplitude and E is the local field amplitude due to field enhancement.¹¹¹ In addition to near-fields, a chemical enhancement effect from the metal surface can also play

a role. Overall, the SERS enhancement factor regularly reaches 10^6 , making it possible to detect single molecules or molecules that have a weak Raman signal.^{108,112,113}

SERS has a wide range of applications in materials science, biotechnology, and environmental science. Its applications include studying the structure and properties of materials at the nanoscale, identifying and quantifying small molecules in complex mixtures, and detecting and analyzing biological molecules such as proteins, DNA, and cells.¹⁰⁸

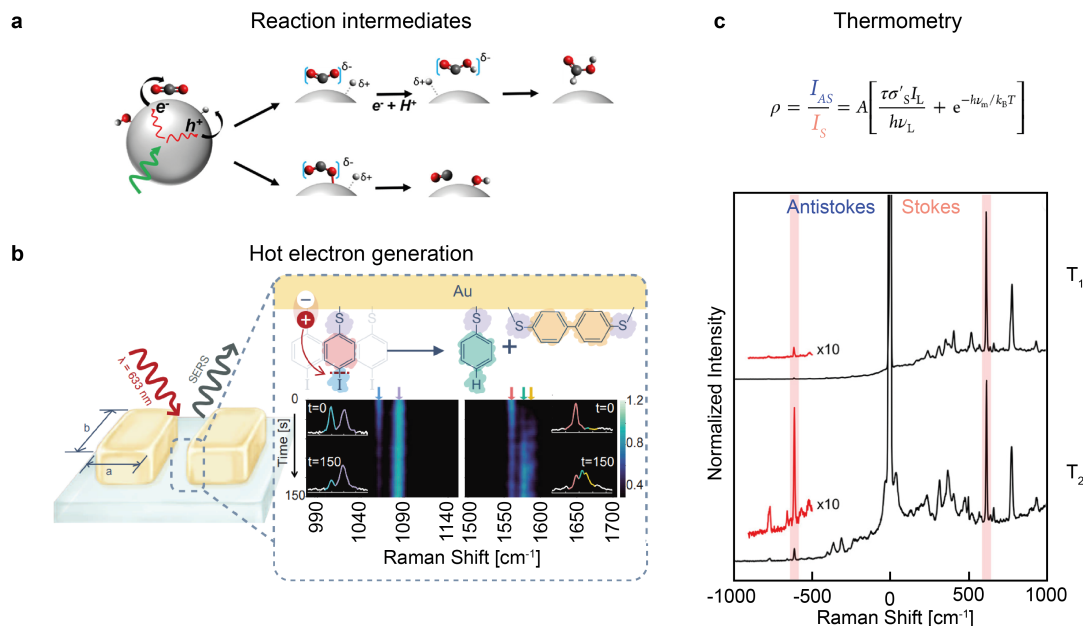


Figure 3.8: **Examples of SERS for nanoantennas for energy conversion.** (a) Plasmon-assisted CO_2 reduction on Ag nanoparticles. Discrete events of adsorption and product generation on individual nanoparticles allow insight into reaction intermediates. (b) Catalytic behavior of hot electrons in dimers with varying gap sizes. (c) Thermometry. The ratio of the Stokes to anti-Stokes ratio depends on the temperature of the molecule. (a) is adapted from Ref.¹¹⁴ (b) is adapted from Ref.¹¹⁵ (c) is adapted from Ref.¹¹⁶

In the context of plasmon-driven catalysis, a single laser is commonly used to both drive catalytic processes and excite the SERS signals of reactants and products, avoiding the need for elaborate setups. Measurements can be performed in both transmission and reflection microscope configurations; the reflection configuration setup is shown in Figure 3.7c. In a typical SERS measurement, a molecule is adsorbed onto the surface of the plasmonic metal, and a focused laser beam is used to excite the plasmonic metal as well as the molecule. Typically, a notch filter blocks out the excitation wavelength and transmits only the Raman signal to a spectrometer. SERS measurements are often performed on densely packed nanoparticle films and clusters of nanoparticles, where abundant interparticle gaps strongly enhance the Raman signal.¹¹⁷

More recently, systematic single-particle SERS measurements have provided valuable catalytic information,^{112,118–122} and a few examples are presented in Figure 3.8a-b. Figure 3.8a illustrates that the temporal information on chemical species present can be exploited to gain mechanistic insight and monitor reaction intermediates. For

example, Kumari *et al.*¹¹⁴ followed a plasmon-assisted CO₂ reduction on Ag nanoparticles. The authors captured discrete events of adsorption and product generation on individual nanoparticles. In this way, the authors were able to observe a surface intermediate, hydrocarboxyl (HOCO·), which represents the very first step in plasmonic CO₂ reduction. This first step is the transfer of a $1e^-/1h^+$ pair from the Ag nanoparticle to CO₂. A second example is shown in Figure 3.8b. Nan *et al.* studied the catalytic behavior of hot electrons by monitoring a plasmon-mediated dehalogenation with varying interparticle distances of a gold dimer. The authors found that by reducing the gap from 20 to 10 nm the reaction rate could be sped up more than two times. A further reduction of the gap size did not improve the reaction rate even though the field-enhancement was significantly higher. Third, an example not directly related to catalysis is shown in Figure 3.8c. The SERS signal from molecules can be used to probe the local temperature^{116,123} by monitoring the ratio of Stokes and anti-Stokes emission. For an anti-Stokes process to happen, the initial state cannot be the ground state, but it must be one of the excited vibrational states. As these excited states are poorly populated at room temperature, the anti-Stokes signals are weak compared to the Stokes signals. Upon increasing temperature, these vibrational states become more populated, increasing the probability of anti-Stokes Raman events. It should be noted that in this way it is possible to probe the temperature of SERS active molecules in vicinity of plasmonic nanoparticles, which is not necessarily the same as the temperature of the nanoparticle itself. Beyond the applications discussed here, single-molecule SERS has also been combined with super-localization microscopy.^{124–126} Overall, SERS is a powerful technique for detecting and analyzing molecules with high sensitivity and specificity.

3.3.3 Photoluminescence spectroscopy

In addition to the widely known and very commonly utilized absorption and scattering of plasmonic nanoparticles, they also exhibit photoluminescence (PL). An exemplary PL spectrum of a gold nanoparticle is shown in Figure 3.9a. The shape of the spectrum closely resembles that of the scattering and absorption spectrum. A single wavelength is used to excite the nanoparticle, shown in green. A notch filter is employed to block the excitation laser from the measured spectrum (Figure 3.9b). At shorter wavelengths lies what is called anti-Stokes (AS) PL, and the Stokes PL is at higher wavelengths from the excitation. These names resemble the SERS terminology of Section 3.3.2. However, the origins of the photoluminescence are not fully understood and three proposed mechanisms are illustrated in Figure 3.9b. Interband transitions from the *d* to *sp* band in gold result in luminescence in gold films, occurring at wavelengths up to around 550 nm. However, these transitions are not possible for longer wavelengths, where PL of plasmonic gold nanoparticles is still observed. Two mechanisms have been proposed to explain luminescence at these longer wavelengths: an electronic Raman process, which involves inelastic scattering,^{127,128} and a photoluminescence process resulting from intraband transitions.^{129–131}

Figure 3.10 shows a technique that is relevant to energy conversion and which we will employ in Chapters 5 and 6. It allows the extraction of temperature information from the photoluminescence spectra of plasmonic nanoparticles. This technique

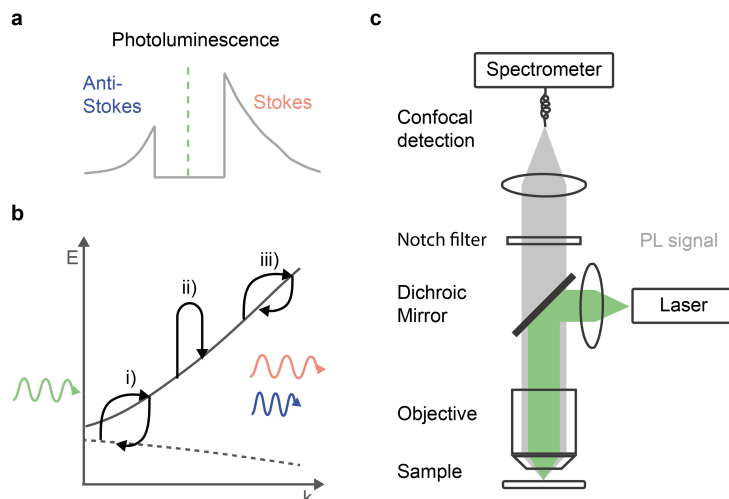


Figure 3.9: **Photoluminescence spectroscopy.** (a) An exemplary PL spectrum of a gold nanoparticle with the anti-Stokes emission at shorter wavelengths and Stokes emissions at longer wavelengths from the excitation laser (dashed line). (b) Potential explanations for PL from plasmonic nanoparticles (i) Interband PL (ii) electronic Raman scattering (iii) Intraband PL. (c) Illustration of a setup to measure the PL of plasmonic nanoparticles.

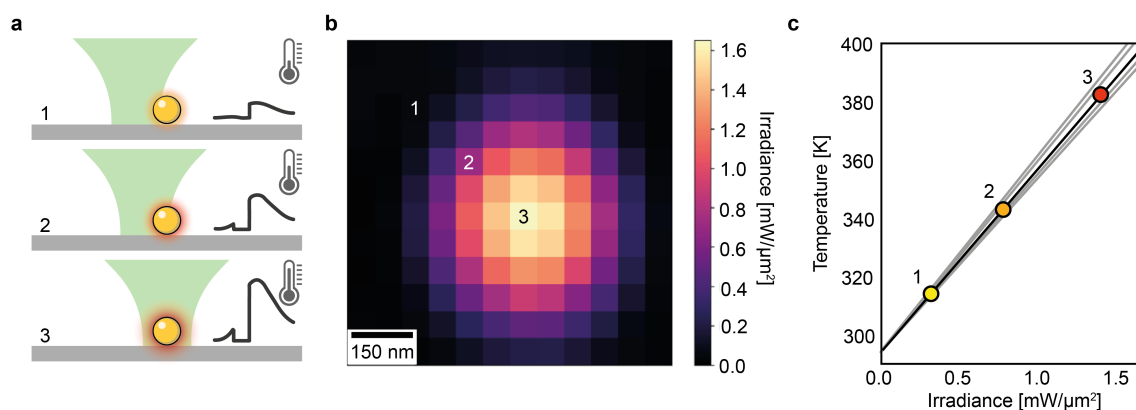


Figure 3.10: **Anti-Stokes photoluminescence thermometry.** (a) Schematic illustration of the heating of a NP at different irradiances achieved by scanning a confocal beam across the NP. (b) Confocal image of an 80 nm AuNP color coded by irradiance on the NP, numbers 1 to 3 corresponding to the labeling in (a). (c) Calculated temperature as a function of the excitation irradiance. Solid black line: Temperature calculated using the mean photothermal coefficient. Adapted from Ref.¹³² Copyright 2021 American Chemical Society.

is called anti-Stokes (AS) thermometry. It takes advantage of the fact that upon illumination with a continuous-wave (CW) laser, the AS part of the photoluminescence spectrum of plasmonic nanoparticles shows a temperature dependence.¹³³ This technique has been used for the thermal characterization of individual monometallic Au nanoparticles such as disks,¹³⁴ pyramids,¹³⁵ rods,^{136,137} bowties,¹³⁸ spheres,^{132,139} and cylinders.¹⁴⁰ Various implementations of AS thermometry have been reported, as reviewed by Baffou.¹⁴¹ Recently, a new implementation called hyperspectral AS thermometry was introduced, which retrieves the photothermal coefficient β of individual nanoparticles from a single PL hyperspectral image.¹³² The photothermal coefficient describes the linear increase in temperature with irradiance. The method is summa-

rized in Figure 3.10. The same laser is employed to heat the nanoparticle and excite the photoluminescence. Depending on the position of the focused beam with respect to the nanoparticle, the nanoparticle experiences a different irradiance and therefore has a different temperature. The hyperspectral confocal image shown in Figure 3.10b provides 10×10 PL spectra that are grouped and subsequently averaged considering similar irradiance values. The classification criterion is the excitation irradiance I_i^{exc} . Then all possible ratios between binned PL spectra are calculated. These ratios are fitted to the expression in Equation 3.1 to extract the photothermal coefficient $\beta_{i,j}$. Finally, all obtained photothermal coefficients $\beta_{i,j}$ are averaged to obtain a single β for the scanned NP. The temperature of the nanoparticle at certain irradiance can then be calculated as $T = T_0 + \beta I$ (Figure 3.10c).

$$Q_{i,j}^{\text{AS}}(\lambda) = \frac{I_i^{\text{exc}} \exp\left(\frac{E(\lambda) - E(\lambda_{\text{exc}})}{k_{\text{B}}[T_0 + \beta_{i,j} I_j^{\text{exc}}]}\right) - 1}{I_j^{\text{exc}} \exp\left(\frac{E(\lambda) - E(\lambda_{\text{exc}})}{k_{\text{B}}[T_0 + \beta_{i,j} I_i^{\text{exc}}]}\right) - 1}, \quad (3.1)$$

Unlike other optical methods for single-particle thermometry of metals,¹⁴² such as those based on fluorescence,¹⁴³ Raman,¹⁴⁴ DNA-PAINT,^{145,146} optical rotation,¹⁴⁷ or refractive index variations,¹⁴⁸ hyperspectral AS thermometry is non-invasive, label-free, and does not require any additional characterization or prior knowledge of the nanoparticles or the properties of the medium.

3.3.4 Electron microscopy

Electron microscopy uses a beam of electrons instead of light to form an image of a sample. As a result of the shorter wavelength of electrons, it allows imaging at much higher magnifications and with a higher resolution than is possible with traditional light microscopy. In electron microscopy, a beam of high-energy electrons is directed at the sample, and the resulting interactions between the electrons and the sample produce an image. This image can provide detailed information about the shape, size, and composition of the sample.

The higher resolution achieved with electron microscopes is related to the diffraction limit postulated by Ernst Abbe in 1873.¹⁴⁹ The diffraction limit is a fundamental constraint on the resolution of any imaging system, including electron microscopes, because of the wave nature of the particles or radiation used for imaging. The resolution of an imaging system can be approximated as follows.

$$d = \frac{\lambda}{2\text{NA}} \quad (3.2)$$

where d is the resolution, λ is the wavelength of the imaging radiation, and NA is the NA of the objective lens.

For electron microscopes, the imaging particles are electrons that have a wavelength determined by their kinetic energy through the applied accelerating voltage. The typical wavelength of electrons in electron microscopes is on the order of a few picometers to a few tenths of an angstrom. This short wavelength allows electron microscopes to achieve much higher resolution compared to light microscopes, which are limited by the longer wavelength of visible light (400-700 nm). There are several dif-

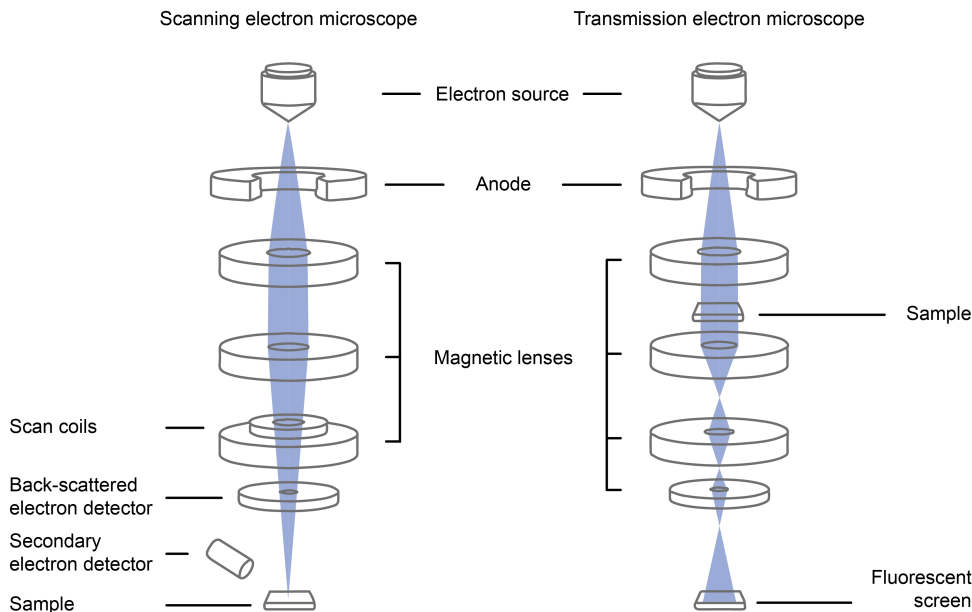


Figure 3.11: **Electron microscopy.** Schematic representations of a scanning electron microscope (**left**) and a transmission electron microscope (**right**).

ferent types of electron microscopy, of which scanning-electron-microscopy (SEM) and transmission-electron-microscopy (TEM) are shown in Figure 3.11. Each type of electron microscopy has advantages and limitations, and the choice of technique depends on the specific scientific question. SEM (shown on the left) is generally better suited for imaging a sample's surface at high resolution. It generates images by scanning an electron beam across the sample and detecting secondary electrons emitted from the surface. SEM is particularly useful for visualizing sample topography and morphology, and it can also provide information about the surface's elemental composition. TEM (shown on the right), on the other hand, is better suited to image a sample's internal structure at high resolution. In TEM, an electron beam passes through the sample, and the image formed by detecting the electrons that have passed through the sample is formed. TEM can provide detailed information about the structure of a material, such as the crystal structure, defects, and interfaces. Electron microscopy is often used to characterize the size, shape, and arrangement of metal nanoparticles, which can strongly affect the plasmonic properties of materials.

In addition to this optical characterization (such images appear frequently throughout this thesis, for example, in Figures 3.1, 4.3, 4.4), the high resolution of electron microscopy can also be employed to track chemical transformations induced by plasmon excitation. In 2017, Cortés *et al.* imaged a hot-electron-driven reaction on silver bowtie nanoantennas. The authors used the ability of hot electrons to locally reduce the terminal group of a self-assembled molecular layer that covers the surface of the nanoantenna (Figure 3.12a-b). This modification was spatially localized using 15 nm gold nanoparticles (AuNPs) specially designed to react only with the converted molecules (Figure 3.12c-d). SEM imaging was used to record the position of the reporter nanoparticles (NPs) after plasmon excitation, thus progressively mapping the reactivity of the nanoantennas (Figure 3.12e). A 2D histogram of 100 bowties shows

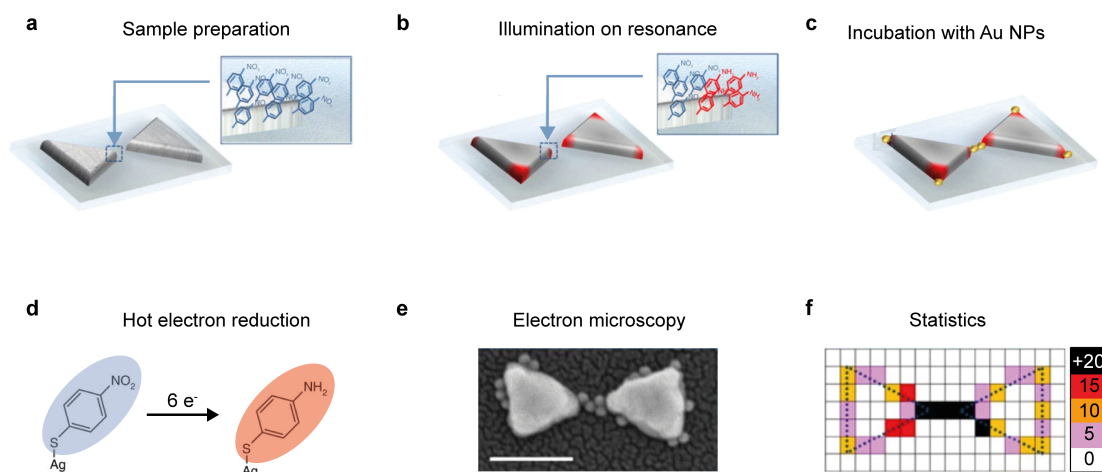


Figure 3.12: **Example of electron microscopy for nanoantennas for energy conversion.** (a) Silver bowties were modified with a monolayer of 4-NTP. (b) 4-NTP-coated antennas were illuminated for different times at their longitudinal plasmon resonance wavelength (633 nm) with a power density of 1 W cm^{-2} . (c) Subsequently, the sample was incubated over night with a AuNP suspension. (d) Scheme of the reaction from 4-NTP to 4-ATP that involves 6 electrons. (e) Scanning electron image of a silver bowtie after the reaction and incubation with AuNPs. The AuNPs allow the visualization of the reaction sites with nanometer resolution. Scale bar 100 nm. (f) 2D histogram of the reactive sites on 100 silver bowtie nanoantennas. Adapted from Ref.¹⁵⁰

that the reaction occurs predominantly in the gap of the dimer (Figure 3.12f). Electron microscopy allows to image the reactive sites with subparticle resolution, however, generally not in operando conditions. Therefore, it is difficult to gain insight into the reaction dynamics. This can be achieved with the method that we will introduce next: Single-molecule localization microscopy.

3.3.5 Single-molecule localization microscopy

In the previous section, we discussed electron microscopy, a powerful imaging technique that provides high-resolution images at the nanometer scale. We introduced the concept of the diffraction limit, which explains the fundamental resolution constraints when using visible light. Despite these limitations, visible-light microscopy has significant advantages over electron microscopy. For instance, it is considerably easier to work with under operando conditions, allowing dynamic insights into various processes, such as plasmonic catalysis. In recognition of the groundbreaking development of a group of techniques that overcame the diffraction limit, the 2014 Nobel Prize in Chemistry was awarded for the invention of *super-resolution microscopy*. Among these innovative techniques is single-molecule localization microscopy.

Single-molecule localization microscopy (SMLM) is a term that describes all microscopical techniques that achieve super-resolution by localizing individual fluorescent molecules with high precision. In this section, we discuss the fundamental principles of SMLM and introduce an example of this technique applied to plasmon-assisted catalysis. The fundamentals are illustrated in Figure 3.13. First, it should be noted

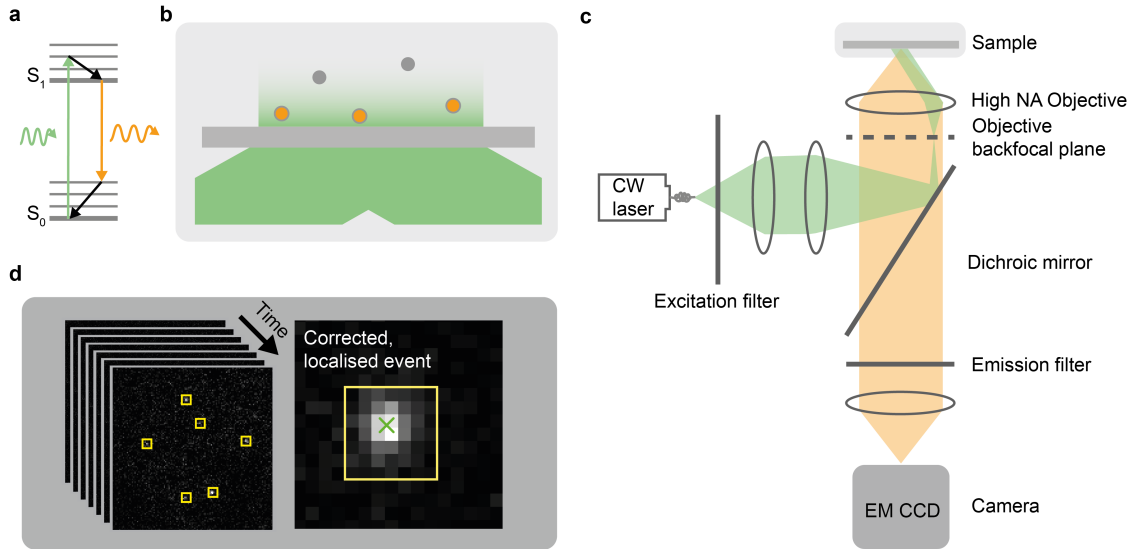


Figure 3.13: **Single-molecule localization microscopy.** (a) Simplified Jablonski diagram of a fluorophore. (b) Illustration of total internal reflection microscopy. Only fluorophores close to the surface are excited, this results in low background and allows single fluorophores to be detected. (c) Illustration of a setup for single-molecule localization microscopy. (d) Illustration of the data acquisition and processing.

that the technique relies on fluorescence, i.e. labeling. Second, in order to detect individual fluorescent molecules, the background has to be reduced to a minimum. This can be achieved by employing total internal reflection (TIRF), illustrated in Figure 3.13b. If light is incident above a critical angle onto an interface from a higher to lower refractive index, the beam is reflected and an evanescent field is created on the sample side. There are different configurations to achieve this, shown in Figure 3.13c is objective-based TIRF. Here, the beam is focused on the back focal plane of a high NA objective. When this focus point is moved off the central axis, the angle of the illumination column can be adjusted to reach the critical angle and achieve TIRF. The evanescent field generated at the sample interface decays exponentially and ensures that only fluorophores in close proximity to the surface (generally around 200 nm) are excited, which reduces the background. The imaging process of SMLM then involves the acquisition of a series of images in which only a small subset of fluorophores is activated at any given time (shown in Figure 3.13d), ensuring that in a diffraction-limited area only one emitter is present at a given time. The position of each activated fluorophore is then determined with sub-diffraction-limited precision by fitting its point spread function (PSF) to a Gaussian function:

$$I(x, y) = I_0 \exp \left[-\frac{(x - x_0)^2}{2\sigma_x^2} - \frac{(y - y_0)^2}{2\sigma_y^2} \right] + B \quad (3.3)$$

where $I(x, y)$ is the intensity at position (x, y) , I_0 is the peak intensity, (x_0, y_0) is the center of the Gaussian (corresponding to the position of the fluorophore), σ_x and σ_y are the standard deviations of the Gaussian in the x and y directions, respectively, and B is the background intensity.

The localization precision, d_{SMLM} , which is the uncertainty in determining the

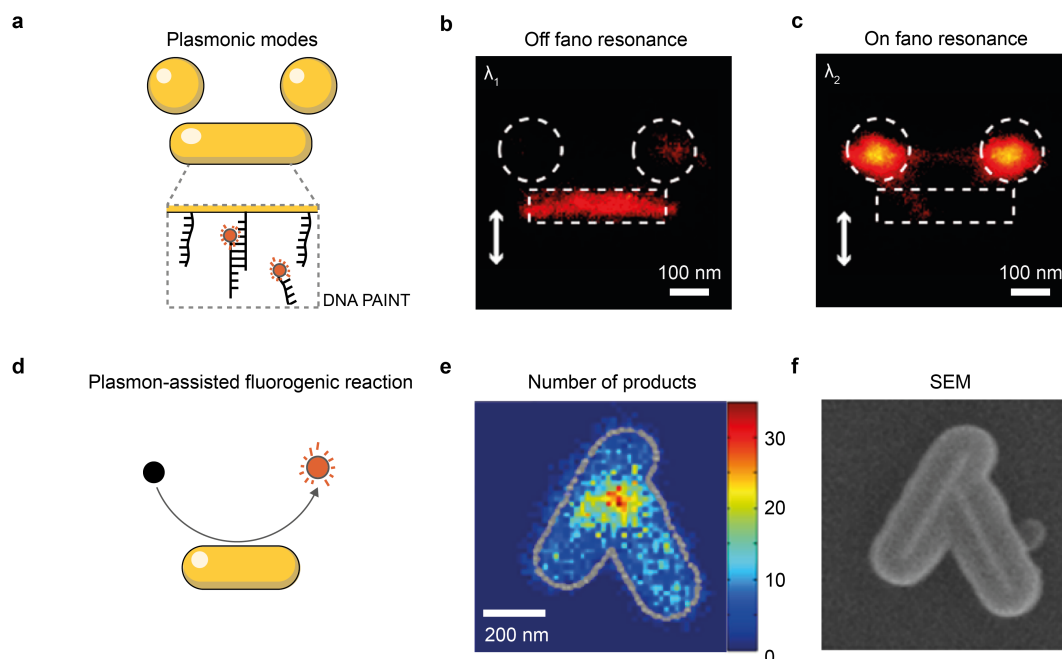


Figure 3.14: **Examples of SMLM for nanoantennas for energy conversion.** (a) DNA-Paint can be used to image plasmon hybridisation. (b) After illuminating the antenna *off* fano resonance, the thiol bonds on the disks are cleaved, rendering them dark in the DNA-Paint images. (c) After illuminating the antenna *on* fano resonance, the thiol bonds on the rod are cleaved, rendering it dark in the DNA-Paint images. (d) A plasmon-assisted fluorogenic reaction allows the imaging of catalytic sites with nanometer resolution under operando conditions. Catalytic hotspots on linked Au-Au nanorod nanostructure. (e) Quantitative super-resolution mapping of catalytic products on a nanostructure. Grey line: structural contour of the nanostructure from its SEM image in (f). (f) SEM image of linked Au-Au nanorod encapsulated in mSiO₂ in (b). (b-c) adapted from Ref.¹⁵¹ Copyright American Chemical Society 2018. (e)-(f) adapted from Ref.¹⁵² Copyright American Chemical Society 2018.

position of a single molecule, depends mainly on the number of photons \sqrt{N} detected.

$$d_{SMLM} \propto \frac{d}{\sqrt{N}}, \quad (3.4)$$

where d is the diffraction limit according to equation 3.2. By localizing many individual molecules on a series of frames and reconstructing the image, SMLM can achieve a resolution in the range of 10-20 nm, significantly improving the diffraction-limited resolution of conventional fluorescence microscopy.

In the context of *Plasmonics*, SMLM has been used, for example, to image plasmon hybridization using DNA paint.¹⁵¹ This is illustrated in Figure 3.14a-c. Here, the surface of the nanoantennas is coated with a single-stranded DNA using a gold-thiol bond. Depending on the wavelength and polarization of light, different plasmonic modes of the system can be excited. The hot-electrons generated from this excitation were used to drive the desorption of the thiolated molecules from the surface. By performing DNA paint measurements after this plasmon-assisted reaction by subsequently adding imager strands (a complementary DNA strand with a fluorophore), the authors were able to visualize the different modes. The imager strands transiently

bind to the remaining docking strands, allowing single-molecule localization. A second example is shown in Figure 3.14d-f. Here, Zou *et al.* used a plasmon-assisted fluorogenic reaction on top of gold nanorod dimers and showed that there was a chemical hot spot in the gap. This example shows the potential of SMLM for plasmonic catalysis under operando conditions, which, in addition to the below diffraction spatial information, also allows kinetic insight. In the following chapter, Chapter 4, we will utilize this technique along with other methods introduced in this chapter. Our focus will be on studying the spatial distributions of plasmon-assisted catalysis to gain a deeper understanding of the underlying mechanisms.

4

Spatial distributions in plasmon-assisted catalysis

In the previous Chapter, we explored the benefits of single-particle techniques in the study of plasmonic nanoparticles for energy conversion. Now, we delve deeper into the subject matter by fabricating single-particle arrays and employing single-molecule super-resolution fluorescence microscopy. Our aim is to understand the mechanisms of plasmonic catalysis at the individual-particle level. Specifically, we observe plasmon-assisted catalysis in situ on ordered arrays of gold nanorods with subparticle resolution. Our study investigates two regimes: excitation tuned to the reactant and excitation tuned to the plasmon resonance. The results provide valuable insights into the spatial distribution of enhancements and the underlying mechanisms of plasmonic catalysis, which can inform the design and optimization of plasmonic nanocatalysts for energy-related chemical reactions.

Based on

Simone Ezendam, Julian Gargiulo, Ana Sousa-Castillo, Joong Bum Lee, Yoon Sung Nam, Stefan A. Maier, and Emiliano Cortés. Spatial distributions of single-molecule reactivity in plasmonic catalysis, *under review at ACS Energy Letters*

Figure 4.0 - Single-molecule fluorescence microscopy. Artistic representation of single-molecule fluorescence data. Bright spots are a few pixels in size and correspond to diffraction-limited single-molecule events. The single events can be fitted to obtain a final resolution far below the diffraction limit.

4.1 Gaining mechanistic insight

In Chapter 2.4.3 we have seen that the reactivity of plasmonic catalysts is dictated by a complex interplay between photons, localized surface plasmons, carriers, phonons, and molecular states.⁷⁵ To optimize the design of plasmonic catalysts, it is important to understand the specific enhancement mechanism behind a reaction, but this can be a complex task.^{39,56,75,153} Approaches to address this challenge include measuring

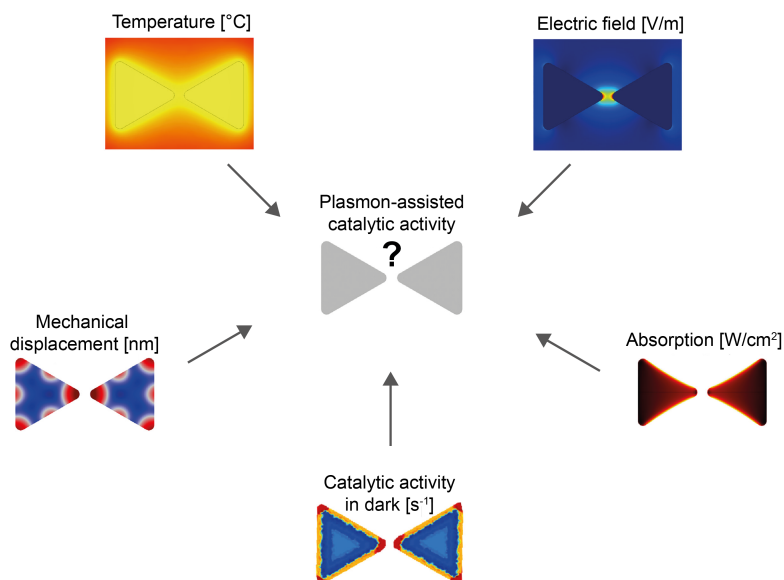
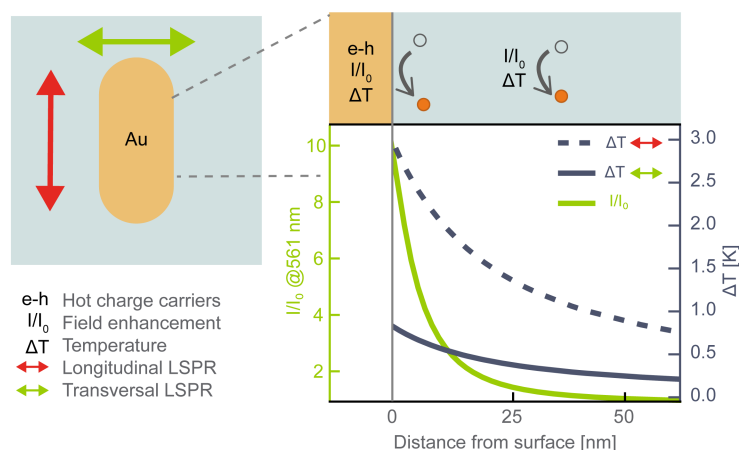


Figure 4.1: **From optical to chemical hot spots in Plasmonics.** Spatial distribution of different phenomena influencing chemical activity in plasmon-assisted chemistry. Adapted from Ref.⁷⁵ Copyright 2019 American Chemical Society. Inset “Catalytic activity in dark” adapted from Ref.¹⁵⁴ Copyright 2013 American Chemical Society

reaction rates at different wavelengths, light intensities, and catalyst surface temperatures.¹⁵⁵ These experiments are often performed at the ensemble level and therefore are limited by the inherent heterogeneity of nanostructures.¹⁵⁶ To overcome this limit and obtain more detailed insights, several single-particle techniques have been explored.¹⁵⁷ Each technique is based on the detection of photon or electron signals that report on the reactants, products, catalysts of the reaction, or changes in the environment caused by the reaction.¹⁵⁸ We have discussed many of these techniques in more detail in Chapter 3.3, the following is a short summary. Among the single-particle approaches is single-particle surface-enhanced Raman spectroscopy (SERS),^{121,122,159} which allows, for example, the identification of reaction intermediates and insight into the reaction kinetics.^{114,160} However, it is generally diffraction limited, works only for SERS-active molecules, and has low throughput. Other techniques such as atomic force microscopy (AFM)¹⁶¹ and scanning electron microscope (SEM)¹⁵⁰ have been used to image reaction products on plasmonic nanostructures. However, these scanning techniques are invasive and generally performed ex-situ, and therefore do not provide quantitative information on the reaction kinetics. Single-molecule super-resolution fluorescence microscopy has been shown to be a powerful tool to study catalysis at the nanoscale employing fluorogenic model reactions,^{154,162–172} but can

also be extended to non-fluorogenic reactions.¹⁷³ It allows *in operando* imaging of reactions with microsecond temporal resolution and nanometer spatial resolution. While the temporal resolution allows for more insight into the reaction kinetics, the spatial resolution allows for a deeper understanding of the enhancement mechanisms. The latter is illustrated in Figure 4.1. Recently, single-molecule fluorescence microscopy has been applied to study plasmonic catalysis with sub-particle resolution. Zou *et al.* imaged catalytic hotspots by monitoring a surface reaction but did not independently excite different modes of the plasmonic system,¹⁶⁵ while Hamans *et al.* monitored a purely photo-driven reaction in the vicinity but without access to the plasmonic metal itself, therefore exploiting only the near field. Thus, in the following, we will design a plasmonic model system that, for the first, time, allows all possible mechanisms to be explored.

4.2 Designing a plasmonic model nanoreactor



Scheme 4.1: **Illustration of the studied catalyst and potential enhancement mechanisms.** High-energy charge carriers, enhanced electro-magnetic fields and increased temperatures are important potential drivers of plasmon-enhanced catalysis. Hot-charge carriers can be extracted from the plasmonic metal only, whereas temperature and field enhancement extend into the vicinity of the plasmonic structure. The studied gold nanorods have two resonances, resulting in different reactivity patterns depending on the mechanism at play. This can be exploited to obtain mechanistic insight.

In this study, we aim to address these limitations by utilizing ordered arrays of gold nanorods (AuNRs) coated with an accessible porous silica shell as nanocatalysts. By utilizing single-molecule super-resolution fluorescence microscopy, we directly observed and quantify the catalytic enhancements with subparticle resolution. We study two regimes: excitation tuned to the reactant and excitation tuned to the plasmon resonance. Our investigation of the correlations between the spatial distribution of turnover events, catalytic enhancements, temperature, and local electric field enhancement aims to provide a more controlled and systematic study of the enhancement mechanisms in plasmon-enhanced catalysis.

To study the two regimes mentioned above, we carefully designed the dimensions of the plasmonic model nanoreactor using optical simulations. The rationale behind the

design is summarized in Scheme 4.1. Plasmon-enhanced catalysis can be driven by high-energy charge carriers, enhanced electromagnetic fields, and increased temperatures. Hot-charge carriers can be extracted only from the plasmonic metal, while temperature and field enhancement can extend into the vicinity of the plasmonic structure. Contrary to nanospheres, nanorods have not only one but two resonances, depending on the polarization employed: a longitudinal resonance and a transversal resonance. The two resonances result in different reactivity patterns, depending on the mechanism involved. The longitudinal resonance is red-shifted from the transversal resonance, and the cross sections (both absorption and scattering) are significantly higher at this wavelength. The goal was the following: The reactant molecule absorbs around the transversal resonance, and a 561 nm laser is used for the excitation. A second red-shifted wavelength can then be used to excite the longitudinal resonance, in our case we tuned the longitudinal resonance to our second excitation wavelength of 647 nm. In Chapter 2.3 we have seen that the resonance positions depend not only on the dimensions and material of the plasmonic component, but also on its surroundings. Therefore, we included a mesoporous silica shell, water, and a glass substrate in our simulations. The mesoporous shell facilitates the detection of reaction products by temporally trapping them and reducing quenching on the catalyst surface.¹⁶³ Appendix A.8 provides more details on the simulation setup. Figure 4.2 shows the results of the optimized structure with the following dimensions: a length of $l = 51$ nm and a radius of $r = 13$ nm. The mesoporous silica shell was designed as a sphere with a radius of 95 nm.

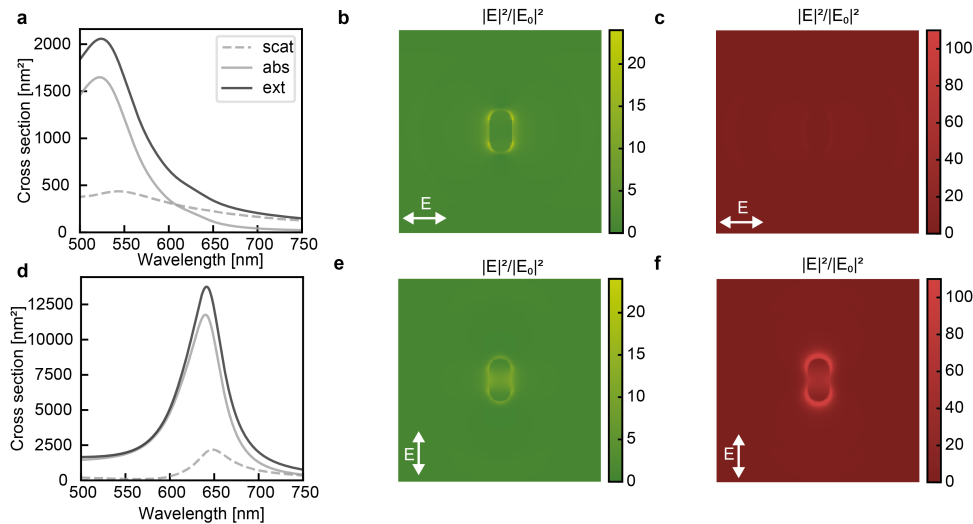


Figure 4.2: **Results of FDTD simulations of the AuNR@mSiO₂ on a substrate in water.** Scattering, absorption and extinction cross sections, z-normal field enhancement maps at 561 nm (green) and 647 nm (red) (a)-(c) Transversal polarization (d)-(e) Longitudinal polarization.

4.3 Ordered arrays of individual plasmonic nanoreactors

After deciding on the desired dimensions of the nanoparticles, we next synthesized AuNRs with a length of 51 ± 7 nm and a width of 28 ± 3 nm using a previously reported seed-mediated process with some modifications (Appendix A.3).¹⁷⁴ We then coated the nanorods with an ~ 95 nm mesoporous SiO_2 (mSiO₂) shell (Figure 4.3a and Appendix A.4). The measured bulk extinction of the system is shown in Figure 4.3b. It shows two characteristic peaks, corresponding to the transversal and longitudinal localized surface plasmon resonance (LSPR).

Typically, colloidal catalysts deposited on substrates have irregular interparticle spac-

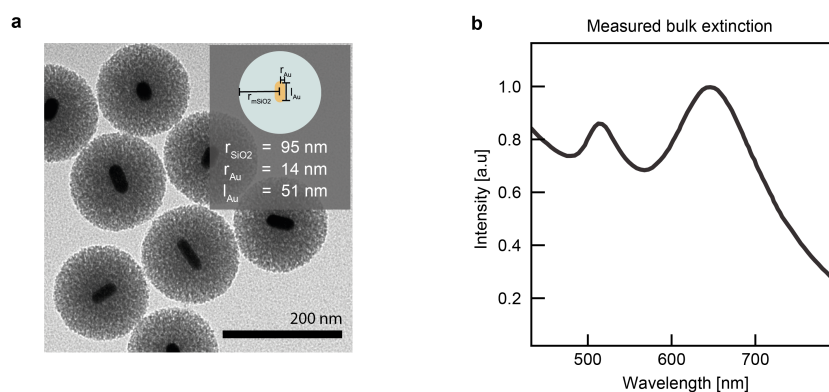


Figure 4.3: **Colloidal gold nanorods.** (a) Exemplary TEM image of the gold nanorods with a mesoporous silica shell (AuNR@mSiO₂). The inset shows the average dimensions. (b) The measured bulk extinction in water of the catalyst shown in (a).

ings, making it difficult to study the enhancement mechanisms at the single-particle level. Using arrays of nanocatalysts instead offers the advantage of investigating a large number of equivalent systems at once. This allows for a more controlled and systematic study of the enhancement mechanisms and simplifies cross-correlation with other single-particle techniques, such as scanning-electron-microscopy (SEM) and dark-field spectroscopy. Therefore, we used interfacial template dissolution interfacial patterning⁸⁵ to pattern individual AuNR@mSiO₂ on a coverslip. This technique was introduced in more detail in Chapter 3.2.1, a simplified scheme is shown in Figure 4.4a. In short: the single particles were assembled into a patterned polymethylmethacrylate (PMMA) template. To this end, the particle suspension was sandwiched between the PMMA template and a clean glass coverslip, which was moved across the assembly template to position the particles within designated trap sites (shown on top). To print the patterned particles, the PMMA template was pressed onto the desired substrate and subsequently dissolved in acetone, leaving the AuNR@m-SiO₂ particles on the cover glass substrate (shown on the bottom).

A SEM image of zoom in of an exemplary array with a controlled spacing of $2 \mu\text{m}$ is shown in Figure 4.4b. A dark-field scattering image of the same area is shown in Figure 4.5a. In the average single-particle dark-field scattering spectrum (shown in Figure 4.5b) only one characteristic peak appears around the position of the

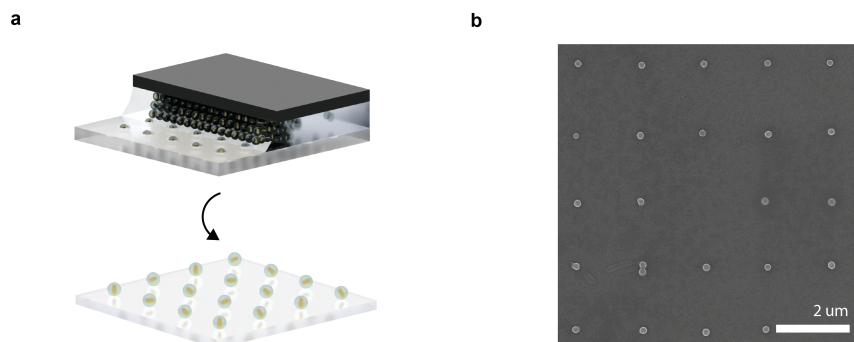


Figure 4.4: **Assembly into arrays.** (a) Assembly of the colloidal catalyst into ordered arrays on a substrate by templated dissolution interfacial patterning (TDIP). (b) Exemplary SEM image of a zoom in of the patterned surface.

longitudinal LSPR of the AuNRs. This is expected, as the absorption dominates for the transversal resonance of our small AuNRs. The final sample was then assembled under a microfluidic channel to ensure a continuous supply of reactants and mounted on an inverted total internal reflection (TIRF) microscope (Figure 4.6a and Appendix A.7).

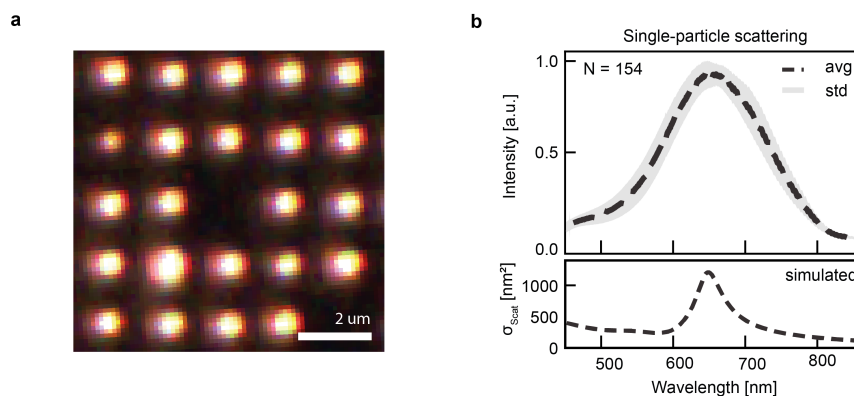


Figure 4.5: **Darkfield characterization.** (a) The same area as imaged in Figure 4.4b under a darkfield microscope. (b) Single-particle scattering spectra of the AuNR@mSiO₂ (top) and simulated scattering cross section (bottom).

4.4 In operando single-molecule plasmonic catalysis

The fluorogenic reaction we followed is the reduction of weakly-fluorescent resazurin (Rz) to fluorescent resorufin (Rf) (Figure 4.6a-b).

The absorption and emission properties of both molecules are shown in Figure 4.6b. We use a 561 nm continuous-wave laser with circular polarization in TIRF configuration to excite the fluorescent product Rf. The fluorescence quantum yield of resazurin (0.11) is much smaller than that of resorufin (0.75),¹⁷⁵ in addition, an

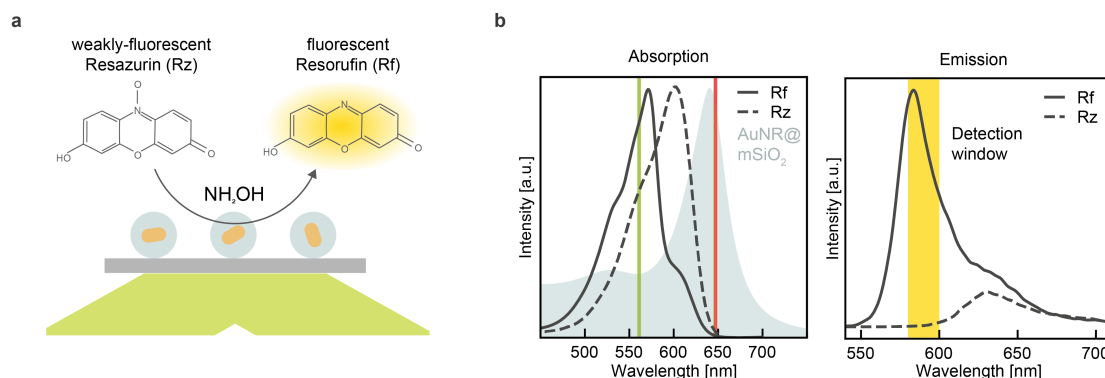


Figure 4.6: **The reaction-catalyst system.** (a) Schematic representation of the catalyst, reaction and setup. Weakly-fluorescent resazurin is converted to fluorescent resorufin in presence of hydroxylamine and the gold surface of the catalyst. The sample is illuminated with a circularly polarized 561 nm (green) continuous wave laser in total internal reflection, in part of the experiments a second laser (647 nm, red) is employed. (b) Left: Absorption properties of the system. Normalized resazurin and resorufin absorbance measured in borate buffer and normalized absorption cross section of the AuNR@mSiO₂ catalyst in water. Green and red vertical lines show the wavelengths employed in the measurements. Right: Only the product molecule resorufin is imaged. Emission spectra of the weakly fluorescent reactant resazurin and fluorescent product resorufin in borate buffer. The yellow bar shows the detection window.

emission bandpass filter between 580-600 nm in the detection pathway ensures that the detected fluorescent events belong to resorufin.

The absorption cross-section of the AuNR@mSiO₂ catalyst is also shown in Figure 4.6b. In some experiments, we used a second laser at 647 nm to excite the longitudinal LSPR. At this wavelength the absorption of both resorufin and resazurin is almost negligible (with $\sim 0.9\%$ and $\sim 4\%$ absorption compared to 561 nm).

It should be noted that the excitation wavelength of 561 nm partially overlaps with the transversal resonance of the AuNR@mSiO₂. This excites photoluminescence emission that results in a constant background for fluorescence imaging (as seen in Figure 4.7a). We used this photoluminescence emission to find the position of each AuNR@mSiO₂. In this way, the reactivity of each NP can be tracked under different reaction conditions.

Typically, we acquired at least 10.000 frames with an integration time of 30 ms. Each conversion event from resazurin to resorufin appears as a fluorescence burst on top of the background (Figure 4.7a). After drift correction and background subtraction, the events were localized with a precision of < 30 nm and assigned to a NP (Figure 4.7c-d and Appendix A.7). In this way, we gained temporal and spatial information on each catalytic event. For each AuNR@mSiO₂, we obtained a super-resolved 2D histogram of reactivity and the reaction dynamics, as shown in Figure 4.7b.

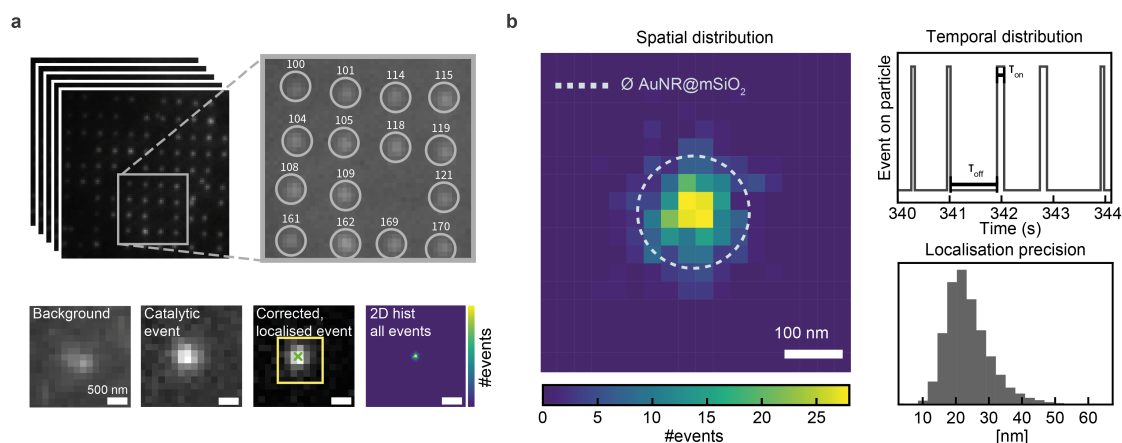


Figure 4.7: **In operando single molecule catalysis.** (a) Illustration of the in operando imaging method. Fluorescent events are detected and super localised on top of photoluminescence background of AuNR@mSiO₂. All scale bars 500 nm. (b) From the processed data, both spatial and temporal distributions of turnover events can be extracted. Events generally last 1 frame and are localized with a precision of < 30 nm.

4.4.1 Probing the reactant accessibility to the gold surface

First, we verified whether the surface of the AuNRs was accessible through the porous silica shell. An accessible Au surface is essential to probe whether the hot-electron mechanism plays an important role in the plasmon-enhanced mechanism (see Figure 4.1). AuNPs have previously been shown to catalyze the reductive deoxygenation of resazurin to resorufin by hydroxylamine in the absence of light.¹⁶⁸ Therefore, we compared the activity of the AuNRs under two conditions. First, with 200 nM resazurin alone and second, adding 100 μ M of hydroxylamine. In both cases, the reactants were supplied in excess.^{165,168} To image the product formation in the single-molecule experiments we cannot completely avoid excitation with the 561 nm laser. Therefore, the measurements were done at a low irradiance below $5 \times 10^6 \text{ W m}^{-2}$.

This minimizes the effect of light on the reaction rates.¹⁶⁸ The histograms of the average turnover rates under both conditions are shown in Figure 4.8. When hydroxylamine was added to the same AuNRs, the average turnover rate showed a significant increase (from $2 \times 10^{-3} \text{ s}^{-1}$ to $25 \times 10^{-3} \text{ s}^{-1}$ on average). The drastic increase in turnover rate upon inclusion of hydroxylamine shows that the Au surface was indeed accessible. All the following experiments were performed in the presence of both resazurin and hydroxylamine.

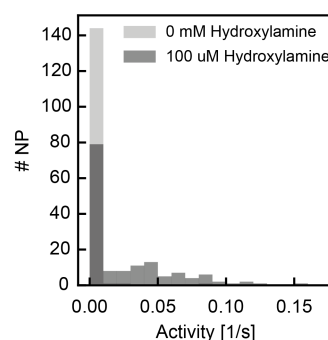
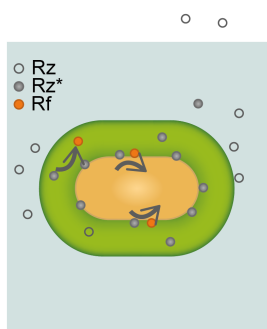


Figure 4.8: Turnover rates with and without 100 μ M hydroxylamine. Histogram of the average turnover rate of the same AuNRs under both conditions. To approximate dark conditions, the irradiance ($< 5 \times 10^6 \text{ W m}^{-2}$)

4.4.2 The effect of photo-exciting the reactant



The photoexcitation of resazurin has been shown to greatly increase its ability to be reduced to resorufin through a number of different pathways.^{152,166,167,175–177} To investigate the role of field enhancement, we investigated the power dependence of the reaction when illuminated at 561 nm (illustrated on the left), a wavelength that excites both resazurin and resorufin. For each individual NP, the excitation irradiance was calculated at the position of the NP (see Figure 7.9) for details). Figure 4.9 shows the average resorufin production rates against irradiance. The uncertainty for the highest irradiance is larger because it contains fewer NPs (11 vs. more than 200 in the lowest bin). The activity was significantly affected by

the excitation irradiance. For low irradiances, activity increases with increasing irradiance. At irradiances larger than $40 \times 10^6 \text{ W m}^{-2}$ the turnover rate saturates. The rate of product formation is expected to be dependent on the number of available photoexcited resazurin (Rz^*) molecules present, given by:

$$[Rz^*] = \frac{k_{abs} \times f \times I}{k_{abs} \times f \times I + k_{rel}} \times [Rz] \quad (4.1)$$

Where k_{abs} is the absorption rate constant, k_{rel} is the relaxation rate constant, I is the excitation irradiance, and f is a wavelength-dependent factor to convert the irradiance to a photon flux. The number of Rz^* can not grow indefinitely because it saturates for high irradiances where Rz^* approaches the value of Rz . However, this is not the only reason why the activity saturates in Figure 4.9 (see Appendix A.10 and A.12). The saturation is also not due to mass transport (see Appendix A.13 for more details). Most likely, the reaction is limited by the saturation of catalytic sites on the Au surface and can be explained by a Langmuir–Hinshelwood mechanism for surface reactions,¹⁷⁸ similarly to what has been reported for the reaction in the absence of light.¹⁶⁸ The reaction rate is then given by

$$\nu = A \frac{B[Rz^*](I)}{(1 + B \times [Rz^*](I))} + C \quad (4.2)$$

where C is the reaction rate in the absence of light,^{154,170} and $[Rz^*](I)$ is the irradiance-dependent concentration of photoexcited Rz^* given by equation 4.1. Close to the AuNR, the irradiance I is given by $I = e \times I_0$, where I_0 is the excitation irradiance and e is the intensity enhancement factor. We performed simulations to calculate the local electric field enhancement (see Appendix A.8 for details). Figure 4.10a shows the calculated intensity enhancement $e = \frac{I}{I_0}$ at 561 nm assuming unpolarized light at normal incidence. The average value on the Au surface is $e \sim 10$ (see Appendix A.8 for details). The solid line in Figure 4.9 shows the reaction rate fitted versus the excitation irradiance at 561 nm given by equations 4.1 and 4.2, with good agreement. It should be noted that a first-order dependence on Rz^* has been assumed in the equation 4.2. Alternative modeling using higher-order dependencies is presented in Appendix A.11). The fitting yields an activity in dark of only 7×10^{-3}

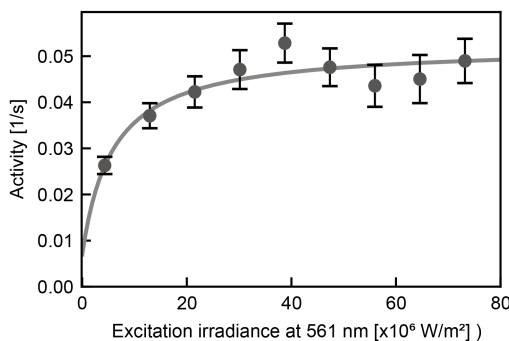


Figure 4.9: **Reaction kinetics enhanced with 561 nm illumination.** Average turnover rates against binned green irradiance with 200 nM resazurin and 100 μ M hydroxylamine. The solid line is given by equation 4.2, with $A = 0.045$ s $^{-1}$, $B = 9.556$ μ M $^{-1}$, $C = 0.007$ s $^{-1}$ and $[Rz^*](I)$ given by equation 4.1 with $I = 10 \times I_0$, $k_{abs} = 2731$ m 2 mol $^{-1}$, $k_{rel} = 1.43 \times 10^9$ s $^{-1}$ and $f = 4.686$ W s μ mol $^{-1}$. Bins contain at least 10 particles and the error bars are the standard error of the mean.

s $^{-1}$. This means that the conversion of resazurin to resorufin is enhanced up to 700% from dark. In summary, the activity enhancement of the catalyst by excitation with 561 nm can be fully explained by the photoexcitation of Rz, benefitting from the local field enhancement due to the plasmonic AuNR.

4.4.3 Spatial distributions of reactivity

To gain more insight into the reaction mechanism, we examine the spatial distribution of reactivity. Figure 4.10b shows an exemplary scatter plot of the position of conversion events. Our AuNRs are small, with dimensions comparable to our localization precision of ≈ 30 nm. Therefore, it is not possible to distinguish catalytic hot spots within a single AuNR. Nevertheless, it is a noticeable fact that conversion events are also observed at locations far from the Au surface. In the following, we will focus on two groups of events: i) The *Superficial* ones, within < 50 nm from the NPs's center, and ii) The ones *Far* from the surface, with positions in the range between 80 to 120 nm from the NPs's center. The upper panel of Figure 4.10c shows the resorufin production rates per unit area versus the excitation irradiance for both groups. The activity is higher for *Superficial* events. However, the fraction of events belonging to the *Far* group increases with increasing irradiance. The lower panel of Figure 4.10c shows the ratio between *Far* and *Superficial* activities. The difference in the irradiance-dependence of both groups indicates that two reaction pathways are present: The Au-catalyzed reaction occurring on the surface, and a second reaction pathway not involving the surface. An alternative way of visualizing the information is through the cumulative distribution, which is defined as the percentage of events occurring within a certain range from the NPs's center. These are shown in Figure 4.10d for three excitation irradiances. In the range of distances up to 50 nm, the distributions are practically identical, independently of the excitation irradiance. This is consistent with a reaction occurring predominantly at the Au surface. On the other hand, increasing the excitation irradiance allows the reaction to occur at positions farther from the Au NR. For example, the radius containing 60 % of events increased

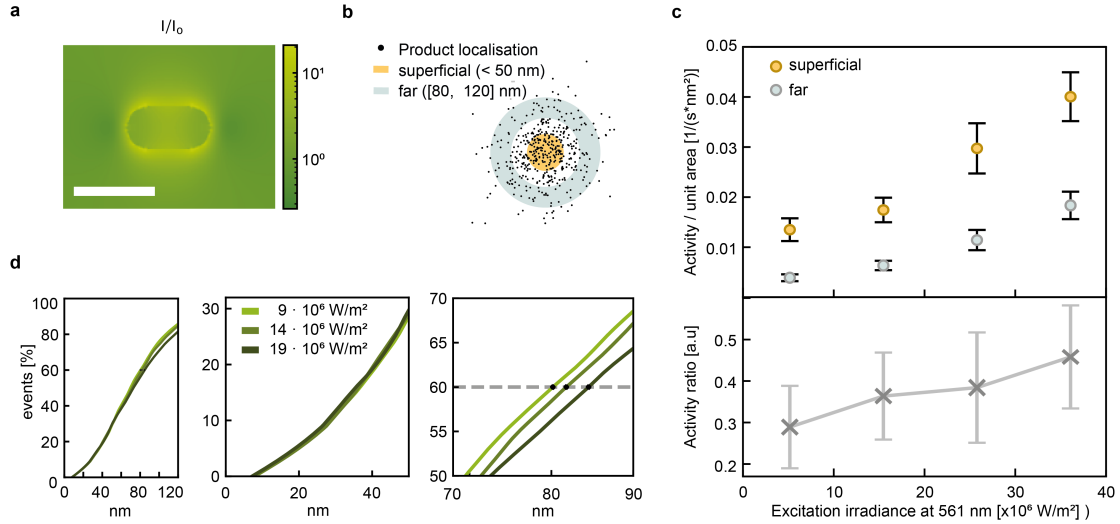


Figure 4.10: **Spatial distributions of reactivity.** (a) Simulated field enhancement $e = \frac{I}{I_0}$ under 561 nm illumination with unpolarized light. Scale bar is 50 nm. (b) Illustration of the *Superficial* and *Far* regions used in (c). Not drawn to scale. (c) Top: Turnover rates of the superficial and far events normalized by the unit area, including only particles with more than 50 events. Each bin contains at least 19 NPs. Bottom: The ratio of the activity far/superficial, illustrating different kinetics. Error bars are standard error of the mean. (d) Cumulative radii of the events at different irradiances. There is no difference in the spatial distribution with increasing green irradiances close to the AuNRs. At higher green irradiance there is small shift towards larger cumulative radii, illustrated at 60%.

from 80 nm to 84 nm when the excitation irradiance increased from $9 \times 10^6 \text{ W m}^{-2}$ to $19 \times 10^6 \text{ W m}^{-2}$. Two mechanisms for the catalytic enhancement away from the surface lay at hand but are difficult to disentangle: electromagnetic fields and temperature. A discussion into these mechanisms can be found further below, after we present the next experiments, which will allow more insight.

4.4.4 The effect of the plasmon resonance

To further understand the role of plasmon excitation on catalytic activity, we next illuminated the AuNRs with a 647 nm laser (illustrated on the left). This laser is tuned only to the longitudinal LSPR of the AuNRs, with negligible absorption of the resazurin (Figure 4.7) and therefore allows us to disentangle the photoexcitation of resazurin and from the plasmon excitation. At this wavelength, the absorption cross section of the AuNRs is significantly higher ($\sigma_{abs}(647\text{nm}) = 5488 \times \text{nm}^2$) compared to $\sigma_{abs}(561\text{nm}) = 1523 \times \text{nm}^2$), resulting in a higher hot electron generation and temperatures. For each AuNR, we calculated its activity enhancement (AE), defined as the ratio between the reaction rate with both 647 nm and 561 nm illumination divided by the rate with only 561 nm illumination

$$AE = \frac{\langle \tau_{off}^{-1} \rangle_{647\text{nm}+561\text{nm}}}{\langle \tau_{off}^{-1} \rangle_{561\text{nm}}} \quad (4.3)$$

The 561 nm irradiance was kept below saturation, ranging from 7 to 15×10^6 W m^{-2} . Figure 4.11 shows the median activity enhancement against the binned 647 nm irradiance, which increases from ~ 1.02 for an irradiance of 71×10^6 W m^{-2} to 1.28 when the irradiance reaches 105×10^6 W m^{-2} . Noticeably, these enhancements are much lower than what can be achieved with illumination at 561 nm at similar irradiances.

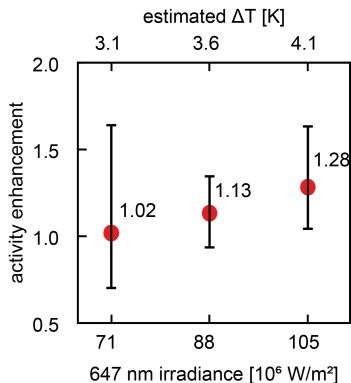


Figure 4.11: **The effect of the plasmon resonance.** Influence of red irradiance on reaction kinetics. Median single-particle activity enhancements against binned red irradiance and estimated temperature increase. Includes AuNRs within the full-width-half-maximum (FWHM) of both green and red irradiance. Each bin contains 13-25 AuNRs.

One possible mechanism for the observed plasmonic enhancement when excited at 647 nm is a photothermal effect. Figure 4.12 shows temperature increase maps calculated using the Finite Element Method and accounting for collective heating effects, (for details, see Appendix A.9). The maps correspond to illumination with 561 nm (left) and 647 nm (right). The temperature increases produced by the 561 nm laser are more than 20 times smaller (0.15 K) and therefore neglected in the overall temperature increase upon illumination with 647 nm. Figure 4.11 (upper axis) shows the Activity Enhancement versus the temperature increase of the AuNR, with a positive correlation. From the activity data alone, we can only speculate about the enhancement mechanism: At 647 nm, the excited hot electrons in AuNR should have enough energy to reduce resazurin.¹⁶⁶ On the other hand, an enhancement of 28% and a temperature increase of around 4 K are not enough to confirm or rule out a thermal contribution.

Again, further insight into the mechanistic details of the reaction system can be obtained by looking at the spatial distribution of reactivity. Figure 4.13 shows the cumulative radial distributions of events, with (red) and without (green) illumination with the 647 nm laser at an irradiance of 105×10^6 W m^{-2} . Interestingly, both distributions overlap, and we do not observe a preferential increase in the reaction rate of events far from the AuNR upon plasmon excitation. Furthermore, the radius containing 60 % of events remains practically unchanged.

This observation indicates that the driving mechanism for the reaction pathway visible in Figure 4.10 observed *Far* from the NR and not involving the Au surface is photoexcitation of resazurin and not a thermal effect. Such a reaction pathway is

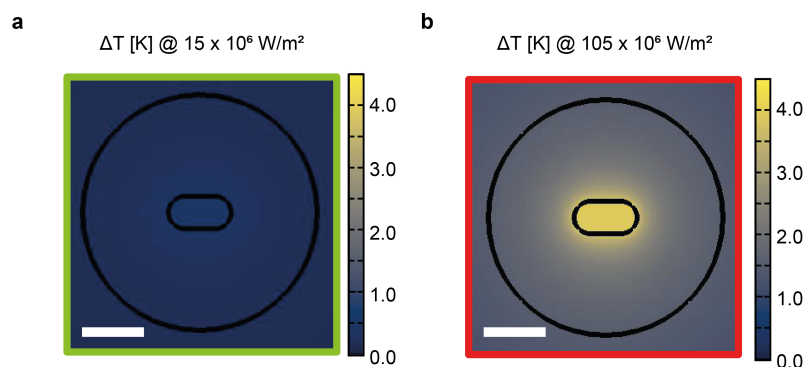


Figure 4.12: **Temperature profiles at different irradiances.** (a) $15 \times 10^6 \text{ W m}^{-2}$ of 561 nm irradiance. (b) $105 \times 10^6 \text{ W m}^{-2}$ of 647 nm irradiance. Scale bars are 50 nm.

compatible with a photodriven disproportionation reaction, as previously observed by Hamans et al.¹⁵⁶ The *Superficial* reaction pathway appears to benefit from enhanced absorption of the AuNR at 647 nm. However, if we compare this turnover rate enhancement with 647 nm to the one at 561 nm, it is 20 times lower. Namely, 600% from dark with 561 nm irradiance vs 28 % enhancement with 647 nm, at similar irradiances. This suggests that, in this reaction system, the photoexcitation of the reactant molecule is the dominant driver, in contrast to the enhancement of the absorption of the catalyst.

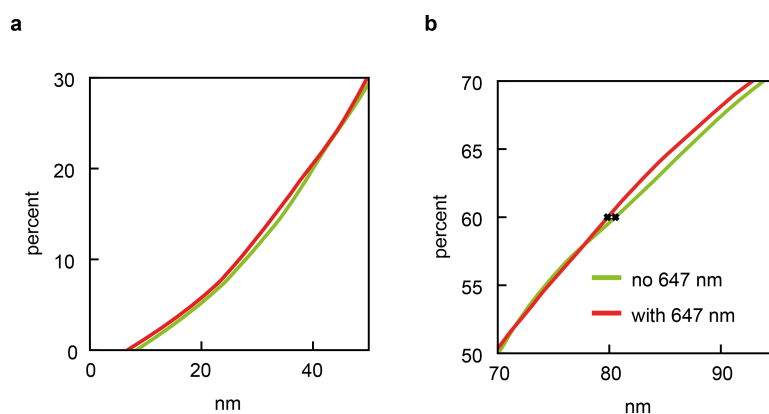
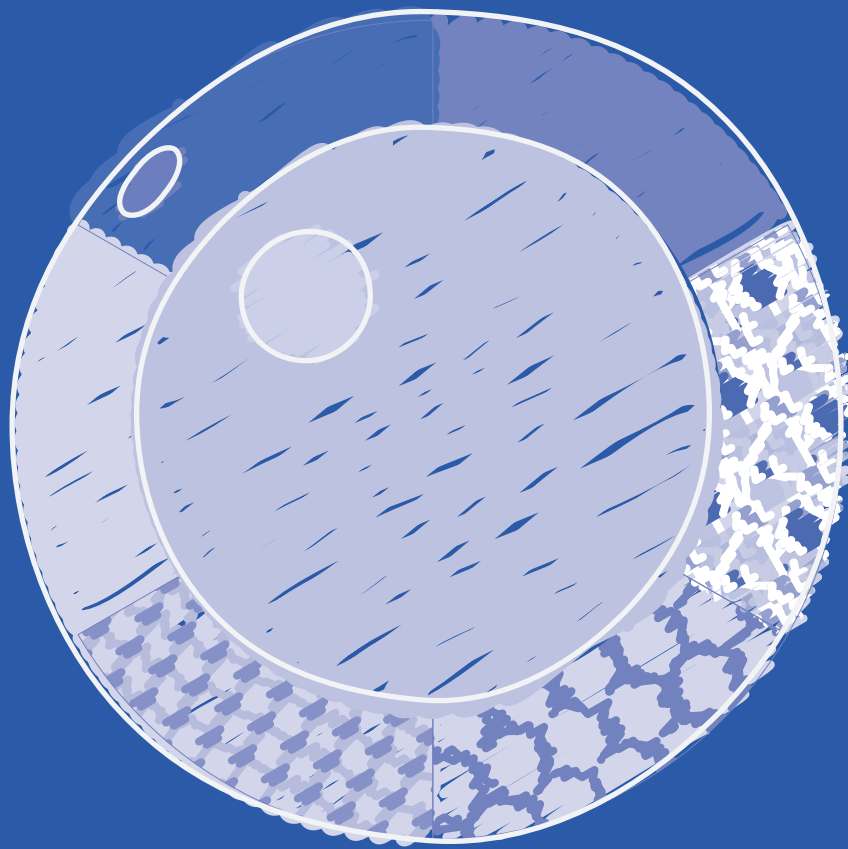


Figure 4.13: **Unaffected spatial distributions.** Cumulative spatial distribution close the nanoparticle center (a) and away from the center (b). Median of the 25 AuNR in the highest red irradiance bin of Figure 4.11. The spatial distribution upon excitation of the longitudinal resonance is unaffected.

4.5 Conclusions

In summary, we have used single-molecule localization microscopy to study plasmon-enhanced catalysis with super-resolution. By exploiting the subparticle resolution, we were able to spatially track different possible reaction mechanisms exhibiting distinct spatial distributions. Our findings indicate that the enhancement of the studied reaction is largely attributed to the photoexcitation of the reactant molecule Rz. Therefore, a design strategy for catalysts optimized to similar reactions is the maximization of the plasmonic field enhancement. Similar reaction pathways have recently been proposed, for example, for the dissociation of the S-S bond in dimethyl disulfide⁷³ or O₂ dissociation.¹⁷⁹ Another approach, for example for H₂ generation or CO₂ dissociation, is to combine the plasmonic antenna with molecular photosensitizers^{60,180–183} into hybrid systems. To maximize the turnover rate in these types of reactions, the plasmonic field enhancement should be tuned specifically to the absorption of the reactant molecule. In this way, the turnover rates can be maximized at low irradiances and facilitate the design of plasmonic nanoparticles to drive chemical transformations without the use of high-intensity lasers. One key take-away is that rate enhancement mechanisms depend not only on the plasmonic structure itself but also largely on the reaction being studied. For example, while field enhancement was the major contributor to the studied reaction, other reactions may rely on hot-electrons or temperature effects.

Building upon this understanding, the next chapter of this thesis discusses recent developments in hybrid plasmonic photocatalysts for solar fuel generation. Instead of having a molecule directly exposed to such strong fields, another approach would be for a second catalytic material to occupy this role, creating hybrid structures in which the performance is enhanced compared to the monometallic counterpart. However, the role of temperature in these systems is often overlooked. To address this issue, we have implemented a single-particle nanothermometry technique for bimetallic plasmonic nanoparticles, which allows us to investigate the link between morphology and light-to-heat conversion.



5

Hybrid plasmonic catalysis

This chapter on hybrid plasmonic photocatalysis builds upon the previous chapter's understanding of plasmonic enhancement's potential to improve catalytic reactions. By combining plasmonic nanoparticles with other catalytic materials, the performance of photocatalysts can be further enhanced. Here, we review the combination of plasmonic nanomaterials with catalytic metals, semiconductors, perovskites, 2D materials, metal–organic frameworks, and electrochemical cells. We provide a critical analysis of the state-of-the-art in hybrid plasmonic photocatalysts, identify the best performing plasmonic systems, and discuss their potential for designing a new generation of plasmonic catalysts. We learn that, even though temperature plays a critical role in plasmonic photocatalysis, in many studies it is not addressed appropriately. For this reason, we implement a single-particle nanothermometry technique for bimetallic plasmonic nanoparticles and investigate the link between morphology and light-to-heat conversion. The results contribute to a better understanding of energy conversion processes in plasmon-assisted catalysis.

Based on

S. Ezendam, M. Herran, L. Nan, C. Gruber, Y. Kang, F. Gröbmeyer, R. Lin, J. Gargiulo, A. Sousa-Castillo, and E. Cortés. Hybrid Plasmonic Nanomaterials for Hydrogen Generation and Carbon Dioxide Reduction, ACS Energy Letters, 2022⁶⁰

J. Gargiulo, M. Herran, I. L. Violi, A. Sousa-Castillo, L. P. Martinez, S. Ezendam, M. Barella, H. Giesler, R. Grzeschik, S. Schlücker, S. A. Maier, F. D. Stefani, E. Cortés. Single particle thermometry in bimetallic plasmonic nanostructures. *Under review at Nature Communications*¹⁸⁴

Figure 5.0 Artistic representation of different hybrid plasmonic catalysts. Simplified from Figure 5.1. By combining plasmonic nanoparticles with other materials, synergistic effects arise.

In the first part of this chapter we will analyze the state-of-the-art in hybrid plasmonic photocatalysis, including the combination of plasmonic nanomaterials with catalytic metals, semiconductors, perovskites, 2D materials, metal-organic frameworks, and electrochemical cells. In this way, we aim to learn which is the best material combination and how the energy can be extracted most efficiently. A quantitative comparison of the demonstrated activity and selectivity of these materials for solar fuel generation in the liquid phase is presented. This critical assessment allows for benchmarking the state-of-the-art of hybrid plasmonic photocatalysts against other existing heterogeneous catalysts and identification of the best performing plasmonic systems for designing a new generation of plasmonic catalysts.

5.1 Hybrid plasmonic nanomaterials for solar fuels

In Chapter 2.4.3 we have seen the various processes through which the excitation of localized surface plasmon resonances can drive reaction and the potential they offer for alternative reaction pathways towards desired products. However, the catalytic activity of typical plasmonic metals is low. For this reason, an increasing number of so-called hybrid plasmonic nanostructures have been investigated.^{185–190} Here, the plasmonic metal is combined with another, typically catalytic, material with synergistic effects. With the field of plasmonic catalysis experiencing exponential growth over the past decade, it is important to assess the materials that have been explored so far, not only in comparison to one another but also in relation to existing heterogeneous catalysts for solar fuel production. Such benchmarking can provide insight into the progress and achievements made thus far, as well as demonstrate the potential of this novel form of (photo)catalysis in the pursuit of sustainable catalysis and clean energy production. In this review, we will focus on the significant strides made in the development of hybrid nanomaterials for the production of solar fuels through plasmon excitation. Many systems with great potential have been investigated for plasmonic catalysis in the gas phase.^{56,187,189,191–197} However, in this review, we are limiting the examples to reactions under mild reaction conditions (i.e., heterogeneous catalysis in the liquid phase). In addition, we will narrow the scope of this review to the reactions that are relevant for solar fuel production, namely H₂ generation and CO₂ reduction, but we will be as broad as possible regarding the evaluation of different types of novel hybrid systems, i.e. not only limit to metals and semiconductors but also include plasmonic hybrids with perovskites, 2D materials and metal-organic frameworks for both pure photocatalysis and photoelectrocatalysis. With the increasing complexity and diversity of hybrid plasmonic nanostructures comes the necessity of a quantitative comparison among them. Here, we propose a series of standard metrics that should be reported for future plasmonic catalysts. Identifying the best performers is essential to design future plasmonic platforms for solar fuel production.

First, we briefly elaborate on the motivation to employ plasmonic materials for photo (electro) catalysis and enumerate the enhanced properties that can be obtained in hybrid nanostructures. Second, we describe the reactions to produce solar fuels that are the focus of interest of this review. Third, we present the performance metrics that

will be used to compare different materials/systems. In the main section of the review article⁶⁰ recent developments in each of the single hybrid systems are reviewed at length. However, in this Chapter, for brevity, we will only include the final discussion that summarizes and compares the different hybrid systems for each reaction in a meta-analysis.

5.1.1 Properties of hybrid plasmonic nanomaterials.

Plasmonic nanoparticles interact strongly with light through the excitation of localized surface plasmon resonance (LSPR), which correspond to the coherent oscillations of their free electrons coupled to the electromagnetic field.²⁴ Plasmonic materials are typically metals with negative real permittivity (i.e., with high concentration of free electrons) such as silver (Ag), gold (Au), copper (Cu), etc. The plasmon resonances are highly tuneable, and their frequency can cover the ultraviolet (UV), visible, and near-infrared (NIR) region of the electromagnetic spectrum (i.e., the totality of solar emission).⁴² When resonantly illuminated, the absorption cross sections of plasmonic nanoparticles reach tens of times their geometrical size, making them efficient harvesters of light. In addition, plasmonic nanoparticles can act as solar light antennas. They can concentrate light in small volumes of typically a few nm^3 near their surface, where the intensity can reach values as high as 10^5 the solar one.⁴¹ That volume is on the order of molecular sizes, transforming the plasmonic nanoparticles into nanoreactors within molecular scales.

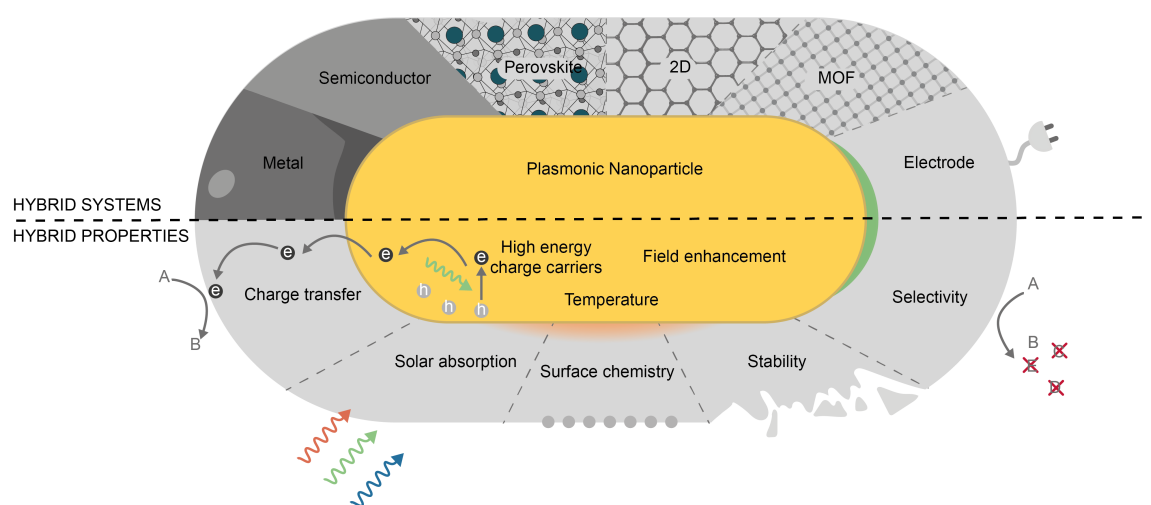


Figure 5.1: **Hybrid plasmonic photocatalysts.** **Top.** Overview of the hybrid plasmonic systems. From left to right: Metal, Semiconductor, Perovskite, 2D, MOF and Electrochemistry. **Bottom.** Desirable properties of an ideal photocatalyst. The plasmonic component can harvest light and transfer the energy through charge carriers, heat and electromagnetic fields. Non-plasmonic materials can add or enhance catalytic properties. The hybrid system can show enhanced stability, selectivity or activity through various mechanisms, e.g. effective charge transfer, surface chemistry or enhanced absorption. Adapted with permission from Ref.⁶⁰

There is a variety of plasmon driven processes that can affect the activity and selectivity of target molecules.^{51,75} Plasmon resonances are of mixed optoelectronic

nature, and as such, the energy from incoming light is partly stored in the kinetic energy of charge carriers and in the electromagnetic field. These resonances can decay radiatively or transfer their energy to a charge carrier. This highly energetic charge carrier then relaxes during which secondary and lower energy charge carriers are excited and ultimately heat is released to the surrounding of the plasmonic nanoparticles. This means that a resonantly illuminated plasmonic nanoparticle can supply a broad range of energy quanta, from highly energetic charge carriers with the energy of the incoming photons ($\approx 2 - 3$ eV) to thermal phonons (≈ 0.025 eV). A nearby molecule or material can use these energy quanta to perform a chemical transformation in thermal or nonthermal ways. The versatility of plasmon-driven processes offers the opportunity to obtain alternative reaction pathways towards a desired but kinetically or thermodynamically unfavourable product. For example, they can operate in a particular intermediate step of a reaction, altering the pathway towards a different product.^{155,198}

However, the catalytic activity of typical plasmonic metals (Au, Ag, Cu, etc.) for solar fuel production is comparatively low.^{199,200} In recent years, plasmonic components have been interfaced with other nanomaterials, searching for superior hybrid plasmonic nanocatalysts. These hybrid plasmonic catalysts are summarized in the top half of Figure 5.1. The promising properties of plasmonic nanoparticles are combined with additional enhanced photocatalytic properties from the second material that are in many cases not present in the single-component counterparts. The bottom half of Figure 5.1 schematizes some of the properties that are desirable (and potentially obtainable) in a hybrid plasmonic catalyst. While the plasmonic component harvests light and supplies energy through charge carriers, heat, or electromagnetic fields, a second (non-plasmonic) component can, for example, improve the interaction with target molecules, enhance the stability of the system or enlarge the lifetime of excited carriers. In the following, we present the particular opportunities that each material/interface opens for plasmonic catalysis.



Figure 5.2: Illustration of bimetallic hybrids with different configurations. Adapted with permission from Ref.⁶⁰

Plasmonic metal - metal. The catalytic activity of plasmonic metals can be improved by combining plasmonic metals with common catalytically active metals such as Palladium (Pd), Platinum (Pt), Rhodium (Rh), etc. The inclusion of such metals can help lower the activation energy of a reaction step or enhance the adsorption/desorption dynamics of reactants/products on the surface of the nanocatalyst. In addition, combining the two metals modifies the electronic energy bands close to their interface, potentially facilitating charge flow, reducing the chemical potential of the charge carriers, and enhancing their extraction.²⁰¹ In bimetallic systems, the decay of plasmon resonances gets altered, favouring non-radiative (excitation of carriers, heat

generation) versus radiative channels (scattering).^{85,202,203} Interestingly, the spatial distribution of absorption can be shifted towards the catalytic metal generating carriers exactly where they are more reactive.^{195,204,205}

Plasmonic metal - semiconductor. The lifetime of photoexcited charge car-

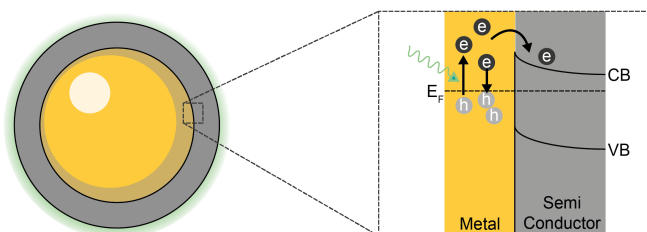


Figure 5.3: Schematic representation of charge transfer at the Schottky barrier of a Metal-Semiconductor interface. Adapted with permission from Ref.⁶⁰

riers in plasmonic metals is typically less than 1 ps.^{29,206} This time is usually too short for the carriers to act on an adsorbate, a detrimental fact for the overall reactivity of the system. Longer charge carrier lifetimes can be attained by interfacing the metal with a semiconductor. The decay of the plasmon can generate charge carriers in the semiconductor through three main mechanisms. First, photoexcited electrons in the metal with sufficient energy can be transferred across the Schottky barrier²⁰⁷ to the conduction band of the semiconductor, in a process called indirect electron transfer.^{55,208} Second, a plasmon can decay by directly exciting an electron into the conduction band of the semiconductor and a hole in the metal, in a process called plasmon-induced charge-transfer transition²⁰⁸ or direct electron transfer.^{44,209} The third mechanism is a plasmon-induced resonant energy transfer,^{210,211} where an electron-hole pair is excited in the semiconductor. The presence of a Schottky barrier at a metal/semiconductor interface²⁰⁷ traps electrons as, depending on the potential difference, electrons with different energies can be harvested^{212,213} and can be prevented or delayed from coming back to the metal.²⁰⁸ Furthermore, structural defects and/or vacancies in the semiconductor can also act as electron traps enhancing their lifetime and are usually the most reactive sites.²¹⁴ These processes allow electrons to become available in the semiconductor to drive reduction reactions while holes remain in the metal for oxidation reactions.⁴⁴ Inversely, there have also been demonstrations of semiconductors harvesting the holes.^{197,215} Without the photoexcited electrons in the plasmonic metal, wide bandgap semiconductors like titanium dioxide (TiO_2) are photocatalytically active only in the UV. The energy transfer mechanisms from the plasmonic material to the semiconductor extend their operational wavelength range, accommodating a larger fraction of the solar spectrum and potentially increasing the solar-to-fuel conversion efficiency.^{34,216}

Plasmonic metal - perovskite. Perovskites are a versatile subclass of semiconduc-

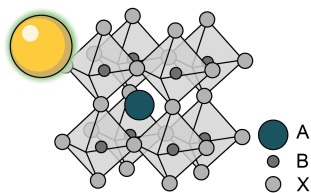


Figure 5.4: Schematic representation of a plasmonic-perovskite hybrid system. Adapted with permission from Ref.⁶⁰

tors with attractive optoelectronic and catalytic properties. They are characterized by their ABX_3 crystal structure, where 'A' and 'B' represent cations and 'X' an anion (Figure 5.4a). As semiconductors, the physical and chemical properties of perovskites leading to a catalytic enhancement are generally as described above. This is especially true for ABO_3 type perovskite oxides, which are cost efficient and can accommodate a wide range of substituting and doping elements to modulate their electronic and catalytic properties, but are generally photocatalytically active only under UV irradiation owing to their wide bandgap. Their combination with plasmonic materials allows the absorption of visible light, making irradiation of wavelengths with photon energies below the bandgap of the perovskite accessible.²¹⁷⁻²²⁰ Both charge or energy transfer from the plasmonic material to the perovskite can occur.^{221,222} The perovskite oxides are in many ways very similar to semiconductors included in the general semiconductor section; However, the perovskite category is included in this review due to a second type of perovskite, namely ABX_3 type perovskite halides ($X=F, Cl, Br, I$). They have a tunable absorption across the entire visible spectrum²²³ as well as long carrier lifetimes.²²⁴ In addition to the benefits discussed above, by combining perovskite halides and plasmonic materials the characteristic absorption spectra of both components can be matched such that the strong near-field enhancement of the plasmonic nanoparticle can significantly enhance the absorption of light by the halide perovskite, potentially boosting their catalytic performance.

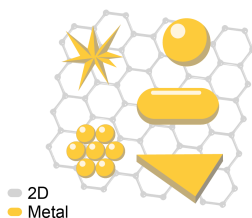


Figure 5.5: Schematic representation of a 2D material loaded with plasmonic metal structures of various shapes, sizes, and chemical compositions. Adapted with permission from Ref.⁶⁰

Plasmonic metal - 2D. A 2D material is the cocatalyst with the largest possible available surface. Of particular interest are materials with outstanding electrical conductivity and mobility, such as carbon-based 2D and transitional metal-based 2D materials. The photogenerated electrons in the plasmonic nanoparticles can transfer

to the 2D material, where they benefit from a longer lifetime that promotes substrate reactivity.²²⁵ Furthermore, electrons can accumulate in the 2D material or promote the formation of charged excitons (with more than one electron coupled to a hole).^{226,227} This accumulation facilitates reactions that require multiple electrons. Finally, the presence of defects, dopants, or oxygenated functional groups in the 2D material can act as catalytic sites for specific reactions.²²⁸

Plasmonic metal - MOFs. Metal-organic frameworks (MOFs) are ordered periodic structures formed by nodes of metal ions linked by organic ligands.^{229–231} Plasmonic materials can gain interesting properties relevant to catalysis when combined with this versatile class of porous materials.^{232–236} First, MOFs can act as substrates that provide support and increase stability.²³⁷ Second, they are highly versatile in composition and pore size, allowing structural tailoring according to the application. For example, their organic linker can be adjusted to catalyse a specific reaction or co-reaction.²³⁸ This property makes them promising systems to achieve high selectivity of product formation. Third, they can be structurally designed so that their catalytic centers lie in the near-field enhancement region of the plasmonic component, enhancing their absorption.²³⁷ Fourth, their high porosity can allow an extraordinarily large surface area for a reaction to occur²³⁹ or the preconcentration of reactants next to the plasmonic nanoparticles.²⁴⁰ Finally, MOFs can also act as a charge carrier mediator to enhance the efficiency of electron-hole pair separation efficiency.²⁴¹

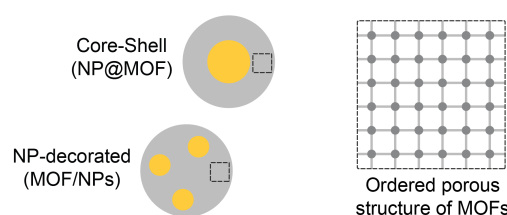


Figure 5.6: Types of plasmonic metal - MOF hybrids. Adapted with permission from Ref.⁶⁰

Plasmon-assisted Electrochemistry. Electrocatalysis, like photocatalysis, has been extensively studied in recent years.²⁴² While promising, electrochemical reactions often require high overpotentials. Plasmonic materials can enhance the performance of electrocatalytic systems by using solar energy. This can result in lower electrical energy consumption and higher product formation, manifested as a reduced overpotential or increased current density.^{243–245} The introduction of a plasmonic material can also modify the chemical landscape, which can affect selectivity by triggering or enhancing otherwise thermodynamically and/or kinetically hindered reactions.²⁴⁶

5.1.2 Plasmon-assisted reactions towards solar fuel generation.

In this review, we discuss hybrid photocatalysts with at least one plasmonic component that is resonantly illuminated. This excludes, for example, systems where the presence of a plasmonic metal can have a positive impact on the catalytic activity of the system

but is either not illuminated or illuminated in a region with negligible absorption.^{247,248} Among the large list of recently demonstrated plasmon-assisted reactions, we focus on a few particularly relevant reactions toward the generation of solar fuels: H₂ generation reactions and CO₂ reduction reactions. We introduced these reactions in Chapter 2.4.3, but to recapitulate:

1. Hydrogen can be a replacement for fossil fuels, given its high energy density, stability, and ability to be stored and transported. However, current hydrogen production methods result in excessive carbon emissions, and thus, hydrogen needs to be produced from renewable energy sources. Photocatalytic hydrogen production from water and hydrogen-containing compounds is of interest, with water splitting being particularly attractive due to the abundance of water and sunlight.
2. Reducing atmospheric carbon dioxide and producing fuels through carbon dioxide conversion. The reactions for carbon dioxide conversion are complex and can lead to various products with different numbers of charge transfers and carbon atoms. Producing desirable C₂+ products is challenging due to the possibility of branching reaction pathways and simultaneous production of multiple products. A suitable large-scale photocatalyst for carbon dioxide reduction should have high efficiency and selectivity to one product.

An overview of all reactions of interest can be found in Table 2.1.

5.1.3 Performance metrics

The main challenge when comparing different hybrid nanocatalysts is to find quantitative and relevant performance metrics. In the previous Chapter this was straight forward, as single-molecule microscopy allows the determination of turnover rates at the single-particle level. However, catalysts are more commonly evaluated in bulk and different aspects of a catalyst performance may be evaluated, such as its activity, selectivity, stability, or temperature of operation. However, it is not straightforward to determine metrics depending only on the nanocatalyst's intrinsic properties because its performance may be strongly altered by reaction conditions such as the illumination characteristics or reactant concentration. The typically reported performance metrics used in the field are discussed in the following. Table 5.1 summarizes the metrics that will be extracted from the original manuscripts, for the tables summarizing each hybrid system, the reader is referred to Ref.⁶⁰ *Activity* is quantified by the formation rate of a product (amount of product generated per time per mass of hybrid catalyst, Eq. 5.1). It should be noted that this metric assumes a linear relation of product formation with respect to time and catalyst concentration, which is often not the case.²⁴⁹

$$R = \frac{n_{product}[\mu\text{mol}]}{mass_{hybrid\ catalyst}[\text{g}] \times time[\text{h}]} \quad (5.1)$$

In this review, we will use the formation rate (Eq. 5.1) as the main metric for activity, as it is most commonly reported. If it is not possible to extract the formation rate, the turnover frequency (TOF) or turnover number (TON = TOF × time) is reported

in the tables. Across the literature, the TOF is used with conflicting definitions. In hybrid nanomaterials where the reaction occurs in only one of the components, the number of catalytic sites might be used instead of the total mass of the catalyst. This value is rarely reported because it is difficult to determine because information on the number of active catalytic sites is not always available or might fluctuate over time. Instead, TOF is more commonly referred to as the mole of product molecules per mole of catalyst per time (Eq. 5.2).

$$TOF = \frac{n_{product}[\text{mol}]}{n_{hybrid\ catalyst}[\text{mol}] \times time[\text{min}]} \quad (5.2)$$

The key role of illumination in plasmon-assisted catalysis is not reflected in the activity metrics discussed so far. Therefore, the quantum efficiency (QE) should be used as a complementary metric (Eq. 5.3).²⁵⁰ It is defined as the number of reacted electrons per absorbed photon and determined for a specific wavelength. Whenever a quantum efficiency is reported, it is usually the apparent quantum efficiency (AQE), defined as the number of reacted electrons per incident photon (Eq. 5.4). This is the case because the number of absorbed photons is often difficult to determine. The AQE is a lower bound for the QE and will be used in this review whenever it is reported.

$$QE = \frac{N_{reacted\ electrons}}{N_{absorbed\ photons}} \times 100\% \quad (5.3)$$

$$AQE = \frac{N_{reacted\ electrons}}{N_{incident\ photons}} \times 100\% \quad (5.4)$$

In photo-electrocatalysis, the metrics reported are different from the ones for photocatalysis. A metric for the activity is the overpotential (mV) at a given current density (mA cm^{-2}) (or vice versa). The onset potential (mV), the potential at which the reaction starts to occur, describes the reaction energy barrier. Finally, the Tafel slope (mV dec^{-1}), obtained by plotting the overpotential as a function of the logarithm of the current density, is used to estimate the reaction kinetics of the system. *Selectivity* is a major concern for CO_2 conversion. For photocatalytic systems, it is generally reported as the ratio between the formation rate of the major product and all products in percent (Eq. 5.5).

$$Selectivity = \frac{n_{major\ product}}{n_{all\ products}} \times 100\% \quad (5.5)$$

For electrocatalytic systems, the Faradaic efficiency is more commonly reported. It describes the proportion of reacted electrons facilitating the formation of a certain product.

The *stability* of the catalyst is referred to as the longest investigated time under operando conditions in which its activity did not significantly decrease. Whenever the stability was not examined, the experiment duration is reported in the table instead. *Temperature* is an important parameter that modulates the rate of reactions through the Arrhenius law. Illuminated plasmonic systems offer the opportunity of driving reactions at mild conditions, without the need for high external temperatures. Here, whenever possible, the operating temperature of the reactor will be used as a metric.

Photocatalysts	
Activity	Formation rate [$\mu\text{mol g}^{-1} \text{h}^{-1}$ or $\mu\text{mol g}^{-1} \text{h}^{-1} \text{e}^{-1}$] Apparent Quantum Efficiency (AQE) [%]
Selectivity	Selectivity [%]
Stability	Stability [h] Duration [h]
Temperature	Reactor Temperature [$^{\circ}\text{C}$]
Light enhancement Plasmonic enhancement	Activity enhancement factor (LE/PE)

Table 5.1: Performance metrics for hybrid plasmonic catalysts

It must be noted that this value might strongly differ from the surface temperature of the nanocatalysts.²⁵¹

The *light enhancement (LE)* aims to quantify the contribution of light to a given reaction. When doing this, one should also compensate for the temperature increase upon illumination,¹³⁹ however this is not frequently done. Here, it will therefore simply be estimated as the ratio between the activity (i.e., formation rate or TOF) of a nanocatalyst in the presence and in the absence of light.

Similarly, the *plasmonic enhancement (PE)* is the activity ratio of the illuminated system in the presence and absence of the plasmonic component. In photo-electrocatalysis, the enhancements are evaluated as a shift in the overpotential at a current density of 10 mA cm^{-2} of the reactions.

5.1.4 State of the art of hybrid plasmonic catalysis

In this section, we will summarize and compare the performance of the hybrid plasmonic photocatalysts reviewed. We quantitatively compare photocatalysts according to their activity and selectivity, breaking down the different reactions of interest for hydrogen production and CO_2 reduction.

In many of the examples reviewed here, the information on reaction conditions is incomplete. In addition, even when reported, conditions vary among the different examples. Nevertheless, we believe that insightful conclusions can be drawn from the comparison of formation rates. Although the comparison between two photocatalysts is not exact under different conditions, we will focus here on evaluations of orders of magnitude in the produced formation rates. In doing so, we aim at identifying the best performers and the ones with the highest potential among the multiple hybrid plasmonic catalysts demonstrated in the last years.

Figure 5.7 shows the formation rates extracted from all tables in this review for photocatalytic H_2 generation (Figure 5.7a) and CO_2 reduction (Figure 5.7b). The exploration of plasmonic systems for H_2 has been the most extensive, accounting

for 71 % of the manuscripts reviewed here. Among the systems used for H₂ production, the most popular were plasmonic metal-2D catalysts (38 %), followed by metal-electrochemistry (25 %), metal-semiconductor (18 %), metal-perovskite (7 %), metal-metal (7 %) and metal-MOF (5 %). For CO₂ reduction, the most popular were also plasmonic metal-2D catalysts (25 %), followed by metal-electrochemistry (20 %), metal-semiconductor (18 %), metal-metal (17 %), metal-MOF (13 %), and metal-perovskite (7 %). The range of formation rates reported and the most efficient systems depend on the reaction under study. We will now break down the analysis into the different reactions of interest.

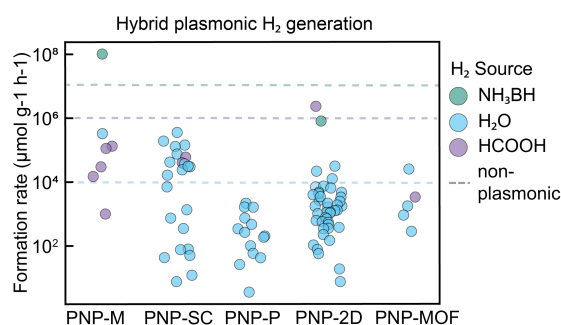


Figure 5.7: **Hybrid plasmonic nanomaterials for the generation of hydrogen.** Formation rates for H₂ generation for the different hybrid photocatalysts reviewed here. Adapted with permission from Ref.⁶⁰

Hybrid plasmonic nanomaterials for photocatalytic hydrogen production. The performance of different plasmonic catalysts will be evaluated for the following three hydrogen production reactions: Ammonia borane dehydrogenation, formic acid dehydrogenation, and water splitting.

The hydrolytic dehydrogenation of ammonia borane was found to be the hydrogen generation reaction with the highest formation rate. An outstandingly high formation rate of 10⁸ μmol g⁻¹ h⁻¹ at 40 °C was observed employing core-shell Ag@Pd nanostructures.²⁵² To put this number into context, one of the highest reported performances of heterogeneous catalytic systems for hydrolysis of ammonia borane at room temperature is 69.8 mol/min using porous Pt₂₅Pd₇₅ nanoparticles.²⁵³ This translates to 3 × 10⁷ μmol g⁻¹ h⁻¹ if a molar ratio of 25 % Pt and 75 % Pd is assumed. Therefore, the core-shell Ag@Pd nanostructures offer a comparable performance with just a 1.3 nm layer of Pd and a relatively mild illumination source of 50 mW cm⁻² (on the order of half the average solar irradiance).

The hydrogen generation from formic acid dehydrogenation was possible with formation rates between 10² and 10⁶ μmol g⁻¹ h⁻¹, as shown in Figure 5.7a. The metal-metal AgPd catalyst loaded on 2D graphitic carbon nitride nanosheets achieved the highest formation rate (2 × 10⁶ μmol g⁻¹ h⁻¹). Furthermore, Au nanoparticles interfaced with a metal (Pd) or semiconductor (CdS) were also capable of photocatalysing formic acid dehydrogenation with formation rates in the order of 10⁵ μmol g⁻¹ h⁻¹.^{252,254} However, metal-semiconductor systems were able to reach these formation rates at room temperatures, while the highest activities in metal-metal systems required temperatures between 40-50 °C. In addition, semiconductors are typically cheaper and more abundant than catalytic metals, indicating that metal-

semiconductors systems could be preferred for this reaction over metal-metal systems. Overall, the best activities for photocatalytic hydrogen generation from formic acid with plasmonic systems are comparable to the activity of heterogeneous catalysis at room temperature and without light, where formation rates on the order of $10^6 \mu\text{mol g}^{-1} \text{h}^{-1}$ were also achieved, e.g. using 2.2 nm $\text{Ag}_{42}\text{Pd}_{58}$ nanoparticles.²⁵⁵

Reviewing H_2 generation from water splitting reactions, we observed formation rates between 10^0 and $10^5 \mu\text{mol g}^{-1} \text{h}^{-1}$. The highest activity was $3.5 \times 10^5 \mu\text{mol g}^{-1} \text{h}^{-1}$, achieved using plasmonic Pt nanoparticles incorporated into nanostructured TiO_2 ,²⁵⁶ closely followed by a dual metal-semiconductor system including both Au@CdS and Ag@SiO_2 and achieving $2 \times 10^5 \mu\text{mol g}^{-1} \text{h}^{-1}$ at a temperature of 15°C .²⁵⁴ In addition, using metal-metal ZnCu plasmonic alloys, formation rates on the order of $10^5 \mu\text{mol g}^{-1} \text{h}^{-1}$ were also achieved, illustrating an interesting demonstration that does not utilize Au or Ag.²⁵⁷ At room temperature, metal-metal hybrids showed lower formation rates in the order of $10^3 \mu\text{mol g}^{-1} \text{h}^{-1}$. Interestingly, there is another example of an efficient photocatalyst that does not use Au or Ag as the plasmonic component. Cunanoparticles interfaced with WS_2 nanosheets produced $10^4 \mu\text{mol g}^{-1} \text{h}^{-1}$ of hydrogen under 1 solar irradiation.²⁵⁸ Finally, it has been shown that it is possible to drive water splitting reactions using perovskites. However, up to date, most examples still show limited efficiencies on the order of $10^3 \mu\text{mol g}^{-1} \text{h}^{-1}$. Remarkably, the highest plasmonic activities for water splitting are one order of magnitude larger than the best activities achieved by other non-plasmonic graphitic carbon nitride-based photocatalysts.^{259,260} This demonstrates that plasmonic nanomaterials have a substantial potential for water splitting reactions.

Hybrid plasmonic nanomaterials for photocatalytic CO_2 reduction. As shown in Figure 5.7b, the formation rates for CO_2 reduction are in general lower than for hydrogen production, in the range of 10^{-1} to $10^2 \mu\text{mol g}^{-1} \text{h}^{-1}$. Moreover, we can observe that the main product of many catalysts for CO_2 reduction is CO (56 %), followed by CH_4 (32 %). Figure 5.7c shows formation rate of each reaction's main product versus its selectivity. The plot has less points than Figure 5.7b because selectivity is less commonly reported. Interestingly, in the cases where it is reported, it is greater than 50 %. It must be noted that there is a lack of examples where products with more than one carbon (such as C_2H_6 , C_2H_4 and C_3H_6) are produced with high selectivity. However, these chemicals have been obtained as minor products in numerous publications. Figure 5.7d shows the reported minor products for CO_2 reduction, showing that C-C coupling reactions are possible with plasmonic catalysts. This is a very interesting but poorly explored route so far.

To date, the highest reported performance for producing CO was obtained using Ag nanoparticles deposited onto a MOF. Specifically, MIL-101(Cr)/Ag showed a CO production of $8 \times 10^2 \mu\text{mol g}^{-1} \text{h}^{-1}$ at 50°C , with a selectivity of 61.3 %.²⁶¹ The hybrids with the next best production rates are plasmonic-2D Ag/rGO achieving $10^2 \mu\text{mol g}^{-1} \text{h}^{-1}$ at 45°C , with a high selectivity close to 100 %.²⁶² Furthermore, plasmonic-semiconductor systems formed by Au/CdSe- Cu_2O obtained a CO formation rate of $80.2 \mu\text{mol g}^{-1} \text{h}^{-1}$.²⁶³ It should be noted that to date, there have been no reports of bimetallic plasmonic nanoparticles for this reaction. The highest activity obtained with plasmonic hybrids is comparable to what can be achieved by a non-plasmonic $\text{g-C}_3\text{N}_4$ nanosheet with B-H bonding decorated MOF ($\sim 10^3 \mu\text{mol g}^{-1} \text{h}^{-1}$).²⁶⁴

comparable to sunlight, further development of sunlight concentrators or focusing devices is still needed as well as novel reactor designs that can maximize light penetration and absorption. Scalability of these technologies seems possible but is scarcely explored so far.^{15,267} On the other hand, carbon dioxide reduction with plasmonic catalysts has not yet shown such appealing results as hydrogen generation. In general, the selectivity and efficiency for this reaction when employing hybrid plasmonic materials is still far from excellent electrocatalysts reported in the literature. In this sense, the combination of plasmonic materials with metal organic frameworks appears as a promising route to explore, with few but remarkable results so far. Additionally, the combination of more than two types of materials into higher-order plasmonic hybrid systems may not only allow the exploitation of the properties of the respective two-component hybrid systems but may also introduce new synergies.^{237,268} Finally, even though we have focused only on solar fuels, plasmonic hybrids could also face interesting opportunities for the production of highly valuable chemicals that in most cases require the use of expensive precious metal (electro)catalysts.²⁶⁹ In this context, earth-abundant plasmonic materials have rarely been explored for catalysis; Al, TiN, some metal oxides, among others are materials that deserve further attention. Interestingly, plasmonic materials as support of single catalytic atoms could also become a promising route for the future development of the field.²⁷⁰ From the analysis of the systems reported in here - the combination of plasmonic materials with also earth-abundant hybrid materials, such as nitrides (TiN, g-C₃N₄) and MOFs may lead to new routes towards efficient and selective sustainable catalysis.

5.1.5 Challenges in hybrid plasmonic catalysis

In the vast majority of the systems explored so far, the plasmonic component was either Au or Ag. Figure 5.9a shows a histogram of the main plasmonic component among the hybrid systems in this review. 68 % use Au, 25 % use Ag and only 7 % use a different material. Reasons for this preference may include the high photostability of Au and the availability of versatile protocols to shape Au into different nanomorphologies with tailored resonances along the visible spectrum. Earth-abundant plasmonic materials have been less explored.

Basing hybrid plasmonic catalysts on expensive, rare metals is a bottleneck in the development of sustainable large-scale photocatalytic methods. New abundant plasmonic materials such as Al,^{271–273} Cu,^{192,215,257,258,274} Mg,²⁷⁵ metal oxides,^{276–278} metal nitrides²⁷⁹ or even 2D materials,²⁴⁵ are emerging candidates in plasmonic catalysis. However, they have been relatively unexplored until now. Moreover, hybrid combinations of these materials are a very interesting and emerging field to explore further. Research in these directions and with these materials could merge plasmonic catalysis with sustainable and large-scale solar-to-chemical energy conversion routes, disclosing the real potential for the industrial application of these concepts.

Another key parameter in (electro)photocatalysis is the light source. Figure 5.9b shows the histogram of the illumination sources among the manuscripts reviewed here. The most used lamp is the Xenon lamp, because its emission spectrum resembles the solar one in the wavelength range of 290–700 nm.²³⁸ They account for 68 % of the examples, followed by monochromatic laser light with 9 %. Lasers are chosen to

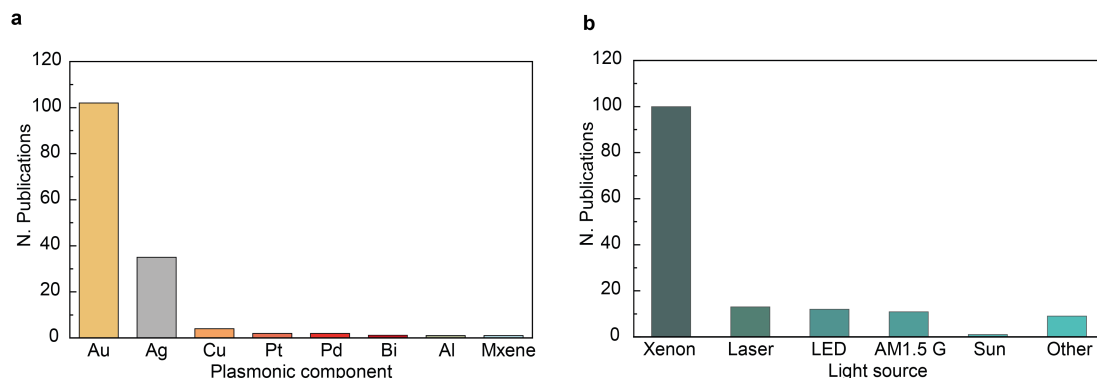


Figure 5.9: Histograms of (a) the main plasmonic component and (b) illumination source used in the manuscripts reviewed. Adapted with permission from Ref.⁶⁰

match the plasmonic absorption peak of the used photocatalyst and are a useful tool to study the wavelength dependence of their properties. In addition, they can provide higher irradiances. The third most frequent illumination source is light-emitting diodes (LEDs), 8 %. 365 nm LEDs are particularly popular for electrochemical CO₂ reduction, as they can induce the generation of allyl alcohol on Ag/Cu hybrids. Only 7 % use AM 1.5 G sources, which are the standard for solar simulators.

Quantitative comparison among different photocatalysts is challenging due to the existing discrepancies in the reported metrics and the high number of relevant experimental parameters involved, usually not reported.^{249,250} We believe that the field can benefit from standardization of reported activity metrics and measurement conditions. The adopted metric should incorporate information on the amount of catalyst and the intensity of the employed light. For this reason, we propose the implementation of the following activity metric:

$$\phi = \frac{n_{product}[\text{mol}]}{m_{catalyst}[\text{mol}] \times time[\text{h}] \times irradiance[\text{mW cm}^{-2}]} \quad (5.6)$$

Where $n_{product}$ is the amount of product generated, t is the time interval, $m_{catalyst}$ is this mass of *illuminated* catalyst and I is the incident light irradiance. This quantity will only be meaningful if measured far from saturation, i.e. with a linear dependence on time and catalyst concentration in a large excess of reactants. Plasmonic systems have resonances, and therefore their activities are expected to be wavelength dependent. For this reason, the spectral composition of the illumination source must always be reported. Standardization of the light sources employed would allow a proper comparison among systems. The reasonable choice for the field of artificial photosynthesis would be AM 1.5 global light sources. Additionally, to investigate the role of the spectral composition of light on the efficiency, measurements of single-wavelength yields using monochromatic irradiation may be useful.

In addition, variations in the geometry of the photoreactors could also lead to discrepancies in the reported performances, even with the same employed catalyst.²⁸⁰ To overcome this issue, the field could benefit from the establishment of a standard photocatalyst, to be used as an internal reference at each laboratory, in a similar fashion as it was proposed for semiconducting photocatalytic materials.²⁸¹

To ensure a fair comparison of plasmonic catalysts, it is crucial to evaluate those that operate at similar temperatures. However, a mere 47% of the reviewed manuscripts have reported on controlled reactor temperatures. Even when a controlled temperature is reported, it is challenging to assess the role of temperature on catalytic enhancement. This is because the temperature at the catalyst surface may be considerably different from the bulk temperature. Measuring or modeling this temperature is not a simple task, and it becomes even more complicated for hybrid materials and more complex geometries. In the second part of this chapter, we will address this challenge.

The second part of this chapter addresses the challenge that we concluded the first part with - assessing the role of temperature on catalytic enhancement in plasmonic-assisted catalysis. This is done by investigating the light-to-heat conversion of one of the hybrid systems we introduced, bimetallic nanoparticles, which combine plasmonic metals with catalytic metals. Specifically, the results of modeling and single-particle measurements will be presented, aimed at investigating the link between morphology and light-to-heat conversion of colloidal Au/Pd nanoparticles with two different configurations: Au core-Pd shell and Au core-Pd satellites. We show that the inclusion of Pd as a shell significantly reduces the photothermal response compared to that of the bare Au cores. However, the inclusion of Pd as satellites keep the photothermal properties almost unaffected. These findings contribute to a better understanding of energy conversion processes in plasmon-assisted catalysis, particularly in relation to the role of temperature.

5.2 Single particle thermometry in bimetallic plasmonic nanostructures

Plasmonic metals are used in a broad range of applications due to their ability to efficiently confine and manipulate light into a subwavelength scale.^{24,282} Most plasmonic materials are intrinsically lossy, meaning that their use is always accompanied by the generation of heat.^{142,283} In the so-called field of thermoplasmonics, thermal effects have been exploited in a wide range of applications.^{142,284} Despite this, quantitative and accurate experimental measurements of the generated nanoscale thermal fields remain a challenge, hindering the understanding of the mechanisms behind experimental results.^{141,285}

One area of research where reliable measurements of temperature are of special concern is plasmon-assisted catalysis.⁵⁰ This was discussed in more detail in Chapters 2.4 and 5.1, the following is a short summary. Processes associated with plasmon excitation and decay can be beneficial for the chemical transformation of nearby molecules in a variety of ways.^{51,75,188} These include charge carrier generation and injections, enhancement of the electromagnetic fields, resonant near-field energy transfers, and heating. All these phenomena can occur simultaneously under illumination, complicating the mechanistic understanding of energy flow during plasmon-assisted catalysis. In particular, understanding the role of heat is critical since the rates of chemical reactions usually present an exponential dependence on the temperature, as dictated by the Arrhenius law.²⁸⁶ Therefore, small temperature variations could lead to significant changes in the reaction rates. For this reason, significant efforts are being done to disentangle thermal and non-thermal effects in plasmon-assisted catalysis,^{153,155,190,287–289} and the problem of reliable assessment of temperature has been identified as one of the bottlenecks for the development of the field.^{47,269,290} A deeper understanding and control of the mechanisms that accelerate reactions would be valuable to achieve superior efficiencies, milder reaction conditions (under solar irradiances and without bulk-scale heating or pressuring of the reactor),¹⁸⁹ or the manipulation of reaction pathways.^{291,292}

Despite the high potential of plasmon-assisted catalysis, traditional plasmonic metals are intrinsically poor catalysts for many reactions of interest. This has motivated the search for new nanocomposites that combine plasmonic metals with conventional catalytic metals (such as Pd, Pt, Rh, etc.), as we discussed in Chapter 5.1.^{194,202,293} In recent years, several morphological configurations of multimetallic plasmonic nanoparticles have been tested, such as spherical core-shell, nanocubes,²⁵² partially coated nanoparticles,²⁹⁴ alloys,²⁹⁵ core-satellites,^{296,297} and core-shell trimers,²⁹⁸ demonstrating promising results in artificial photosynthesis and the production of solar fuels.^{59,60} However, the addition of new materials to a plasmonic nanoparticle also alters the processes of light absorption and heat conduction, in non-trivial ways depending on the overall composition of the material and its spatial distribution.^{285,299–302} Here, this challenge is addressed both theoretically using an analytical model, simulations and experimentally.

The experimental technique we will employ was introduced in Chapter 3.3.3 - Anti-stokes (AS) thermometry. In short, AS thermometry takes advantage of the fact that, upon illumination with a CW laser, the AS part of the photoluminescence (PL) spectrum of plasmonic nanoparticles shows a temperature dependence.¹³³ Unlike other optical methods for single particle thermometry of metals,¹⁴² it is non-invasive, label-free and does not require any extra characterization or prior knowledge about the nanoparticles or the medium properties. This technique has been used for the thermal characterization of individual monometallic Au nanoparticles such as disks,¹³⁴ pyramids,¹³⁵ rods,^{136,137} bowties,¹³⁸ spheres,^{132,139} and cylinders,¹⁴⁰ but not for hybrid plasmonic systems.

Here, the optical and photothermal properties of bimetallic plasmonic nanoparticles are studied. First, Au@Pd core-shell nanoparticles with different shell thicknesses are designed to investigate changes in their on-resonance photothermal response. It is shown that a Pd shell strongly reduces heat generation compared with naked Au cores. The experimental studies are complemented with an analytical model for the photothermal response of CS-nanoparticles. Second, the effect of the geometric configuration of bimetallic plasmonic nanoparticles is assessed. Pd is shaped as either a shell or as satellites around the same Au nanospheres, keeping the plasmon frequency almost unaffected. It is found that the absorption of light is larger if Pd is included as satellites around the Au core than if it is included as a shell, which is reflected in a higher measured photothermal coefficient. This highlights the role of the Au-Pd interfaces in the photothermal response. These results shed light on the role of the catalytic material in the photon-phonon conversion processes of plasmonic-catalytic hybrids.

5.2.1 Theoretical estimations in core shell nanoparticles

In this section, we first discuss how the addition of a palladium shell changes the optical properties of the system. We will evaluate whether the nanoparticle temperature can still be assumed to be constant, as this is an assumption that is made in AS thermometry. Additionally, we discuss the role of the substrate in both the light absorption and heat dissipation. Finally, we predict a range for the experimental values, based on thermal constants from the literature.



Figure 5.10: **Gold palladium core shell nanoparticles.** Illustration of gold palladium core shell nanoparticles with increasing shell thickness. Adapted with permission from Ref.¹⁸⁴

Simulated optical properties

When a second material is introduced to the gold nanoparticles, the optical as well as the thermal properties change. In particular, a change in absorption changes the amount of heat generated. Additionally, different materials have different thermal properties, leading to a change in the heat dissipation to the environment. Figure 5.12 shows the absorption, scattering and extinction cross section of the same gold core with increasing palladium shell thickness. The plasmon is damped, as can be seen by a broadening of the linewidth.³⁰³ Increased damping could be due to surface effects (increased electron-surface scattering, plasmon decay into interfacial states) or bulk effects (ohmic damping in the Pd shell).^{304–306} In the following, we will first estimate how this change affects the photothermal properties and then evaluate this experimentally using Antistokes thermometry.

To model the optical properties of the core-shell particles, we simulated the optical cross sections for different palladium shell thicknesses in water (Figure 5.11). For the single-particle measurements later, the particles will be deposited on a substrate. The interface between the particle and the substrate is not easy to model at the nanoscale and we therefore investigated three geometries: the core-shell particles were either put directly on the substrate, embedded 2 nm or at a height 2 nm from the substrate (illustrated in Figure 5.11b). The absorption cross sections in Figure 5.12 shows the results for the 67 nm Au cores. The simulations show that the inclusion of the substrate has an effect of max. 3 % on the absorption cross section and the effect of the variation of the substrate height is even smaller. All the values at a wavelength of 532 nm (this is the wavelength used in the experiments later) are summarized in Table 5.2.

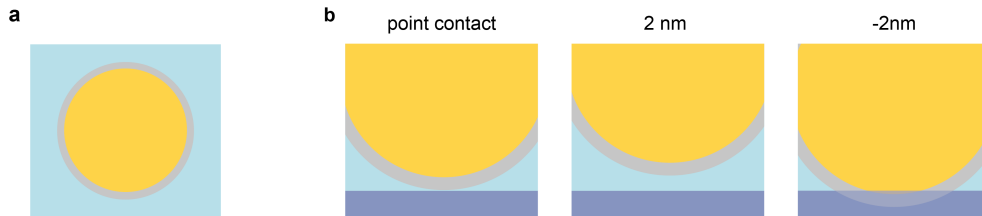


Figure 5.11: **Optical modelling of the interface.** (a) Sketch of the gold palladium core shell nanoparticle in water. (b) Illustration of the zoom in of the three modelled substrate geometries.

Au 67 nm core	No substrate	substrate at 0 nm	substrate at 2 nm	substrate at -2 nm
Pd 0 nm	1.4469	1.4490 (0.15%)	1.4494 (0.17%)	1.4490 (0.14%)
Pd 1nm	1.3640	1.3814 (1.28%)	1.3791 (1.11%)	1.3843 (1.49%)
Pd 2nm	1.2855	1.3089 (1.82%)	1.3056 (1.56%)	1.3129 (2.13%)
Pd 3nm	1.2380	1.2637 (2.08%)	1.2601 (1.79%)	1.2681 (2.43%)
Pd 4nm	1.2137	1.2407 (2.23%)	1.2371 (1.93%)	1.2452 (2.59%)
Pd 5nm	1.2060	1.2338 (2.31%)	1.2302 (2.01%)	1.2382 (2.67%)
Pd 6nm	1.2112	1.2393 (2.32%)	1.2358 (2.04%)	1.2436 (2.68%)

Table 5.2: Calculated absorption cross sections at 531.4 nm (10^{-14} m²) and their dependence on the presence of a substrate at different distances.

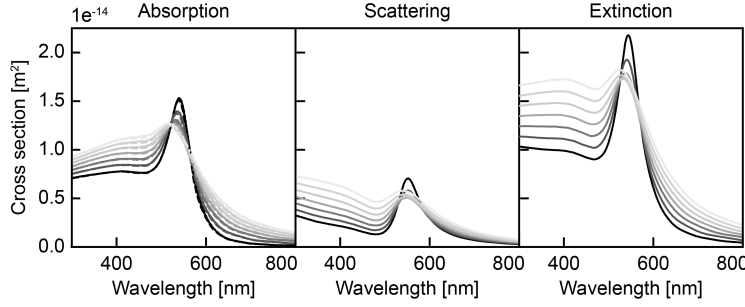


Figure 5.12: **Optical cross sections of Au-Pd coreshell nanoparticles.** Calculated for 67 nm cores and palladium shell thicknesses from 0 to 6 nm (from dark to light). The line style is as follows. Dashed: no substrate, solid: substrate at 0 nm distance from the nanoparticle, dotted: nanoparticle embedded into substrate by 2 nm. Adapted with permission from Ref.¹⁸⁴

A theoretical model for the thermal properties

Under CW illumination, a gold nanosphere has a homogeneous temperature,¹⁴⁸ T^{NP} , and we will now prove that this is the case in gold-palladium core-shell nanoparticles as well. The parameters used for the analytical model are shown in Figure 5.13a.

The temperature field $T(r)$ of core@shell nanoparticles can be calculated using the heat diffusion equation: $-\kappa \frac{1}{r^2} \partial r (r^2 \partial r T) = q$. Therefore, for a system in which the core is material 1, the shell is material 2 and the surrounding medium is material 3, the solution with radial symmetry in the steady state reads:

$$r < b : T(r) = -\frac{-q_1}{6\kappa_1} r^2 + \frac{c_0}{r} + c_1 \quad (5.7a)$$

$$b < r < a : T(r) = -\frac{-q_2}{6\kappa_2} r^2 + \frac{c_2}{r} + c_3 \quad (5.7b)$$

$$r > a : T(r) = -\frac{c_4}{r} + c_5 \quad (5.7c)$$

$$(5.7d)$$

where c_0 to c_5 are integration constants. $c_5 = T(\infty) = T_0$ with T_0 equal to room temperature. Non-divergence at $T(0)$ leads to $c_0 = 0$. The four other constants can be obtained from the following boundary conditions. The calculated constants can be found in Appendix B.3.

1. Energy conservation demands that the integrated heat flux J crossing interface 2-3 should be equal to the absorbed heat Q by the nanoparticle.
2. Heat flux conservation at the interface 2-3
3. Temperature boundary condition at the interface 2-3
4. Temperature boundary condition at the interface 1-2

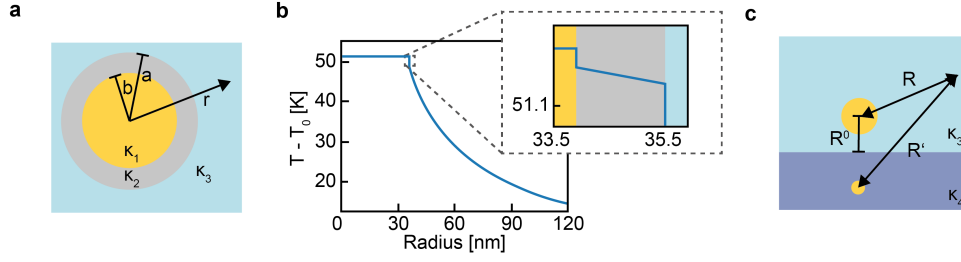


Figure 5.13: **Heat diffusion for a spherical core-shell nanoparticle.** (a) Geometry of the system. (b) The temperature within the particle (core and shell) can be assumed to be constant. A list of the parameters used can be found in B.3. (c) Schematic of the system composed of a nanoparticle in a medium of thermal conductivity κ_3 close to a substrate with thermal conductivity κ_4 . Adapted with permission from Ref.¹⁸⁴

From these expressions, it can be shown that $\frac{T(a^-) - T(0)}{T(a^+) - T_0} \leq 10^{-3}$, meaning that temperature variations inside the nanoparticle are negligible. In that case, the temperature inside the nanoparticle becomes

$$T^{NP} = \left(\frac{1}{4\pi\kappa_3 a} + \frac{R_{2-3}^{th}}{4\pi a^2} \right) \sigma_{abs} I_{Exc} + T_0 \quad (5.8)$$

We can now define the photothermal coefficient β as

$$T^{NP} = \beta I_{exc} + T_0 \quad (5.9)$$

where T^{NP} and T_0 are the temperature of the particle in the presence and absence of light, respectively. For our system, *beta* becomes

$$\beta^{CS} = \left(\frac{1}{4\pi\kappa_3 a} + \frac{R_{2-3}^{th}}{4\pi a^2} \right) \sigma_{abs} \quad (5.10)$$

Equation 5.10 dictates that the photothermal coefficient β^{CS} depends on the radius of the nanoparticle (a), the interfacial thermal resistances between the shell and the surrounding media (Kapitza, $R_{Pd-H_2O}^{th}$) and the conductivity of the surrounding media (κ_{H_2O}). Figure 5.13b shows the calculated temperature increase $T(r) - T_0$ as a function of the radial coordinate r for a 67 nm gold nanoparticle with a 2 nm Palladium shell immersed in water under illumination at 532 nm with an irradiance of $I_{Exc} = 1 \text{ mW}/\mu\text{m}^2$. The temperature is practically constant inside the nanoparticle, since it only predicts a small drop $\nabla T_{(Au-Pd)}$ at the Au/Pd interface, shown in Figure 5.13b. The temperature variations within the nanoparticle are 10^{-3} times smaller than the temperature increase on the surface. Hence, the nanoparticle can be described by a single, uniform temperature T^{NP} . This is a consequence of the high thermal conductivities of Au and Pd with respect to water and the high electronic thermal conductance of the Au/Pd interface that allows efficient heat transfer through electron-electron scattering.³⁰⁷

For a nanoparticle on a substrate there is no analytical solution, however, this problem is equivalent to solving the electrostatic problem of charge sources in front of an infinite planar conductor because both are governed by the Laplace equation. In analogy to the electrostatic image method, the effect of the substrate can be calculated

by considering a virtual charge image on the substrate side. This is illustrated in Figure 5.13c. For a spherical nanoparticle located at the position $(0, 0, R^0)$ with total absorbed heat Q , the virtual image is a point source $-Q$ located at $(0, 0, -R^0)$. The temperature T at a position R outside the nanoparticle and the upper medium is the sum of the real and virtual heat sources:

$$T(R) = \frac{Q}{4\pi\kappa_3} \left(\frac{1}{|R|} - \frac{\kappa_4 - \kappa_3}{\kappa_4 + \kappa_3} \frac{1}{|R'|} \right), \quad (5.11)$$

where $|R|$ and $|R'|$ are the distances to the real and virtual sources, respectively. The average surface temperature $\langle T^S \rangle$ on a spherical nanoparticle of radius a in contact with the substrate can be calculated to be (see the appendix B.3 for details):

$$\langle T^S \rangle = \frac{Q}{4\pi a \kappa_3} \left(1 - \frac{1}{2} \frac{\kappa_4 - \kappa_3}{\kappa_4 + \kappa_3} \right) = f \frac{Q}{4\pi a \kappa_3} \quad (5.12)$$

where $f = 1 - \frac{1}{2} \left(\frac{\kappa_4 - \kappa_3}{\kappa_4 + \kappa_3} \right)$. The result is the well-known expression of an isolated nanoparticle in a homogeneous medium $Q/(4\pi a \kappa_3)$, multiplied by a factor $f = 1 - \frac{1}{2} \left(\frac{\kappa_4 - \kappa_3}{\kappa_4 + \kappa_3} \right)$. For a nanoparticle immersed in water on a glass substrate, the value of f is 0.875. For a point contact, this simple method works well, as we confirmed by

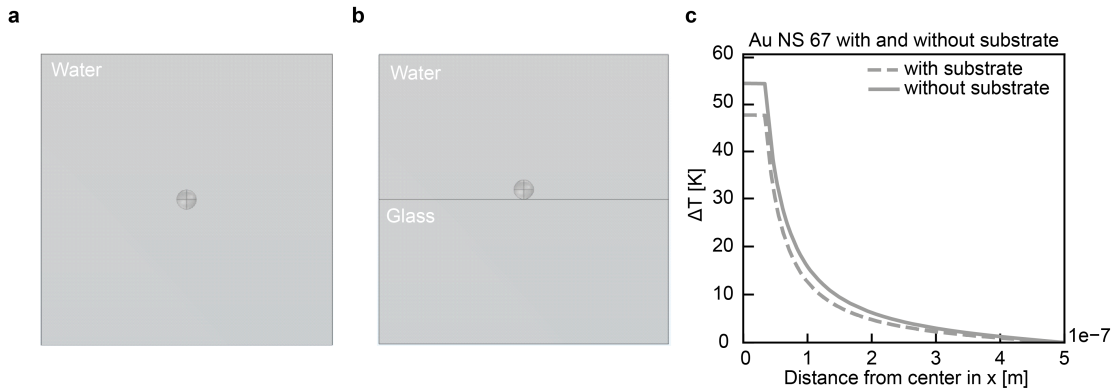


Figure 5.14: **Influence of substrate calculated by COMSOL Multiphysics.** (a) 2D view of the simulation setup of the NS in water. (b) 2D view of the simulation setup of the NS on a substrate. The inset shows a zoom in, the particle touches the substrate in one point. (c) Resulting temperature profiles from the center of the NS in x direction. Adapted with permission from Ref. ¹⁸⁴

performing numerical calculations in COMSOL Multiphysics. More details on the simulation can be found in Appendix B.3 (Figure 7.20). The geometries are shown in Figure 5.14a-b. As can be seen in Figure 5.14c, the resulting temperature in the nanosphere (NS) on the substrate is 87.8 % of the temperature of the NS in water. Remarkably, this value is in high agreement with the obtained using the image method (87.5 %). However, at the nanoscale, heat dissipation that occurs through the substrate is not easy to model. The assumption of a point contact between the nanoparticle and the substrate is a simplification. We see that practically no deviations occurs when small deviations occur when the shell is modelled as an icosahedron (the faceted structure resembles the colloiddally synthesized particles more closely)

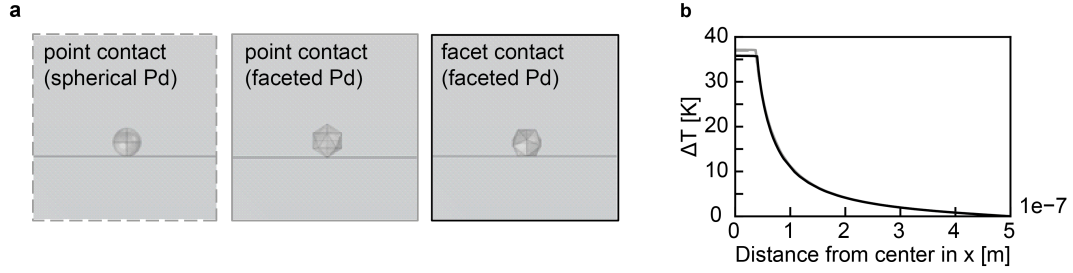


Figure 5.15: **Thermal modelling of the interface.** (a) The Pd shell is simulated as a sphere (left) and an icosahedron. The icosahedron can be placed on the substrate with a single point of contact (middle) or a facet contact (left). (b) The temperature profiles from the center of the nanoparticles in x direction. Adapted with permission from Ref. ¹⁸⁴

and brought into contact with the substrate with one of its facets (Figure 5.15). For simplicity and to allow an easy extension to other materials, will use the simple calculation of the image method.

Theoretical results

The calculation requires several thermodynamical constants for which accurate experimental values are scarce. This is the case for example for the Kapitza resistance between Pd and water R_{2-3}^{th} . For this reason, we have included a maximum and a minimum calculated value, to represent the large dispersions of available data in the literature. A list of used parameters is shown in Table 5.3. To correctly estimate the temperature, one needs to accurately predict the absorption cross section. We will later experimentally determine the photothermal coefficient of colloidal core shell particles with a core size of around 67 nm, so we will use them as an example here. To account for the inherent size distribution, we numerically calculate the absorption cross section for sizes between 63.6 nm and 71 nm (Table 5.4, for details see Appendix B.3).

Parameter	Min value	Max value
$R_{Au-H_2O}^{th}$	$4 \times 10^{-9} \text{ m}^2 \text{ K W}^{-1}$ ^{308,309}	$15 \times 10^{-9} \text{ m}^2 \text{ K W}^{-1}$ ³¹⁰
$R_{Pd-H_2O}^{th}$	$1.8 \times 10^{-9} \text{ m}^2 \text{ K W}^{-1}$ ³¹¹	$2.4 \times 10^{-9} \text{ m}^2 \text{ K W}^{-1}$ ³¹²
κ_{H_2O}	$0.6 \text{ W m}^{-1} \text{ K}^{-1}$ ¹¹⁴⁸	$0.68 \text{ W m}^{-1} \text{ K}^{-1}$ ¹¹⁴⁸
κ_{Glass}	$1 \text{ W m}^{-1} \text{ K}^{-1}$	$1.2 \text{ W m}^{-1} \text{ K}^{-1}$ ¹¹⁴⁸
σ_{abs}	Table 5.4	
a (r_{Pd})	b+Pd shell thickness	
b (r_{Au})	63.6 nm (size distribution)	71 nm (size distribution)

Table 5.3: Parameters for photothermal coefficient estimation in Au@Pd CS-nanoparticles. Adapted with permission from Ref. ¹⁸⁴

Pd shell thickness	63.6 nm Au	71 nm Au
0 nm	1.3268	1.5985
1 nm	1.2391	1.5537
2 nm	1.1594	1.4904
3 nm	1.1131	1.4457
4 nm	1.0909	1.4200
5 nm	1.0866	1.4104
6 nm	1.0947	1.4122

Table 5.4: Absorption cross sections depending on the Pd shell thickness at 531.4 nm (in units of 10^{-14} m^2) for core sizes of 63.6 nm and 71 nm Au, all in water and on a glass substrate (distance 0 nm). Adapted with permission from Ref.¹⁸⁴

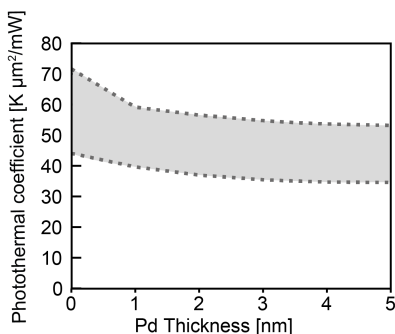


Figure 5.16: **Theoretically estimated photothermal properties.** Adapted with permission from Ref.¹⁸⁴

5.2.2 Antistokes thermometry on single core shell nanoparticles

Figure 5.17a illustrates the colloidal nanoparticles. They consist of gold nanospheres (AuNSs) with a diameter of 67 nm, and Au@Pd core-shell (CS) nanoparticles with an Au core of 67 nm and Pd shells of ~ 2 and ~ 4 nm in thickness. The nanoparticles were prepared using a seed-mediated growth strategy.²⁹⁶ This method starts with the synthesis of small (seed) AuNS and the subsequent growth to the desired size, as described in Appendix B.3. Two different shell thicknesses were obtained by varying the ratio of Au core to Pd salt. The three colloids are stabilized in water by means of cetyltrimethylammonium chloride (CTAC) capping. Figure 5.17b shows transmission-electron-microscopy (TEM) images of the colloidal nanoparticles obtained. The Au nanoparticles are spherical, while the Au@Pd are more faceted. The spatial distribution of the two metals measured by Energy Dispersive X-Ray Spectroscopy (EDX) is presented as an inset in the bottom panel of Figure 5.17b. While the Au signal is confined to the core region, the Pd signal is uniformly distributed around the entire particle, as expected for a homogeneous coverage. Particle size histograms were obtained from TEM images and are shown in Figure 5.17c. The median diameter of the AuNS is (66.6 ± 0.2) nm with a standard deviation of $\sigma = 1.3$ nm, while the two CS-nanoparticles colloids have median sizes of (71.5 ± 0.1) nm with a standard deviation of $\sigma = 1.2$ nm and (73.8 ± 0.2) nm with a standard deviation of $\sigma = 1.7$ nm. These

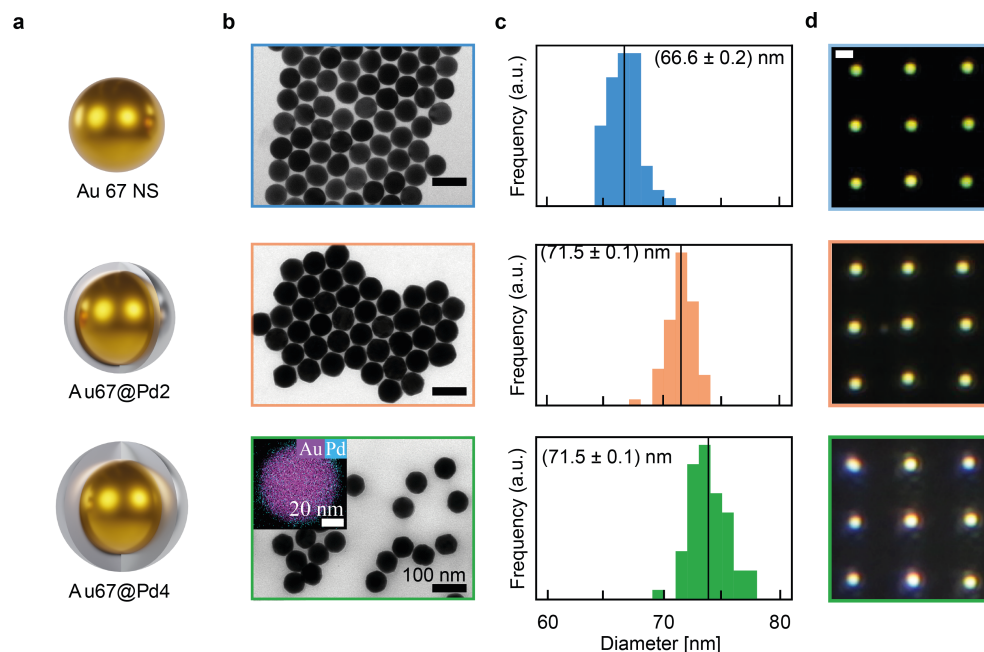


Figure 5.17: **Fabricated gold palladium core shell samples.** Visual illustration (a) and TEM images of the three different studied nanoparticles (b) Scale bars: 100 nm. The inset shows an EDX with the spatial distribution of the two metals. Au is shown in magenta and Pd in cyan. (c) Size distributions. Medians are indicated with a black line and displayed in the labels. Sample sizes are $N > 70$ in all cases. (d) Dark-field images of optically printed grids of individual nanoparticles. Scale bar: 1 μm . In all figures, blue, orange and green correspond to Au67 NS, Au67@Pd2, and Au67@Pd4, respectively. Adapted with permission from Ref.¹⁸⁴

values correspond to median Pd thicknesses of (2.4 ± 0.3) nm, and (3.6 ± 0.3) nm, respectively. In addition, Inductive Coupled Plasma Atomic Emission Spectroscopy (ICP-AES) was employed to quantify the Pd to Au mass ratio of each CS-nanoparticle. Using this information, the thicknesses of the Pd shells were estimated to be (1.8 ± 0.4) nm, and (3.4 ± 0.4) nm, as described in Appendix B.3. For simplicity, we name the colloids Au67 NS, Au67@Pd2 and Au67@Pd4. To study optical and photothermal properties at the single particle level, arrays of well-separated individual nanoparticles were fabricated on glass substrates using optical printing. Exemplary dark-field images of the optically printed grids are displayed in Figure 5.17d. A general introduction to optical printing and dark field can be found in Chapter 3.2.1 & 3.3.1, more details can be found in the Materials & Methods in Appendix B.1. Having ordered arrays ensures the nanoparticles are isolated and facilitates the automation of data acquisition and allows the collection of larger datasets. It must be noted that the printing process does not alter the stability or composition of the nanoparticles, as further discussed Appendix B.3.

Figure 5.18 shows darkfield scattering spectra of the printed nanoparticles, as well as photoluminescence spectra excited with CW laser excitation at 532 nm. The shape of the PL spectra follows the characteristics of the scattering one, as previously reported for other nanoparticles.^{313–316} The amplitude of the photoluminescence emission decreases with increasing Pd thicknesses. This decrease is a result of the Pd damping the plasmon resonance of the Au core, in line with the optical simulations

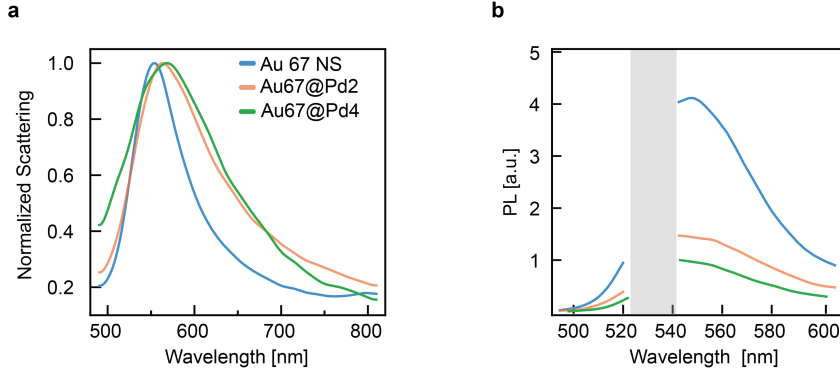


Figure 5.18: **Optical characterization of single Au@Pd core-shell nanoparticles.** (a) Average of single particle scattering spectra, normalized to their maximum. (b) Average of single particle PL emission spectra, excited with $1 \text{ mW}/\mu\text{m}^2$ of laser light at 532 nm. Grey band with no data corresponds to the laser rejection filter. Adapted with permission from Ref.¹⁸⁴

in Figure 5.12.

After the optical characterization of the individual nanoparticles, their photothermal response was measured using hyperspectral Anti-Stokes thermometry with a CW 532 nm laser. The technique, as introduced by Barella et al.,¹³² allows single-particle photothermal characterization by scanning a laser over the nanoparticle (see Appendix B.1 for experimental details). In this way, heating and PL excitation are performed simultaneously with the same beam. Throughout the scanning, the relative position between the beam and the nanoparticle changes, leading to different excitation irradiances and hence different steady state temperatures. For each nanoparticle, a square raster scan consisting of 10×10 pixels in the range of $0.8 \times 0.8 \mu\text{m}^2$ is performed. On each pixel, the PL spectra is measured with an integration time of 2.5 s. In such a manner, a set of one hundred temperature-dependent PL emission spectra is collected. Figure 5.18b shows three PL spectra for different levels of irradiance for an illuminated Au₆₇@Pd₂ CS-nanoparticle. Processing the set of acquired PL spectra allows one to find the photothermal coefficient β , defined as

$$T^{\text{NP}} = \beta I_{\text{exc}} + T_0, \quad (5.13)$$

where T^{NP} and T_0 are the temperature of the particle in the presence and absence of light, respectively. For details on data acquisition and processing, see Appendix B.1. Figure 5.19a shows histograms of the measured photothermal coefficients for the three systems under study. The median value obtained for the AuNS is $\beta_{\text{Au67}} = (51 \pm 1) \text{ K } \mu\text{m}^2 \text{ mW}^{-1}$, in line with the one reported by Barella et al. for 64 nm AuNS (Barella; et al. 2021). Interestingly, a significant reduction of β is observed for the CS-nanoparticles. The obtained median values of the Au67@Pd2 and Au67@Pd4 were $\beta_{\text{Au67@Pd2}} = (38 \pm 1) \text{ K } \mu\text{m}^2 \text{ mW}^{-1}$ and $\beta_{\text{Au67@Pd4}} = (35 \pm 1) \text{ K } \mu\text{m}^2 \text{ mW}^{-1}$, respectively. The standard deviation of the three measurements is $\sigma = 8 \text{ K } \mu\text{m}^2 \text{ mW}^{-1}$. Figure 5.19b (solid lines) shows the temperature increase versus excitation irradiance as in the theory section, corresponding to the median β of each type of nanoparticle. In dashed lines, the maximum irradiances used in each experiment are shown. The maximum temperature reached by the nanoparticles was around 100 °C. It must be noted that at

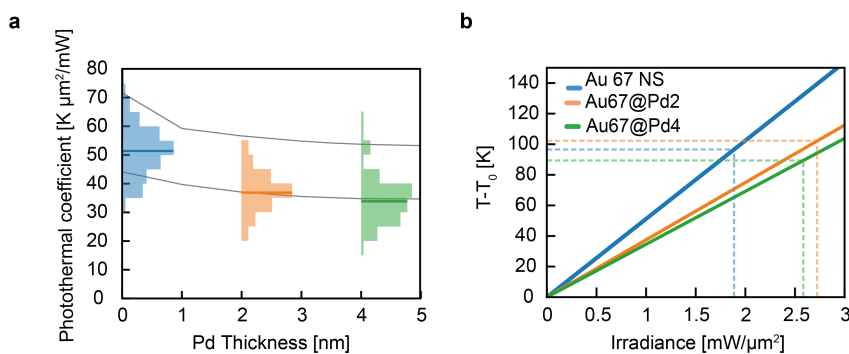


Figure 5.19: **Photothermal properties of single Au@Pd core-shell nanoparticles.** (a) Histograms of the experimental measured β for the three systems under study. Blue: Au67 NS, Orange: Au67@Pd2, Green: Au67@Pd4. At least 85 different nanoparticles were measured for each system, with a maximum of 250 nanoparticles. Solid lines indicate the maximum and minimum theoretical calculation of photothermal coefficient β versus thickness of the Pd shell using Equation 2. Parameters used in the calculus are listed in the Materials and Methods Section. (b) Temperature increase versus irradiance for the three studied systems. Blue: Au67 NS, Orange: Au67@Pd2, Green: Au67@Pd4. The dashed lines correspond to the maximum irradiances used in the experiments. In all calculations and experiments presented in this figure, the nanoparticles are immersed in water and irradiated at 532 nm. Adapted with permission from Ref.¹⁸⁴

these temperatures, the nanoparticles are stable and no changes in their scattering or PL spectrum were observed during or after the measurements (see appendix B.3). The solid black lines in Figure 5.19a correspond to the photothermal coefficient β predicted in the theoretical section for Au@Pd CS-nanoparticles as a function of the Pd shell thickness, for nanoparticles on glass, surrounded by water and illuminated at 532 nm, as in the experiments. The calculations reasonably predict the experimental trends. However, it must be noted that for Au@Pd, half of the measured CS-nanoparticles had a value below the predicted range. This could be due to several factors:

- An overestimation of the absorption cross sections: The simulations predict a 10 nm blue shift in the resonant frequency of CS-nanoparticles, which is not observed experimentally. However, considering that the resonances are broad, a 10 nm detuning of the spectrum versus the excitation wavelength only modifies the absorption cross sections by less than 2%.
- The influence of the surfactant CTAC in the thermal resistance of the Pd-water interface.³⁰⁸
- An overestimation of the factor f accounting for the effect of the substrate in heat dissipation. For a spherical nanoparticle immersed in water on a glass substrate, f takes a value of 0.875. However, Au@Pd CS-nanoparticles are faceted, as shown in Figure 5.17, and can present a larger contact area with the substrate, enhancing heat dissipation. Thermal simulations estimate a value of $f = 0.843$ for faceted nanoparticles, which is 4% smaller than its spherical counterpart.

To summarize, accurate theoretical predictions require a complete knowledge and modeling of every geometrical boundary, also including the liquid-substrate interface.

Having a precise description of all these factors is challenging, making most predictions only approximate, and reinforcing the need for methods able to measure the temperature of nanoscale objects in their operation environments (i.e., in situ).

5.2.3 Core satellite nanoparticles

The functionalities of bimetallic nanostructures are not only determined by the material composition, but also by the spatial distribution of the constituents.²⁹⁶ In the following, the effect of morphology on light-to-heat conversion for different Au-Pd bimetallic structures is investigated. To this end, we compare the photothermal properties of the naked cores, a core-shell and a core-satellite configuration. We have already seen how the optical properties change with the incorporation of a Pd shell, let us now take a look at what happens for Pd satellites.



Figure 5.20: **Gold palladium nanoparticles with different geometries.** Illustration of spherical gold palladium core shell nanoparticles with different geometries. Adapted with permission from Ref.¹⁸⁴

Optical properties of core-satellite nanoparticle

Core-satellite nanoparticles can be achieved, for example, by solvent-induced electrostatic self-assembly between a positive CTAC capped Au nanoparticle and negative Polyvinylpyrrolidone (PVP) capped Pd satellites. Therefore, the gap between both surfaces is expected to be on the order of magnitude of the size of the capping molecules. To investigate the role of the gap size on the optical properties, we performed numerical simulations. To this end, 50 palladium satellites of 6.5 nm diameter were evenly distributed around a 60 nm gold core. Figure 5.21 shows the absorption cross sections for the particles with different gap sizes. We found that the change in absorption at 532 nm, relative to an Au core without satellites, was small. Based on these results, we expect that the photothermal properties of the core-satellite system resemble those of the naked core more than those of the core-shell system.

Photothermal properties of core satellite particles

To compare the influence of the geometric distribution of the second metal, we used the same Au nanoparticles with a diameter of 60 nm with Pd in two different configurations: i) assembled with (6.3 ± 0.2) nm spherical Pd satellite nanoparticles (named Au60-Pd-sat) and ii) coated with a homogeneous (1.8 ± 0.3) nm Pd shell (named Au60@Pd2). Figure 5.22 shows an illustration of the three synthesized systems, as well as their corresponding TEM images. Detailed characterizations of the three systems are provided in Appendix B. The average number of satellites per nanoparticle

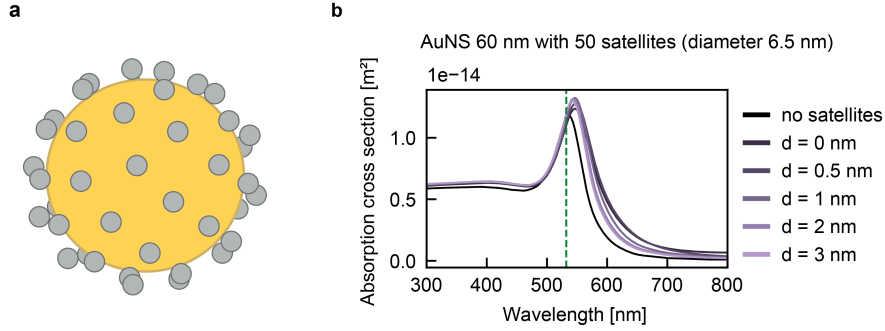


Figure 5.21: **Absorption cross sections of core satellite nanoparticle.** (a) . (b) Absorption cross sections for different gap sizes between the satellites and the Au surface. Adapted with permission from Ref. ¹⁸⁴

of the Au60-Pd-sat was estimated to be $\langle N_s \rangle = (51 \pm 6)$. ICP-AES was employed to quantify the Pd to Au mass ratio M_{Pd}/M_{Au} of each system, yielding the values $M_{Pd}/M_{Au} = (0.073 \pm 0.004)$ and $M_{Pd}/M_{Au} = (0.036 \pm 0.002)$, for Au60@Pd2 and Au60-Pd-sat respectively. This means that the amount of Pd is on the same order of magnitude for both configurations, being the total mass of Pd in the satellites approximately half the mass in a 2 nm Pd shell. Arrays of single AuNS 60 nm and Au60@Pd2 CS-nanoparticles were fabricated through optical printing on glass substrates. The Au60-Pd-sat were deposited by a drop-casting method, because the solution was not stable enough for the optical printing process. Next, the photothermal coefficient of each system was determined using hyperspectral AS thermometry. The resulting histograms are presented in Figure 5.22. The median photothermal coefficient for the Au 60 NS cores was $\beta_{Au60} = (47 \pm 1) \text{ K } \mu\text{m}^2 \text{ mW}^{-1}$ with a standard deviation of $8 \text{ K } \mu\text{m}^2 \text{ mW}^{-1}$. Remarkably, there's no significant difference with the median value for the core-satellites $\beta_{Au60-Pd-sat} = (46 \pm 1) \text{ K } \mu\text{m}^2 \text{ mW}^{-1}$, with a larger standard deviation of $13 \text{ K } \mu\text{m}^2 \text{ mW}^{-1}$. If the PL is mostly emitted by the Au, the measured β corresponds to the temperature of the core. This result can be explained by a small reduction of the absorption cross section of the Au60-Pd-sat system with respect to the Au cores, as discussed in Appendix B.3. On the contrary, a significant reduction of the photothermal coefficient is observed for the CS-nanoparticles, with a median of $\beta_{Au60@Pd2} = (29 \pm 1) \text{ K } \mu\text{m}^2 \text{ mW}^{-1}$ and a standard deviation of $5 \text{ K } \mu\text{m}^2 \text{ mW}^{-1}$, in line with the results presented in the previous section of this work. Overall, the experiments of this section point out that the presence of an interface between the two metals is crucial, as it dictates the photothermal response of the bimetallic nanostructures. The direct contact between Au and Pd enhances surface damping of the Au plasmon, leading to a poorer quality factor and lower absorption.

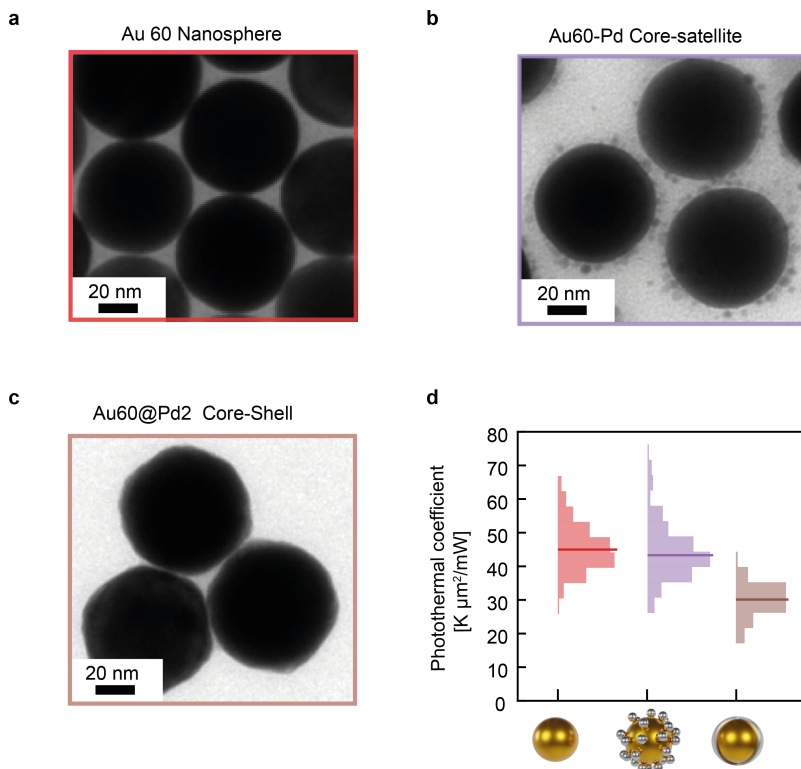


Figure 5.22: **Photothermal comparison between core-shell and core-satellites AuPd nanoparticles.** (a)-(c) TEM images of the synthesized nanoparticles. (d) Histograms of the experimental measured photothermal coefficient β for the three systems on glass substrates and immersed in water, at 532 nm. Adapted with permission from Ref.¹⁸⁴

5.2.4 Predictions for other metal-metal hybrids

The expression found through the thermal model can in principle be used to predict the photothermal response of Au@M core shell nanoparticles of dimensions similar to the ones studied in this chapter. Here, Au is the core material, and M is a different metallic shell material. Evaluating Equation 5.8, we realize that the main parameters that determine the response are the metal-solvent resistance (Kapitza), the size of the shell, the role of the substrate and the absorption cross-section ($\sigma_{abs}^{Au@M}$). If we assume the same shell thickness as in this work, and the substrate and interfacial resistances cause a similar effect in the heat dissipation, it is the absorption cross section σ_{abs} that determines the temperature increase in such structures. Figure 5.23 shows the temperature increase calculated from the simulated absorption cross sections. It is worth mentioning that this is an approximate model. For Au@Pd core-shell nanoparticles this model correctly predicted the trend and similar temperatures. The data shown in Figure 5.23 is expected to be an estimation of the expected temperature of isolated metal-metal core-shell nanoparticles on a substrate, however, the heat flow across the metal-metal interface as well as the interaction with the substrate should be carefully evaluated, since a change in resistance would impact the temperature.

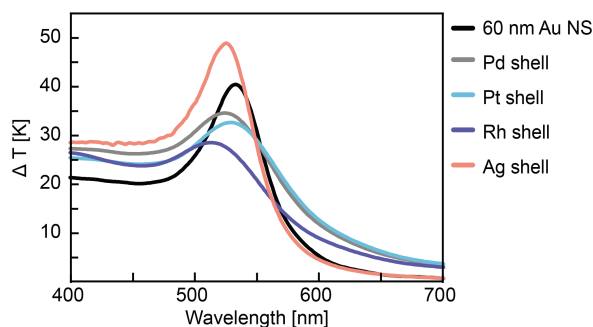


Figure 5.23: **Predictions for other metal-metal hybrids.** Predicted temperature increase as a function of wavelength, corresponding to an irradiance of $1 \text{ mW } \mu\text{m}^{-2}$. All systems are Au@M core-shell nanoparticles with a core size of 60 nm and a 2 nm shell. Adapted with permission from Ref.¹⁸⁴

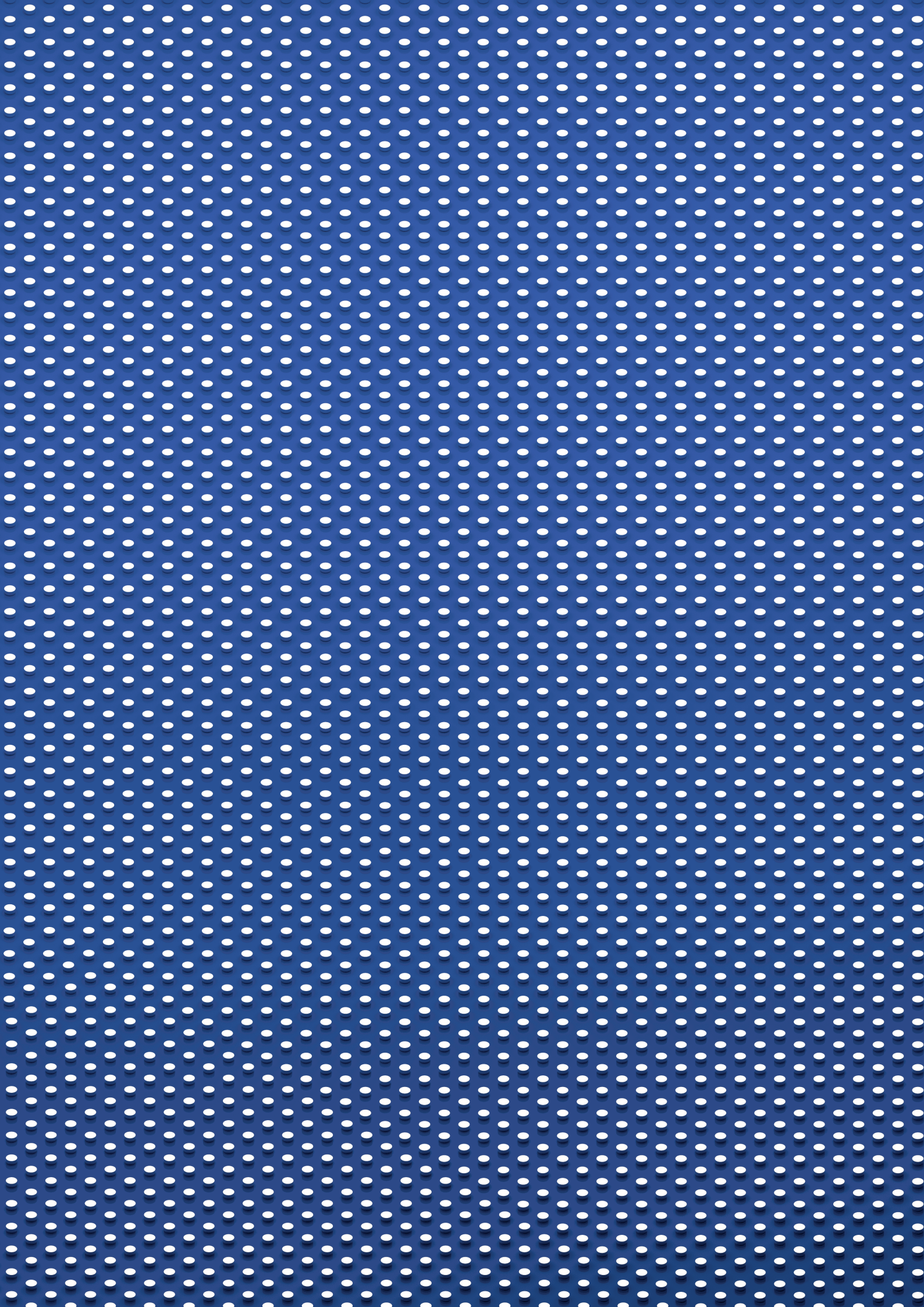
5.3 Conclusions

In this chapter, we have looked at the latest developments in hybrid plasmonic photocatalysis for solar fuel production. Plasmonic nanoparticles show promise for efficient hydrogen generation and carbon dioxide reduction reactions by confining solar energy into molecular regions. Combining plasmonic nanomaterials with other catalysts has produced results comparable to non-plasmonic catalysts that are typically powered by fossil fuels. However, there are still some gaps in our understanding, such as the role of temperature in the enhancement mechanism.

To address these gaps, we have introduced a photothermal model for bimetallic core-shell nanoparticles that allows the estimation of temperature for a wide range of systems. Additionally, we have introduced a characterization technique that helps to address these gaps by providing insight into the link between the nanoparticle structure and heat generation. Anti-Stokes thermometry is a label-free, non-invasive, and in situ technique that can be equally useful to study other complex/hybrid plasmonic interfaces with catalytic relevance, including metal-semiconductors or metal-organic materials.

By integrating plasmonic photocatalysis and photothermal characterization techniques, we can better understand the role of temperature in catalysis and improve the development of new, efficient, and sustainable energy conversion technologies.

In the next chapter, we will move closer to large-scale applications and move away from single particles.



6

Beyond single particles

This final chapter of the thesis builds upon the knowledge gained from single-particle studies of plasmonic nanoparticles. The focus is on extending the use of anti-Stokes thermometry to ensembles of multiple identical particles, providing guidelines on how to perform this extension and validating the accuracy and reliability of the technique. The use of planar structures, known as "metasurfaces," is explored as an attractive strategy for scaling up plasmonic nanoparticle systems for industrial applications. These structures derive their properties from the collective response of individual nanostructures, and their properties can be tuned through the material used and the subwavelength geometry and size of the meta-atoms. The findings of this study provide valuable insights into how to optimize plasmonic nanoparticle systems for various applications such as plasmonic sensors, solar energy conversion, and photothermal therapy. This work highlights the importance of single-particle studies in understanding the properties of plasmonic nanoparticles and how this knowledge can be applied to scale up these systems for industrial applications.

Based on

E. Cortés, F. J. Wendisch, L. Sortino, A. Mancini, S. Ezendam, S. Saris, L. de S. Menezes, A. Tittl, H. Ren, and S. A. Maier. Optical Metasurfaces for Energy Conversion, *Chemical Reviews*, 2022²⁸

S. Ezendam, L. Nan, I. Violi, S. A. Maier, E. Cortés, G. Baffou, and J. Gargiulo. Anti-Stokes Thermometry for Plasmonic ensembles. *in preparation*.

Figure 6.0 - Scaling up plasmonics. Artistic representation of a metasurface. Many hundreds of nanoparticles are ordered on a substrate and give rise to new phenomena.

6.1 Scaling up plasmonics

Single-particle studies are crucial to our understanding of plasmonic nanoparticles and their properties. By investigating individual nanoparticles, we learn how to optimize them for energy conversion applications. However, while single-particle studies are essential to guide the design of plasmonic nanoparticle systems, scaling up these systems for industrial applications presents several challenges.

1. Plasmonic nanoparticles typically use expensive materials such as gold and silver, which can be a barrier to scaling up their production for energy conversion applications. Developing cost-effective synthesis methods and exploring alternative materials is important to reduce the overall cost of plasmonic nanoparticles.
2. Plasmonic nanoparticles in laboratory environments are typically fabricated in small quantities using methods that are difficult to scale up. Developing efficient and cost-effective synthesis methods is crucial to enable the large-scale production of plasmonic nanoparticles.
3. Plasmonic nanoparticles in large photoreactors are not used efficiently. When light enters a colloidal dispersion, some of it is absorbed or scattered by the nanoparticles, and the remaining light continues to propagate through the solution. However, as light travels deeper into the solution, it encounters more and more nanoparticles, which absorb or scatter a greater proportion of the remaining light. This means that a large fraction of the expensive material cannot be used to its full potential.

For the third problem mentioned, moving from colloidal suspensions to a planar configuration is an attractive strategy. These planar structures are often called "metasurfaces". These "metasurfaces" (from Greek $\mu\epsilon\tau\alpha$, meta, meaning beyond) derive their properties from the shape of their sub-wavelength and nano-sized building blocks, often described as 'metaatoms', that govern their resonant properties. In addition, new properties can arise. These are summarized in the following section.

6.2 Collective effects

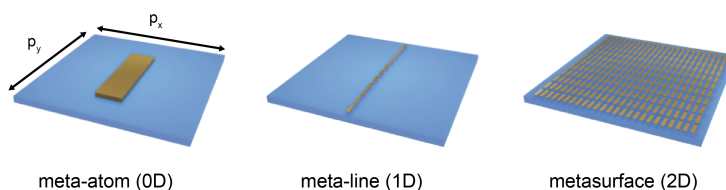


Figure 6.1: **Periodic arrangements of plasmonic resonators.** Building higher dimensional meta-arrays from single meta-atoms. Adapted from Ref.²⁸ Copyright American Chemical Society 2022.

The functionalities of single plasmonic resonators discussed in previous chapters can be further extended when the single nanostructures are arranged into periodic

arrays. In this context, the resonators, often called meta-atoms, can be arranged into one-dimensional (1D) arrays, or metachains, in two-dimensional (2D) metasurfaces and, with more extensive fabrication processes, into three-dimensional (3D) metamaterials (Figure 6.1). Most of the research is focused on the realization of metasurfaces, due to the wider parameter space to tailor their properties in the 2D array. In this context, meta-atom geometries utilized for optical metasurfaces range from simple rods or disks to more complex shapes such as split-ring resonators or dimers with broken symmetry. When a unit cell consists of multiple structures, it is sometimes referred to as a meta-molecule instead of a meta-atom. At its core, the electromagnetic response of the array is based on the properties of the meta-atom, which can be tuned both in the material used and the subwavelength geometry and size, as discussed in the previous Chapters. However, when the meta-atoms are engineered in periodic arrays, novel phenomena can arise because of the collective response of the individual nanostructures.

6.2.1 Near-field coupling

Going from individual resonators to the case of two or more nanoparticles, their arrangement in space also influences the electric field (E-field) enhancement and resonance properties. Nanoparticle dimers, formed from two nanoparticles separated by small nanoscale gaps significantly smaller than their resonance wavelength, can show significant near-field coupling and create a plasmonic hot spot in the resulting cavity. In such hotspots, the electric field enhancement can reach very high values, as illustrated in Figure 6.2a. This phenomenon can be extended further from dimer structures to 1D, 2D, and 3D arrays of nanostructures. Compared to the single structure, this hybridization of plasmonic resonances leads to significant spectral shifts accompanied by higher local electromagnetic field intensities in the nanometer-sized hotspots.

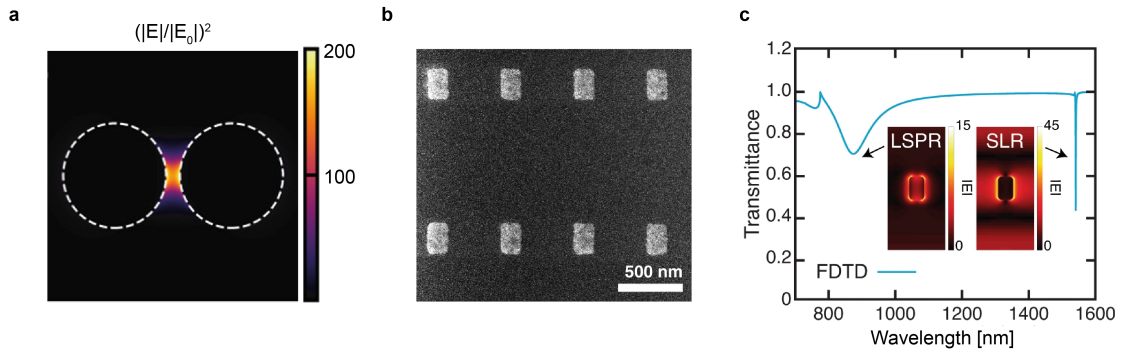


Figure 6.2: **Collective optical response.** (a) Near-field coupling of two (b) Electron microscopy image of a plasmonic nanoantenna array sustaining high Q factor surface lattice resonances (SLRs). (c) Numerical finite-difference time domain (FDTD) calculations of the transmission spectrum of this metasurface for excitation light polarized along the x direction. Inset: numerical calculation of the electric field for a unit cell, for both localized surface plasmon resonance (LSPR) and SLR resonances, in the x-y plane. (a) adapted from Ref.²⁸ (b-c) adapted from Ref.³¹⁷

6.2.2 Plasmonic surface lattice resonances

A second possible collective response is achieved when the in-plane oscillations of the field scattered by single meta-atoms are in-phase with the field scattered by the neighboring structures in the periodic array. This effect is illustrated in Figures 6.2b-c and leads to the emergence of the so-called SLR resulting in a significant improvement of the quality factor.³¹⁸ SLRs are a result of far-field (radiative) coupling of the individual scatterers by in-plane diffraction orders of the periodic array. When particles are randomly distributed, the scattered fields of surrounding particles that impinge on a given particle have no large effect. However, high Q-factor SLR resonances can emerge when the particles are periodically arranged with a wavelength of $\lambda_{SLR} \approx n_{env} \cdot P$, where λ_{SLR} is the wavelength of the SLR resonance, n_{env} is the refractive index of either the substrate or the surrounding medium (e.g. air), and P is the period of the array.³¹⁹

6.2.3 Collective heating

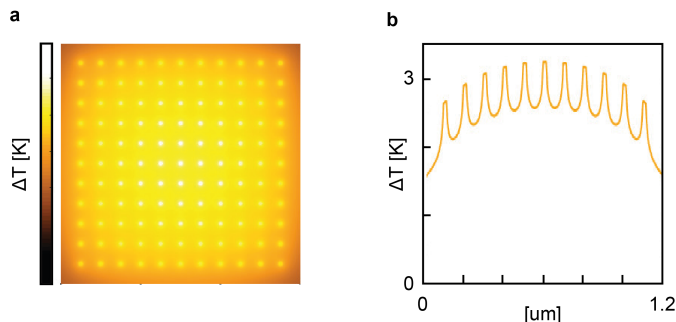


Figure 6.3: **Collective thermal response.** Numerical simulations carried out on a square ($1 \times 1 \mu\text{m}^2$) lattice of 16 nm spherical gold NPs with a particle interdistance of $p = 100$ nm. (a) Temperature map when illuminating the NP lattice with a CW uniform laser beam. $I = 3.2 \times 10^8 \text{ W m}^{-2}$. (b) Temperature cross cut. Adapted from Ref.³²⁰ Copyright 2013 American Chemical Society.

Apart from the near- and far-field coupling discussed in the previous sections, a third phenomenon has to be taken into account when many plasmonic nanoparticles are in close proximity. When illuminating a large number of gold nanoparticles, even when dispersed in solution, the temperature profile throughout the system may no longer be localized around each nanoparticle due to collective thermal effects.³²¹ The temperature can become uniform throughout the ensemble of nanoparticles, although the size of the heat sources is nanometric.³²⁰ The temperature increase of a given nanoparticle now has two contributions: First ΔT^S , the increase in temperature of a single particle and second ΔT^{ext} delivered by the surrounding nanoparticles. Figure 6.3 illustrates this effect. Numerical simulations of a $1 \times 1 \mu\text{m}^2$ square array with a uniform continuous-wave (CW) illumination are shown in Figure 6.3a. The temperature cross cut in Figure 6.3b shows a delocalization regime, where the collective heating is higher than the individual heating. Theoretical expressions for a variety of geometrical arrangements and illumination conditions can be found in the manuscript from Baffou *et al.*,³²⁰ the following are the relevant equations for a Gaussian illumina-

tion of an infinite square array. The single-particle temperature increase at the center of the illumination can be estimated as

$$\Delta T_0^S = \frac{\sigma_{abs} I(0)}{4\pi\bar{\kappa}R} = \frac{\ln(2)\sigma_{abs}P}{\pi^2 H^2 \bar{\kappa}R}. \quad (6.1)$$

Here, σ_{abs} is the absorption cross section, $I(0)$ is the irradiance at the center of the beam, P is the power measured at the sample position, H is the full-width-half-maximum (FWHM) of the Gaussian beam, $\bar{\kappa}$ is the averaged thermal conductivity of the surrounding media and R is the Laplace radius²⁵¹ that takes into account the geometry of the individual nanoparticle. The collective temperature increase at the center of the illumination can be estimated as

$$\Delta T_0^{ext} \approx \frac{\sigma_{abs}P}{\bar{\kappa}} \sqrt{\frac{\ln(2)}{4\pi}} \frac{1}{HA} \left(1 - \frac{4\sqrt{\ln(2)A}}{\pi H}\right). \quad (6.2)$$

where $A = p^2$ and p is the particle distance. The occurrence of a localization vs. delocalization regime can be predicted by considering a dimensionless parameter ζ_2 that estimates the ratio $\Delta T_{0,s}/\Delta T_{0,ext}$.

$$\zeta = \frac{3HR}{p^2} \quad (6.3)$$

6.3 Metasurfaces for energy conversion

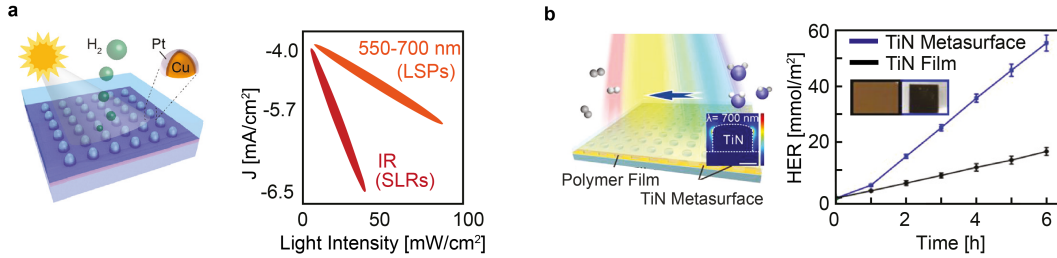


Figure 6.4: **Examples of metasurfaces for photocatalysis.** (a) Core-shell Cu/Pt lattices with individual LSPRs and collective plasmonic SLRs. (b) Refractory TiN metasurfaces as broad-band solar light absorbers. (a) Adapted from Ref.³²² Copyright 2021 American Chemical Society. (b) Adapted from Ref.³²³ Copyright 2021 American Chemical Society.

The following list summarizes some of the most important benefits of metasurfaces for energy conversion that make them stand out compared to current technologies and are discussed in more detail in reference:²⁸

- Tunable absorption across solar spectrum
- Dynamic tuning of optical properties
- Conversion of photons into different energies
- Fine-tuned absorption for enhanced power conversion

- Compact and cost-effective photodetectors with advanced functionalities
- Enhanced sensitivity of chemically selective spectroscopies
- Localized absorption where needed
- Higher absorption at lower volumes
- Conversion of light into heat for thermal nanophotonics
- Increased photocatalytic efficiency through charge-carrier concentration

Two examples in which the properties of plasmonic metasurfaces are exploited for plasmon-assisted water splitting are shown in Figure 6.4. In one example, Deng *et al.* fabricated a 2D array of bimetallic Cu–Pt core–shell nanoparticle lattices.³²² As discussed in Chapter 5, such bimetallic systems are expected to act as good photocatalysts for hydrogen evolution reaction (HER) due to the combination of highly catalytically active Pt sites with the plasmonic effects of Cu. In addition to interband transitions and the LSPR modes of single Cu particles, the lattices are engineered to exhibit a strong SLR mode in the near-IR region to extend the absorbed solar energy range of the material (Figure 6.4a). Excitation of either mode is expected to generate hot-carriers on plasmonic Cu, which can then be injected on the overlaying Pt shell. Wavelength-dependent measurements exciting the LSPR and SLR modes revealed the largest photocurrent densities under near-IR illumination. In this way, the SLRs were shown to be the main contributor to the observed photocurrent enhancement under white-light illumination, surpassing LSPR excitations with 2-fold improvement in HER catalytic activity because of greater light absorption and highly confined electromagnetic fields exhibited by the lattice modes. A second example is shown in Figure 6.4b. Refractory plasmonic materials have received great attention for various applications due to their low cost, high temperature resistance, and easy processability.^{324,325} In a very recent example, Yu *et al.* showed that titanium nitride (TiN) nanodisc metasurfaces, fabricated by electron beam lithography (EBL), can be used to realize broad near-unity absorption (92% of incident light) compared to TiN thin film absorption (42% of incident light).³²³ This increase was attributed to the emergence of a broad LSPR mode after nanostructuring, which peaks at 700 nm. The LSPR mode complements the high-energy interband transitions of the material to cover the entire visible range. The hot-carriers generated on the TiN metasurface are then utilized by a polymer HER catalyst deposited on top of the structure, with a threefold enhancement in photocatalytic H₂ production efficiency compared to thin-film control samples.

Similarly to single nanoparticles discussed in the previous chapters, the mechanisms that lead to enhancement are multi-varied and need to be addressed carefully. In the following, we discuss a technique that allows the direct measurement of the temperature of ensembles of nanoparticles on a substrate, as is the case for metasurfaces.

6.4 Anti-Stokes thermometry for plasmonic ensembles

Anti-Stokes (AS) thermometry is a promising method for measuring the temperature of plasmonic nanoparticles. It takes advantage of the fact that upon illumination with a continuous-wave laser, the AS part of the photoluminescence spectrum of the particles shows a temperature dependence. AS thermometry is a novel technique that works at the single-particle level. In Chapter 3.3.3, we introduced this technique and applied it in Section 5.2 to study individual nanoparticles. There are only a limited number of techniques that can operate with such a high sensitivity, making comparison of results difficult. Until now, its measurements have only been validated with theoretical estimations or macroscopic heating. In this section, we demonstrate the implementation of AS thermometry for plasmonic ensembles. Here, at the ensemble level, our results are supported not only by theoretical estimates,³²⁰ but also by temperature measurements using quadriwave lateral shearing interferometry.¹⁴⁸ This allows us to establish not only AS thermometry for plasmonic ensembles but also verify the method itself.

6.4.1 From one nanoparticle to plasmonic ensembles

We will limit the discussion to the case where both heating and photoluminescence excitation are performed simultaneously with the same laser, which is the most common scenario. For AS thermometry, the laser needs to be tuned to the resonance of the nanoparticle to have both anti-Stokes and Stokes emission, where there is typically also absorption. To explain the conditions under which AS thermometry is valid for ensembles of nanoparticles, let us first take a closer look at the method previously published for **individual nanoparticles**.¹³² For one nanoparticle, the anti-Stokes ($I_{AS}(\lambda, \lambda_{exc}, T)$) and Stokes ($I_S(\lambda, \lambda_{exc})$) photoluminescence is given by:

$$I^{AS}(\lambda, \lambda_{exc}, T) \propto f_I(I_{exc})f_{PL}(\lambda, \lambda_{exc})n(\lambda, \lambda_{exc}, T) \quad (6.4)$$

$$I^S(\lambda, \lambda_{exc}) \propto f_I(I_{exc})f_{PL}(\lambda, \lambda_{exc}) \quad (6.5)$$

Here, f_I describes the dependence of the signal intensity on the excitation irradiance I_{exc} (often assumed to be linear), f_{PL} is the intrinsic photoluminescence, and $n(\lambda, \lambda_{exc}, T)$ is the temperature-dependent distribution of states responsible for the anti-Stokes emission.

The function $n(T)$ expresses the energy distribution of the thermally available states that provide the extra energy for anti-Stokes emission. It has already been established that $n(T)$ is well described by a Bose-Einstein (BE) distribution in the context of anti-Stokes emission of plasmonic nanoparticles under continuous-wave excitation.¹⁴⁸

$$n(\lambda, \lambda_{exc}, T) = \frac{1}{e^{[E(\lambda) - E(\lambda_{exc})]/k_B T} - 1} \quad (6.6)$$

Here, k_B is the Boltzmann constant, and T refers indistinctly to the lattice or the electron gas temperature, as differences between the two temperatures are negligible under most experimental conditions with continuous-wave illumination. More details on alternative modeling can be found in the Appendix C.3.

We extract the temperature from the anti-Stokes ratios at two different temperatures:

$$Q_{i,j}^{AS} = \frac{I_i^{AS}}{I_j^{AS}} = \frac{f(I_{exc,i}) e^{[E(\lambda) - E(\lambda_{exc})]/k_B T_j} - 1}{f(I_{exc,j}) e^{[E(\lambda) - E(\lambda_{exc})]/k_B T_i} - 1} \quad (6.7)$$

Assuming that the temperature is linear with the irradiance $T = T_0 + \beta I_{exc}$, this expression has only one free parameter, β , which is the photothermal coefficient. For each pair of irradiances i, j , we extract a value of $\beta_{i,j}$ from a fit to $Q_{i,j}^{AS}$, and then determine the average value of β .

For an **ensemble of nanoparticles**, the collected signal is the sum of the individual signals, as illustrated in Figure 6.5:

$$I_N^{AS}(\lambda, \lambda_{exc}, T) \propto f(I_{exc}) \sum_k^N f_{PL,k}(\lambda, \lambda_{exc}) n(\lambda, \lambda_{exc}, T_k) \quad (6.8)$$

Here, $f_{PL,k}$ is the intrinsic photoluminescence of particle k and T_k is the temperature of particle k , and N is the number of nanoparticles that are being measured. It should be noted that we have assumed here that all particles show the same dependence on intensity $f(I_{exc})$.

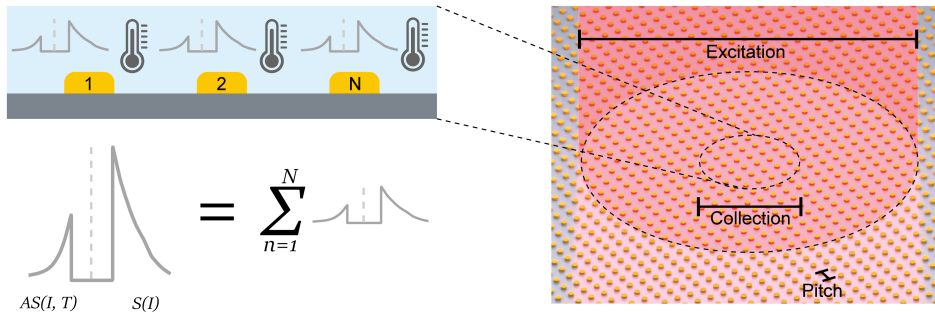


Figure 6.5: **Collective anti-Stokes signals.** Left: Illustration of the constant temperature of the N particles whose photoluminescence is collected. The anti-Stokes signal detected on the spectrometer is the sum of the individual signals. Right: Illustration of the conditions for measuring collective heating using anti-Stokes Thermometry (not to scale). A collection of nanoparticles in an array with pitch p are excited with a Gaussian beam of size s_{exc} and therefore heated at the same time. The collection size s_{col} must be smaller than the excitation to ensure that photoluminescence is detected from an area where the particles can be assumed to have the same temperature.

Now, we can imagine two scenarios under which this expression can be simplified. First, we could be dealing with a collection of non-identical particles that all have the same temperature. Equation 6.8 would then simplify to:

$$I_N^{AS}(\lambda, \lambda_{exc}, T) \propto f(I_{exc}) \left(\sum_k^N f_{PL,k}(\lambda, \lambda_{exc}) \right) n(\lambda, \lambda_{exc}, T) \quad (6.9)$$

Equation 6.9 can be simplified even further under the assumption of identical particles:

$$I_N^{AS}(\lambda, \lambda_{exc}, T) \propto f(I_{exc}) N f_{PL}(\lambda, \lambda_{exc}) n(\lambda, \lambda_{exc}, T) \quad (6.10)$$

In both cases, for non-identical and identical particles, the intrinsic photoluminescence is canceled out when computing the AS ratios:

$$Q_{i,j_N}^{AS} = Q_{i,j}^{AS} = \frac{f(I_{exc,i}) e^{[E(\lambda) - E(\lambda_{exc})]/k_B T_j} - 1}{f(I_{exc,j}) e^{[E(\lambda) - E(\lambda_{exc})]/k_B T_i} - 1} \quad (6.11)$$

This is identical to the single-particle equivalent (Equation 6.7). To simplify the discussion, in the following, we consider a square array of identical nanodisks, shown in Figure 6.5. However, the technique could be employed for disordered nanoparticles and/or non-identical nanoparticles, as long as the assumption of a constant temperature across the collection of nanoparticles is valid. We design the properties of the array to ensure that we are in a delocalization regime throughout the collection area, where the temperature profile is smooth throughout the system despite the nanometric nature of the heat sources. This approximation is only true for the center of the illuminated array, and therefore the excitation size should be significantly larger than that of the collection.

6.4.2 Optimizing sample and setup

In this section, we describe the sample and setup used to investigate the collective heating of nanoparticles via AS thermometry. We designed three different sizes of disks with resonances close to our excitation wavelength of 647 nm, so that we have significant Stokes and anti-Stokes emission. The simulated dimensions are $D = 70$ nm (D070), $D = 100$ nm (D100), $D = 150$ nm (D150), with heights of 40 nm. The simulated optical properties of the single disks are shown in Figure 6.6.

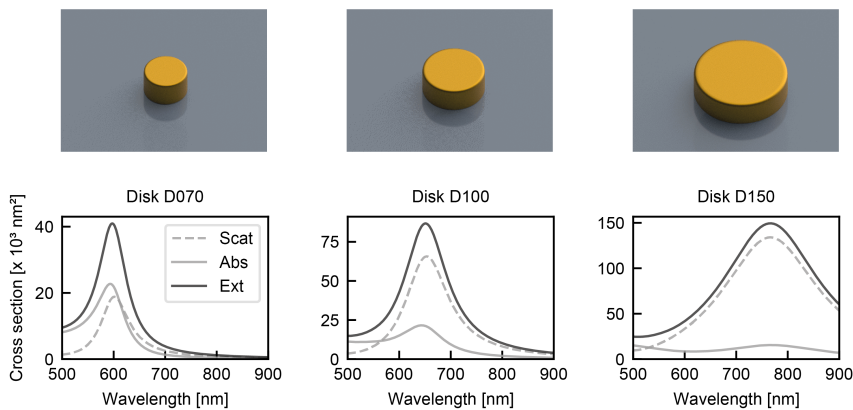


Figure 6.6: **Optical simulations of single disks.** Simulated scattering, absorption and extinction cross sections of disks with 70, 100, and 150 nm diameter and 40 nm height.

The sample layout is illustrated in Figure 6.7a. The arrays are $40 \times 40 \mu\text{m}^2$, with a pitch of 250 nm for D070 and D100, and for D150 the pitch was increased to 350

nm. Figure 6.7b shows the optical transmission of three exemplary arrays measured in water, together with the excitation wavelength of 647 nm that is used for photothermal measurements.

Recent implementations of anti-Stokes thermometry for single nanoparticles such as Ref.¹³² or the previous chapter 5.2, rely on a confocal excitation and detection scheme. To achieve wide-field illumination and simultaneously excite thousands of nanoparticles, we focused a 647 nm laser on the backfocal plane of the imaging objective, as shown in Figure 6.7c. This epi-widefield illumination has a FWHM of around 18 μm , and the emitted photoluminescence is spatially filtered using a fiber with a core size of 400 μm . This corresponds to a collection size in the sample of around 6 μm . Before reaching the spectrometer, the signal is filtered with a rejection filter for the 647 nm laser. With a pitch of 250 nm, this means that within the FWHM of the Gaussian illumination there are around 4000 nano particles, and the signal collected is from around 450 nanoparticles in the center of the beam.

To ensure that the assumption of a delocalization regime is valid, we calculated the value of ζ (according to Equation 6.3, explained in Section 6.2.3), which corresponds to the ratio between collective and individual heating. For an excitation beam of 18 μm (FWHM), ζ is between 0.027 and 0.041, indicating that we are indeed in a delocalization regime and that the assumption of constant temperature throughout the collection area is valid.

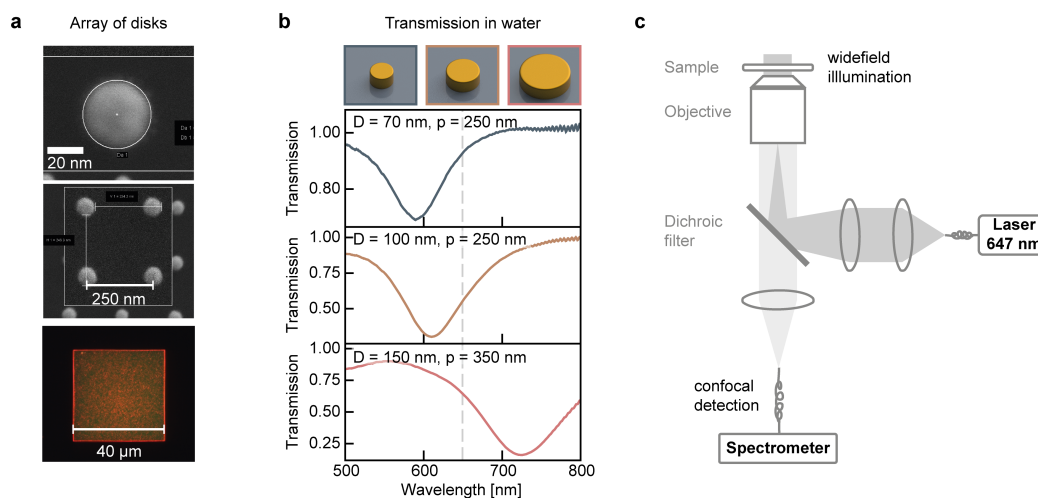


Figure 6.7: **Setup and sample.** (a) Exemplary SEM and dark-field images of the arrays. SEM images of the $D = 70$ nm disks, dark-field image of the $D = 100$ nm array. (b) Normalized transmission in water of arrays with three different disk sizes. Dashed line illustrates the laser wavelength of 647 nm. (c) Illustration of the setup. The 647 nm excitation laser is focused on the backfocal plane of the objective to achieve wide-field illumination. The emitted photoluminescence is transmitted to a spectrometer after being spatially filtered using a fiber.

6.4.3 Photothermal properties of arrays of gold nanodisks

To determine the photothermal coefficient (β) for each array, we performed photoluminescence measurements at seven different laser power settings. Before each measurement, the arrays were illuminated for 2 min at maximum power, to stabilize the

signal. We believe that the initial change in signal can be attributed to both a bleaching of the background and a possible annealing effect, during which the disks likely reshape to more of a dome-like geometry. We attribute this change to a reshaping of the antennas during heating. In this reshaping process, the disks would most likely round out into a dome-like shape. This is supported by a change in the transmission and single-particle dark-field spectra (for more details, see Appendix C.2). Figure 6.8a displays four representative photoluminescence spectra obtained from a D100 array, while the bottom portion shows some of the anti-Stokes and Stokes ratios. The Stokes ratios were relatively constant, although compared to usually reported although they are less than linear with excitation intensity. The anti-Stokes ratios exhibited a characteristic slope that could be fitted using Equation 6.11, where we have substituted $f(I_{exc})$ for $I_S(I_{exc})$, the integrated intensity of the Stokes signal. The dashed lines indicate the resulting fits. The histograms in Figure 6.8b depict the obtained photothermal coefficient values for all three types of arrays. In particular, the D100 array demonstrated the highest photothermal coefficient, consistent with numerical simulations that showed that the D100 disks had the highest absorption cross section at the excitation wavelength of 647 nm.

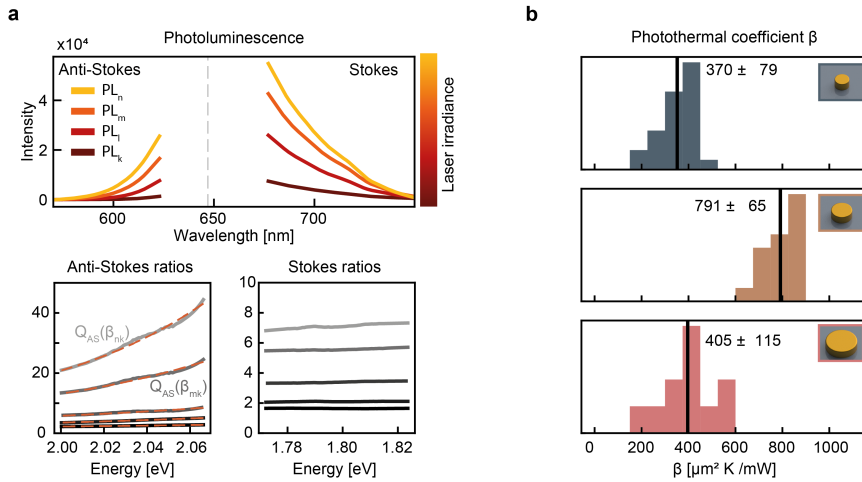


Figure 6.8: **Photothermal measurements.** (a) Overview of the data and analysis of photoluminescence spectra. The top panel shows the full photoluminescence spectra, which consist of both the anti-Stokes and Stokes components, here the spectra using four different laser powers are shown. The bottom panel displays the anti-Stokes and Stokes ratios, with the anti-Stokes fitted for the beta value shown in orange. (b) Histograms of the photothermal coefficients for the three different disk sizes. The photothermal coefficients were obtained from the photoluminescence spectra using photothermal analysis.

6.4.4 Comparison with wavefront imaging

Next, we verify our findings with quadriwave lateral shearing interferometry (QLSI). This technique was first introduced by Baffou in 2012.¹⁴⁸ The data were analyzed following the methodology outlined in Baffou’s original publication. To minimize any potential sources of heterogeneity in the sample and experimental setup, we took temperature measurements in the same sample positions with the same excitation

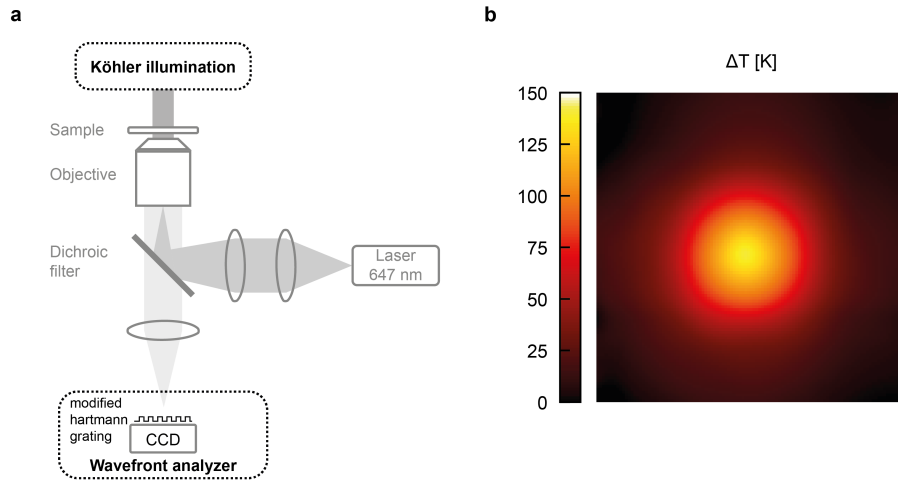


Figure 6.9: **Quadriwave shearing interferometry.** (a) Illustration of the setup to measure temperature using quadriwave shearing interferometry. (b) Exemplary extracted 2D temperature map.

power and in the same setup, almost simultaneously. The setup is as shown in a previous figure (Figure 6.7b), with the exception that an additional lamp in a Köhler configuration is included and the signal is directed to a wavefront analyzer comprised of a CCD camera with a modified Hartmann grating. The basics of the QLSI setup are illustrated in Figure 6.9a. The grating detects changes in the wavefront due to changes in the refractive index, from which the temperature of the sample can be calculated quantitatively. An exemplary temperature map is included in Figure 6.9b. To compare these measurements with the temperature measurements using AS thermometry, we extract the temperature of the center of the array. It is noteworthy that this is the first time that QLSI and AS thermometry have been compared with another technique, thereby verifying the accuracy of both methods against each other.

Comparison of experimental results Figure 6.10 shows the experimental results for both techniques, QLSI and AS thermometry, with a good fit. This shows that both QLSI and AS thermometry allow a reliable temperature estimation of plasmonic ensembles. Additionally, we estimated the temperature increase theoretically. The single and collective heating can be calculated using Equations 6.1 and 6.2. The values of the absorption cross sections were taken from Figure 6.6 and the results are shown in Figure 6.10a (dashed lines). Although the trends are predicted reasonably well, the temperatures for D100 are overestimated by more than a factor of two. This might be caused by an overestimation of the absorption cross section. The correct estimation relies not only on the estimation of the correct sizes, but also on the correct shape. The simulations shown in Figure 6.6 were performed under the assumption of a perfect disk with the desired size. However, at the time of submission of this thesis, we have not yet acquired scanning-electron-microscopy (SEM) images of the disks, as the sample is with our collaborator Guillaume Baffou for further characterization. As we suspect a reshaping process, we try an alternative model with more rounded geometry, called a "dome", as discussed in Section 6.4.3. The results

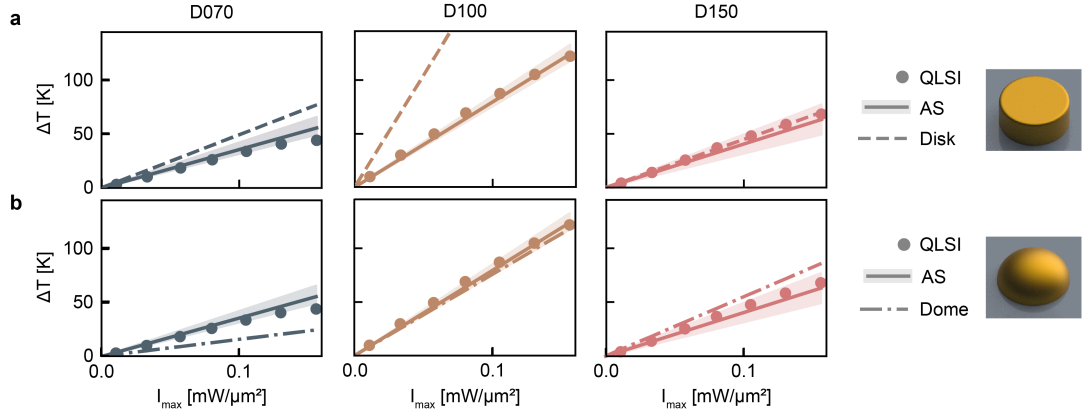


Figure 6.10: **Verification of measured temperatures.** (a) Experimental results of QLSI and AS thermometry. The line shows the temperature increase against maximum irradiance estimated from the median photothermal coefficient β , shaded area shows the 1st and 3rd quantile. Data points show the temperature determined by QLSI. Dashed line estimated temperature increase at the center of the array calculated from Equations 6.1 and 6.2 for both disk-shaped nanoparticles. (b) Same as in (a) but the theoretical estimations are shown for dome-shaped (dash-dotted line) nanoparticles.

are shown in Figure 6.10b. Our measurements with both QLSI and AS thermometry are within this theoretically predicted range defined by the disks and domes. The theoretical estimations can most likely be improved with further characterizations of the sample, such as exact dimensions to improve the accuracy of the simulated absorption cross sections, or the experimental measurement of the absorption cross section.³²⁶ However, this illustrates the applicability of AS thermometry, which does not require any previous characterization for the temperature measurements.

6.5 Conclusions

In conclusion, we have demonstrated the applicability and accuracy of anti-Stokes thermometry for investigating the collective heating of plasmonic ensembles. We designed and manufactured square arrays of gold nanodisks with varying sizes and investigated their photothermal properties. By employing anti-Stokes thermometry and quadriwave lateral shearing interferometry to measure the temperature, we were able to validate the accuracy and reliability of both techniques. Our experimental results showed a good agreement between the two techniques, further establishing anti-Stokes thermometry as a reliable method for temperature estimations in plasmonic ensembles. This further validates anti-Stokes thermometry also for single-particles, where a comparison is technically more difficult.

Until now, anti-Stokes thermometry has mainly been used at the single-particle level. Here, we have shown that it can be extended to ensembles of multiple identical particles, and provided guidelines on how to perform this extension. It must be noted that the method can be further extended to non-ordered arrays or non-identical particles and is therefore useful for the wide ranges of applications of plasmonic ensembles, such as photothermal therapy, plasmonic sensors, and solar energy conversion.

7

Conclusions and Outlook

In this thesis, I have explored the fundamental mechanisms underlying plasmon-enhanced catalysis using single-molecule localization microscopy, investigated the role of temperature in hybrid plasmonic photocatalysts for solar fuel generation, and demonstrated the applicability and accuracy of anti-Stokes thermometry for investigating the collective heating of plasmonic ensembles such as metasurfaces.

Our study of plasmon-enhanced catalysis revealed that the enhancement of the studied reaction is largely attributed to the photoexcitation of the reactant molecule. We identified that maximizing the plasmonic field enhancement is crucial for optimizing catalysts for similar reactions. By tuning the plasmonic field enhancement to the absorption of the reactant molecule, we can maximize turnover rates at low irradiances, enabling the design of plasmonic nanoparticles for driving chemical transformations without the use of high-intensity lasers.

In the investigation of hybrid plasmonic photocatalysis, we highlighted the importance of understanding the role of temperature in the enhancement mechanism. We introduced a photothermal model for bimetallic core-shell nanoparticles and a characterization technique, anti-Stokes thermometry, which allowed us to establish a link between nanoparticle structure and heat generation. This label-free, non-invasive, and in situ technique can be extended to other complex/hybrid plasmonic interfaces with catalytic relevance, providing valuable insights into their behavior.

Lastly, we successfully demonstrated the applicability and accuracy of anti-Stokes thermometry for investigating the collective heating of plasmonic ensembles. By comparing the results obtained from anti-Stokes thermometry and quadriwave shearing interferometry, we validated the reliability of both techniques. This study not only provides valuable insights into the photothermal properties of plasmonic ensembles but also paves the way for future research on their potential applications in areas such as photothermal therapy, plasmonic sensors, and solar energy conversion, where meta-

surfaces (more than single particles) are a prominent research direction to efficiently exploit the light-matter interactions of plasmonic nanoantennas. Furthermore, our findings emphasize the importance of developing and validating advanced characterization techniques, such as anti-Stokes thermometry, to improve our understanding of the complex behavior of nanomaterials and their interactions with light.

In conclusion, this thesis has contributed to the advancement of plasmonic nanoantennas for energy conversion by shedding light on the underlying mechanisms, investigating the role of temperature in hybrid plasmonic systems, and validating a novel characterization technique for temperature estimation. The insights gained from this work will be instrumental in guiding the design of more efficient and sustainable energy conversion technologies, as well as expanding our understanding of plasmonic materials and their applications.

As during any PhD we had many good (and bad ideas) along the way, and never enough time to explore them all. I want to use this final chapter not only to summarize findings within this thesis and highlight their relevance, but also to suggest promising routes to explore. To keep this section concise, I will only provide a brief overview of these ideas here, but I have included a few more details and preliminary results in Appendix D.

For example, in the area of single-molecule localization microscopy for plasmonic catalysis, it would be beneficial to use ordered arrays and orient the nanoantennae on the substrate to disentangle the effect of different resonances and map distinct catalytic hotspots. To this end, we experimented with various protocols to create porous silica films on top of these samples, and I have included our optimized protocol in Appendix D.1. In addition, we propose that mapping the near-field of plasmonic antennae would be a valuable shift in focus, as we have found that the model reaction system is largely driven by near-field enhancement. Furthermore, we have explored a different reaction system using a CO-sensitive fluorescent probe, which could be useful in mapping the technologically relevant CO₂ reduction. Details on these ideas can be found in Appendix D.2.

In the field of nanothermotry, we have established anti-Stokes thermometry as a tool to characterize the photothermal properties of ensembles of plasmonic nanoparticles. Going forward, we believe that this technique will be useful for monitoring the temperature of catalysts in situ. One particularly interesting example is surface lattice resonances, which have been shown to enhance photocatalytic activity more than individual localized surface plasmons. In this context, we suggest that the surface lattice resonance wavelength could be used to drive photocatalysis, while the photoluminescence could be excited at the localized surface plasmon resonance, allowing for in situ temperature monitoring.

Appendix

Contents

A	Supplemental material associated with Chapter 4	118
A.1	Chemicals and Materials	118
A.2	Optical characterization	118
A.3	Synthesis of gold nanorods (AuNRs)	118
A.4	Mesoporous silica coating of AuNR and etching treatment	119
A.5	Assembly into arrays	119
A.6	Size distributions of the AuNR with silica	120
A.7	Single-molecule fluorescence microscopy	120
	The setup	120
	Final sample preparations and reactant flow	121
	Drift correction and background subtraction	122
	Identification and localization of events	123
	Single particle analysis	123
A.8	FDTD simulations	124
	Optical cross sections and field enhancement maps	126
	Local irradiance close to the surface.	126
A.9	Temperature estimations	126
	Temperature simulations in COMSOL	126
	Collective heating in ordered arrays	127
	Estimated temperatures	129
A.10	Photostationary state of Rz	130
A.11	Excited Resazurin and Langmuir-Hinshelwood	131
A.12	The reaction kinetics without hydroxylamine	131
A.13	The reaction kinetics are not mass-transport limited	131
B	Supplemental material associated with Chapter 5	133
B.1	Materials and Methods	133
	Chemicals	133
	Synthesis of 60 and 67 nm Au NS	133
	Synthesis of Au@Pd CS-NPs	133
	Synthesis of Au–Pd Core-Satellites NPs	134
	Inductively coupled plasma – atomic emission spectroscopy	134
	Optical Printing	134
	Dark field microscopy and spectroscopy	135
	Hyperspectral Confocal PL images	135
	AS Hyperspectral thermometry	135

	Optical simulations	136
	Temperature Simulations using COMSOL Multiphysics	137
B.2	Further characterizations of the chemical structure	137
	Characterization of the Pd shells of Au@Pd CS-NPs	137
	Characterization of Au ₆₀ -Pd-sat NPs	138
	Stability of the printed nanoparticles	141
B.3	More detailed derivation of the temperature model	142
	Heat diffusion for a spherical core-shell nanoparticle	142
	Temperature drop within the nanoparticle	143
	Particle on a substrate	144
C	Supplemental material associated with Chapter 6	145
C.1	Materials and methods	145
	Fabrication	145
	Optical characterization	145
	Anti-Stokes photothermal measurements	145
	QLSI photothermal measurements	146
	Numerical calculations	146
C.2	Annealing	146
C.3	Influence of choice of distribution	148
D	Supplemental material associated with Chapter 7	149
D.1	Single-molecule catalysis on EBL structures	149
	Porous film on top of EBL structure	149
	Protocol for porous silica films	149
	Images of porous films on different substrates	150
	Accessibility of the porous films	150
	Stability of porous silica films	151
D.2	Single-molecule imaging of non-fluorescent reactions	151
E	Personal contributions	153

A Supplemental material associated with Chapter 4

A.1 Chemicals and Materials

Tetraethylorthosilicate 98 % (TEOS), ammonium hydroxide solution 28 - 30 % (NH_4OH), tetrachloroauric acid ($\text{HAuCl}_4 \cdot 3 \text{H}_2\text{O}$), cetyltrimethylammonium bromide (CTAB), sodium borohydride (NaBH_4), silver nitrate (AgNO_3), L-ascorbic acid ($\text{C}_6\text{H}_8\text{O}_6$), concentrated hydrochloric acid (HCl, 37 %), hydroxylamine hydrochloride (5540), resorufin sodium salt (R7017) were purchased from Sigma-Aldrich. 20x borate buffer (28341), resazurin sodium salt (R12204) and fluorescent beads (F8801) were purchased from Thermofisher. All chemicals were used as received. Pure grade ethanol and Milli-Q grade water were used in all preparations.

A.2 Optical characterization

TEM images were obtained using a JEOL JEM 1010 transmission electron microscope operating at an acceleration voltage of 100 kV. SEM images in Figure 1 and 7.2 were obtained using a field emission scanning electron microscope (Zeiss). UV-Vis absorbance spectra in H_2O were recorded on a Perkin-Elmer UV/Vis/NIR spectrophotometer LAMBDA 750 and collected from a 1-cm path length quartz cuvette. Dark-field images and scattering spectra were taken using a WITec microscope (Germany) using a 100x air objective with 0.9 NA (Zeiss, Germany). The single-particle catalysis measurements are described detail in A.7.

A.3 Synthesis of gold nanorods (AuNRs)

AuNRs were synthesized following the seed-mediated method with some modification.¹⁷⁴ To prepare the seeds, 25 μL of 50 mM HAuCl_4 solution was added to 4.7 mL of 0.1 M CTAB and slowly stirred for 5 min at 27- 30 °C. Then, 300 μL of a freshly prepared 0.01 M NaBH_4 solution was rapidly injected under vigorous stirring. After 1 min the solution was kept 3 h unstirred. To prepare the gold nanorods, 41.8 μL HAuCl_4 (0.1196 M) is added to 10 mL, CTAB (0.1 M); the mixture is gently shaken and kept for 10 min thermostated at 27 °C in a water bath to ensure complexation between gold salt and CTAB. Afterwards, 45 μL of AgNO_3 (0.01 M) is added to the mixture, which is gently shaken for few seconds. Subsequently, 15.4 μL of HCl (37 %) was added and 80 μL of ascorbic acid solution (0.1 M) is then added to the growth solution and thoroughly shaken turning colorless immediately. Finally, 10 μL of seeds@CTAB is added to the mixture and the solution is vigorously shaken and then left undisturbed at 30 °C for 12 h. The dimensions obtained from TEM were 51 ± 7 nm of length and 28 ± 3 nm of thickness.

A.4 Mesoporous silica coating of AuNR and etching treatment

A solution of AuNR (5 mL, 0.35 mM) was added dropwise under sonication to a solution of CTAB (25 mg), water (5 mL), ethanol (4 mL) and ammonia (120 μL). Then, 150 μL of a 20 % (v/v) TEOS solution in ethanol was added dropwise to the previous suspension under sonication. This mixture was stirred for 48 h. Subsequently, the mixture was centrifugated and redispersed in ethanol four times to remove unreacted species (4500 RPM, 20 min). Finally, to remove CTAB and make larger mesopores, an etching process was used as previously described with some modifications.¹⁵² AuNRm-SiO₂ were re-suspended in 11 mL ethanol/water (10:1) solution. Subsequently, 70 μL 0.1 M NaOH was added. The solution was put in an oven, unstirred, at 90 °C for 2 h. After that, the nanostructures were recovered as precipitates after centrifugation at 4500 RPM, 20 min, and were then washed thoroughly with ethanol three times. The AuNRm-SiO₂ nanostructures were redispersed in ethanol (10 mL). Figure 7.1 shows the extinction spectra with and without mSiO₂ in water.

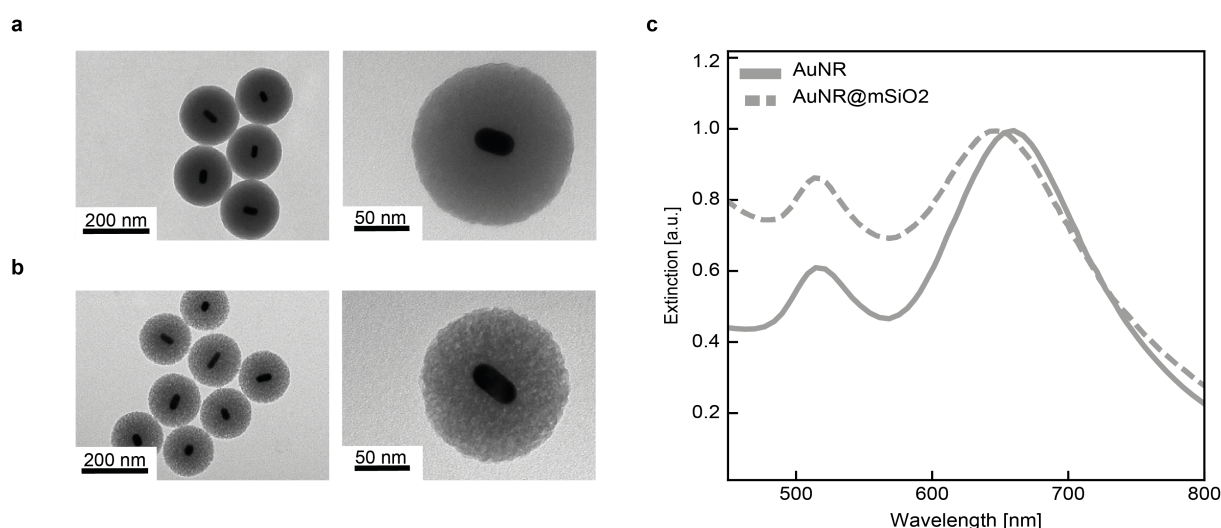


Figure 7.1: **Mesoporous silica coating of AuNRs** (a)-(b) TEM images before and after etching, (c) UV-VIS spectra of the AuNRs in water with and without mSiO₂.

A.5 Assembly into arrays

The AuNRm-SiO₂ were positioned as arrays on glass using a template dissolution interfacial patterning (TDIP) method as previously reported.⁸⁵ First, using a custom-built setup, single AuNRm-SiO₂ particles were assembled via capillary-assisted particle assembly into a topographical PMMA template stripped from a Si master substrate using polyimide tape. A small volume of the particle suspension (100 μL) was sandwiched between the PMMA template and a clean glass coverslip, which was moved across the assembly template at a uniform speed of 2 $\mu\text{m s}^{-1}$ using a piezoelectric motor. The motion created a receding meniscus at the coverslip edge allowing

the AuNRm-SiO₂ particles to experience the convective and capillary forces at the vapor/liquid/solid substrate contact line necessary to position the particles within the designated trap sites. To print the patterned particles, the polyimide tape containing the PMMA template was pressed down against a precision cover glass (#1.5 H thickness, 22 mm × 22 mm, Thorlabs) pre-cleaned by sonication in acetone and isopropanol, dried with N₂ gas, and O₂ plasma treated for 2 min. The tape-attached cover glass was fully immersed in an acetone bath for 1- 1.5 h, after which the dissolution of PMMA in acetone removed the tape from the cover glass to leave behind the AuNRm-SiO₂ printed on the cover glass substrate. Figure 7.2 shows exemplary SEM images of the arrays at different magnifications.

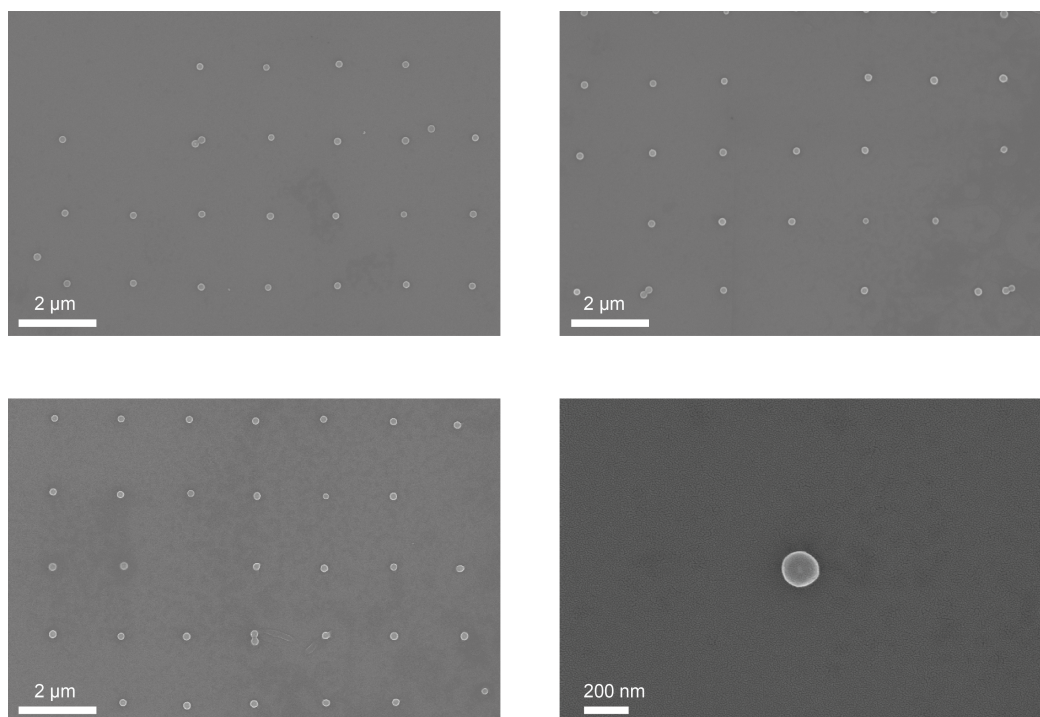


Figure 7.2: SEM images of assembled AuNR@mSiO₂.

A.6 Size distributions of the AuNR with silica

Figure 7.3 shows the distributions of the AuNR width and lengths, as well as the radius of the AuNR@mSiO₂ distributions.

A.7 Single-molecule fluorescence microscopy

The setup All single-molecule fluorescence experiments were performed on a home-built objective-type total internal reflection (TIRF) fluorescence microscope based on a Nikon TI Eclipse microscope. A continuous-wave circularly polarized 561 nm laser (Cobolt Jive) was used to excite both the fluorescence of the catalytic product resorufin and to enhance the reaction rate. A continuous-wave circularly polarized

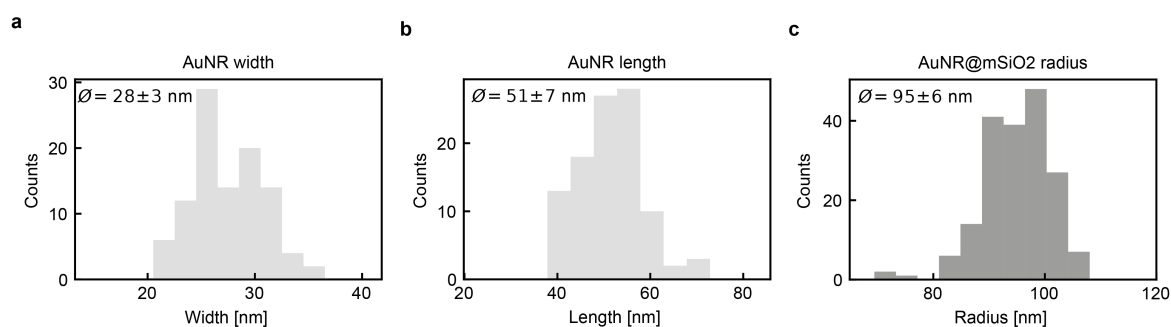


Figure 7.3: **Measured size distributions of the AuNR@mSiO₂ nanoparticles.** Number inset shows the average and standard deviation.

laser of wavelength 647 nm (OBIS 647 nm LX) was used to excite the longitudinal resonance LSPR of the catalyst. Both lasers were combined and reflected onto the sample with a dichroic beamsplitter (Quad Line Beamsplitter zt405/488/561/647rpc flat, Chroma). A 100x 1.49 oil immersion objective (CFI Apochromat TIRF 100XC oil) was used for both excitation and collection. The fluorescence was filtered (*FF01* – 586/20, Semrock) and detected by an EMCCD camera (Evolve 512) operated with an electromagnetic gain of 200, sensitivity of 3e/ADU and an integration time of 30 ms, resulting in a frame rate of around 15 frames/s, depending on the size of the region of interest. The pixel size in this configuration was determined to be around 163 nm. A simplified scheme is shown in Figure 7.4. Z drift was corrected during the measurement using a home-built focus lock system based on a CW 850 nm laser (LDM850, Thorlabs) and a z-motor (ES10ZE Focus Controller, Prior).

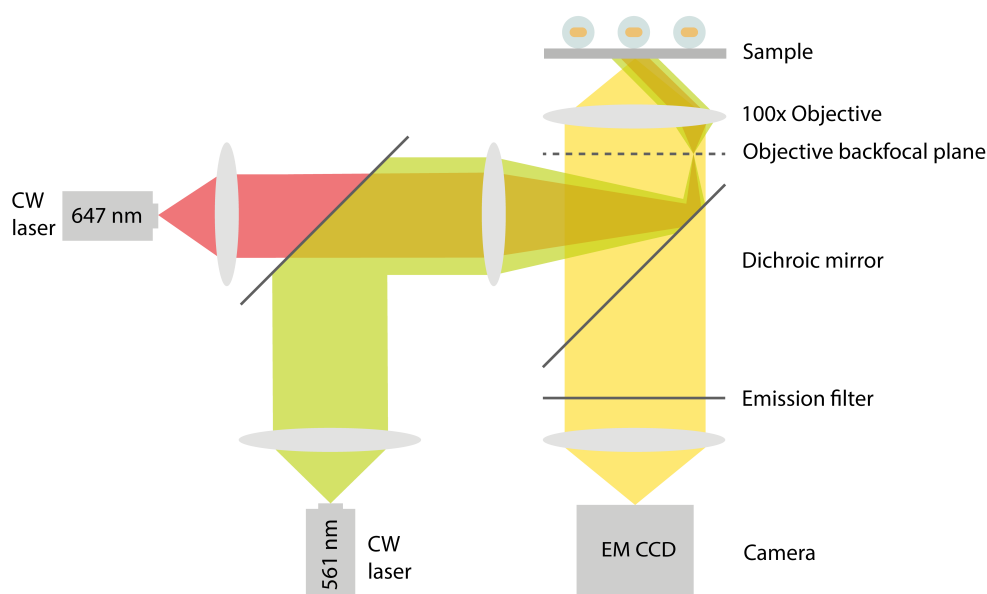


Figure 7.4: **Schematic illustration of the fluorescence microscopy setup.**

Final sample preparations and reactant flow After UV-ozone cleaning 10 hours at 1 hour intervals, each interval followed by washing with EtOH to ensure the pores

were open, the sample was mounted on a microfluidic channel with a volume of 30 μL (sticky-Slide VI 0.4, Ibidi). The aqueous reactant solution containing 200 nM resazurin, 0.1 - 10 mM in borate buffer was flowed through the channel at a rate of 15 $\mu\text{L min}^{-1}$ using a syringe pump (Model 100, KDSscientific). At these concentrations, reaction rates have been reported to no longer be sensitive to reactant concentrations.¹⁶⁸ After adding a new reactant, we waited 15 min before acquiring any images.

Drift correction and background subtraction Z drift was corrected during the measurement. After the measurement, the first steps of the data analysis are to remove the xy drift and to remove the background. To remove xy drift we relied on the photoluminescence background of the AuNRs and AuNR clusters. To this end, the image stack is segmented into bins of 25 frames and the average of each stack is compared to the first stack. An exemplary drift trajectory is shown in Figure 7.5.

After drift correction, the background was removed by subtracting the average of

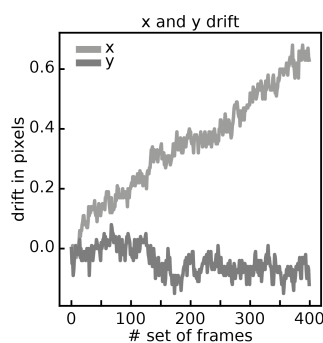


Figure 7.5: **Drift correction.** Calculated x and y drift.

each stack from each stack (Figure 7.6).

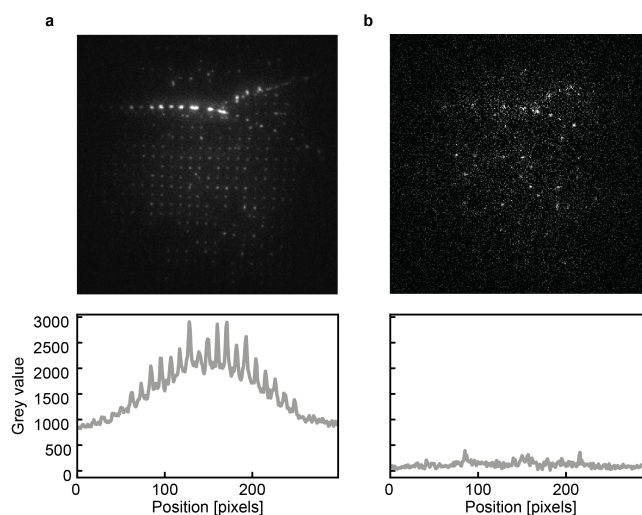


Figure 7.6: **Background subtraction.** (a) Exemplary frame and profile in before background subtraction (b) Same as (a) but after background subtraction.

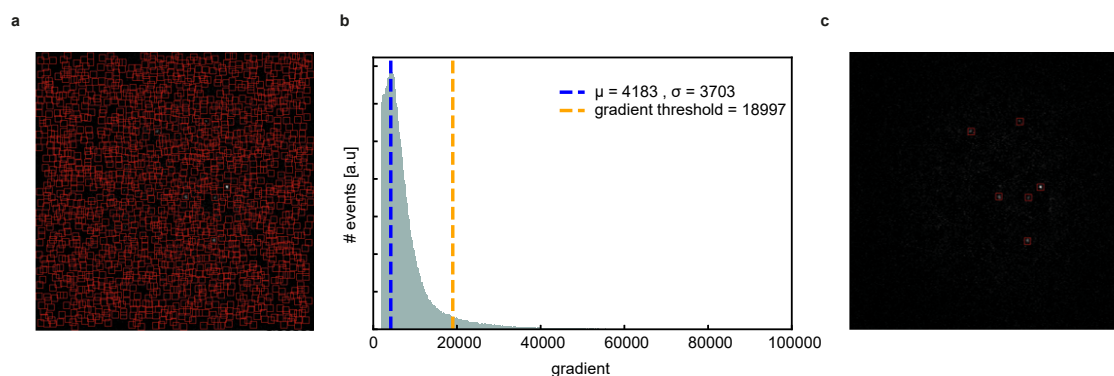


Figure 7.7: **Identification and localization of events.** (a) Identifications in one frame with low threshold of 500. (b) Histogram of the gradient of the identified noise with threshold determination. (c) the same frame with remaining localizations after thresholding.

Identification and localization of events After drift and background correction, the image stacks are processed to identify and localize turnover events using functions from Picasso.³²⁷

Here, events are identified using two characteristics: the box size, depending on the actual point spread function and pixel size (in our case 7 pixels), and the threshold of gradient. The number of detected events is very sensitive to the selected minimum net gradient. To avoid introducing any bias by manually selecting the minimum net gradient, we use the following automated approach, visualized in Figure 7.7 using the Picasso GUI but typically performed without:

We first localize all videos with a minimum net gradient of 500. Doing this, all detected events can be assumed to be noise. We then fit the histogram of the gradient with a Gaussian. We then determine the minimum net gradient for this data set to be the mean plus four times the standard deviation of the noise. The resulting identifications for an exemplary data set are shown in Figure 7.7.

Additionally, we exclude outliers by filtering out the following characteristics: fitted PSF size smaller than 0.5 pixels or larger than 2 pixels, localization precision larger than 0.4 pixels. Events in consecutive frames are linked. Figure 7.8 shows the obtained parameters for the detected product molecules.

Single particle analysis *Determining which particle an event belongs to*

We first roughly determine each particle position manually by clicking the PL background image or the final rendered super resolution image. Alternatively, one could overlay a grid and automatize the extraction.

After that, the event positions are correlated with the particle positions. All events are counted towards a particle if they lie within a 4 pixel (~ 650 nm) radius. We chose this large radius because the particle position itself at this stage has a low accuracy. Most of the events actually occur much closer (< 100 nm) of the particle center (this can be seen, for example, in Figure 2, 3, 4 and and Figure 7.10a). Therefore the exact magnitude of this arbitrary threshold does not affect the results.

Single particle irradiance

To determine the irradiance for each particle, we first measure the total power at

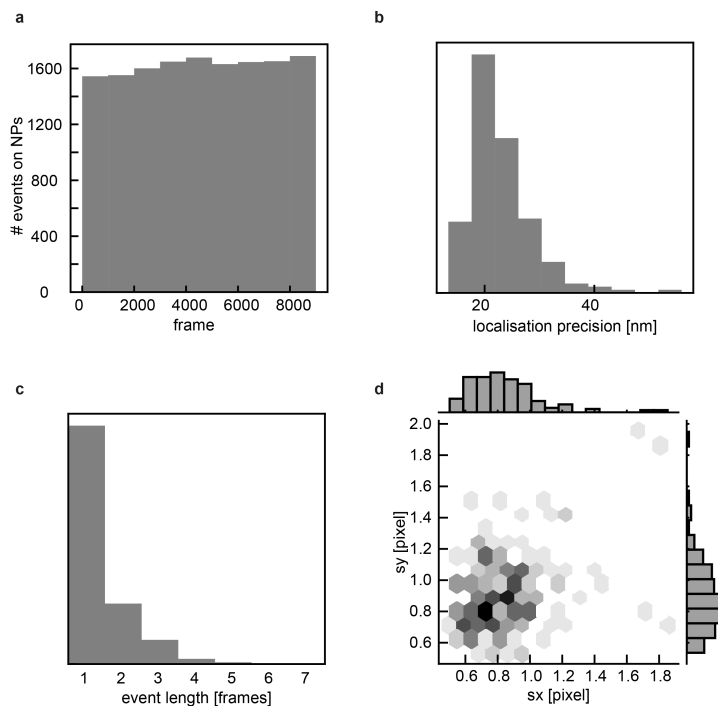


Figure 7.8: **Exemplary resulting characteristics of the fitted events.** (a) #events/1000 frames throughout the measurement. (b) Histogram of the localization precision. (c) Histogram of length of events. (d) Fitted PSF sizes. b-d for one exemplary particle, maybe replot for many

the sample position with a powermeter slide (S170C, Thorlabs). Next, we determine the beam profiles on the sample using a probe with fluorescent beads that allows us to see both lasers on the camera with the same set of filters used in the in operando catalysis experiments. The irradiance for each position can then be calculated from this profile. Figure 7.9 shows the measurement and the fitted 2D Gaussian profiles in (a) and (b), and (c) shows the $1/e^2$ outline on top of a sample. In Figure 3 and 4 in the main text, the catalytic activity is plotted against this binned irradiance.

Correcting for multiple particles at the same position

From the diffraction-limited photoluminescence it is not possible to tell whether there is truly a single particle at the grid position. To correct for this, the super-localized catalysis maps (Figures 7.10a). This yielded: 82% single particles, 12 % two particles, and 1 % three particles. The remaining grid positions were excluded because without SEM imaging, we were unable to safely determine the number of particles. For the kinetics the average turnover rate was then divided by the number of particles, for the spatial distributions only $n=1$ were considered.

A.8 FDTD simulations

Optical properties of the AuNR@mSiO₂ particles were investigated using FDTD simulations (ANSYS Lumerical Software ULC, Release 2022 R1, Version 8.27.2898). The gold (Johnson & Christy) nanorod was simulated as a cylinder capped with hemispheres (rounded cylinder), with dimensions $l = 51$ nm and $r = 13$ nm. The meso-

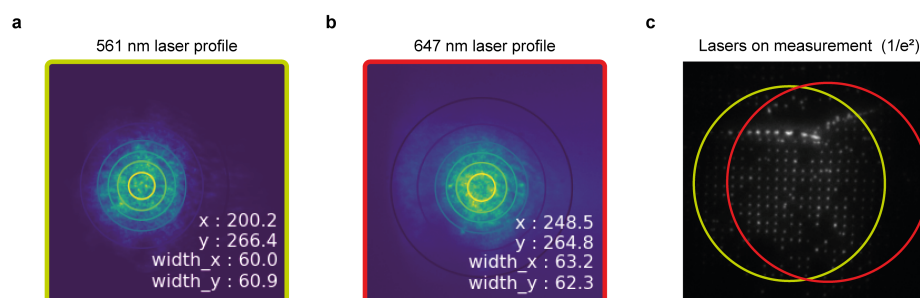


Figure 7.9: **Beam profiles.** (a) Green laser with fluorescent beads on full field of view, fitted with 2d Gaussian. (b) Red laser with fluorescent beads on full field of view, fitted with 2d Gaussian. (c) $1/e^2$ profile on region of interest. Position and size in pixels.

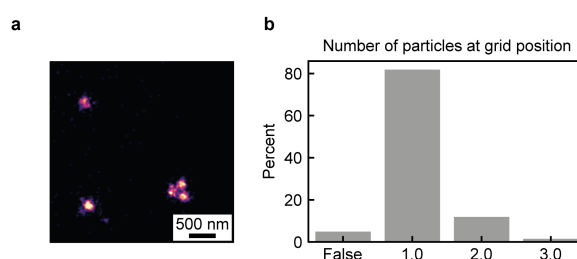


Figure 7.10: **Correcting for more than 1 particle at grid position.** (a) Determining number of particles at grid position from super-resolved catalysis maps, (b) Histogram of the number of particles at grid position.

porous silica shell ($n = 1.4$) was simulated as a sphere with a radius of 95 nm with a mesh order lower than that of Au. To simulate an aqueous medium, the surrounding medium was set to a refractive index of 1.333. The substrate was simulated as a rectangular prism composed of glass (Palik), touching the mSiO₂ at one point, as shown in Figure 7.11. To calculate absorption and scattering cross-sections a TFSF source was used. The injection was simulated perpendicular to the substrate. The absorption cross section was calculated using an analysis group inside the TFSF source. The analysis group consisted of six 2D monitors that form a closed box and measure the net power flowing in/out of the box. Similarly, the scattering cross section was calculated by an analysis group outside the TFSF source. Since this simulation has a plane

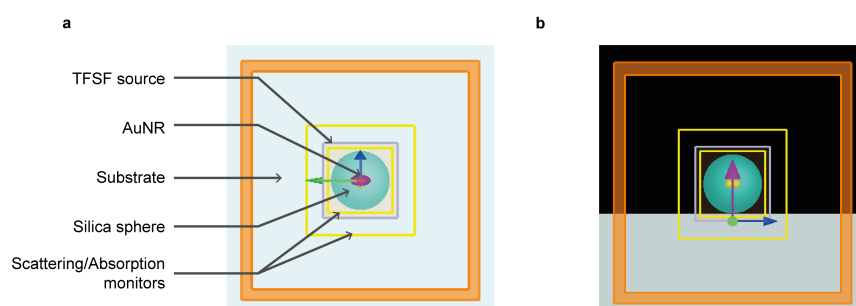


Figure 7.11: **Optical simulations in Lumerical FDTD.** (a) XY view of the simulation setup. (b) YZ view of the simulation setup.

of symmetry in the x and y dimensions, the simulation time can be reduced using boundary conditions. All simulations were performed for both polarizations along the axes of the AuNR. A mesh override region with $d = 1$ nm with the same dimensions as the TFSS source was used for the calculation of the cross sections. For the field enhancements a z-normal 2D frequency domain power monitor through the center of the AuNR was used and the mesh override was set to $d = 0.5$ nm.

The profiles resulting after processing as described in Figure 7.12 are shown in Figure 4.2.

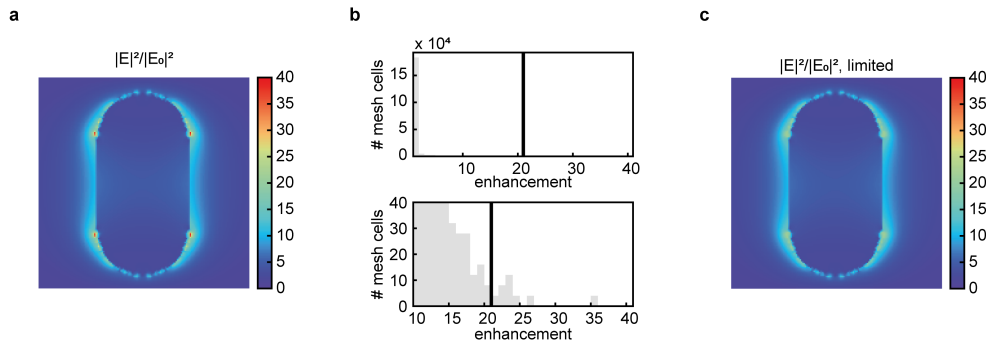


Figure 7.12: **Determining maximum field enhancement.** Due to the limited mesh size, a few mesh cells have unphysically high values (Figure 7.12a). Figure 7.12b shows a histogram of the enhancement within the monitor. By clipping the values to the first time where only 4 mesh cells are within a bin of size 1, these "hot pixels" were removed (Figure 7.12c).

Optical cross sections and field enhancement maps The resulting cross sections and field enhancements simulated as described in A.8 are shown in Figure 4.2.

Local irradiance close to the surface. For the reaction occurring on the gold surface, the local irradiance can be more than an order of magnitude larger than the incident irradiance. Figure 7.13 shows the fields above an increasing threshold. Additionally, the average intensity enhancement in the region is shown.

A.9 Temperature estimations

Temperature simulations in COMSOL The temperature increase of a single AuNRmSiO₂ was investigated using COMSOL Multiphysics. The simulation setup is illustrated in Figure 7.14.

Medium. Geometry: Dimensions 1000 nm x 1000 nm x 500 nm. Material: Water, $k = 0.6$ W/(m × K).

Substrate. Geometry: Dimensions 1000 nm x 1000 nm x 500 nm. Material: Glass, $k=1$ W/(m × K).

Particle. Geometry: as in A.8. Material: Gold, $k = 318$ W/(m × K) and Glass, $k = 0.8$ W/(m × K)

Physics. Heat transfer in solids with AuNR as a user-defined heat source with $Q = (\sigma_{abs} * I)/V$, where the absorption cross section (σ_{abs}) is used as calculated using

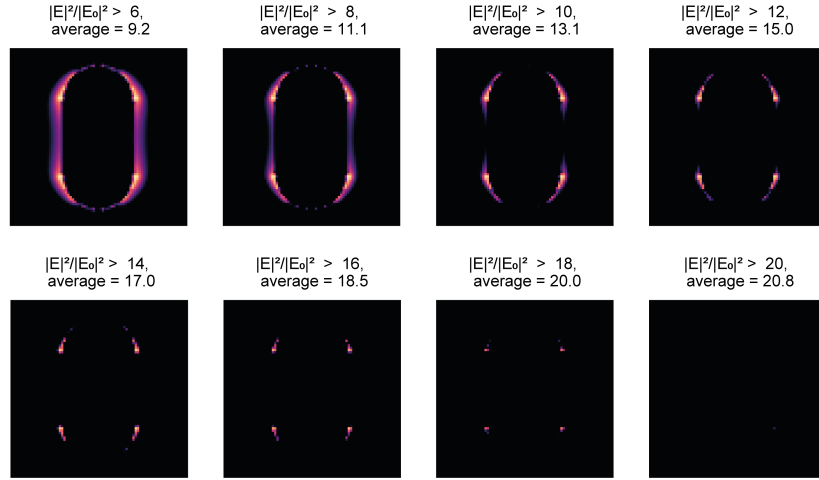


Figure 7.13: Field enhancements close to surface.

Lumerical FDTD ($\sigma_{abs}(647) = 5.488032 \times 10^{-15} \text{ m}^2$, $\sigma_{abs}(561) = 1.5234025 \times 10^{-15} \text{ m}^2$), I is the irradiance and V is the volume of AuNR. The simulation boundaries (in this case, the outer surfaces of the water and substrate, shown in blue) and the initial temperatures are set to $T_0 = 293 \text{ K}$.

The resulting temperature map in the xy plane and the temperature profile from the center in the x direction are shown at an irradiance of 100 W m^{-2} in Figure 7.15.

Collective heating in ordered arrays When plasmonic nanoparticles are in close proximity, the temperature profile throughout the system may no longer be localized around each nanoparticle (see Figure 7.14) due to collective thermal effects. Instead, the temperature increase of a given NP now has two contributions: First ΔT^S , the increase in temperature of a single particle as we simulated in A.9, and second ΔT^{ext} delivered by the surrounding NPs.

We estimated the temperature due to collective thermal effects using the theoretical description of Baffou *et al.*³²⁰ Specifically, we used the expression for a Gaussian illumination of an infinite square 2D array.

The single-particle temperature increase at the center of the illumination can be estimated as

$$\Delta T_0^S = \frac{\sigma_{abs} I(0)}{4\pi\bar{\kappa}R} = \frac{\ln(2)\sigma_{abs}P}{\pi^2 H^2 \bar{\kappa}R}. \quad (7.1)$$

Here, σ_{abs} is the absorption cross section calculated in A.8, $I(0)$ is the irradiance at the center of the beam, P is the power measured at the sample position, H is the FWHM of the Gaussian beam as determined in A.7, $\bar{\kappa}$ is the averaged thermal conductivity of the surrounding media and R is the Laplace radius²⁵¹ calculated from $R_L = \sqrt[3]{\frac{(3D-d)d^2}{16}}$, where D and d are the width and length of the AuNR.

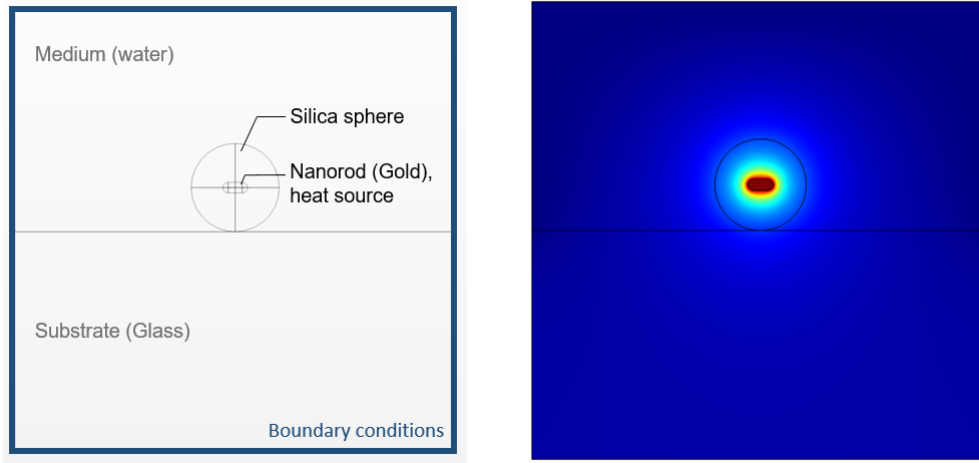


Figure 7.14: **Temperature simulations in COMSOL.** Left: 2D view of the simulation setup. Right: Exemplary 2D Temperature profile of the same view.

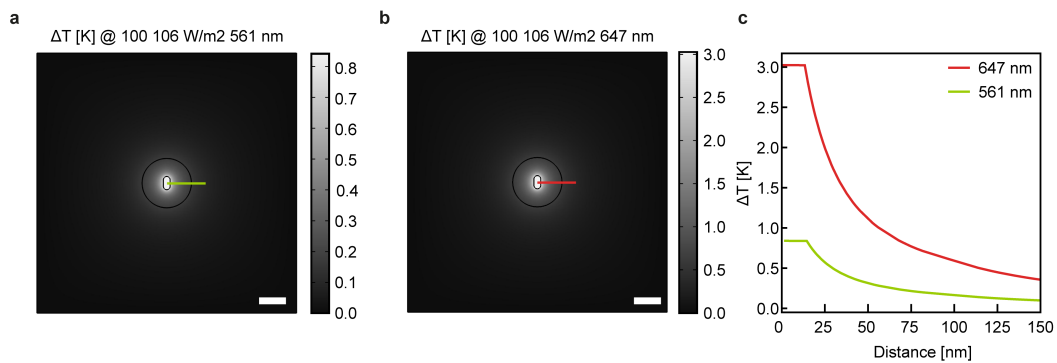


Figure 7.15: **Results of single-particle temperature simulations in COMSOL at $I = 100 \times 10^6$ W m^{-2} .** 2D temperature map of the center XY plane illuminated at 561 nm (a) and 647 nm (b). Scale bars 100 nm. (c) Temperature profiles as indicated in a and b.

$I(0)$	$100 \times 10^6 \text{ W m}^{-2}$
H^{647nm}	$23.797811375082772 \times 10^{-6}$
H^{561nm}	$23.030140040402683 \times 10^{-6} \text{ m}$
$\bar{\kappa}$	$0.8 \text{ W m}^{-1} \text{ K}^{-1}$
R_L	$17.905757435533784 \times 10^{-9} \text{ m}$
p	$2 \times 10^{-6} \text{ m}$
σ_{abs}^{647nm}	$5.488032 \times 10^{-15} \text{ m}^2$
σ_{abs}^{561nm}	$1.5234025 \times 10^{-15} \text{ m}^2$

Table 7.1: Optical and thermal parameters

Wavelength	ΔT_0^S	ΔT_0^{ext}	ΔT
561 nm	0.87 K	0.26 K	< 1.13 K
647 nm	3.12 K	0.95 K	< 4.07 K

Table 7.2: **Estimation of single-particle heating and collective effects.** Calculated at the center position. Maximum irradiance of $100 \times 10^6 \text{ W m}^{-2}$.

The collective temperature increase at the center of the illumination can be estimated as

$$\Delta T_0^{ext} \approx \frac{\sigma_{abs} P}{\bar{\kappa}} \sqrt{\frac{\ln(2)}{4\pi}} \frac{1}{HA} \left(1 - \frac{4\sqrt{\ln(2)A}}{\pi H} \right). \quad (7.2)$$

Where $A = p^2$ and p is the particle interdistance. Using these equations and the parameters in Table 7.1, we estimate the ratio between the single and collective effects to be around 3. For comparison with the single-particle temperature increase calculated with COMSOL (A.9), the estimated single-particle and collective heating at $100 \times 10^6 \text{ W m}^{-2}$ are shown in Table 7.2.

Estimated temperatures Using the results of A.9 and A.9, we estimate the temperature at a certain irradiance I in the following:

$$\Delta T_I = \Delta T_I^S + 0.3 \times \max(\Delta T_{I_{max}}^S) \quad (7.3)$$

I is the irradiance at the NP position, I_{max} is the maximum irradiance of the Gaussian illumination. T_I^S and $\Delta T_{I_{max}}^S$ are calculated using COMSOL. Table 7.3 shows the resulting NP temperatures for 647 nm irradiance. Figure 4 in the main text shows the 2D temperature profiles including collective effects calculated in the same way. While the particles are also illuminated with 561 nm for imaging, the irradiance is too low to induce significant heating.

Wavelength [nm]	561		647		
Irradiance [$\times 10^6 \text{ W m}^{-2}$]	20	40	71	88	105
ΔT [K]	0.2	0.4	3.1	3.6	4.1

Table 7.3: **Estimated temperatures at the irradiances used in the main text.**

A.10 Photostationary state of Rz

To estimate the probability that Rz is in a photoexcited state at a certain photon flux, we use the photophysical properties reported by Bueno *et al.*¹⁷⁵

This probability is known as the photostationary state of the fluorophore and is determined by the absorption rate of photons by the fluorophore and the relaxation rate from the excited state (Rz^*) to the ground state (Rz^0).

To calculate the photostationary state of a fluorophore, one can use the following equation:

$$Rz = Rz^* + Rz^0 \quad (7.4)$$

$$Rz^* = k_{abs} * [F] * Rz^0 - k_{rel} * Rz^* \quad (7.5)$$

$$\Rightarrow P_{excited} = \frac{k_{abs} * [F]}{k_{abs} * [F] + k_{rel}} \quad (7.6)$$

where $P_{excited}$ is the probability of the fluorophore being in the excited state, k_{abs} is the absorption rate constant, $[F]$ is the photon flux, and k_{rel} is the relaxation rate constant.

The absorption rate constant, k_{abs} , is determined using the absorption spectrum of the fluorophore, which specifies the probability that the fluorophore absorbs a photon of a particular wavelength. The absorption rate constant for Rz in water at pH 9.5 at 602 nm is $47000 \text{ M}^{-1} \text{ cm}^{-2} = 4700 \text{ m}^2 \text{ mol}^{-1}$. At 561 nm the absorption is lower (58%) $k_{abs} = 2731 \text{ m}^2 \text{ mol}^{-1}$.

The relaxation rate constant, k_{rel} , is determined by the radiative and non-radiative decay rates of the excited state of the fluorophore back to the ground state. Lifetime measurements of Rz in water at pH 9.5 found a fluorescence lifetime of $\tau = 0.7 \text{ ns}$, corresponding to $k_{rel} = \frac{1}{\tau} = 1.43 \times 10^9 \text{ s}^{-1}$.

The photon flux can be calculated from the irradiance. At an excitation wavelength of 561 nm, an irradiance of $1 \times 10^6 \text{ W m}^{-2}$ corresponds to a photon flux of $[F] = 4.69 \times 10^3 \text{ mol m}^{-2} \text{ s}^{-1}$.

Figure 7.16a shows the probability of Rz being in a photoexcited state at a certain irradiance. This alone does not sufficiently saturate to explain the measured activity in Figure 3c of the main text. However, in proximity to the AuNR, local fields can be significantly higher. Therefore, we have fitted the field enhancement necessary to explain the reaction kinetics purely by the photostationary state of Rz. In Figure 7.16b, the results are shown for three reaction orders. In all cases, the measured catalytic activity against irradiance for field enhancement and different reaction orders. Fitting the data predicts field enhancements of 19, 32, and 46 for a first-, second-, or third-order reaction. However, the enhancement in proximity to the surface is around 10 (Figure 7.13). Additionally, the reaction without hydroxylamine described in A.12 should also saturate, which is not the case. In conclusion, the saturation of the photostationary state is not enough to explain our the saturation of the activity at higher irradiances.

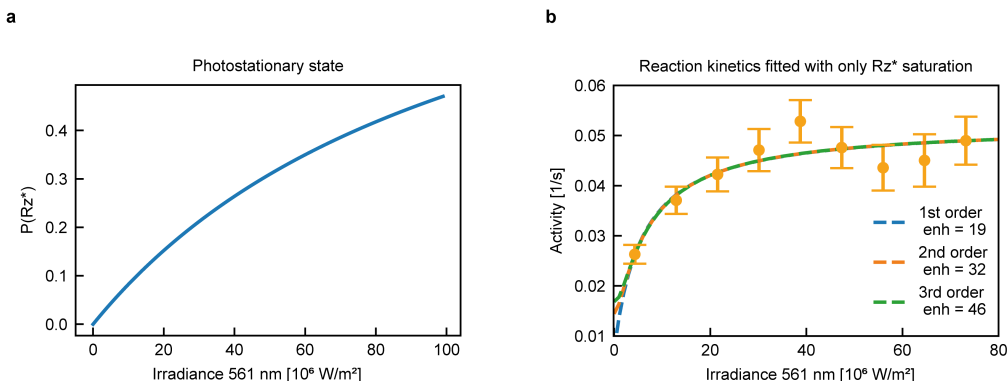


Figure 7.16: Photostationary state of resazurin.

A.11 Excited Resazurin and Langmuir-Hinshelwood

In the previous section, we showed that the saturation of the excited Rz^* concentration at high irradiances alone does not explain the saturation in the reaction kinetics. It has been reported previously, that in dark, the reductive deoxygenation of Rz by hydroxylamine follows a first-order Langmuir-Hinshelwood mechanism. In the main text we also present a fit with first-order Langmuir-Hinshelwood kinetics against irradiance, because it is the simplest model that describes our data. However, 2nd and 3rd order fit equally well.

If we combine equation 7.4 with the equation for Langmuir-Hinshelwood kinetics or order n , we get:

$$\nu = A \frac{B^2 \left(\frac{k_{abs}*[I]}{k_{abs}*[I] + k_{rel}} \right)^n}{\left(1 + B \times \frac{k_{abs}*[I]}{k_{abs}*[I] + k_{rel}} \right)^n} + C \quad (7.7)$$

Where $I = e \times I_0$ and e is the intensity enhancement of 10 near the surface.

As can be seen in Figure 7.17, the difference lies only in the behavior at very low irradiances. This regime is not possible to measure because we rely on the photoexcitation of the product Rf to image.

A.12 The reaction kinetics without hydroxylamine

Without any catalyst the conversion of resazurin to resorufin by light has been reported to be a photodriven disproportionation.^{166,175–177} In a study on bimetallic AuPd catalysts by Chen *et al.* this reaction has been reported to follow a second-order power dependence when uncatalyzed, while in the presence of a Au or Pd catalyst the same reaction had a first-order power dependence.¹⁶⁶ In our system of AuNRs both a linear and a quadratic model fit reasonably well (Figure 7.18) and do not saturate.

A.13 The reaction kinetics are not mass-transport limited

The amount of resazurin available at any given time is much greater than the amount consumed by the reaction. We use 200 nM of resazurin and a flow rate of $15 \mu\text{L min}^{-1}$,

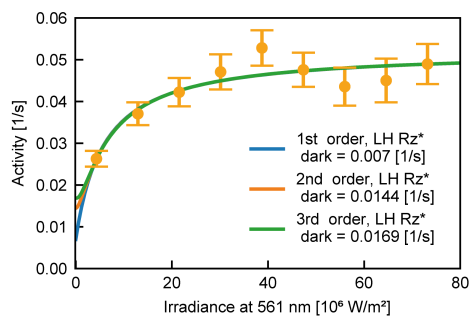


Figure 7.17: **Alternative fittings of different reaction orders.** 1st, 2nd and 3rd order Langmuir-Hinselwood mechanism according to Equation 7.7, taking into account that field enhancement is around 10.

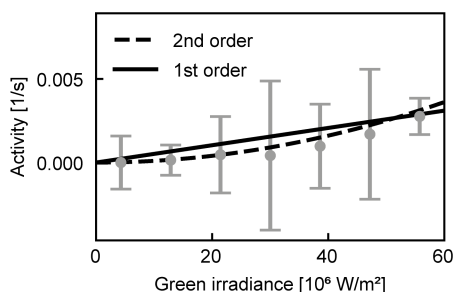


Figure 7.18: **The reaction kinetics without hydroxylamine.** Turnover rates (y) against binned green irradiance (x) without Hydroxylamine. Two measurements on the same NPs combined (10mW & 30mW). All bins contain at least 10 particles.

the dimensions of the channel are approximately 0.4 mm x 17 mm x 3.8 mm. Assuming a uniform flow (neglecting the velocity profile within the channel) and only considering the first 0.5 μm in height as the reaction volume, this would correspond to a supply with resazurin of $6.25 \times 10^{-14} \text{ mol s}^{-1}$. Next, we estimate the number of AuNRs on the surface. The lattice constant of the NP array is 2 μm , with a total channel surface of 0.6 cm^2 , this corresponds to 2.5×10^7 AuNRs within the reaction volume. This is an overestimation because not the entire is patterned. If we now assume an activity of 0.03 s^{-1} , corresponding to the catalytic activity in "dark", this would correspond to a production of resorufin of $1.25 \times 10^{-18} \text{ mol s}^{-1}$, which is 4 orders of magnitude lower than the supply of resazurin.

For the diffusion from the bulk solution through the porous silica shell to the gold surface, a detailed calculation can be found in the supplement of Andoy *et al.*¹⁵⁴

B Supplemental material associated with Chapter 5

B.1 Materials and Methods

Chemicals

Gold (III) chloride trihydrate ($\text{HAuCl}_4 \cdot 3 \text{H}_2\text{O}$, $\geq 99.9\%$), ascorbic acid (AA, $\geq 99.0\%$), sodium borohydride (NaBH_4 , $\geq 98\%$), cetyltrimethylammonium bromide (CTAB, $\geq 99.0\%$), cetyltrimethyl chloride (CTAC, 25wt% in water), tetraethylorthosilicate 98% (TEOS), Polyvinylpyrrolidone (PVP, MW:10.000), ammonium hydroxide solution (NH_4OH , 27 wt% in water) and absolute ethanol (EtOH) were all purchased from Sigma-Aldrich and used without further purification. In all experiments, ultrapure water with a resistivity of 18.2 $\text{M}\Omega \text{ cm}$ was used.

Synthesis of 60 and 67 nm Au NS

Au nanoparticles were prepared using a seed-mediated growth strategy described by Zheng et al.³⁰⁴ with some modifications to scale up the reaction. This protocol involves the synthesis of Au seed particles and the subsequent growth to the desired size.

Step 1 - Au Clusters: The initial Au seeds were formed by reducing 5 mL of an aqueous solution containing 0.25 mM HAuCl_4 and 0.1 M CTAB with 300 μL of a freshly prepared 10 mM NaBH_4 solution (ice-bath). The solution turns brownish within seconds indicating clusters formation. The clusters were kept undisturbed for 3 h at 27 °C.

Step 2 - 10 nm Au NS Synthesis: In a 20 mL glass vial, 4 mL of a 200 mM CTAC solution, and 3 mL of a 100 mM ascorbic acid (AA) solution were mixed, followed by the addition of 100 μL of previously prepared CTAB capped Au seeds. After the solution was stirred at 300 rpm and left at 27 °C for 10 min, 4 mL of 0.5 mM HAuCl_4 were added in a quick one-shot injection. The resulting 10 nm Au spheres were centrifuged twice at 13400 rpm (12045 rcf) for 30 min and finally redispersed in 1 mL of a 20 mM CTAC solution.

Step 3 - 60 nm and 67 nm Au NS Synthesis: 200 mL of a 100 mM CTAC solution were mixed with 1.3 mL of a 100 mM AA solution and 225 μL or 250 μL of 10 nm Au NS solution in order to obtain 67 nm and 60 nm Au NS, respectively. The whole solution was kept stirred at 800 rpm using stirring bars at 27 °C for 20 min. Then, 10 mL of 10 mM HAuCl_4 were pumped at a rate of 20 mL h^{-1} and once pumping was completed, it was left stirring for 30 min. After two centrifugation-redispersion cycles (4000 rpm, 2147 rcf, 10 min) the Au NS were finally redispersed in 35 mL of ultrapure H_2O .

Synthesis of Au@Pd CS-NPs

To grow a 2 nm Pd shell on top of the 60 nm and 67 nm Au cores, we used a method described in the literature (36). Firstly, a solution containing 1.785 mL of a 1 mM CTAC solution, 2.30 mL of a 0.2 M CTAB solution, 400 μL of a 10 mM K_2PdCl_4 and 13.96 mL of ultrapure H_2O were kept at 100 °C for 60 min. Secondly, 1.753 mL of an

aqueous solution containing $\approx 7.5 \times 10^{11}$ Au NS were added at 100 °C, followed by the quick injection of 1 mM AA solution. The solutions immediately turned purple and were left at 100 °C for another 60 min. Finally, two centrifugation-redispersion cycles (1207 rcf, for 10 min) were carried out. Alternatively, to grow a 4 nm Pd shell on 67 nm Au NS, the same procedure was followed, but using 1.753 mL of an aqueous solution containing 6.0×10^{11} Au NS. The Au67@Pd2 and Au67@Pd4 were redispersed in 20 mM CTAC, while Au60@Pd2 was redispersed in ultrapure H₂O.

Synthesis of Au–Pd Core-Satellites NPs

Step 1 - Synthesis of Palladium satellites: PVP-stabilized Pd nanoparticles (Pd NPs) were synthesized according to a method described in the literature with some modifications. (82) Briefly, 45 mL of aqueous solution containing 1.05 mM PVP and 4.25 mM of AA was heated up to 100 °C under reflux for 10 min. Subsequently, 5.0 mL containing 10 mM of Na₂PdCl₄ was added in one shot. The reaction was allowed to continue at 100 °C for 3 h to obtain Pd NPs.

Step 2 - Assembly of Au-Pd Core- Satellite NPs: 4 mL of EtOH were added to 2.77 mL of a 2.72×10^{14} Au NS/L aqueous solution, followed by the addition of 350 μ L of non-washed Pd satellites. After stirring the solution at 400 rpm for 30 min, it was washed in low-binding DNA Eppendorf tubes twice at 604 rcf for 20 min. The method is fully described by Herran et al.²⁹⁶

Inductively coupled plasma – atomic emission spectroscopy

ICP-AES (Agilent 5800) was used to quantify the material composition of the bimetallic nanoparticles. The sample preparation consisted of dissolving 300 μ L of each colloidal solution with 500 μ L of fresh reversed aqua regia (HNO₃:HCl 3:1), followed by a dilution to 4 mL using HCl 2% wt. Details can be found in section S15 of the SM. The components of the sample, Au and Pd, were identified based on their characteristic emissions ($\lambda_{\text{Au}} = 242$ nm, $\lambda_{\text{Pd}} = 340$ nm). First, a calibration curve between concentration and emission intensity was obtained by preparing 5, 10, 30, and 50 ppm (mg L⁻¹) Au and Pd solutions from a 1000 ppm original solution purchased from Sigma-Aldrich. The calibration is shown in the Figure S25. Then, the amount of material present in the investigated in the Au and AuPd NPs was determined from the intensity of emitted light.

Optical Printing

NPs were optically printed onto glass substrates according to the process described in previous works.^{91,328} Briefly, the NP suspension is placed on top of a positive substrate functionalized with Poly-(diallyl-dimethylammoniumchlorid) PDPA (Sigma-Aldrich, MW $\sim 400.000 - 500.000$). The process is carried out in an open chamber, employing a 532 nm laser (Ventus, Laser Quantum) and a 60x water-immersion (Olympus) objective with a NA=1. The printing irradiance was adjusted for each system to optimize the printing time and avoid morphological changes during the optical printing process. Typically, 8 mW/ μm^2 was used to print 60 nm and 67 nm Au NP. For the

Au67@Pd CS-NPs, the irradiance was set to $6 \text{ mW}/\mu\text{m}^2$ and for the Au60@Pd it was $5.4 \text{ mW}/\mu\text{m}^2$.

Dark field microscopy and spectroscopy

Dark field images and single NP spectra were acquired by employing a high-intensity visible-NIR light source (Thorlabs, OSL2IR) which was scattered by the sample and focused on 60x water-immersion (Olympus) through a dark field condenser. A digital color camera (Canon EOS-500D) was used to obtain dark field images of the NPs supported on the glass substrate. Unpolarized scattering spectra of each NP were measured with a Shamrock 500i spectrometer (Andor) and an EMCCD camera (Andor Ixon EM + 885), in a spectral range between 450 and 850 nm (1 nm resolution).

Hyperspectral Confocal PL images

For confocal hyperspectral PL imaging, a continuous wave 532 nm laser was focused near its diffraction limit with a mean beam waist of 311 nm. Scanning was achieved with a closed-loop piezoelectric stage (PI). Each confocal image was obtained with 10×10 pixels on a range of $0.8 \times 0.8 \mu\text{m}^2$, with a high electron multiplying gain (usually 150) and an integration time of 2.5 s each pixel. The PL spectra were measured from 500 nm to 600 nm range, employing two 532 nm notch filters to filter the laser line. Hyperspectral confocal images of 67 nm NS, Au67@Pd2 CS-NPs and Au67@Pd4 CS-NPs were acquired using a maximum irradiance of 2.1, 2.8, and 2.7 $\text{mW}/\mu\text{m}^2$ respectively. For 60 nm Au NS, 60nm core-satellites AuNP@Pd, and Au60@Pd2 CS-NPs, the irradiances were 2.0, 2.4, and 4.9 $\text{mW}/\mu\text{m}^2$, respectively.

AS Hyperspectral thermometry

The method was applied as described in Barella et al.¹³² The hyperspectral confocal image provides 10×10 PL spectra that are grouped and subsequently averaged considering similar irradiance values. The sorting criterion is the excitation irradiance I_i^{exc} . Figure S9A shows the hyperspectral image for an Au60@Pd2 CS-NPs after being binned into 10 irradiance values. Figure S9B shows the PL average spectra of each bin. Then, all possible ratios between binned PL spectra are calculated. Figure S9C shows calculated ratios between Stokes PL spectra, named $Q_{i,j}^S$. Since PL Stokes emission is linear with excitation irradiance, $Q_{i,j}^S = \frac{I_i^{\text{exc}}}{I_j^{\text{exc}}}$. Figure 7.19e shows a few calculated ratios between AS PL emission spectra, named $Q_{i,j}^{\text{AS}}$. These ratios are fitted with the expression Eq. 7.8 to extract the photothermal coefficient $\beta_{i,j}$. Finally, all obtained photothermal coefficients $\beta_{i,j}$ are averaged to obtain a single β for the scanned NP.

$$Q_{i,j}^{\text{AS}}(\lambda) = \frac{I_i^{\text{exc}} \exp\left(\frac{E(\lambda) - E(\lambda_{\text{exc}})}{k_{\text{B}}[T_0 + \beta_{i,j} I_j^{\text{exc}}]}\right) - 1}{I_j^{\text{exc}} \exp\left(\frac{E(\lambda) - E(\lambda_{\text{exc}})}{k_{\text{B}}[T_0 + \beta_{i,j} I_i^{\text{exc}}]}\right) - 1}, \quad (7.8)$$

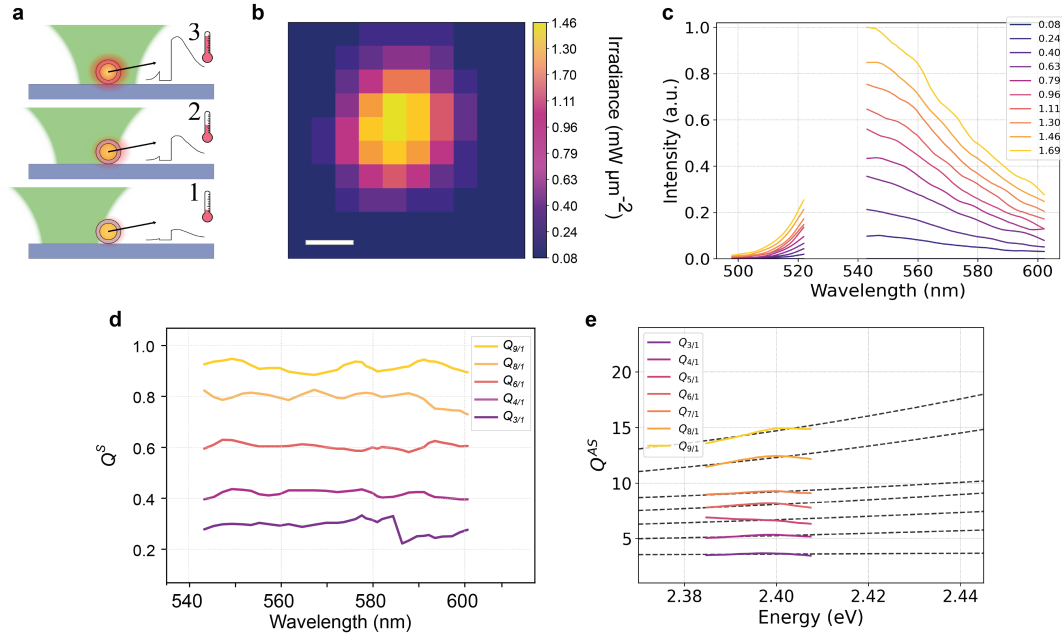


Figure 7.19: **AS Hyperspectral thermometry.** (a) Illustration of the method for hyperspectral AS thermometry. (b) Hyperspectral PL emission image, binned according to the excitation irradiance. (c) Average PL emission spectra of each bin. The estimated excitation irradiance is indicated in the label. (d) Example of ratios between PL Stokes spectra used to calculate $Q_{i,j}^S$. (e) Ratio between PL AS Stokes spectra. Experimental data are the colored solid lines, while dashed black lines indicate the fits with $Q_{i,j}^{AS}(\lambda)$. Adapted with permission from Ref. ¹⁸⁴

Optical simulations

Optical properties of the core-shell bimetallic nanoparticles were investigated using FDTD simulations (ANSYS Lumerical Software ULC, Release 2022 R1, Version 8.27.2898). The dimensions of the spherical Au (Johnson & Christy) cores were chosen as measured from the TEM images (diameters of 60 and 67 nm). The Pd shell was simulated at different thicknesses ranging from 1 nm to 6 nm by a Pd (Palik) with a lower mesh order than the Au. To simulate an aqueous medium the surrounding medium was set to a refractive index of 1.333. The substrate, when included, was simulated as a rectangular prism consisting of Glass (Palik). To calculate absorption and scattering cross-sections a TFSF source was used. The injection was simulated along the z-axis. The absorption cross-section is calculated using an analysis group inside the TFSF source. The analysis group consists of six 2D monitors that form a closed box and measure the net power flowing in/out of the box. Similarly, the scattering cross-section is calculated by an analysis group outside the TFSF source. Since this simulation has a plane of symmetry in x and in y dimension, the simulation time was reduced by setting the x min boundary condition to anti-symmetric and the y min boundary condition to symmetric. A mesh override region with $d = 0.5$ nm until 30 nm around the nanoparticle in all dimensions was used.

Temperature Simulations using COMSOL Multiphysics

Medium. Geometry: Cube with dimensions 1000 nm x 1000 nm x 1000 nm. Material: Water, $k = 0.6 \text{ W}/(\text{m}^*\text{K})$.

Particle. Geometry: Sphere with radius $r = 33.5 \text{ nm}$. Material: Gold, $k = 318 \text{ W}/(\text{m}^*\text{K})$.

Physics. Heat transfer in solids with the nanoparticle as a user-defined heat source (shown in yellow) with $Q = (\sigma_{abs} \times I)/V$, where the absorption cross-section is $\sigma_{abs} = 1.4469 \times 10^{-14} \text{ m}^2$ (as calculated using Lumerical), $I = 1 \text{ mW}/\mu\text{m}^2$ and the volume for the Au 67 NP $V = 157479 \text{ nm}^3$. The simulation boundaries (in this case the outer surfaces of the cube of water, shown in blue) and the initial temperatures are set to $T_0 = 293 \text{ K}$.

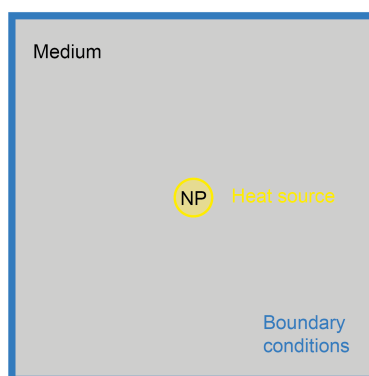


Figure 7.20: **2D view of the 3D simulation in COMSOL Multiphysics.** The boundary conditions are applied to the blue boundaries, the NP acts as the heat source. Adapted with permission from Ref.¹⁸⁴

B.2 Further characterizations of the chemical structure

Characterization of the Pd shells of Au@Pd CS-NPs

The thicknesses of the Pd shells were calculated in two ways. 1) From Transmission Electron Microscopy (TEM) images and 2) Using Inductive Coupled Plasma Atomic Emission Spectroscopy (ICP-AES).

1. The area A of each NP was measured, and a characteristic diameter was calculated as $d = 2\sqrt{\frac{A}{\pi}}$. At least 100 NPs were measured for each colloid, and the median \bar{d} and standard deviation σ_d of the distributions were calculated. The standard deviations were in the range between 1 nm and 2 nm for all the colloids studied in the manuscript. The standard errors of the means were calculated as $\sigma_{\bar{d}} = \frac{\sigma_d}{\sqrt{N}}$ with N the sample size.

For Core Shells, the thickness t of the Pd shell was estimated as $t = \bar{d}_{CS} - \bar{d}_C$, where \bar{d}_{CS} and \bar{d}_C are the median diameters of the Core Shell and Au Cores respectively. The error in the thickness t is the addition of the absolute standard errors of the median diameters.

TEM images and size distributions for Au67 NS, Au67@Pd2 and Au67@Pd4 are shown in Figure 5.17 of the main manuscript. Figure 7.21 shows TEM images and size distributions for Au60 NS, and Au60@Pd2.

- Additional characterization of the Core Shell NPs was performed using (ICP-AES). This technique allows the quantification of the ratio between the Au and Pd mass (see section S15 for details). Using this information, knowing the size of the Au cores, and assuming a perfectly spherical geometry for the cores and the CS, the thickness of the Pd shell can be estimated as

$$t = \sqrt[3]{\frac{3}{4\pi}(V_C + V_S)} - r_C = r_C \left(\sqrt{1 + \frac{\rho_C M_S}{\rho_S M_C}} - 1 \right)$$

With $V_C = 4/3\pi r_c^3$, $V_S = V_C \rho_C / \rho_S M_S / M_C$, where V is the volume, r is the radius, M is the mass and ρ is the density. Subscripts C and S refer to the core and the shell, respectively. The ratios M_S / M_C are measured using (ICP-AES).

The obtained results using both methods are summarized in Table 7.4.

Core Size (TEM)	Pd/Au	M_S / M_C	Pd Thickness (ICP-AES)
Au67@Pd2	(66.6 ± 0.2) nm	(0.105 ± 0.005)	(1.8 ± 0.4) nm (2.4 ± 0.3) nm
Au67@Pd4	(66.6 ± 0.2) nm	(0.21 ± 0.01)	(3.4 ± 0.4) nm (3.6 ± 0.3) nm
Au60@Pd2	(59.7 ± 0.2) nm	(0.073 ± 0.004)	(1.1 ± 0.4) nm (1.8 ± 0.3) nm

Table 7.4: Summary of size characterization of CS-NP.

Characterization of Au60-Pd-sat NPs

The Au60-Pd-sat system is produced by solvent-induced electrostatic self-assembly between Au60 NS and Pd satellites. Figure 7.22 shows a size characterization of the Pd satellites, performed by Transmission Electron Microscopy (TEM).

Figure 7.23 shows a Scanning Transmission Electron Microscopy (STEM) in High Angle Annular Darkfield (HAADF) mode of a Au60-Pd-sat NP. The spatial distribution of the two metals measured by Energy Dispersive X-Ray Spectroscopy (EDX). The Au is mostly confined to the core, while Pd is only seen at the satellites.

The number of satellites was estimated in two ways: 1) Using TEM images and 2) Using ICP-AES.

- Figure 7.24a shows the histogram of the number of visible satellites N_{visible} per Au core, estimated by counting satellites on the TEM images. The mean value is $(\bar{N}_{\text{visible}}) = (27 \pm 1)$ with a standard deviation of $\sigma = 6$.

However, TEM images are 2D, so some satellites will not be visible. Only satellites close to the equator of the Au core will be visible. On the contrary, if

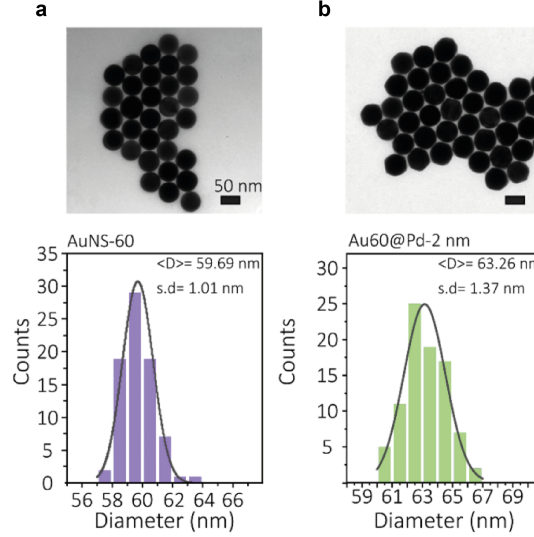


Figure 7.21: **Size Characterization of Core-shell nanoparticles.** Top: TEM image. Bottom: corresponding size distribution. (a) Au NS-60. (b) Au60@Pd. Adapted with permission from Ref. ¹⁸⁴

the position of the satellite is below or above the Au core, it will be masked by the Au core.

Figure 7.24b illustrates this situation. It is considered that satellites in positions marked with a #1 will be visible, #2 will be partially visible and #3 and #4 will not be visible. The blue-shaded angle correspond to the solid angle of the sphere where satellites are visible or partially visible. This angle can be estimated as $\cos \alpha_T = r_C / (r_C + D_S)$, where r_C is the radius of the core and D_S is the diameter of the satellite.

The fraction F of the surface area that is visible can then be calculated as a surface integral:

$$F = \frac{\int_0^{2\pi} \int_{\frac{\pi}{2}-\alpha_T}^{\frac{\pi}{2}+\alpha_T} r^2 \sin \theta, d\theta, d\phi}{4\pi r^2} = \frac{1}{2} \int_{\frac{\pi}{2}-\alpha_T}^{\frac{\pi}{2}+\alpha_T} \sin \theta, d\theta = \sin \alpha_T$$

Using $r_C = (29.9 \pm 0.2)$ nm and $D_S = (6.3 \pm 0.2)$ nm, $\alpha_T \approx 34.3^\circ$ this yields $F = (0.56 \pm 0.03)$.

This means that around 56% of the satellites will be visible in the 2D TEM images. The average number of satellites N_s can be calculated as $N_s = N_{\text{visible}} / F = (48 \pm 4)$.

- As described in section B.1, ICP-AES was used to determine the mass ratio between Pd and Au $M_{\text{Pd}} / M_{\text{Au}} = (0.036 \pm 0.002)$, where M_{Pd} is the added mass of all the Pd satellites and M_{Au} is the mass of the Au core. See section S15 for details on the ICP-AES characterization. The total volume of palladium per NP is $N_s V_{\text{sat}} = V_C \rho_{\text{Au}} / \rho_{\text{Pd}} M_{\text{Pd}} / M_{\text{Au}}$, with V_C the volume of a Au core, V_{sat} the volume of a Pd satellite and N_s the number of satellites.

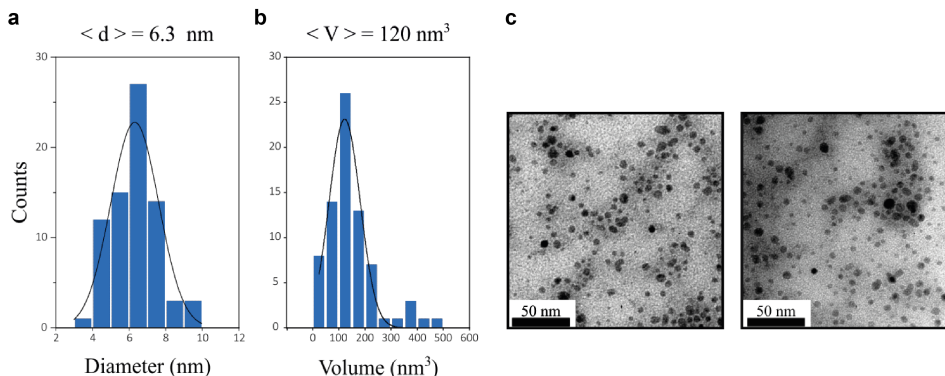


Figure 7.22: **Size characterization of Pd satellites.** (a) Histogram of the diameter of Pd Satellites. The mean diameter is $d = 6.3 \text{ nm}$ with a standard deviation of $\sigma_d = 1.3 \text{ nm}$. (b) Histogram of the diameter of Pd Satellites. The mean volume of a single Pd satellite was estimated to be $V = 120 \text{ nm}^3$ with a standard deviation of $\sigma_V = 100 \text{ nm}^3$. (c) TEM images of the Pd satellites.. Adapted with permission from Ref.¹⁸⁴

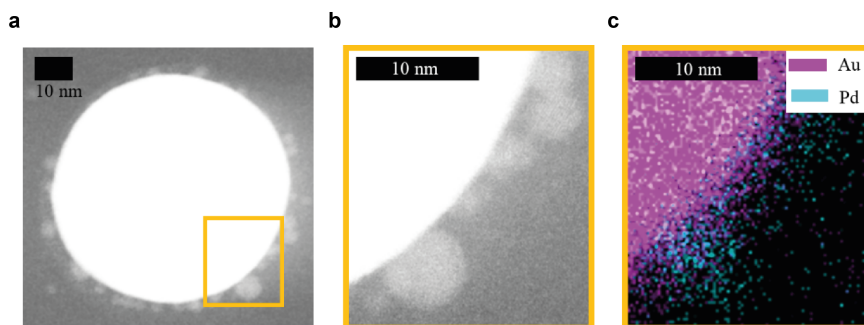


Figure 7.23: **EDX analysis of Au₆₀-Pd satellites.** (a) STEM-HAADF image of a Au₆₀-Pd-sat NP. (b) Zoom in of the region marked in (a) with an orange square. (c) Spatial distribution of Au and Pd in the same region is determined by EDX. Au (magenta) is mostly confined to the core, while Pd (cyan) is only seen at the satellites. Adapted with permission from Ref.¹⁸⁴

Assuming spherical shape of Au core with a diameter of $(59.7 \pm 0.2) \text{ nm}$ and $V_{\text{sat}} = (120 \pm 10) \text{ nm}^3$, $N_s = (54 \pm 7)$.

Both methods provide similar values for the number of satellites. The average value is $\langle N_s \rangle = (51 \pm 6)$.

The Au₆₀-Pd-sat system is produced by solvent-induced electrostatic self-assembly between a positive CTAC capped Au NP and negative Polyvinylpyrrolidone (PVP) capped Pd satellites. Therefore, the gap between both surfaces is expected to be in the order of magnitude of the size of the capping molecules. To confirm this, we have performed STEM-HAADF, as shown in Figure 7.25. Due to the 3D geometry of the system, the satellites that are above or below the equatorial plane of the Au sphere appear like they are penetrating the Au core. For this reason, the gap was measured in the satellites that look further from the Au surface. The distance between surfaces is approximately 1 nm, which can be considered to be an upper bound. On the other hand, the fact that we observed a gap for the NPs in the equatorial plane suggest that such a gap exists in most cases, and that the contact surface between materials is negligible.

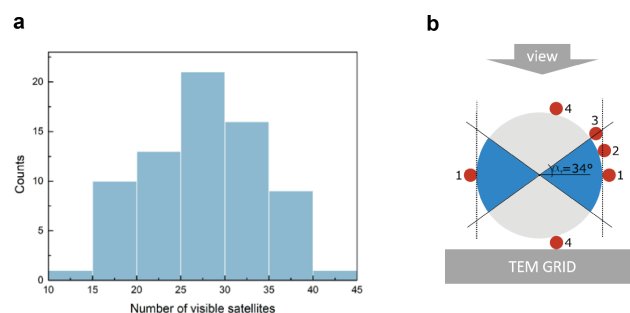


Figure 7.24: **Number of satellites using TEM images.** (a) Histogram of the number of visible satellites N_{visible} . The mean value is $\bar{N}_{\text{visible}} = (27 \pm 1)$ with a standard deviation of $\sigma = 6$. (b) Illustration of the TEM imaging. The large sphere represents the Au core, and the small red spheres represent the Pd satellites. The satellites that are between the two vertical dashed lines are not visible in the TEM images. The blue shaded area corresponds to the solid angle of the sphere that has visible satellites. Adapted with permission from Ref.¹⁸⁴

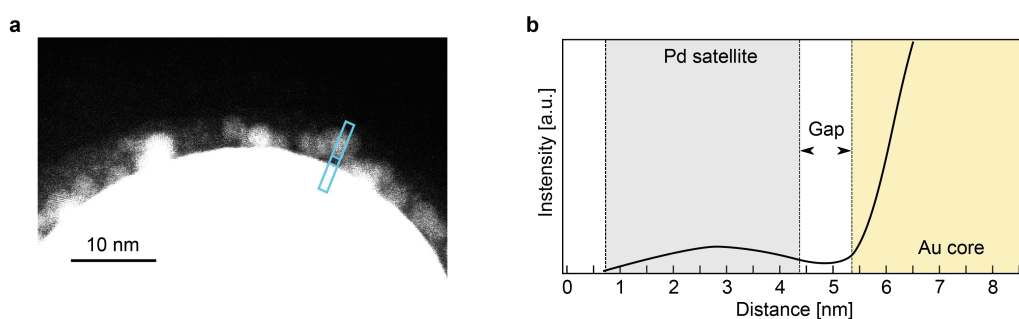


Figure 7.25: **Determination of gap sizes.**(a) Scanning Transmission Electron Microscopy of a Au₆₀-Pd satellites NP. The two profiles drawn in the figure are plot in (b). Adapted with permission from Ref.¹⁸⁴

Stability of the printed nanoparticles

In order to test the stability of the NPs under the high irradiances used for printing, a set of NPs was illuminated at $I = I_{\text{Printing}}$ and $I = 2I_{\text{Printing}}$ for 2 minutes. It must be noted that 2 minutes is much longer than the printing time that is typically some milliseconds.³²⁸ In addition, irradiances used for photothermal characterizations were always lower than the printing one.

The scattering spectrum of each NP before and after irradiation was compared. Figure 7.26a shows a dark field image of 10 Au₆₀@2Pd CS-NPs before and after 2 minutes at $I = I_{\text{Printing}}$. The average scattering spectra is mostly unchanged, as shown in the upper figure of 7.26B, indicating that the CS-NPs are stable under this irradiance.

Then, another set of 10 CS-NPs was irradiated at twice the printing irradiance. In this case, the scattering spectra significantly changes, as evident both from the dark field images shown at Figure 7.26c and the average spectra shown in the lower Figure of 7.26b.

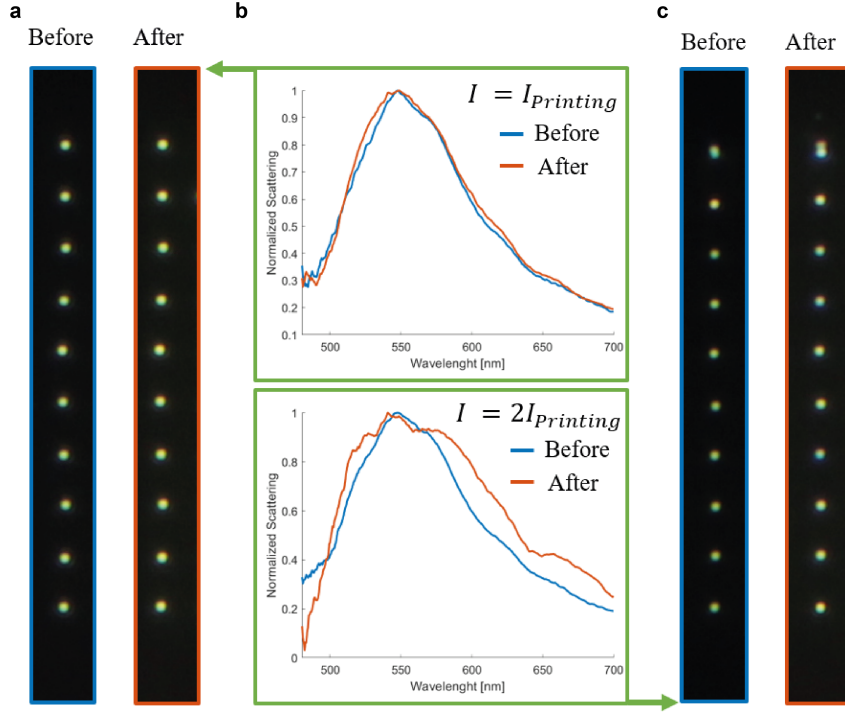


Figure 7.26: **Stability Test.**A) Dark-field image of 10 Au60@2Pd before and after irradiation at the printing irradiance for 2 minutes. B) Average scattering spectra before and after irradiation. C) Dark-field image of 10 Au60@2Pd before and after irradiation at the twice the printing irradiance for 2 minutes. Adapted with permission from Ref.¹⁸⁴

B.3 More detailed derivation of the temperature model

Heat diffusion for a spherical core-shell nanoparticle

The temperature field $T(r)$ of core@shell NPs can be calculated using the heat diffusion equation: $-\kappa \frac{1}{r^2} \partial r (r^2 \partial r T) = q$. Therefore, for a system in which core is material 1, shell is material 2 and the surrounding medium is material 3, the solutions with radial symmetry in the steady states reads:

$$r < b : T(r) = -\frac{-q_1}{6\kappa_1} r^2 + \frac{c_0}{r} + c_1 \quad (7.9a)$$

$$b < r < a : T(r) = -\frac{-q_2}{6\kappa_2} r^2 + \frac{c_2}{r} + c_3 \quad (7.9b)$$

$$r > a : T(r) = -\frac{c_4}{r} + c_5 \quad (7.9c)$$

$$(7.9d)$$

where c_0 to c_5 are integration constants. $c_5 = T(\infty) = T_0$ with T_0 equal to room temperature. Non-divergence at $T(0)$ leads to $c_0 = 0$. The four other constants can be obtained from the following boundary conditions.

1. Energy conservation demands that the integrated heat flux J crossing interface 2-3 should be equal to the absorbed heat Q by the NP.

$$4\pi a^2 |J(a^+)| = Q \quad (7.10)$$

Using $J(r) = \kappa \nabla T(r)$ leads to

$$c_4 = \frac{Q}{4\pi \kappa_3} \quad (7.11)$$

2. Heat flux conservation at the interface 2-3

$$|J(a^-)| = |J(a^+)| \quad (7.12)$$

Leads to

$$c_2 = \frac{\kappa_3}{\kappa_2} c_4 - \frac{q_2 a^3}{3\kappa_2} \quad (7.13)$$

3. Temperature boundary condition at the interface 2-3

$$T(a^-) - T(a^+) = |J(a^+)| R_{2-3}^{th} \quad (7.14)$$

R_{2-3}^{th} is the Kapitza interfacial thermal resistance between materials 2 and 3. This leads to

$$c_3 = \frac{\kappa_3 R_{2-3}^{th} c_4}{a^2} + \frac{c_4}{a} + \frac{q_2 a^2}{6\kappa_2} - \frac{c_2}{a} + T_0 \quad (7.15)$$

4. Temperature boundary condition at the interface 1-2

$$T(b^-) - T(b^+) = |J(b)| R_{1-2}^{th} \quad (7.16)$$

Using $4\pi b^2 J(b) = \frac{4}{3} \pi b^3 q_1$, leads to

$$c_1 = \frac{1}{3} q_1 b R_{1-2}^{th} + c_3 + \frac{c_2}{b} + \frac{q_1 b^2}{6\kappa_1} - \frac{q_2 b^2}{6\kappa_2} \quad (7.17)$$

Temperature drop within the nanoparticle

The temperature drop within the Au volume is

$$\nabla T_{Au} = T(b) - T(0) = -\frac{q_1}{6\kappa_1} b^2 \quad (7.18)$$

The temperature drop at the Au/Pd interface is

$$\nabla T_{(Au-Pd)} = T(b^-) - T(b^+) = \frac{1}{3} q_1 b R_{(Au-Pd)th}. \quad (7.19)$$

The temperature drop in Pd is

$$\nabla T_{Pd} = T(a) - T(b) = -\frac{q_2}{6\kappa_1} (b^2 - a^2) + c_2 \left(\frac{1}{b} - \frac{1}{a} \right). \quad (7.20)$$

For Figure 5.17b, the following parameters were used: $\kappa_1 = 318$ W/mK, $\kappa_2 = 71$ W/mK, $\kappa_3 = 0.6$ W/mK, $R_{2-3}^{th} = 3 \times 10^{-9} (\text{m}^2\text{K})/\text{W}$, $R_{1-2}^{th} = 0.03 \times 10^{-9} (\text{m}^2\text{K})/\text{W}$, $\sigma_{abs} = 1.49 \times 10^{-14} \text{m}^2$, $b = 33.5 \text{nm}$, $a = 35.5 \text{nm}$, $I_{exc} = 1 \text{mW}/\mu\text{m}^2$, $Q = \sigma_{abs} I_{exc}$, $q_1 = 0.7Q/(4/3\pi b^3)$, and $q_2 = 0.3Q/(4/3\pi(a^3 - b^3))$.

Particle on a substrate

The problem of thermal conduction close to a substrate is equivalent to solving the electrostatic problem of charge sources in front of an infinite planar conductor because both are governed by the Laplace equation. In analogy with the image method of electrostatics, the effect of the substrate can be calculated by considering a virtual charge image on the substrate side. For a spherical NP located at the position $(0, 0, R^0)$ with total absorbed heat Q , the virtual image is a point source $-Q$ located at $(0, 0, -R^0)$.

The temperature T at a position R outside the NP and the upper medium is the sum of the real and virtual heat sources:

$$T(R) = \frac{Q}{4\pi\kappa_3} \left(\frac{1}{|R|} - \frac{\kappa_4 - \kappa_3}{\kappa_4 + \kappa_3} \frac{1}{|R'|} \right), \quad (7.21)$$

where $|R|$ and $|R'|$ are the distances to the real and virtual sources, respectively.

The average surface temperature $\langle T^S \rangle$ on a spherical NP of radius a is given by the surface integral:

$$\langle T^S \rangle = \frac{1}{4\pi a^2} \iint_{\theta, \phi} T(a, \theta, \phi) \sin \theta d\theta d\phi, \quad (7.22)$$

where θ is the polar angle and ϕ is the azimuthal angle. The problem has symmetry in ϕ , so we have:

$$\langle T^S \rangle = \frac{1}{2} \int_0^\pi \frac{Q}{4\pi\kappa_3} \left(\frac{1}{a} - \frac{\kappa_4 - \kappa_3}{\kappa_4 + \kappa_3} \frac{1}{|R'(\theta)|} \right) \sin \theta, d\theta, \quad (7.23)$$

where $|R'(\theta)| = \sqrt{|2R^0|^2 + |a|^2 - 2a|2R^0| \cos(\pi - \theta)}$.

If the NP is in contact with the substrate, $|R^0| = a$. We then have:

$$\langle T^S \rangle = \frac{1}{2} \frac{Q}{4\pi\kappa_3} \int_0^\pi \left(\frac{1}{a} - \frac{\kappa_4 - \kappa_3}{\kappa_4 + \kappa_3} \frac{1}{\sqrt{5a^2 + 4a^2 \cos(\theta)}} \right) \sin \theta d\theta \quad (7.24)$$

which simplifies to:

$$\langle T^S \rangle = \frac{Q}{4\pi a \kappa_3} \left(1 - \frac{1}{2} \frac{\kappa_4 - \kappa_3}{\kappa_4 + \kappa_3} \right) = f \frac{Q}{4\pi a \kappa_3} \quad (7.25)$$

where $f = 1 - \frac{1}{2} \left(\frac{\kappa_4 - \kappa_3}{\kappa_4 + \kappa_3} \right)$

For a NP immersed in water on a glass substrate, the value of f is 0.875. Remarkably, a temperature simulation using COMSOL Multiphysics (see the main text for details) gives the value of $f = 0.878$ for a spherical NP in a water environment and touching a glass substrate on a single contact point.

C Supplemental material associated with Chapter 6

C.1 Materials and methods

Fabrication

The samples were fabricated with a standard topdown fabrication method. The masks were written with electron beam lithography on 120 nm 950K PMMA with 30 kV acceleration voltage. Subsequently, the mask was developed in isopropanol-MIBK developer and deposited with 40 nm gold with electron beam evaporation.

Optical characterization

Dark-field images, scattering spectra, and transmission spectra were taken using a WITec microscope (Germany). Transmission spectra were acquired with a 20x water immersion objective (Zeiss) by illuminating the sample from the bottom with a collimated beam. The transmission spectra were normalized by the lamp spectrum. Single-particle dark-field scattering spectra were acquired using a transmission configuration employing a condenser and 63x water immersion objective (Zeiss). The dark-field scattering spectra were normalized by subtracting the background and then dividing by the background.

Anti-Stokes photothermal measurements

Data was acquired with a 60x water immersion objective (Olympus) on a Nikon Ti-Eclipse inverted microscope, equivalent to a 67x magnification. A 647 nm CW laser (OBIS) was focused on the backfocal plane of the objective to achieve wide-field illumination. With fluorescent beads we determined the beam size to be around 18 μm (FWHM). Power calibration was performed using a powermeter slide (Thorlabs) and the maximum irradiance was calculated for the center of the beam. The collection fiber has a core size of 400 μm (TP02815630). The signal was filtered transmitted to a spectrometer (Princeton instruments, SP-2-500i) with a 50 g/mm grating and Pixis 100B camera. The integration time was 30s. The background was acquired in the same way, in a position without array. We tried to account for a bleaching of the background by keeping the ratio between data and background spectrum in the region from 770 nm to 800 nm constant, using the lowest power as a reference. This decision was guided by the raw data for D070 and D100, because the raw intensity in this region is identical to the background spectrum. Here, scaling the background to a constant ratio is the same as scaling the background in this region to be equal to the raw spectrum. Due to the redshifted photoluminescence spectrum of D150 the signal from 770 nm to 800 nm is dominated by the antenna itself and the scaling does hardly effect the background correction.

QLSI photothermal measurements

The setup described above was modified slightly to allow a quasi-simultaneous measurement using QLSI thermometry. A Köhler illumination was added in transmission and the signal was instead sent to a CCD with a modified hartmann grating (Phasics), again first filtered by a rejection filter 647 nm. More details on the data analysis will be added to the to be submitted manuscript by our collaborator.

Numerical calculations

The optical properties of the nanodisks were investigated using FDTD simulations (ANSYS Lumerical Software ULC, Release 2022 R1, Version 8.27.2898). The gold disks (Johnson & Christy) were 70 nm, 100 nm and 150 nm in diameter, and the height was 40 nm for all. To simulate an aqueous medium the surrounding medium was set to a refractive index of 1.333. The substrate was simulated as a rectangular prism consisting of Glass (Palik). To calculate absorption and scattering cross-sections a TFSF source was used. The injection was simulated along the z-axis. The absorption cross-section is calculated using an analysis group inside the TFSF source. The analysis group consists of six 2D monitors that form a closed box and measure the net power flowing in/out of the box. Similarly, the scattering cross-section is calculated by an analysis group outside the TFSF source. Since this simulation has a plane of symmetry in x and in y dimension, the simulation time was reduced by setting the x min boundary condition to anti-symmetric and the y min boundary condition to symmetric. A mesh override region with $d = 1$ nm in a region of 250 nm from the center was used in all dimensions. The resulting spectra are shown in Figure 6.6 in the main text.

C.2 Annealing

To investigate the photothermal properties of the arrays, we annealed them at maximum power for 2 min. We observed a change in transmission on the QLSI images. To investigate this further, we acquired transmission spectra on illuminated and non-illuminated arrays. As can be seen in Figure 7.27, there is significant blue-shift, suggesting that the disks in the arrays may have rounded during annealing (in the main text the transmission after annealing is shown, as these were the conditions under which we measured the photothermal properties).

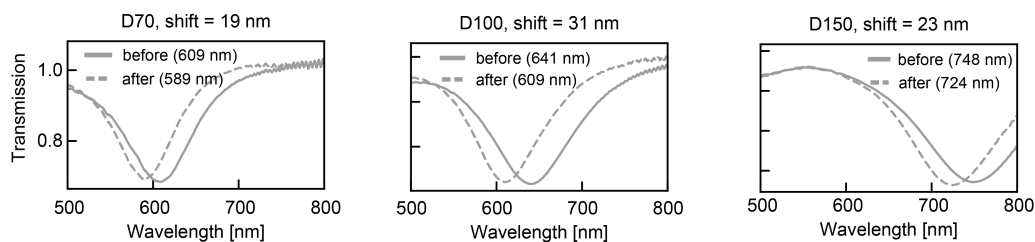


Figure 7.27: **Changing transmission spectra.** The transmission spectra for all three sizes show a blue-shift in the transmission after annealing.

To confirm this hypothesis, we simulated dome-shaped nanoparticles with the same height and diameter as the disks (Figure 7.28a). The normalized simulated scattering cross sections shown in Figure 7.28b present a larger blue-shift (40-70 nm) than the measured blue-shift in the transmission spectra (20-30 nm), but both shifts were consistent with a rounding of the disks. We also compared the simulated scattering spectra to single-particle dark-field scattering spectra for the D100 sample. We designed the EBL samples to have a few single disks under each of the densely packed arrays. The not-annealed single-disks spectrum was very similar to the simulated spectrum. Upon annealing the single disks with a focused 633 nm laser with 10 to 20 mW, we witnessed a quick blue shift that did not change upon further illumination (Figure ??c). This blue shift was again on the order of 30 nm, similar to the shift in the transmission of the arrays. In summary, our results suggest that annealing causes the disks in the arrays to round, leading to a blue-shift in the transmission spectra. However, the exact geometry and dimensions of the disks are not known, so further investigation would be necessary to adequately model the disks.

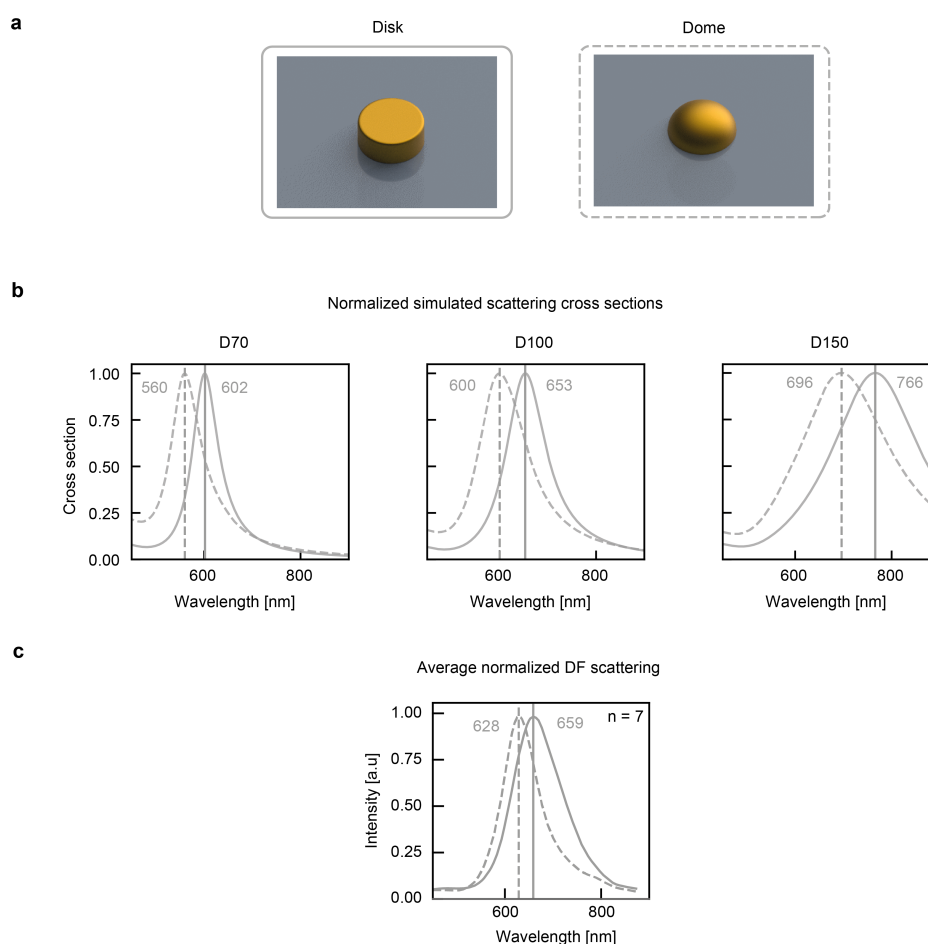


Figure 7.28: **Optical simulations of disks and domes.** (a) Illustration of the disk vs. dome geometry. (b) Normalized simulated scattering cross sections of both geometries. (c) Average dark-field spectrum of 7 single disks before and after annealing.

C.3 Influence of choice of distribution

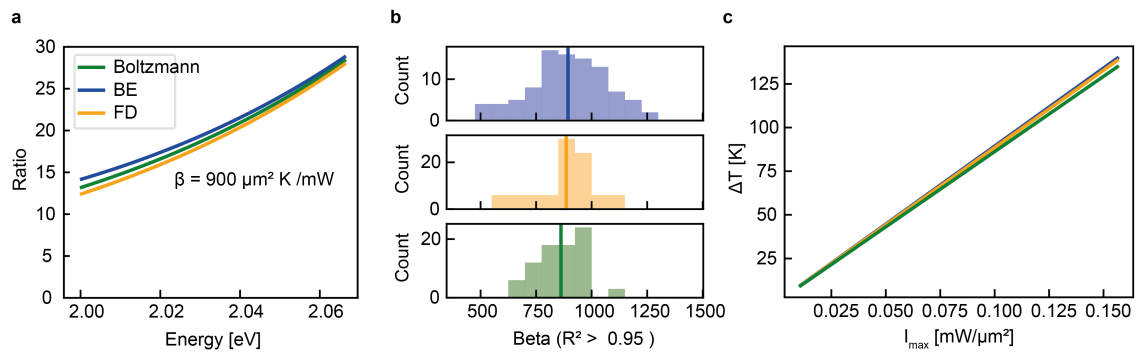


Figure 7.29: **Influence of the distribution.** (a) Simulated anti-Stokes ratios under the same conditions with only a change in the choice of distribution (Boltzmann, Bose-Einstein and Fermi-Dirac) (b) Fitted photothermal coefficient to the same three D100 arrays using the different distributions. (c) Temperature increase against irradiances from the median photothermal coefficient from (b), showing that the choice of distribution has a very minor effect.

D Supplemental material associated with Chapter 7

D.1 Single-molecule catalysis on EBL structures

This work was done in collaboration with Lin Nan, Dr. Ana Sousa-Castillo and Dr. Julian Gargiulo. I also want to acknowledge Iania Voili for useful discussions on porous films and Namvar Jahanmehr for hours spent with me at the SEM each time we were trying to see if we finally had porous structures.

In the work presented in Chapter 4, we used colloidal gold nanorods with a mesoporous silica shell that we arranged into arrays using capillary forces. To easier disentangle the effect of the excitation of different resonances, and to easier map distinct catalytic hotspots, it would be beneficial not only to use ordered arrays but also to orient the nanoantennae on the substrate. It is standard practice in the field of single-molecule localization-based photocatalysis to coat the particles with a porous silica shell to facilitate the detection of fluorescent products. When lithographically made nanoantenna arrays are employed, one has to find a different way to achieve this. We have tried numerous protocols to create porous silica films on top of these samples, from spin-coating, dip coating, sputtering, to solution growth approaches. The following is our optimized protocol and characterizations.

Porous film on top of EBL structure

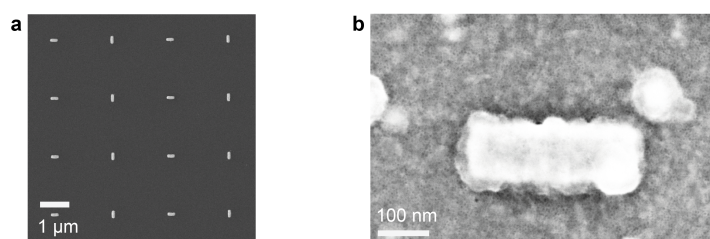


Figure 7.30: **Porous film on top of EBL structure.** (a) Ordered array of gold nanorods on glass. Alternating orientation allows both polarizations to be studied simultaneously. **Porous silica film on top of EBL sample. To facilitate imaging the rod was written on top of ITO.**

Protocol for porous silica films

The biphasic system consists of an oil phase containing tetraethyl orthosilicate (TEOS) as the silicon source, and an aqueous phase containing cetyltrimethylammonium chloride (CTAC) as the template. It is reported that as the micelles continuously form at the oil-water interface, they slowly drive into the aqueous phase and deposit at the substrate surface to form vertically aligned channels. After removal of the template, the porous films are obtained.

This is the protocol we use for a 100 mL round-bottom flask with up to 6 substrates:

1. Precision cover glasses (#1.5H thickness, 22 x 22 mm, Thorlabs) are cut in half and then subsequently cleaned by sonication in a soap solution (2% of Hellmanex III), water, acetone and ethanol for 5 min each.

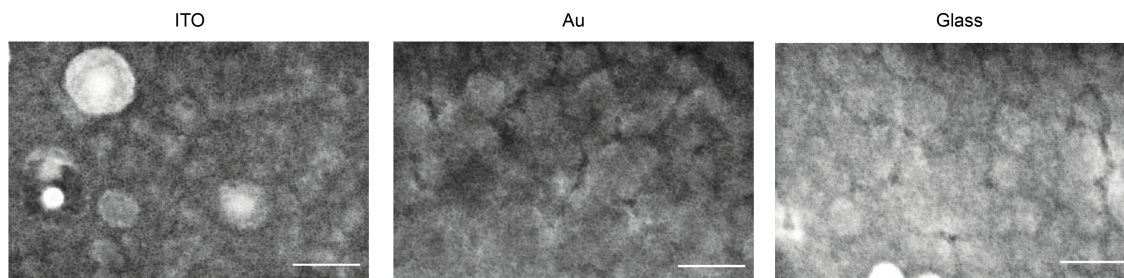


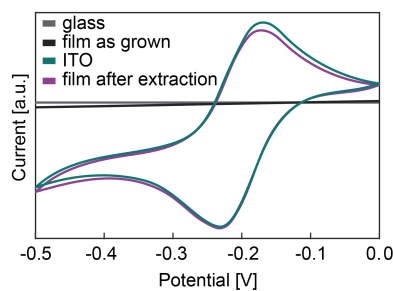
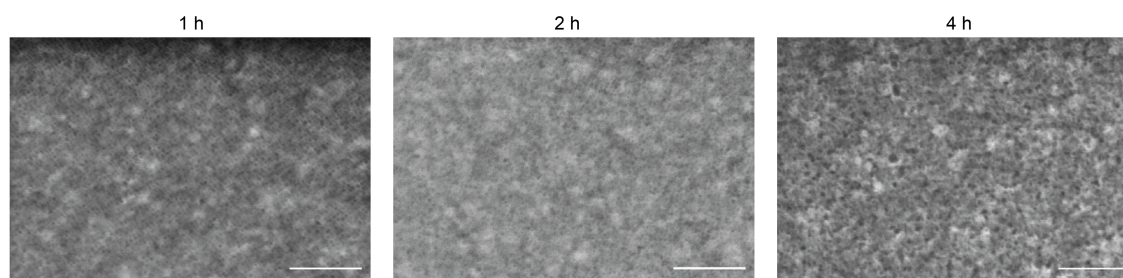
Figure 7.31: **SEM of porous silica films.** On different substrates. All scale bars 100 nm. The films on glass are the most difficult to image as charging becomes a bigger obstacle for non-conductive substrates.

2. Heat an oil bath to 60°C stirring at 150 rpm for about 20 min.
3. In a bottle, mix 43.75 mL of H₂O with 18.75 CTAC 25% and 225 μL Triethanolamine (TEA).
4. Sonicate this mixture for 15 min at frequency 37 and 100% power.
5. In the meantime, put precleaned substrates into the Teflon substrate holders and plasma treat them with oxygen (for 3 min at 40% power and a pressure of 0.8 mbar).
6. Together with a magnetic stirring bar, put the holder with substrates into a 100 mL round-bottom flask.
7. Add 62.725 mL of the CTAC solution to the round-bottom flask and put it in the preheated oil bath.
8. After 1 hour, change the stirring speed to 250 rpm and add 21.25 mL of TEOS/1-octadecene 10% v/v dropwise.
9. Leave the reaction for 4 hours.
10. Remove the substrates from the biphasic solution, rinse with ethanol and dry at 60°C for 1 hour.
11. To remove the CTAC template, treat the substrates with a UV-Ozone cleaner for 2 hours.
12. Potential APTES functionalization to reduce electrostatic repulsion of resazurin and porous silica films that we did not explore: modification of the mesoporous silica layer with amino groups reduces this repulsion, the silica coated-coverslips can be immersed into a 1% (v/v) APTES solution in acetonitrile for 20 min.

Images of porous films on different substrates

Accessibility of the porous films

To verify that the pores are accessible, cyclic voltammetry (CV) of conductive substrates with and without films is a useful tool.^{329,330} To this end, the porous films

Figure 7.32: **Accessibility of the porous films.**Figure 7.33: **Stability of the porous films.** 1h, 2h, 4h in borate buffer from left to right, all on ITO. Scale bars 100nm.

were grown on ITO-coated glass substrates. Following the procedure reported by Lu *et al.*,³³⁰ cyclic voltammograms (CVs) of 1 mM $\text{Ru}(\text{NH}_3)_6^{3+}$ in 1M KCl were recorded on a bare ITO electrode and ITO electrodes covered by mesoporous silica films before and after surfactant extraction.

Stability of porous silica films

There is no visible difference 1h or 2h, however, some degradation appears after 4h. For this reason, single-molecule images should be acquired within 2 hours after the addition of borate buffer (or other aqueous buffer).

D.2 Single-molecule imaging of non-fluorescent reactions

This work was done in collaboration with Ana Sousa-Castillo, Julian Gargiulo, William Pelever and Katie McGuire. The reaction we studied in Chapter 4 from Resazurin to Resorufin is a fluoregenic model reaction. A lot of insight gain be gained from this system, however, it would be particualry interesting to explore technologically relevant reactions. Recently, the in the group of Peng Chen, the Resorufin system has been used as fluoregenic reaction that compeits with the reaction of interest in order to gain insight into the nonfluorogenic reaction.⁷ Another approach might be to use a fluorogenic probe for the product of interest. Nile Red-Pd acetate complexes (NR-PdA) have been shown to react with biological CO sources³³¹ to the fluorescent probe Nilered. This system could be useful to study CO_2 to CO reduction at the single-molecule level. Katie and William synthesized the NR-PdA complexes and we started to work on an immobilization of the complex on the porous silica, as we

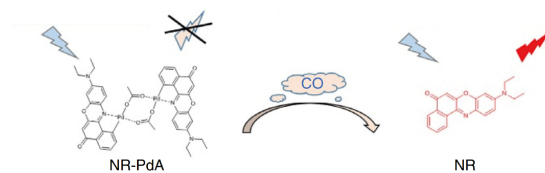


Figure 7.34: **Single-molecule imaging of non-fluorescent reactions.** NR-PdA becomes NR after reacting with CO and could be employed to image CO generation. Adapted from Ref.³³¹ Copyright 2018 Springer Nature.

thought this would be the most promising route to ensure that the product CO can be detected upon generation. However, we did not continue this further to focus on other projects.

E Personal contributions

Science is becoming increasingly collaborative, and none of the work presented in this thesis would have been possible alone. In the different projects that I have been involved in, I have made significant contributions to the research. In the context of this PhD Thesis, I would like to clarify my personal contributions to the results that were presented in chapters 4, 5 and 6. In my first-author publications I will clarify experimental work that was not by me, while I will clarify my contribution in the other projects. I will focus here on the experimental/theoretical work but want to emphasize that in all of the projects, every author was crucial to the discussions and the final product.

In Chapter 4, Ana Sousa-Castillo performed the synthesis and Joong-Bum Lee the capillary assisted assembly, while I did the optical and thermal simulations, experiments, and data analysis. Julian Gargiulo also performed experiments and helped me build the setup. In Chapter 5, I was first-author of a review that we wrote with the group that is the basis of part 1 and performed theoretical (optical and thermal) modeling in part 2.

In Chapter 6 part of the introduction is based on a review that I was part of. Parts of the text I used in this thesis and figures presented were compiled by me, but I want to acknowledge in particular Luca Sortino who also wrote part of the introduction of the review, as well as Seryio Saris who was the main author of the metasurfaces for photocatalysis section. Regarding the work on the photothermal properties of ensembles, I performed thermometry experiments with Julian Gargiulo and Guillaume Baffou on the setup that Julian and I built. Lin Nan fabricated the samples, and I performed optical characterization, simulations, and data analysis of the photoluminescence data. The thermal imaging data was analyzed by Guillaume Baffou.

It has been an exceptional experience to collaborate with a diverse group of scientists from different fields and cultures. I have learned so much from my colleagues. Moreover, working with researchers from different cultural backgrounds has broadened my perspective also beyond scientific research. I am grateful for the opportunity to work with such a talented and diverse team. I am grateful for everyone's contributions and equally grateful to have been given the opportunity to give mine.

Bibliography

- [1] Max Roser. The world's energy problem - Our World in Data, 2020.
- [2] Hannah Ritchie, Max Roser, and Pablo Rosado. Energy.
- [3] Our World in Data. Climate Change Impacts.
- [4] Max Roser. The world's energy problem - Our World in Data, 2020.
- [5] Pierre Friedlingstein, Michael O'sullivan, Matthew W. Jones, Robbie M. Andrew, Luke Gregor, Judith Hauck, Corinne Le Quéré, Ingrid T. Luijkx, Are Olsen, Glen P. Peters, Wouter Peters, Julia Pongratz, Clemens Schwingshackl, Stephen Sitch, Josep G. Canadell, Philippe Ciais, Robert B. Jackson, Simone R. Alin, Ramdane Alkama, Almut Arneeth, Vivek K. Arora, Nicholas R. Bates, Meike Becker, Nicolas Bellouin, Henry C. Bittig, Laurent Bopp, Frédéric Chevalier, Louise P. Chini, Margot Cronin, Wiley Evans, Stefanie Falk, Richard A. Feely, Thomas Gasser, Marion Gehlen, Thanos Gkritzalis, Lucas Gloege, Giacomo Grassi, Nicolas Gruber, Özgür Gürses, Ian Harris, Matthew Hefner, Richard A. Houghton, George C. Hurtt, Yosuke Iida, Tatiana Ilyina, Atul K. Jain, Annika Jersild, Koji Kadono, Etsushi Kato, Daniel Kennedy, Kees Klein Goldewijk, Jürgen Knauer, Jan Ivar Korsbakken, Peter Landschützer, Nathalie Lefèvre, Keith Lindsay, Junjie Liu, Zhu Liu, Gregg Marland, Nicolas Mayot, Matthew J. Mcgrath, Nicolas Metzl, Natalie M. Monacci, David R. Munro, Shin Ichiro Nakaoka, Yosuke Niwa, Kevin O'brien, Tsuneo Ono, Paul I. Palmer, Naiqing Pan, Denis Pierrot, Katie Pocock, Benjamin Poulter, Laure Resplandy, Eddy Robertson, Christian Rödenbeck, Carmen Rodriguez, Thais M. Rosan, Jörg Schwinger, Roland Séférian, Jamie D. Shutler, Ingunn Skjelvan, Tobias Steinhoff, Qing Sun, Adrienne J. Sutton, Colm Sweeney, Shintaro Takao, Toste Tanhua, Pieter P. Tans, Xiangjun Tian, Hanqin Tian, Bronte Tilbrook, Hiroyuki Tsujino, Francesco Tubiello, Guido R. Van Der Werf, Anthony P. Walker, Rik Wanninkhof, Chris Whitehead, Anna Willstrand Wranne, Rebecca Wright, Wenping Yuan, Chao Yue, Xu Yue, Sönke Zaehle, Jiye Zeng, and Bo Zheng. Global Carbon Budget 2022. *Earth System Science Data*, 14(11):4811–4900, nov 2022.
- [6] The World Bank. World Development Indicators — Data Catalog, 2023.
- [7] Marc Perez and Richard Perez. Update 2022 – A fundamental look at supply side energy reserves for the planet. *Solar Energy Advances*, 2:100014, jan 2022.
- [8] V Masson-Delmotte, P Zhai, HO Pörtner Global Warming of 1.5 . . . , and Undefined 2018. IPCC SPECIAL REPORT Summary for Policymakers Summary for Policymakers. *IPCC Geneva*, 2018.
- [9] Global Carbon Project. Supplementary data of Global Carbon Budget 2021. Technical Report 4, 2022.
- [10] Naciones Unidas. World Population Prospects: The 2017 Revision. *Economic and Social Affairs*, 1-53(December):53, 2017.

- [11] Bastien Girod, Detlef Peter van Vuuren, and Edgar G. Hertwich. Climate policy through changing consumption choices: Options and obstacles for reducing greenhouse gas emissions. *Global Environmental Change*, 25(1):5–15, mar 2014.
- [12] Arnold Tukker, Tanya Bulavskaya, Stefan Giljum, Arjan de Koning, Stephan Lutter, Moana Simas, Konstantin Stadler, and Richard Wood. Environmental and resource footprints in a global context: Europe’s structural deficit in resource endowments. *Global Environmental Change*, 40:171–181, sep 2016.
- [13] Daniel W. O’Neill, Andrew L. Fanning, William F. Lamb, and Julia K. Steinberger. A good life for all within planetary boundaries. *Nature Sustainability*, 1(2):88–95, feb 2018.
- [14] Hannah Ritchie. Global inequalities in CO₂ emissions - Our World in Data, 2018.
- [15] Yigao Yuan, Linan Zhou, Hossein Robotjazi, Junwei Lucas Bao, Jingyi Zhou, Aaron Bayles, Lin Yuan, Minghe Lou, Minhan Lou, Suman Khatiwada, Emily A. Carter, Peter Nordlander, and Naomi J. Halas. Earth-abundant photocatalyst for H₂ generation from NH₃ with light-emitting diode illumination. *Science (New York, N. Y.)*, 378(6622):889–893, nov 2022.
- [16] Mark L. Brongersma. Introductory lecture: Nanoplasmonics. *Faraday Discussions*, 178(0):9–36, jun 2015.
- [17] Ian Freestone, Nigel Meeks, Margaret Sax, and Catherine Higgitt. The Lycurgus Cup — A Roman nanotechnology. *Gold Bulletin*, 40(4):270–277, dec 2007.
- [18] D. J. BARBER and I. C. FREESTONE. AN INVESTIGATION OF THE ORIGIN OF THE COLOUR OF THE LYCURGUS CUP BY ANALYTICAL TRANSMISSION ELECTRON MICROSCOPY. *Archaeometry*, 32(1):33–45, feb 1990.
- [19] Shinji Hayashi and Takayuki Okamoto. Plasmonics: Visit the past to know the future, oct 2012.
- [20] M. A. Garcia. Surface plasmons in metallic nanoparticles: Fundamentals and applications, jul 2011.
- [21] Michael Faraday. X. The Bakerian Lecture. —Experimental relations of gold (and other metals) to light. *Philosophical Transactions of the Royal Society of London*, 147:145–181, dec 1857.
- [22] The British Museum. Lycurgus - British Museum, 2021.
- [23] The Corning Museum of Glass. Exhibitions — Corning Museum of Glass.
- [24] Stefan A. Maier. *Plasmonics: Fundamentals and Applications*. Springer, 2007.
- [25] Uwe Kreibig and Peter Zacharias. Surface plasma resonances in small spherical silver and gold particles. *Zeitschrift für Physik*, 231(2):128–143, apr 1970.

- [26] Gustav Mie. Beiträge zur Optik trüber Medien, speziell kolloidaler Metallösungen. *Annalen der Physik*, 330(3):377–445, jan 1908.
- [27] Craig F. Bohren and Donald R. Huffman. *Absorption and Scattering of Light by Small Particles*. Wiley, apr 1998.
- [28] Emiliano Cortés, Fedja J. Wendisch, Luca Sortino, Andrea Mancini, Simone Ezendam, Seryio Saris, Leonardo De S. Menezes, Andreas Tittl, Haoran Ren, and Stefan A. Maier. Optical Metasurfaces for Energy Conversion, oct 2022.
- [29] Mark L. Brongersma, Naomi J. Halas, and Peter Nordlander. Plasmon-induced hot carrier science and technology. *Nature Nanotechnology*, 10(1):25–34, jan 2015.
- [30] Craig F. Bohren. How can a particle absorb more than the light incident on it? *American Journal of Physics*, 51(4):323–327, apr 1983.
- [31] Stephan Link and Mostafa A. El-Sayed. Spectral Properties and Relaxation Dynamics of Surface Plasmon Electronic Oscillations in Gold and Silver Nanodots and Nanorods. *Journal of Physical Chemistry B*, 103(40):8410–8426, oct 1999.
- [32] S. Link and M. A. El-Sayed. Shape and size dependence of radiative, non-radiative and photothermal properties of gold nanocrystals, 2000.
- [33] Yoon Hee Jang, Yu Jin Jang, Seokhyoung Kim, Li Na Quan, Kyungwha Chung, and Dong Ha Kim. Plasmonic Solar Cells: From Rational Design to Mechanism Overview, dec 2016.
- [34] Harry A. Atwater and Albert Polman. Plasmonics for improved photovoltaic devices. *Nature Materials*, 9(3):205–213, 2010.
- [35] Sara B. Aboeleneen, Mackenzie A. Scully, Jenna C. Harris, Eric H. Sterin, and Emily S. Day. Membrane-wrapped nanoparticles for photothermal cancer therapy, dec 2022.
- [36] Andrew M. Smith, Michael C. Mancini, and Shuming Nie. Bioimaging: Second window for in vivo imaging, 2009.
- [37] Kyeong Seok Lee and Mostafa A. El-Sayed. Dependence of the enhanced optical scattering efficiency relative to that of absorption for gold metal nanorods on aspect ratio, size, end-cap shape, and medium refractive index. *Journal of Physical Chemistry B*, 109(43):20331–20338, nov 2005.
- [38] Guillaume Baffou. *Thermoplasmonics*. Cambridge University Press, oct 2017.
- [39] Guillaume Baffou, Frank Cichos, and Romain Quidant. Applications and challenges of thermoplasmonics, sep 2020.
- [40] Jinxing Chen, Zuyang Ye, Fan Yang, and Yadong Yin. Plasmonic Nanostructures for Photothermal Conversion. *Small Science*, 1(2):2000055, feb 2021.

- [41] Vincenzo Giannini, Antonio I. Fernández-Domínguez, Susannah C. Heck, Stefan A. Maier, Antonio I. Fernández-Domínguez, Susannah C. Heck, and Stefan A. Maier. Plasmonic nanoantennas: Fundamentals and their use in controlling the radiative properties of nanoemitters. *Chemical Reviews*, 111(6):3888–3912, mar 2011.
- [42] Eduardo A. Coronado, Ezequiel R. Encina, and Fernando D. Stefani. Optical properties of metallic nanoparticles: Manipulating light, heat and forces at the nanoscale. *Nanoscale*, 3(10):4042–4059, 2011.
- [43] Syed Mubeen, Joun Lee, Nirala Singh, Stephan Krämer, Galen D. Stucky, and Martin Moskovits. An autonomous photosynthetic device in which all charge carriers derive from surface plasmons. *Nature Nanotechnology*, 8(4):247–251, feb 2013.
- [44] Yuchao Zhang, Shuai He, Wenxiao Guo, Yue Hu, Jiawei Huang, Justin R. Mulcahy, and Wei David Wei. Surface-Plasmon-Driven Hot Electron Photochemistry. *Chemical Reviews*, 118(6):2927–2954, mar 2018.
- [45] Siwei Li, Peng Miao, Yuanyuan Zhang, Jie Wu, Bin Zhang, Yunchen Du, Xijiang Han, Jianmin Sun, and Ping Xu. Recent Advances in Plasmonic Nanostructures for Enhanced Photocatalysis and Electrocatalysis. *Advanced Materials*, 33(6):2000086, feb 2021.
- [46] Hung Ji Huang, Jeffrey Chi Sheng Wu, Hai Pang Chiang, Yuan Fong Chou Chau, Yung Sheng Lin, Yen Han Wang, and Po Jui Chen. Review of experimental setups for plasmonic photocatalytic reactions. *Catalysts*, 10(1):1–25, 2020.
- [47] Chao Zhan, Martin Moskovits, and Zhong Qun Tian. Recent Progress and Prospects in Plasmon-Mediated Chemical Reaction. *Matter*, 3(1):42–56, 2020.
- [48] Prashant K. Jain. Taking the Heat off of Plasmonic Chemistry. *Journal of Physical Chemistry C*, 123(40):24347–24351, 2019.
- [49] Gabriella Graziano. All-plasmonic water splitting. *Nature Nanotechnology 2021*, pages 1–1, oct 2021.
- [50] Pedro H. C. Camargo and Emiliano. Cortes. *Plasmonic Catalysis From Fundamentals to Applications*. John Wiley and Sons, Ltd, 2021.
- [51] John Mark P Martirez, Junwei Lucas Bao, and Emily A Carter. First-Principles Insights into Plasmon-Induced Catalysis. *Annual Review of Physical Chemistry*, 72(1):99–119, apr 2021.
- [52] Siwei Li, Peng Miao, Yuanyuan Zhang, Jie Jeffrey Chi Sheng Wu, Bin Zhang, Yunchen Du, Xijiang Han, Jianmin Sun, Ping Xu, Mahak Dhiman, Hung Ji Huang, Jie Jeffrey Chi Sheng Wu, Hai Pang Chiang, Yuan Fong Chou Chau, Yung Sheng Lin, Yen Han Wang, Po Jui Chen, Luca Mascaretti, Alberto Naldoni, Yugang Sun, Zhiyong Tang, Chao Zhan, Martin Moskovits, Zhong Qun

- Tian, Xueqian Li, Henry O. Everitt, Jie Liu, Alexandra Gellé, Tony Jin, Luis De La Garza, Gareth D. Price, Lucas V. Besteiro, Audrey Moores, Rifat Kamarudheen, Guus J. W. Aalbers, Ruben F. Hamans, Leon P. J. Kamp, Andrea Baldi, Yonatan Sivan, Joshua H. Baraban, and Yonatan Dubi. Synergy between thermal and nonthermal effects in plasmonic photocatalysis. *Nano Research*, 3(1):20–25, 2020.
- [53] Yonatan Sivan, Joshua H. Baraban, and Yonatan Dubi. Experimental practices required to isolate thermal effects in plasmonic photo-catalysis: lessons from recent experiments. *OSA Continuum*, 3(3):483, 2020.
- [54] Yugang Sun and Zhiyong Tang. Photocatalytic hot-carrier chemistry. *MRS Bulletin*, 45(1):20–25, 2020.
- [55] Shunqin Luo, Xiaohui Ren, Huiwen Lin, Hui Song, and Jinhua Ye. Plasmonic photothermal catalysis for solar-to-fuel conversion: current status and prospects. *Chemical Science*, 12(16):5701–5719, apr 2021.
- [56] Luca Mascaretti and Alberto Naldoni. Hot electron and thermal effects in plasmonic photocatalysis. *Journal of Applied Physics*, 128(4):041101, jul 2020.
- [57] Dinamol Devasia, Ankita Das, Varun Mohan, and Prashant K Jain. Control of Chemical Reaction Pathways by Light–Matter Coupling. *Annual Review of Physical Chemistry*, 72(1):423–443, apr 2021.
- [58] Alexandra Gellé, Tony Jin, Luis De La Garza, Gareth D. Price, Lucas V. Besteiro, and Audrey Moores. Applications of Plasmon-Enhanced Nanocatalysis to Organic Transformations. *Chemical Reviews*, 120(2):986–1041, 2020.
- [59] Rishi Verma, Rajesh Belgamwar, and Vivek Polshettiwar. Plasmonic Photocatalysis for CO₂ Conversion to Chemicals and Fuels. *ACS Materials Letters*, 3(5):574–598, 2021.
- [60] Simone Ezendam, Matias Herran, Lin Nan, Christoph Gruber, Yicui Kang, Franz Gröbmeyer, Rui Lin, Julian Gargiulo, Ana Sousa-Castillo, and Emiliano Cortés. Hybrid Plasmonic Nanomaterials for Hydrogen Generation and Carbon Dioxide Reduction. *ACS Energy Lett*, 7(2):778–815, feb 2022.
- [61] Jörg Eppinger and Kuo Wei Huang. Formic Acid as a Hydrogen Energy Carrier. *ACS Energy Letters*, 2(1):188–195, jan 2017.
- [62] Nicola Armaroli and Vincenzo Balzani. The Hydrogen Issue. *ChemSusChem*, 4(1):21–36, jan 2011.
- [63] Paul Kruger. Appropriate technologies for large-scale production of electricity and hydrogen fuel. *International Journal of Hydrogen Energy*, 33(21):5881–5886, nov 2008.
- [64] Stephan Enthaler, Jan Von Langermann, and Thomas Schmidt. Carbon dioxide and formic acid - The couple for environmental-friendly hydrogen storage? *Energy and Environmental Science*, 3(9):1207–1217, aug 2010.

- [65] Frances H. Stephens, Vincent Pons, and R. Tom Baker. Ammonia–borane: The hydrogen source par excellence? *Journal of the Chemical Society. Dalton Transactions*, 0(25):2613–2626, may 2007.
- [66] D. M.F. Santos and C. A.C. Sequeira. Sodium borohydride as a fuel for the future. *Renewable and Sustainable Energy Reviews*, 15(8):3980–4001, oct 2011.
- [67] Tyler A. Jacobson, Jasdeep S. Kler, Michael T. Hernke, Rudolf K. Braun, Keith C. Meyer, and William E. Funk. Direct human health risks of increased atmospheric carbon dioxide. *Nature Sustainability*, 2(8):691–701, aug 2019.
- [68] Sungju Yu, Andrew J. Wilson, Jaeyoung Heo, and Prashant K. Jain. Plasmonic Control of Multi-Electron Transfer and C-C Coupling in Visible-Light-Driven CO₂ Reduction on Au Nanoparticles. *Nano Letters*, 18(4):2189–2194, 2018.
- [69] Fengxia Tong, Xizhuang Liang, Fahao Ma, Xiaolei Bao, Zeyan Wang, Yuanyuan Liu, Peng Wang, Hefeng Cheng, Ying Dai, Baibiao Huang, and Zhaoke Zheng. Plasmon-Mediated Nitrobenzene Hydrogenation with Formate as the Hydrogen Donor Studied at a Single-Particle Level. *ACS Catalysis*, 11(7):3801–3809, apr 2021.
- [70] Iyad Sarhid, Ibrahim Abdellah, Cyril Martini, Vincent Huc, Diana Dragoë, Patricia Beaunier, Isabelle Lampre, and Hynd Remita. Plasmonic catalysis for the Suzuki-Miyaura cross-coupling reaction using palladium nanoflowers. *New Journal of Chemistry*, 43(11):4349–4355, mar 2019.
- [71] Yuki Takeuchi, Tetsuya Fujita, and Nobuyuki Takeyasu. Plasmon-mediated chemical transformation from alkane to alkene on a silver nanoparticle array under 532 nm excitation. *Physical Chemistry Chemical Physics*, 21(14):7502–7507, apr 2019.
- [72] Chun Hu, Tianwei Peng, Xuexiang Hu, Yulun Nie, Xuefeng Zhou, Jiuhui Qu, and Hong He. Plasmon-induced photodegradation of toxic pollutants with Ag-AgI/Al₂O₃ under visible-light irradiation. *Journal of the American Chemical Society*, 132(2):857–862, jan 2010.
- [73] Emiko Kazuma, Jaehoon Jung, Hiromu Ueba, Michael Trenary, and Yousoo Kim. Real-space and real-time observation of a plasmon-induced chemical reaction of a single molecule. *Science*, 360(6388):521–526, may 2018.
- [74] John Mark P. Martinez and Emily A. Carter. Prediction of a low-temperature N₂ dissociation catalyst exploiting near-IR-to-visible light nanoplasmonics. *Science Advances*, 3(12), dec 2017.
- [75] Julian Gargiulo, Rodrigo Berté, Yi Li, Stefan A. Maier, Emiliano Cortés, Stefan A. Maier, and Emiliano Cortés. From Optical to Chemical Hot Spots in Plasmonics. *Accounts of Chemical Research*, 52(9):2525–2535, aug 2019.

- [76] Tapan K. Sau and Andrey L. Rogach. Nonspherical Noble Metal Nanoparticles: Colloid-Chemical Synthesis and Morphology Control. *Advanced Materials*, 22(16):1781–1804, apr 2010.
- [77] Rajesh Sardar, Alison M. Funston, Paul Mulvaney, and Royce W. Murray. Gold nanoparticles: Past, present, and future. *Langmuir*, 25(24):13840–13851, dec 2009.
- [78] Marek Grzelczak, Jorge Pérez-Juste, Paul Mulvaney, and Luis M. Liz-Marzán. Shape control in gold nanoparticle synthesis. *Chemical Society Reviews*, 37(9):1783–1791, aug 2008.
- [79] Younan Xia and Naomi J. Halas. Shape-controlled synthesis and surface plasmonic properties of metallic nanostructures. *MRS Bulletin*, 30(5):338–343, jan 2005.
- [80] Guillermo González-Rubio, Pablo Díaz-Núñez, Antonio Rivera, Alejandro Prada, Gloria Tardajos, Jesús González-Izquierdo, Luis Bañares, Pablo Llombart, Luis G. Macdowell, Mauricio Alcolea Palafox, Luis M. Liz-Marzán, Ovidio Peña-Rodríguez, and Andrés Guerrero-Martínez. Femtosecond laser reshaping yields gold nanorods with ultranarrow surface plasmon resonances. *Science*, 358(6363):640–644, nov 2017.
- [81] Qian Wang, Zongpeng Wang, Zhe Li, Junyan Xiao, Hangyong Shan, Zheyu Fang, and Limin Qi. Controlled growth and shape-directed self-assembly of gold nanoarrows. *Science Advances*, 3(10), 2017.
- [82] You Jin Lee, Nicholas B. Schade, Li Sun, Jonathan A. Fan, Doo Ri Bae, Marcelo M. Mariscal, Gaehang Lee, Federico Capasso, Stefano Sacanna, Vinothan N. Manoharan, and Gi Ra Yi. Ultraspherical, highly spherical monocrystalline gold particles for precision plasmonics. *ACS Nano*, 7(12):11064–11070, dec 2013.
- [83] Maxime Bronchy, Lucien Roach, Laurent Mendizabal, Céline Feautrier, Etienne Durand, Jean Marc Heintz, Etienne Duguet, and Mona Tréguer-Delapierre. Improved Low Temperature Sinter Bonding Using Silver Nanocube Superlattices. *Journal of Physical Chemistry C*, 126(3):1644–1650, jan 2022.
- [84] Jessi E.S. Van Der Hoeven, Tom A.J. Welling, Tiago A.G. Silva, Jeroen E. Van Den Reijen, Camille La Fontaine, Xavier Carrier, Catherine Louis, Alfons Van Blaaderen, and Petra E. De Jongh. In Situ Observation of Atomic Redistribution in Alloying Gold-Silver Nanorods. *ACS Nano*, 12(8):8467–8476, aug 2018.
- [85] Joong Bum Lee, Harriet Walker, Yi Li, Tae Won Nam, Aliaksandra Rakovich, Riccardo Sapienza, Yeon Sik Jung, Yoon Sung Nam, Stefan A. Maier, and Emiliano Cortés. Template Dissolution Interfacial Patterning of Single Colloids for Nanoelectrochemistry and Nanosensing. *ACS Nano*, 14(12):17693–17703, dec 2020.

- [86] Julián Gargiulo, Ianina L. Violi, Santiago Cerrota, Lukáš Chvátal, Emiliano Cortés, Eduardo M. Perassi, Fernando Diaz, Pavel Zemánek, and Fernando D. Stefani. Accuracy and Mechanistic Details of Optical Printing of Single Au and Ag Nanoparticles. *ACS Nano*, 11(10):9678–9688, oct 2017.
- [87] Jaekwon Do, Michael Fedoruk, Frank Jäckel, and Jochen Feldmann. Two-color laser printing of individual gold nanorods. *Nano Letters*, 13(9):4164–4168, sep 2013.
- [88] Julián Gargiulo, Santiago Cerrota, Emiliano Cortés, Ianina L. Violi, and Fernando D. Stefani. Connecting Metallic Nanoparticles by Optical Printing. *Nano Letters*, 16(2):1224–1229, feb 2016.
- [89] Mason J. Guffey and Norbert F. Scherer. All-optical patterning of Au nanoparticles on surfaces using optical traps. *Nano Letters*, 10(11):4302–4308, nov 2010.
- [90] Alexander S. Urban, Andrey A. Lutich, Fernando D. Stefani, and Jochen Feldmann. Laser printing single gold nanoparticles. *Nano Letters*, 10(12):4794–4798, dec 2010.
- [91] Ianina L. Violi, Luciana P. Martinez, Mariano Barella, Cecilia Zaza, Lukáš Chvátal, Pavel Zemánek, Marina V. Gutiérrez, María Y. Paredes, Alberto F. Scarpettini, Jorge Olmos-Trigo, Valeria R. Pais, Iván Díaz Nóbrega, Emiliano Cortes, Juan José Sáenz, Andrea V. Bragas, Julian Gargiulo, and Fernando D. Stefani. Challenges on optical printing of colloidal nanoparticles. *Journal of Chemical Physics*, 156(3):034201, jan 2022.
- [92] Spas Nedev, Alexander S. Urban, Andrey A. Lutich, and Jochen Feldmann. Optical force stamping lithography. *Nano Letters*, 11(11):5066–5070, nov 2011.
- [93] Tianhong Chen and Björn M. Reinhard. Assembling Color on the Nanoscale: Multichromatic Switchable Pixels from Plasmonic Atoms and Molecules. *Advanced Materials*, 28(18):3522–3527, may 2016.
- [94] Yu Zhou, Xiaozhu Zhou, Daniel J. Park, Korosh Torabi, Keith A. Brown, Matthew R. Jones, Chuan Zhang, George C. Schatz, and Chad A. Mirkin. Shape-selective deposition and assembly of anisotropic nanoparticles. *Nano Letters*, 14(4):2157–2161, apr 2014.
- [95] Valentin Flauraud, Massimo Mastrangeli, Gabriel D. Bernasconi, Jeremy Butet, Duncan T.L. Alexander, Elmira Shahrabi, Olivier J.F. Martin, and Juergen Brugger. Nanoscale topographical control of capillary assembly of nanoparticles. *Nature Nanotechnology*, 12(1):73–80, jan 2017.
- [96] Yi Cui, Mikael T. Björk, J. Alexander Liddle, Carsten Sönnichsen, Benjamin Bousset, and A. Paul Alivisatos. Integration of colloidal nanocrystals into lithographically patterned devices. *Nano Letters*, 4(6):1093–1098, jun 2004.

- [97] Tobias Kraus, Laurent Malaquin, Heinz Schmid, Walter Riess, Nicholas D. Spencer, and Heiko Wolf. Nanoparticle printing with single-particle resolution. *Nature Nanotechnology*, 2(9):570–576, sep 2007.
- [98] Laurent Malaquin, Tobias Kraus, Heinz Schmid, Emmanuel Delamarche, and Heiko Wolf. Controlled particle placement through convective and capillary assembly. *Langmuir*, 23(23):11513–11521, nov 2007.
- [99] Weikun Zhu, Peter F. Satterthwaite, Patricia Jastrzebska-Perfect, Roberto Brenes, and Farnaz Niroui. Nanoparticle contact printing with interfacial engineering for deterministic integration into functional structures. *Science Advances*, 8(43), oct 2022.
- [100] C. Sönnichsen, T. Franzl, T. Wilk, G. von Plessen, J. Feldmann, O. Wilson, and P. Mulvaney. Drastic Reduction of Plasmon Damping in Gold Nanorods. *Physical Review Letters*, 88(7):077402, jan 2002.
- [101] Mark W. Knight, Jonathan Fan, Federico Capasso, and Naomi J. Halas. Influence of excitation and collection geometry on the dark field spectra of individual plasmonic nanostructures. *Optics Express*, 18(3):2579, feb 2010.
- [102] Jun Hee Yoon, Florian Selbach, Ludmilla Schumacher, Jesil Jose, and Sebastian Schlücker. Surface Plasmon Coupling in Dimers of Gold Nanoparticles: Experiment and Theory for Ideal (Spherical) and Nonideal (Faceted) Building Blocks. *ACS Photonics*, 6(3):642–648, mar 2019.
- [103] Carolina Novo, Alison M. Funston, and Paul Mulvaney. Direct observation of chemical reactions on single gold nanocrystals using surface plasmon spectroscopy. *Nature Nanotechnology*, 3(10):598–602, oct 2008.
- [104] Wei Jiang, Huatian Hu, Qian Deng, Shunping Zhang, and Hongxing Xu. Temperature-dependent dark-field scattering of single plasmonic nanocavity. *Nanophotonics*, 9(10):3347–3356, aug 2020.
- [105] P. Zijlstra and M. Orrit. Single metal nanoparticles: optical detection, spectroscopy and applications. *Reports on Progress in Physics*, 74(10):106401, oct 2011.
- [106] Xiang Wang, Sheng-Chao Huang, Shu Hu, Sen Yan, and Bin Ren. Fundamental understanding and applications of plasmon-enhanced Raman spectroscopy. *Nature Reviews Physics*, 2(5):253–271, apr 2020.
- [107] Zhenglong Zhang, Tanja Deckert-Gaudig, and Volker Deckert. Label-free monitoring of plasmonic catalysis on the nanoscale, jul 2015.
- [108] Judith Langer, Dorleta Jimenez de Aberasturi, Javier Aizpurua, Ramon A. Alvarez-Puebla, Baptiste Auguie, Jeremy J. Baumberg, Guillermo C. Bazan, Steven E.J. Bell, Anja Boisen, Alexandre G. Brolo, Jaebum Choo, Dana Cialla-May, Volker Deckert, Laura Fabris, Karen Faulds, F. Javier García de Abajo, Royston Goodacre, Duncan Graham, Amanda J. Haes, Christy L. Haynes,

- Christian Huck, Tamitake Itoh, Mikael Käll, Janina Kneipp, Nicholas A. Kotov, Hua Kuang, Eric C. Le Ru, Hiang Kwee Lee, Jian Feng Li, Xing Yi Ling, Stefan A. Maier, Thomas Mayerhöfer, Martin Moskovits, Kei Murakoshi, Jwa Min Nam, Shuming Nie, Yukihiro Ozaki, Isabel Pastoriza-Santos, Jorge Perez-Juste, Juergen Popp, Annemarie Pucci, Stephanie Reich, Bin Ren, George C. Schatz, Timur Shegai, Sebastian Schlücker, Li Lin Tay, K. George Thomas, Zhong Qun Tian, Richard P. van Duyne, Tuan Vo-Dinh, Yue Wang, Katherine A. Willets, Chuanlai Xu, Hongxing Xu, Yikai Xu, Yuko S. Yamamoto, Bing Zhao, and Luis M. Liz-Marzán. Present and future of surface-enhanced Raman scattering, jan 2020.
- [109] Andrew J. Wilson, Dinumol Devasia, and Prashant K. Jain. Nanoscale optical imaging in chemistry, aug 2020.
- [110] C.V. Raman. A New Radiation. *Indian J. Phys.*, 2:387, 1927.
- [111] Song Yuan Ding, En Ming You, Zhong Qun Tian, and Martin Moskovits. Electromagnetic theories of surface-enhanced Raman spectroscopy, jul 2017.
- [112] Zhenglong Zhang, Tanja Deckert-Gaudig, Pushkar Singh, and Volker Deckert. Single molecule level plasmonic catalysis - A dilution study of p-nitrothiophenol on gold dimers. *Chemical Communications*, 51(15):3069–3072, feb 2015.
- [113] P. G. Etchegoin and E. C. Le Ru. A perspective on single molecule SERS: Current status and future challenges, oct 2008.
- [114] Gayatri Kumari, Xueqiang Zhang, Dinumol Devasia, Jaeyoung Heo, and Prashant K. Jain. Watching visible light-driven CO₂ reduction on a plasmonic nanoparticle catalyst. *ACS Nano*, 12(8):8330–8340, aug 2018.
- [115] Lin Nan, Jesus Giraldez Martinez, Andrei Stefancu, Li Zhu, Min Liu, Alexander O. Govorov, Lucas V. Besteiro, and Emiliano Cortés. Investigating plasmonic catalysis kinetics on hot-spot engineered nanoantennae. *Nano Letters*, 2023.
- [116] Eric A. Pozzi, Alyssa B. Zrimsek, Clotilde M. Lethiec, George C. Schatz, Mark C. Hersam, and Richard P. Van Duyne. Evaluating Single-Molecule Stokes and Anti-Stokes SERS for Nanoscale Thermometry. *Journal of Physical Chemistry C*, 119(36):21116–21124, sep 2015.
- [117] Wei Xie, Bernd Walkenfort, and Sebastian Schlücker. Label-free SERS monitoring of chemical reactions catalyzed by small gold nanoparticles using 3D plasmonic superstructures. *Journal of the American Chemical Society*, 135(5):1657–1660, feb 2013.
- [118] Xin Shi, Hao Wen Li, Yi Lun Ying, Chang Liu, Li Zhang, and Yi Tao Long. In situ monitoring of catalytic process variations in a single nanowire by dark-field-assisted surface-enhanced Raman spectroscopy. *Chemical Communications*, 52(5):1044–1047, jan 2016.

- [119] Dan Wang, Faxing Shi, Jesil Jose, Yanfang Hu, Cancan Zhang, Aonan Zhu, Roland Grzeschik, Sebastian Schlücker, and Wei Xie. In Situ Monitoring of Palladium-Catalyzed Chemical Reactions by Nanogap-Enhanced Raman Scattering using Single Pd Cube Dimers. *Journal of the American Chemical Society*, 144(11):5003–5009, mar 2022.
- [120] Leilei Kang, Ping Xu, Bin Zhang, Hsinhan Tsai, Xijiang Han, and Hsing Lin Wang. Laser wavelength- and power-dependent plasmon-driven chemical reactions monitored using single particle surface enhanced Raman spectroscopy. *Chemical Communications*, 49(33):3389–3391, mar 2013.
- [121] Kun Zhang, Yujie Liu, Yuning Wang, Jingjing Zhao, and Baohong Liu. Direct SERS tracking of a chemical reaction at a single 13 nm gold nanoparticle. *Chemical Science*, 10(6):1741–1745, feb 2019.
- [122] Han Kyu Choi, Won Hwa Park, Chan Gyu Park, Hyun Hang Shin, Kang Sup Lee, and Zee Hwan Kim. Metal-Catalyzed Chemical Reaction of Single Molecules Directly Probed by Vibrational Spectroscopy. *Journal of the American Chemical Society*, 138(13):4673–4684, apr 2016.
- [123] Sangwon Park, Gyu Jin Yeon, Hankyul Lee, Hyun Hang Shin, and Zee Hwan Kim. Self-Referenced SERS Thermometry of Molecules on a Metallic Nanostructure. *Journal of Physical Chemistry C*, 126(1):451–458, jan 2022.
- [124] Andrew J. Wilson and Katherine A. Willets. Visualizing site-specific redox potentials on the surface of plasmonic nanoparticle aggregates with superlocalization SERS microscopy. *Nano Letters*, 14(2):939–945, feb 2014.
- [125] Katherine A. Willets. Super-resolution imaging of SERS hot spots, jun 2014.
- [126] Nathan C. Lindquist, Ariadne Tückmantel Bido, and Alexandre G. Brolo. Single-Molecule SERS Hotspot Dynamics in Both Dry and Aqueous Environments. *Journal of Physical Chemistry C*, 126(16):7117–7126, apr 2022.
- [127] James T. Hugall and Jeremy J. Baumberg. Demonstrating Photoluminescence from Au is Electronic Inelastic Light Scattering of a Plasmonic Metal: The Origin of SERS Backgrounds, apr 2015.
- [128] Jan Mertens, Marie Elena Kleemann, Rohit Chikkaraddy, Prineha Narang, and Jeremy J. Baumberg. How Light Is Emitted by Plasmonic Metals. *Nano Letters*, 17(4):2568–2574, apr 2017.
- [129] Kai Qiang Lin, Jun Yi, Shu Hu, Juan Juan Sun, Jue Ting Zheng, Xiang Wang, and Bin Ren. Intraband Hot-Electron Photoluminescence from Single Silver Nanorods. *ACS Photonics*, 3(7):1248–1255, jul 2016.
- [130] Da Huang, Chad P. Byers, Lin Yung Wang, Anneli Hoggard, Ben Hoener, Sergio Dominguez-Medina, Sishan Chen, Wei Shun Chang, Christy F. Landes, and Stephan Link. Photoluminescence of a Plasmonic Molecule. *ACS Nano*, 9(7):7072–7079, jul 2015.

- [131] Yi Yu Cai, Jun G. Liu, Lawrence J. Tauzin, Da Huang, Eric Sung, Hui Zhang, Anneli Joplin, Wei Shun Chang, Peter Nordlander, and Stephan Link. Photoluminescence of Gold Nanorods: Purcell Effect Enhanced Emission from Hot Carriers. *ACS Nano*, 12(2):976–985, feb 2018.
- [132] M Barella. In situ photothermal response of single gold nanoparticles through hyperspectral imaging anti-stokes thermometry. *ACS Nano*, 15:2458–2467, 2021.
- [133] Y He. Surface enhanced anti-Stokes one-photon luminescence from single gold nanorods. *Nanoscale*, 7:577–582, 2015.
- [134] Lihong Xie, Zhuyu Ai, Meng Zhang, Runze Sun, and Weirong Zhao. Enhanced hydrogen evolution in the presence of plasmonic Au-photo-sensitized g-C₃N₄ with an extended absorption spectrum from 460 to 640 nm. *PLoS ONE*, 11(8):1–22, 2016.
- [135] James T. Hugall and Jeremy J. Baumberg. Demonstrating Photoluminescence from Au is Electronic Inelastic Light Scattering of a Plasmonic Metal: The Origin of SERS Backgrounds, apr 2015.
- [136] A Carattino, M Caldarola, and M Orrit. Gold Nanoparticles as Absolute Nanothermometers. *Nano Lett*, 18:874–880, 2018.
- [137] Y.-Y. Cai. Anti-Stokes Emission from Hot Carriers in Gold Nanorods. *Nano Lett*, 19:1067–1073, 2019.
- [138] Steven Jones, Daniel Andrén, Pawel Karpinski, and Mikael Käll. Photothermal Heating of Plasmonic Nanoantennas: Influence on Trapped Particle Dynamics and Colloid Distribution. *ACS Photonics*, 5(7):2878–2887, jul 2018.
- [139] Evangelina Pensa, Julian Gargiulo, Alberto Lauri, Sebastian Schlücker, Emiliano Cortés, and Stefan A. Maier. Spectral Screening of the Energy of Hot Holes over a Particle Plasmon Resonance. *Nano Letters*, 19(3):1867–1874, mar 2019.
- [140] Shengxiang Wu, Nicki Hogan, and Matthew Sheldon. Hot Electron Emission in Plasmonic Thermionic Converters. *ACS Energy Lett*, 4(10):2508–2513, sep 2019.
- [141] G Baffou. Anti-Stokes Thermometry in Nanoplasmonics. *ACS Nano*, 15:5785–5792, 2021.
- [142] Guillaume Baffou. *Thermoplasmonics: Heating metal nanoparticles using light*. Cambridge University Press, oct 2017.
- [143] Michael T. Carlson, Aurangzeb Khan, and Hugh H. Richardson. Local temperature determination of optically excited nanoparticles and nanodots. *Nano Letters*, 11(3):1061–1069, mar 2011.

- [144] Zheyu Fang, Yu Rong Zhen, Oara Neumann, Albert Polman, F. Javier García De Abajo, Peter Nordlander, and Naomi J. Halas. Evolution of light-induced vapor generation at a liquid-immersed metallic nanoparticle. *Nano Letters*, 13(4):1736–1742, 2013.
- [145] Sjoerd W Nooteboom, Yuyang Wang, Swayandipta Dey, and Peter Zijlstra. Real-Time Interfacial Nanothermometry Using DNA-PAINT Microscopy. *Small*, 18(31):2201602, aug 2022.
- [146] Phillip A. Reinhardt, Abigail P. Crawford, Claire A. West, Gabe DeLong, Stephan Link, David J. Masiello, and Katherine A. Willets. Toward Quantitative Nanothermometry Using Single-Molecule Counting. *Journal of Physical Chemistry B*, 125(44):12197–12205, 2021.
- [147] Faegheh Hajizadeh, Lei Shao, Daniel Andrés, Peter Johansson, Halina Rubinsztein-Dunlop, and Mikael Käll. Brownian fluctuations of an optically rotated nanorod. *Optica*, 4(7):746, 2017.
- [148] G Baffou. Thermal imaging of nanostructures by quantitative optical phase analysis. *ACS Nano*, 6:2452–2458, 2012.
- [149] Ernst Abbe. Beiträge zur Theorie des Mikroskops und der mikroskopischen Wahrnehmung. *Archiv für mikroskopische Anatomie*, 9:413–468, 1973.
- [150] Emiliano Cortés, Wei Xie, Javier Cambiasso, Adam S. Jermyn, Ravishankar Sundararaman, Prineha Narang, Sebastian Schlücker, and Stefan A. Maier. Plasmonic hot electron transport drives nano-localized chemistry. *Nature Communications*, 8(1):1–10, mar 2017.
- [151] Sabrina Simoncelli, Yi Li, Emiliano Cortés, and Stefan A. Maier. Imaging Plasmon Hybridization of Fano Resonances via Hot-Electron-Mediated Absorption Mapping. *Nano Letters*, 18(6):3400–3406, 2018.
- [152] Ningmu Zou, Guanqun Chen, Xianwen Mao, Hao Shen, Eric Choudhary, Xiaochun Zhou, and Peng Chen. Imaging Catalytic Hotspots on Single Plasmonic Nanostructures via Correlated Super-Resolution and Electron Microscopy. *ACS Nano*, 12(6):5570–5579, jun 2018.
- [153] Rifat Kamarudheen, Gabriel W. Castellanos, Leon P.J. Kamp, Herman J.H. Clercx, and Andrea Baldi. Quantifying Photothermal and Hot Charge Carrier Effects in Plasmon-Driven Nanoparticle Syntheses. *ACS Nano*, 12(8):8447–8455, aug 2018.
- [154] Nesha May Andoy, Xiaochun Zhou, Eric Choudhary, Hao Shen, Guokun Liu, and Peng Chen. Single-molecule catalysis mapping quantifies site-specific activity and uncovers radial activity gradient on single 2D nanocrystals. *Journal of the American Chemical Society*, 135(5):1845–1852, feb 2013.

- [155] Linan Zhou, Dayne F. Swearer, Chao Zhang, Hossein Robotjazi, Hangqi Zhao, Luke Henderson, Liangliang Dong, Phillip Christopher, Emily A. Carter, Peter Nordlander, and Naomi J. Halas. Quantifying hot carrier and thermal contributions in plasmonic photocatalysis. *Science*, 362(6410):69–72, 2018.
- [156] Ruben F. Hamans, Rifat Kamarudheen, and Andrea Baldi. Single Particle Approaches to Plasmon-Driven Catalysis. *Nanomaterials*, 10(12):2377, nov 2020.
- [157] Sabrina Simoncelli, Evangelina L. Pensa, Thomas Brick, Julian Gargiulo, Alberto Lauri, Javier Cambiasso, Yi Li, Stefan A. Maier, and Emiliano Cortés. Monitoring plasmonic hot-carrier chemical reactions at the single particle level. *Faraday Discussions*, 214:73–87, 2019.
- [158] Emiliano Cortés, Roland Grzeschik, Stefan A. Maier, and Sebastian Schlücker. Experimental characterization techniques for plasmon-assisted chemistry, apr 2022.
- [159] Eitan Oksenberg, Ilan Shlesinger, Angelos Xomalis, Andrea Baldi, Jeremy J. Baumberg, A. Femius Koenderink, and Erik C. Garnett. Energy-resolved plasmonic chemistry in individual nanoreactors. *Nature Nanotechnology*, 16(12):1378–1385, dec 2021.
- [160] Hacksung Kim, Kathryn M. Kosuda, Richard R. Van Duyne, and Peter C. Stair. Resonance Raman and surface- and tip-enhanced Raman spectroscopy methods to study solid catalysts and heterogeneous catalytic reactions. *Chemical Society Reviews*, 39(12):4820–4844, nov 2010.
- [161] Kevin G. Stamplecoskie, Natalia L. Pacioni, Dayle Larson, and Juan C. Sciano. Plasmon-mediated photopolymerization maps plasmon fields for silver nanoparticles. *Journal of the American Chemical Society*, 133(24):9160–9163, jun 2011.
- [162] Maarten B. J. Roeffaers, Gert De Cremer, Julien Libeert, Rob Ameloot, Peter Dedecker, Anton-Jan Bons, Matthias Bückins, Johan A. Martens, Bert F. Sels, Dirk E. De Vos, and Johan Hofkens. Super-Resolution Reactivity Mapping of Nanostructured Catalyst Particles. *Angewandte Chemie International Edition*, 48(49):9285–9289, nov 2009.
- [163] Xiaochun Zhou, Nesha May Andoy, Guokun Liu, Eric Choudhary, Kyu Sung Han, Hao Shen, and Peng Chen. Quantitative super-resolution imaging uncovers reactivity patterns on single nanocatalysts. *Nature Nanotechnology*, 7(4):237–241, feb 2012.
- [164] Zoran Ristanović, Alexey V. Kubarev, Johan Hofkens, Maarten B.J. Roeffaers, and Bert M. Weckhuysen. Single Molecule Nanospectroscopy Visualizes Proton-Transfer Processes within a Zeolite Crystal. *Journal of the American Chemical Society*, 138(41):13586–13596, oct 2016.

- [165] Ningmu Zou, Xiaochun Zhou, Guanqun Chen, Nesha May Andoy, Won Jung, Guokun Liu, and Peng Chen. Cooperative communication within and between single nanocatalysts. *Nature Chemistry*, 10(6):607–614, jun 2018.
- [166] Guanqun Chen, Ningmu Zou, Bo Chen, Justin B. Sambur, Eric Choudhary, and Peng Chen. Bimetallic Effect of Single Nanocatalysts Visualized by Super-Resolution Catalysis Imaging. *ACS Central Science*, 3(11):1189–1197, nov 2017.
- [167] Ruben F. Hamans, Matteo Parente, and Andrea Baldi. Super-Resolution Mapping of a Chemical Reaction Driven by Plasmonic Near-Fields. *Nano Letters*, 21(5):2149–2155, mar 2021.
- [168] Weilin Xu, Jason S. Kong, Yun Ting E. Yeh, and Peng Chen. Single-molecule nanocatalysis reveals heterogeneous reaction pathways and catalytic dynamics. *Nature Materials*, 7(12):992–996, nov 2008.
- [169] Xiaochun Zhou, Weilin Xu, Guokun Liu, Debashis Panda, and Peng Chen. Size-dependent catalytic activity and dynamics of gold nanoparticles at the single-molecule level. *Journal of the American Chemical Society*, 132(1):138–146, jan 2010.
- [170] Xiaochun Zhou, Eric Choudhary, Nesha May Andoy, Ningmu Zou, and Peng Chen. Scalable parallel screening of catalyst activity at the single-particle level and subdiffraction resolution. *ACS Catalysis*, 3(7):1448–1453, jul 2013.
- [171] Wei Li, Junjian Miao, Tianhuan Peng, Hui Lv, Jun Gang Wang, Kun Li, Ying Zhu, and Di Li. Single-Molecular Catalysis Identifying Activation Energy of the Intermediate Product and Rate-Limiting Step in Plasmonic Photocatalysis. *Nano Letters*, 20(4):2507–2513, apr 2020.
- [172] Tao Chen, Fengxia Tong, Jörg Enderlein, and Zhaoke Zheng. Plasmon-driven modulation of reaction pathways of individual pt-modified au nanorods. *Nano Letters*, 20(5):3326–3330, may 2020.
- [173] Xianwen Mao, Chunming Liu, Mahdi Hesari, Ningmu Zou, and Peng Chen. Super-resolution imaging of non-fluorescent reactions via competition. *Nature Chemistry*, 11(8):687–694, aug 2019.
- [174] Leonardo Scarabelli, Ana Sánchez-Iglesias, Jorge Pérez-Juste, and Luis M. Liz-Marzán. A "Tips and Tricks" Practical Guide to the Synthesis of Gold Nanorods. *Journal of Physical Chemistry Letters*, 6(21):4270–4279, nov 2015.
- [175] C. Bueno, M. L. Villegas, S. G. Bertolotti, C. M. Previtali, M. G. Neumann, and M. V. Encinas. The Excited-State Interaction of Resazurin and Resorufin with Amines in Aqueous Solutions. Photophysics and Photochemical Reaction. *Photochemistry and Photobiology*, 76(4):385–390, oct 2002.
- [176] A. Balcerzyk and G. Baldacchino. Implementation of laser induced fluorescence in a pulse radiolysis experiment - A new way to analyze resazurin-like reduction mechanisms. *Analyst*, 139(7):1707–1712, mar 2014.

- [177] Walter A. Prütz, John Butler, and Edward J. Land. Photocatalytic and free radical interactions of the heterocyclic N-oxide resazurin with NADH, GSH, and Dopa. *Archives of Biochemistry and Biophysics*, 327(2):239–248, mar 1996.
- [178] Charles N. Satterfield. *Heterogeneous catalysis in practice*. McGraw-Hill Company, may 1980.
- [179] Bhogeswararao Seemala, Andrew J. Therrien, Minhan Lou, Kun Li, Jordan P. Finzel, Ji Qi, Peter Nordlander, and Phillip Christopher. Plasmon-Mediated Catalytic O₂ Dissociation on Ag Nanostructures: Hot Electrons or Near Fields? *ACS Energy Letters*, 4(8):1803–1809, aug 2019.
- [180] Bishnu P. Biswal, Hugo A. Vignolo-González, Tanmay Banerjee, Lars Grunenberg, Gökçen Savasci, Kerstin Gottschling, Jürgen Nuss, Christian Ochsenfeld, and Bettina V. Lotsch. Sustained Solar H₂ Evolution from a Thiazolo[5,4-d]thiazole-Bridged Covalent Organic Framework and Nickel-Thiolate Cluster in Water. *Journal of the American Chemical Society*, 141(28):11082–11092, jun 2019.
- [181] Hiroyuki Takeda, Yu Monma, Haruki Sugiyama, Hidehiro Uekusa, and Osamu Ishitani. Development of visible-light driven Cu(I) complex photosensitizers for photocatalytic CO₂ reduction. *Frontiers in Chemistry*, 7(JUN):418, jun 2019.
- [182] Katja Willinger and Mukundan Thelakkat. Photosensitizers in solar energy conversion. In *Photosensitizers in Medicine, Environment, and Security*, volume 9789048138, pages 527–617. Springer Netherlands, mar 2014.
- [183] Nathan T. La Porte, Jose F. Martinez, Subhajyoti Chaudhuri, Svante Hedström, Victor S. Batista, and Michael R. Wasielewski. Photoexcited radical anion super-reductants for solar fuels catalysis. *Coordination Chemistry Reviews*, 361:98–119, apr 2018.
- [184] Julian Gargiulo, Matias Herran, Ana Sousa-Castillo, Luciana Martinez, Simone Ezendam, Mariano Barella, Helene Giesler, Roland Grzeschik, Sebastian Schluecker, Stefan Maier, Fernando Stefani, and Emiliano Cortes. Single particle thermometry in bimetallic plasmonic nanostructures. pages 1–25, dec 2022.
- [185] Suljo Linic, Phillip Christopher, and David B. Ingram. Plasmonic-metal nanostructures for efficient conversion of solar to chemical energy. *Nature Materials*, 10(12):911–921, 2011.
- [186] Phillip Christopher, Hongliang Xin, and Suljo Linic. Visible-light-enhanced catalytic oxidation reactions on plasmonic silver nanostructures. *Nature Chemistry*, 3(6):467–472, jun 2011.
- [187] Phillip Christopher, Hongliang Xin, Andiappan Marimuthu, and Suljo Linic. Singular characteristics and unique chemical bond activation mechanisms of photocatalytic reactions on plasmonic nanostructures. *Nature Materials*, 11(12):1044–1050, dec 2012.

- [188] Suljo Linic, Umar Aslam, Calvin Boerigter, and Matthew Morabito. Photochemical transformations on plasmonic metal nanoparticles. *Nature Materials*, 14(6):567–576, may 2015.
- [189] Shaunak Mukherjee, Florian Libisch, Nicolas Large, Oara Neumann, Lisa V. Brown, Jin Cheng, J. Britt Lassiter, Emily A. Carter, Peter Nordlander, and Naomi J. Halas. Hot electrons do the impossible: Plasmon-induced dissociation of H₂ on Au. *Nano Letters*, 13(1):240–247, jan 2013.
- [190] Rifat Kamarudheen, Guus J. W. Aalbers, Ruben F. Hamans, Leon P. J. Kamp, and Andrea Baldi. Distinguishing Among All Possible Activation Mechanisms of a Plasmon-Driven Chemical Reaction. *ACS Energy Letters*, 5(8):2605–2613, aug 2020.
- [191] Steven Bardey, Audrey Bonduelle-Skrzypczak, Antoine Fécant, Zhenpeng Cui, Christophe Colbeau-Justin, Valérie Caps, and Valérie Keller. Plasmonic photocatalysis applied to solar fuels. *Faraday Discussions*, 214(0):417–439, may 2019.
- [192] Andiappan Marimuthu, Jianwen Zhang, and Suljo Linic. Tuning selectivity in propylene epoxidation by plasmon mediated photo-switching of Cu oxidation state. *Science*, 340(6127):1590–1593, mar 2013.
- [193] Shaunak Mukherjee, Linan Zhou, Amanda M. Goodman, Nicolas Large, Ciceron Ayala-Orozco, Yu Zhang, Peter Nordlander, and Naomi J. Halas. Hot-electron-induced dissociation of H₂ on gold nanoparticles supported on SiO₂. *Journal of the American Chemical Society*, 136(1):64–67, jan 2014.
- [194] Dayne F. Swearer, Hangqi Zhao, Linan Zhou, Chao Zhang, Hossein Robatjazi, John Mark P. Martinez, Caroline M. Krauter, Sadegh Yazdi, Michael J. McClain, Emilie Ringe, Emily A. Carter, Peter Nordlander, and Naomi J. Halas. Heterometallic antenna-reactor complexes for photocatalysis. *Proceedings of the National Academy of Sciences of the United States of America*, 113(32):8916–8920, aug 2016.
- [195] Umar Aslam, Steven Chavez, and Suljo Linic. Controlling energy flow in multimetallic nanostructures for plasmonic catalysis. *Nature Nanotechnology*, 12(10):1000–1005, 2017.
- [196] Juan Li, Xiaohao Xu, Baibiao Huang, Zaizhu Lou, and Baojun Li. Light-Induced in Situ Formation of a Nonmetallic Plasmonic MoS₂/MoO_{3-x} Heterostructure with Efficient Charge Transfer for CO₂ Reduction and SERS Detection. *ACS Applied Materials and Interfaces*, 13(8):10047–10053, 2021.
- [197] Rengui Li, Wen Hui Cheng, Matthias H. Richter, Joseph S. Duchene, Wenming Tian, Can Li, and Harry A. Atwater. Unassisted Highly Selective Gas-Phase CO₂ Reduction with a Plasmonic Au/p-GaN Photocatalyst Using H₂O as an Electron Donor. *ACS Energy Letters*, 6(5):1849–1856, 2021.

- [198] Emiliano Cortés. Activating plasmonic chemistry: Plasmonic photocatalysts can reduce activation barriers and unlock reaction pathways. *Science*, 362(6410):28–29, oct 2018.
- [199] B. Hammer and J. K. Norskov. Why gold is the noblest of all the metals. *Nature*, 376(6537):238–240, jul 1995.
- [200] Jacques A. Esterhuizen, Bryan R. Goldsmith, and Suljo Linic. Theory-Guided Machine Learning Finds Geometric Structure-Property Relationships for Chemisorption on Subsurface Alloys. *Chem*, 6(11):3100–3117, nov 2020.
- [201] Pekka Peljo, José A. Manzanares, and Hubert H. Girault. Contact Potentials, Fermi Level Equilibration, and Surface Charging. *Langmuir*, 32(23):5765–5775, 2016.
- [202] Kun Li, Nathaniel J. Hogan, Matthew J. Kale, Naomi J. Halas, Peter Nordlander, Phillip Christopher, Nathaniel J. Hogan, Matthew J. Kale, Naomi J. Halas, Peter Nordlander, and Phillip Christopher. Balancing Near-Field Enhancement, Absorption, and Scattering for Effective Antenna-Reactor Plasmonic Photocatalysis. *Nano Letters*, 17(6):3710–3717, may 2017.
- [203] Jhon Quiroz, Eduardo C. M. Barbosa, Thaylan P. Araujo, Jhonatan L. Fiorio, Yi-Chi Chi Wang, Yi-Chao Chao Zou, Tong Mou, Tiago V. Alves, Daniela C. de Oliveira, Bin Wang, Sarah J. Haigh, Liane M. Rossi, Pedro H. C. Camargo, Eduardo C.M. Barbosa, Thaylan P. Araujo, Jhonatan L. Fiorio, Yi-Chi Chi Wang, Yi-Chao Chao Zou, Tong Mou, Tiago V. Alves, Daniela C. De Oliveira, Bin Wang, Sarah J. Haigh, Liane M. Rossi, and Pedro H.C. Camargo. Controlling Reaction Selectivity over Hybrid Plasmonic Nanocatalysts. *Nano Letters*, 18(11):7289–7297, oct 2018.
- [204] Steven Chavez, Umar Aslam, and Suljo Linic. Design Principles for Directing Energy and Energetic Charge Flow in Multicomponent Plasmonic Nanostructures. *ACS Energy Letters*, 3(7):1590–1596, jun 2018.
- [205] Christian Engelbrekt, Kevin T. Crampton, Dmitry A. Fishman, Matt Law, and Vartkess Ara Apkarian. Efficient Plasmon-Mediated Energy Funneling to the Surface of Au@Pt Core-Shell Nanocrystals. *ACS nano*, 14(4):5061–5074, apr 2020.
- [206] Hideyuki Inouye, Koichiro Tanaka, and Ichiro Tanahashi. Ultrafast dynamics of nonequilibrium electrons in a gold nanoparticle system. *Physical Review B - Condensed Matter and Materials Physics*, 57(18):11334–11340, 1998.
- [207] Huang Jing Wei Li, Huimin Zhou, Kejun Chen, Kang Liu, Shi Li, Kexin Jiang, Wenhao Zhang, Yanbo Xie, Zhou Cao, Hongmei Li, Hui Liu, Xiaowen Xu, Hao Pan, Junhua Hu, Dongsheng Tang, Xiaoqing Qiu, Junwei Fu, and Min Liu. Metallic MoO₂-Modified Graphitic Carbon Nitride Boosting Photocatalytic CO₂ Reduction via Schottky Junction. *Solar RRL*, 4(8):1900416, aug 2020.

- [208] K. Wu, J. Chen, J. R. McBride, and T. Lian. Efficient hot-electron transfer by a plasmon-induced interfacial charge-transfer transition. *Science*, 349(6248):632–635, aug 2015.
- [209] Priyank V. Kumar, Tuomas P. Rossi, Daniel Marti-Dafcik, Daniel Reichmuth, Mikael Kuisma, Paul Erhart, Martti J. Puska, and David J. Norris. Plasmon-Induced Direct Hot-Carrier Transfer at Metal-Acceptor Interfaces. *ACS Nano*, 13(3):3188–3195, mar 2019.
- [210] Jiangtian Li, Scott K. Cushing, Fanke Meng, Tess R. Senty, Alan D. Bristow, and Nianqiang Wu. Plasmon-induced resonance energy transfer for solar energy conversion. *Nature Photonics*, 9(9):601–607, sep 2015.
- [211] Scott K. Cushing, Jiangtian Li, Fanke Meng, Tess R. Senty, Savan Suri, Mingjia Zhi, Ming Li, Alan D. Bristow, and Nianqiang Wu. Photocatalytic activity enhanced by plasmonic resonant energy transfer from metal to semiconductor. *Journal of the American Chemical Society*, 134(36):15033–15041, sep 2012.
- [212] Bob Y. Zheng, Hangqi Zhao, Alejandro Manjavacas, Michael McClain, Peter Nordlander, and Naomi J. Halas. Distinguishing between plasmon-induced and photoexcited carriers in a device geometry. *Nature Communications*, 6(1):1–7, jul 2015.
- [213] Alberto Naldoni, Urcan Guler, Zhuoxian Wang, Marcello Marelli, Francesco Malara, Xiangeng Meng, Lucas V. Besteiro, Alexander O. Govorov, Alexander V. Kildishev, Alexandra Boltasseva, and Vladimir M. Shalaev. Broadband Hot-Electron Collection for Solar Water Splitting with Plasmonic Titanium Nitride. *Advanced Optical Materials*, 5(15):1601031, aug 2017.
- [214] Jacqueline B. Priebe, Jörg Radnik, Alastair J. J. Lennox, Marga-Martina Martina Pohl, Michael Karnahl, Dirk Hollmann, Kathleen Grabow, Ursula Bentrup, Henrik Junge, Matthias Beller, Angelika Brückner, Jacqueline B. Priebe, Jörg Radnik, Alastair J.J. Lennox, Marga-Martina Martina Pohl, Michael Karnahl, Dirk Hollmann, Kathleen Grabow, Ursula Bentrup, Henrik Junge, Matthias Beller, and Angelika Brückner. Solar Hydrogen Production by Plasmonic Au-TiO₂ Catalysts: Impact of Synthesis Protocol and TiO₂ Phase on Charge Transfer Efficiency and H₂ Evolution Rates. *ACS Catalysis*, 5(4):2137–2148, mar 2015.
- [215] Joseph S. Duchene, Giulia Tagliabue, Alex J. Welch, Xueqian Li, Wen Hui Cheng, and Harry A. Atwater. Optical Excitation of a Nanoparticle Cu/p-NiO Photocathode Improves Reaction Selectivity for CO₂ Reduction in Aqueous Electrolytes. *Nano Letters*, 20(4):2348–2358, apr 2020.
- [216] Umar Aslam, Vishal Govind Rao, Steven Chavez, and Suljo Linic. Catalytic conversion of solar to chemical energy on plasmonic metal nanostructures. *Nature Catalysis*, 1(9):656–665, sep 2018.

- [217] Aaron Bayles, Sol Carretero-Palacios, Laura Calió, Gabriel Lozano, Mauricio E. Calvo, and Hernán Míguez. Localized surface plasmon effects on the photo-physics of perovskite thin films embedding metal nanoparticles. *Journal of Materials Chemistry C*, 8(3):916–921, jan 2020.
- [218] Krystyna Kolwas and Anastasiya Derkachova. Modification of Solar Energy Harvesting in Photovoltaic Materials by Plasmonic Nanospheres: New Absorption Bands in Perovskite Composite Film. *Journal of Physical Chemistry C*, 121(8):4524–4539, 2017.
- [219] S. Carretero-Palacios, M. E. Calvo, and H. Míguez. Absorption Enhancement in Organic-Inorganic Halide Perovskite Films with Embedded Plasmonic Gold Nanoparticles. *Journal of Physical Chemistry C*, 119(32):18635–18640, 2015.
- [220] Maogang Gong, Mohammed Alamri, Dan Ewing, Seyed M. Sadeghi, and Judy Z. Wu. Localized Surface Plasmon Resonance Enhanced Light Absorption in AuCu/CsPbCl₃ Core/Shell Nanocrystals. *Advanced Materials*, 32(26):2002163, jul 2020.
- [221] Duo Xu, Dong Liu, Tao Xie, Yue Cao, Jun Gang Wang, Zhi Jun Ning, Yi Tao Long, and He Tian. Plasmon resonance scattering at perovskite CH₃NH₃PbI₃ coated single gold nanoparticles: Evidence for electron transfer. *Chemical Communications*, 52(64):9933–9936, 2016.
- [222] Yanbin Huang, Jun Liu, Dawei Cao, Zheming Liu, Kuankuan Ren, Kong Liu, Aiwei Tang, Zhanguo Zhijie Wang, Long Li, Shengchun Qu, and Zhanguo Zhijie Wang. Separation of hot electrons and holes in Au/LaFeO₃ to boost the photocatalytic activities both for water reduction and oxidation. *International Journal of Hydrogen Energy*, 44(26):13242–13252, may 2019.
- [223] Sampson Adjokatse, Hong Hua Fang, and Maria Antonietta Loi. Broadly tunable metal halide perovskites for solid-state light-emission applications. *Materials Today*, 20(8):413–424, oct 2017.
- [224] Lu Qiao, Wei Hai Fang, Run Long, and Oleg V. Prezhdo. Photoinduced Dynamics of Charge Carriers in Metal Halide Perovskites from an Atomistic Perspective. *Journal of Physical Chemistry Letters*, 11(17):7066–7082, sep 2020.
- [225] Yimin Kang, Sina Najmaei, Zheng Liu, Yanjun Bao, Yumin Wang, Xing Zhu, Naomi J. Halas, Peter Nordlander, Pulickel M. Ajayan, Jun Lou, and Zheyu Fang. Plasmonic Hot Electron Induced Structural Phase Transition in a MoS₂ Monolayer. *Advanced Materials*, 26(37):6467–6471, oct 2014.
- [226] Songmei Sun, Qi An, Motonori Watanabe, Junfang Cheng, Hack Ho Kim, Taner Akbay, Atsushi Takagaki, and Tatsumi Ishihara. Highly correlation of CO₂ reduction selectivity and surface electron Accumulation: A case study of Au-MoS₂ and Ag-MoS₂ catalyst. *Applied Catalysis B: Environmental*, 271:118931, 2020.

- [227] C H Lui, A J Frenzel, D V Pilon, Y.-H. Lee, X Ling, G M Akselrod, J Kong, and N Gedik. Trion-Induced Negative Photoconductivity in Monolayer MoS₂. *Phys. Rev. Lett.*, 113(16):166801, oct 2014.
- [228] Rongrong Pan, Jia Liu, and Jiatao Zhang. Defect Engineering in 2D Photocatalytic Materials for CO₂ Reduction. *ChemNanoMat*, 7(7):737–747, jul 2021.
- [229] Maw Lin Foo, Ryotaro Matsuda, and Susumu Kitagawa. Functional Hybrid Porous Coordination Polymers. *Chemistry of Materials*, 26(1):310–322, nov 2013.
- [230] Gérard Férey. Hybrid porous solids: past, present, future. *Chemical Society Reviews*, 37(1):191–214, 2008.
- [231] Hiroyasu Furukawa, Kyle E Cordova, Michael O’Keeffe, and Omar M Yaghi. The Chemistry and Applications of Metal-Organic Frameworks. *Science*, 341(6149):1230444, aug 2013.
- [232] Charlynn Sher Lin Koh, Howard Yi Fan Sim, Shi Xuan Leong, Siew Kheng Boong, Carice Chong, and Xing Yi Ling. Plasmonic Nanoparticle-Metal-Organic Framework (NP-MOF) Nanohybrid Platforms for Emerging Plasmonic Applications. *ACS Materials Letters*, 3(5):557–573, may 2021.
- [233] Minmin Wang, Yanfeng Tang, and Yongdong Jin. Modulating Catalytic Performance of Metal-Organic Framework Composites by Localized Surface Plasmon Resonance. *ACS Catalysis*, 9(12):11502–11514, dec 2019.
- [234] Guodong Li, Shenlong Zhao, Yin Zhang, and Zhiyong Tang. Metal-organic frameworks encapsulating active nanoparticles as emerging composites for catalysis: Recent progress and perspectives. *Advanced Materials*, 30(51):1800702, dec 2018.
- [235] Feihu Mu, Benlin Dai, Wei Zhao, Shijian Zhou, Haibao Huang, Gang Yang, Dehua Xia, Yan Kong, and Dennis Y C Leung. Construction of a novel Ag/Ag₃PO₄/MIL-68(In)-NH₂ plasmonic heterojunction photocatalyst for high-efficiency photocatalysis. *Journal of Materials Science and Technology*, 101(28):37–48, 2021.
- [236] Li-Wei Chen, Yu-Chen Hao, Yu Guo, Qinghua Zhang, Jiani Li, Wen-Yan Gao, Lantian Ren, Xin Su, Linyu Hu, Nan Zhang, Siwu Li, Xiao Feng, Lin Gu, Ya-Wen Zhang, An-Xiang Yin, and Bo Wang. Metal-Organic Framework Membranes Encapsulating Gold Nanoparticles for Direct Plasmonic Photocatalytic Nitrogen Fixation. *Journal of the American Chemical Society*, 143(15):5727–5736, apr 2021.
- [237] Kyung Min Choi, Dohyung Kim, Bunyarat Rungtaweivoranit, Christopher A. Trickett, Jesika Trese Deniz Barmanbek, Ahmad S. Alshammari, Peidong Yang, and Omar M. Yaghi. Plasmon-enhanced photocatalytic CO₂ conversion within metal-organic frameworks under visible light. *Journal of the American Chemical Society*, 139(1):356–362, jan 2017.

- [238] Meicheng Wen, Kohsuke Mori, Yasutaka Kuwahara, and Hiromi Yamashita. Plasmonic Au@Pd nanoparticles supported on a basic metal-organic framework: Synergic boosting of H₂ production from formic acid. *ACS Energy Letters*, 2(1):1–7, jan 2017.
- [239] Jorge Becerra, Duc-Trung Nguyen, Vishnu-Nair Gopalakrishnan, and Trong-On Do. Plasmonic Au Nanoparticles Incorporated in the Zeolitic Imidazolate Framework (ZIF-67) for the Efficient Sunlight-Driven Photoreduction of CO₂. *ACS Applied Energy Materials*, 3(8):7659–7665, 2020.
- [240] Hossein Robatjazi, Daniel Weinberg, Dayne F. Swearer, Christian Jacobson, Ming Zhang, Shu Tian, Linan Zhou, Peter Nordlander, and Naomi J. Halas. Metal-organic frameworks tailor the properties of aluminum nanocrystals. *Science Advances*, 5(2):eaav5340, feb 2019.
- [241] Juan Ding Xiao, Lili Han, Jun Luo, Shu Hong Yu, and Hai Long Jiang. Integration of Plasmonic Effects and Schottky Junctions into Metal–Organic Framework Composites: Steering Charge Flow for Enhanced Visible-Light Photocatalysis. *Angewandte Chemie - International Edition*, 57(4):1103–1107, jan 2018.
- [242] Electrocatalysis for the generation and consumption of fuels, mar 2018.
- [243] Esteban Landaeta, Rafael A. Masitas, Thomas B. Clarke, Simon Rafacz, Darby A. Nelson, Mauricio Isaacs, and Zachary D. Schultz. Copper-Oxide-Coated Silver Nanodendrites for Photoelectrocatalytic CO₂ Reduction to Acetate at Low Overpotential. *ACS Applied Nano Materials*, 3(4):3478–3486, apr 2020.
- [244] Weiwei Lu, Fengyang Ju, Kaisheng Yao, and Xuefeng Wei. Photoelectrocatalytic reduction of CO₂ for efficient methanol production: Au nanoparticles as electrocatalysts and light supports. *Industrial and Engineering Chemistry Research*, 59(10):4348–4357, mar 2020.
- [245] Xianhong Wu, Junhui Wang, Zhiyu Wang, Fu Sun, Yuzhao Liu, Kaifeng Wu, Xiangyu Meng, and Jieshan Qiu. Boosting the Electrocatalysis of MXenes by Plasmon-Induced Thermalization and Hot-Electron Injection. *Angewandte Chemie - International Edition*, 60(17):9416–9420, 2021.
- [246] Erin B. Creel, Elizabeth R. Corson, Johanna Eichhorn, Robert Kostecki, Jeffrey J. Urban, and Bryan D. McCloskey. Directing Selectivity of Electrochemical Carbon Dioxide Reduction Using Plasmonics. *ACS Energy Letters*, 4(5):1098–1105, may 2019.
- [247] Emily K. Piggott, Taylor O. Hope, Bry W. Crabbe, Pierre Michel Jalbert, Galina Orlova, and Geniece L. Hallett-Tapley. Exploiting the photocatalytic activity of gold nanoparticle-functionalized niobium oxide perovskites in nitroarene reductions. *Catalysis Science and Technology*, 7(23):5758–5765, nov 2017.

- [248] Jiawen Liu, Yue Sun, Zhonghua Li, Shuying Li, and Jingxiang Zhao. Photocatalytic hydrogen production from water/methanol solutions over highly ordered Ag-SrTiO₃ nanotube arrays. *International Journal of Hydrogen Energy*, 36(10):5811–5816, may 2011.
- [249] Severin N. Habisreutinger, Lukas Schmidt-Mende, and Jacek K. Stolarczyk. Photocatalytic reduction of CO₂ on TiO₂ and other semiconductors. *Angewandte Chemie - International Edition*, 52(29):7372–7408, jul 2013.
- [250] Silvia E. Braslavsky, André M. Braun, Alberto E. Cassano, Alexei V. Emeline, Marta I. Litter, Leonardo Palmisano, Valentin N. Parmon, and Nick Serpone. Glossary of terms used in photocatalysis and radiation catalysis (IUPAC recommendations 2011). *Pure and Applied Chemistry*, 83(4):931–1014, mar 2011.
- [251] Guillaume Baffou, Romain Quidant, and F. Javier García De Abajo. Nanoscale control of optical heating in complex plasmonic systems. *ACS Nano*, 4(2):709–716, feb 2010.
- [252] Peng Xu, Weiwei Lu, Jinjin Zhang, and Li Zhang. Efficient Hydrolysis of Ammonia Borane for Hydrogen Evolution Catalyzed by Plasmonic Ag@Pd Core-Shell Nanocubes. *ACS Sustainable Chemistry and Engineering*, 8(33):12366–12377, 2020.
- [253] Kaisheng Yao, Chenchen Zhao, Nan Wang, Tianji Li, Weiwei Lu, and Jianji Wang. An aqueous synthesis of porous PtPd nanoparticles with reversed bimetallic structures for highly efficient hydrogen generation from ammonia borane hydrolysis. *Nanoscale*, 12(2):638–647, 2020.
- [254] Jing Liang Yang, Yong Lin He, He Ren, Han Liang Zhong, Jia Sheng Lin, Wei Min Yang, Ming De Li, Zhi Lin Yang, Hua Zhang, Zhong Qun Tian, and Jian Feng Li. Boosting photocatalytic hydrogen evolution reaction using dual plasmonic antennas. *ACS Catalysis*, 11(9):5047–5053, 2021.
- [255] Sen Zhang, Önder Metin, Dong Su, and Shouheng Sun. Monodisperse AgPd alloy nanoparticles and their superior catalysis for the dehydrogenation of formic acid. *Angewandte Chemie - International Edition*, 52(13):3681–3684, 2013.
- [256] Lipei Qin, Guojing Wang, and Yiwei Tan. Plasmonic Pt nanoparticles—TiO₂ hierarchical nano-architecture as a visible light photocatalyst for water splitting. *Scientific Reports*, 8(1):1–13, 2018.
- [257] Shunqin Luo, Huiwen Lin, Qi Wang, Xiaohui Ren, David Hernández-Pinilla, Tadaaki Nagao, Yao Xie, Gaoliang Yang, Sijie Li, Hui Song, Mitsutake Oshikiri, and Jinhua Ye. Triggering Water and Methanol Activation for Solar-Driven H₂ Production: Interplay of Dual Active Sites over Plasmonic ZnCu Alloy. *Journal of the American Chemical Society*, 143(31):12145–12153, aug 2021.
- [258] Xiaoyong Xu, Fengting Luo, Wenshuai Tang, Jingguo Hu, Haibo Zeng, and Yong Zhou. Enriching Hot Electrons via NIR-Photon-Excited Plasmon in WS₂@Cu

- Hybrids for Full-Spectrum Solar Hydrogen Evolution. *Advanced Functional Materials*, 28(43):1–8, 2018.
- [259] Zhao Mo, Hui Xu, Zhigang Chen, Xiaojie She, Yanhua Song, Jiabiao Lian, Xingwang Zhu, Pengcheng Yan, Yucheng Lei, Shouqi Yuan, and Huaming Li. Construction of MnO_2 /Monolayer g- C_3N_4 with Mn vacancies for Z-scheme overall water splitting. *Applied Catalysis B: Environmental*, 241:452–460, 2019.
- [260] Shuaijun Wang, Jinqiang Zhang, Bin Li, Hongqi Sun, and Shaobin Wang. Engineered Graphitic Carbon Nitride-Based Photocatalysts for Visible-Light-Driven Water Splitting: A Review. *Energy & Fuels*, 35(8):6504–6526, apr 2021.
- [261] Fan Guo, Sizhuo Yang, Yi Liu, Peng Wang, Jier Huang, and Wei-Yin Sun. Size Engineering of Metal–Organic Framework MIL-101(Cr)–Ag Hybrids for Photocatalytic CO_2 Reduction. *ACS Catalysis*, 9(9):8464–8470, 2019.
- [262] Rui Zhou, Yuanchao Yin, Deng Long, Jingqin Cui, Huangping Yan, Wanshan Liu, and Jia Hong Pan. PVP-assisted laser ablation growth of Ag nanocubes anchored on reduced graphene oxide (rGO) for efficient photocatalytic CO_2 reduction. *Progress in Natural Science: Materials International*, 29(6):660–666, 2019.
- [263] Hongzhi Wang, Hongpan Rong, Dong Wang, Xinyuan Li, Erhuan Zhang, Xiaodong Wan, Bing Bai, Meng Xu, Jiajia Liu, Jiajia Liu, Wenxing Chen, and Jiatao Zhang. Highly Selective Photoreduction of CO_2 with Suppressing H_2 Evolution by Plasmonic Au/CdSe– Cu_2O Hierarchical Nanostructures under Visible Light. *Small*, 16(18):2000426, 2020.
- [264] Guilan Xu, Huabin Zhang, Jing Wei, Hai Xia Zhang, Xin Wu, Yang Li, Chunsen Li, Jian Zhang, and Jinhua Ye. Integrating the g- C_3N_4 Nanosheet with B-H Bonding Decorated Metal-Organic Framework for CO_2 Activation and Photoreduction. *ACS Nano*, 12(6):5333–5340, 2018.
- [265] Muhammad Tahir and Beenish Tahir. Constructing a Stable 2D/2D Heterojunction of Oxygen-Cluster-Modified Ti_3AlC_2 MAX Cocatalyst with Proton-Rich C_3N_4 for Highly Efficient Photocatalytic CO_2 Methanation. *Industrial and Engineering Chemistry Research*, 59(21):9841–9857, 2020.
- [266] Liyong Chen, Yanxin Wang, Fengyang Yu, Xiaoshuang Shen, and Chunying Duan. A simple strategy for engineering heterostructures of Au nanoparticle-loaded metal-organic framework nanosheets to achieve plasmon-enhanced photocatalytic CO_2 conversion under visible light. *Journal of Materials Chemistry A*, 7(18):11355–11361, 2019.
- [267] Emiliano Cortés. Light-activated catalysts point the way to sustainable chemistry. *Nature*, feb 2023.

- [268] Zaizhu Lou, Mamoru Fujitsuka, and Tetsuro Majima. Two-Dimensional Au-Nanoprism/Reduced Graphene Oxide/Pt-Nanoframe as Plasmonic Photocatalysts with Multiplasmon Modes Boosting Hot Electron Transfer for Hydrogen Generation. *Journal of Physical Chemistry Letters*, 8(4):844–849, 2017.
- [269] Emiliano Cortés, Lucas V. Besteiro, Alessandro Alabastri, Andrea Baldi, Giulia Tagliabue, Angela Demetriadou, and Prineha Narang. Challenges in Plasmonic Catalysis. *ACS Nano*, 14(12):16202–16219, dec 2020.
- [270] Linan Zhou, John Mark P. Martirez, Jordan Finzel, Chao Zhang, Dayne F. Swearer, Shu Tian, Hossein Robatjazi, Minhan Lou, Liangliang Dong, Luke Henderson, Phillip Christopher, Emily A. Carter, Peter Nordlander, and Naomi J. Halas. Light-driven methane dry reforming with single atomic site antenna-reactor plasmonic photocatalysts. *Nature Energy*, 5(1):61–70, jan 2020.
- [271] Chao Zhang, Hangqi Zhao, Linan Zhou, Andrea E. Schlather, Liangliang Dong, Michael J. McClain, Dayne F. Swearer, Peter Nordlander, and Naomi J. Halas. Al-Pd Nanodisk Heterodimers as Antenna-Reactor Photocatalysts. *Nano Letters*, 16(10):6677–6682, oct 2016.
- [272] Dayne F. Swearer, Hossein Robatjazi, John Mark P. Martirez, Ming Zhang, Linan Zhou, Emily A. Carter, Peter Nordlander, and Naomi J. Halas. Plasmonic Photocatalysis of Nitrous Oxide into N₂ and O₂ Using Aluminum-Iridium Antenna-Reactor Nanoparticles. *ACS Nano*, 13(7):8076–8086, jul 2019.
- [273] Limin Guo, Caifu Zhong, Jinqing Cao, Yanan Hao, Ming Lei, Ke Bi, Qijun Sun, and Zhong Lin Wang. Enhanced photocatalytic H₂ evolution by plasmonic and piezotronic effects based on periodic Al/BaTiO₃ heterostructures. *Nano Energy*, 62(April):513–520, 2019.
- [274] Tingbo Huang, Zhixiong Xu, Gongchang Zeng, Piyong Zhang, Ting Song, Youliang Wang, Tingting Wang, Shaobin Huang, Tingting Wang, and Heping Zeng. Selective deposition of plasmonic copper on few layers graphene with specific defects for efficiently synchronous photocatalytic hydrogen production. *Carbon*, 143:257–267, 2019.
- [275] Florian Sterl, Nikolai Strohfeldt, Ramon Walter, Ronald Griessen, Andreas Tittl, and Harald Giessen. Magnesium as novel material for active plasmonics in the visible wavelength range. *Nano Letters*, 15(12):7949–7955, dec 2015.
- [276] Ilka Kriegel, Francesco Scotognella, and Liberato Manna. Plasmonic doped semiconductor nanocrystals: Properties, fabrication, applications and perspectives, feb 2017.
- [277] Ankit Agrawal, Shin Hum Cho, Omid Zandi, Sandeep Ghosh, Robert W. Johns, and Delia J. Milliron. Localized Surface Plasmon Resonance in Semiconductor Nanocrystals, mar 2018.

- [278] Narayan Pradhan, Samrat Das Adhikari, Angshuman Nag, and D. D. Sarma. Luminescence, Plasmonic, and Magnetic Properties of Doped Semiconductor Nanocrystals. *Angewandte Chemie International Edition*, 56(25):7038–7054, jun 2017.
- [279] Gururaj V. Naik, Vladimir M. Shalaev, and Alexandra Boltasseva. Alternative Plasmonic Materials: Beyond Gold and Silver. *Advanced Materials*, 25(24):3264–3294, jun 2013.
- [280] Horst Kisch and Detlef Bahnemann. Best Practice in Photocatalysis: Comparing Rates or Apparent Quantum Yields? *Journal of Physical Chemistry Letters*, 6(10):1907–1910, may 2015.
- [281] ISO. ISO - ISO 22197-1:2016 - Fine ceramics (advanced ceramics, advanced technical ceramics) — Test method for air-purification performance of semiconducting photocatalytic materials — Part 1: Removal of nitric oxide, 2016.
- [282] V Amendola, R Pilot, M Frasconi, O M Maragò, and M A Iatì. Surface plasmon resonance in gold nanoparticles: a review. *J. Phys. Condens. Matter*, 29:203002, 2017.
- [283] Jacob B. Khurgin. How to deal with the loss in plasmonics and metamaterials. *Nature Nanotechnology*, 10(1):2–6, 2015.
- [284] Guohua Liu, Jinliang Xu, Ting Chen, and Kaiying Wang. Progress in thermo-plasmonics for solar energy applications. *Physics Reports*, 981:1–50, 2022.
- [285] Marta Quintanilla, Christian Kuttner, Joshua D. Smith, Andreas Seifert, Sara E. Skrabalak, and Luis M. Liz-Marzán. Heat generation by branched Au/Pd nanocrystals: Influence of morphology and composition. *Nanoscale*, 11(41):19561–19570, 2019.
- [286] Ira N. Levine. *Physical Chemistry*. McGraw-Hill Education, sixth edit edition, 2009.
- [287] Y Dubi and Y Sivan. "Hot" electrons in metallic nanostructures—non-thermal carriers or heating? *Light Sci. Appl*, 8, 2019.
- [288] X Zhang. Plasmon-Enhanced Catalysis: Distinguishing Thermal and Nonthermal Effects. *Nano Lett*, 18:1714–1723, 2018.
- [289] G Baffou, I Bordacchini, A Baldi, and R Quidant. Simple experimental procedures to distinguish photothermal from hot-carrier processes in plasmonics. *Light Sci. Appl*, 9:108, 2020.
- [290] Luca Mascaretti, Andrea Schirato, Tiziano Montini, Alessandro Alabastri, Alberto Naldoni, and Paolo Fornasiero. Challenges in temperature measurements in gas-phase photothermal catalysis. *Joule*, 6(8):1727–1732, 2022.

- [291] Dinumol Devasia, Andrew J. Wilson, Jaeyoung Heo, Varun Mohan, and Prashant K. Jain. A rich catalog of C–C bonded species formed in CO₂ reduction on a plasmonic photocatalyst. *Nature Communications*, 12(1):1–10, dec 2021.
- [292] Chao Zhan, Qiu-Xiang Wang, Jun Yi, Liang Chen, De-Yin Wu, Ye Wang, Zhao-Xiong Xie, Martin Moskovits, and Zhong-Qun Tian. Plasmonic nanoreactors regulating selective oxidation by energetic electrons and nanoconfined thermal fields. *Science Advances*, 7(10), oct 2022.
- [293] Katherine Sytwu, Michal Vadai, and Jennifer A. Dionne. Bimetallic nanostructures: combining plasmonic and catalytic metals for photocatalysis. *Advances in Physics: X*, 4(1), 2019.
- [294] Zaizhu Lou, Mamoru Fujitsuka, and Tetsuro Majima. Pt-Au Triangular Nanoprisms with Strong Dipole Plasmon Resonance for Hydrogen Generation Studied by Single-Particle Spectroscopy. *ACS Nano*, 10(6):6299–6305, jun 2016.
- [295] Naixin Kang, Qi Wang, Rodrigue Djeda, Wenjuan Wang, Fangyu Fu, Marta Martinez Moro, Maria De Los Angeles Ramirez, Sergio Moya, Emerson Coy, Lionel Salmon, Jean-Luc Pozzo, and Didier Astruc. Visible-Light Acceleration of H₂ Evolution from Aqueous Solutions of Inorganic Hydrides Catalyzed by Gold-Transition-Metal Nanoalloys. *ACS Applied Materials Interfaces*, 12(48):53816–53826, dec 2020.
- [296] Matias Herran, Ana Sousa-Castillo, Chenghao Fan, Seunghoon Lee, Wei Xie, Markus Döblinger, Baptiste Auguie, and Emiliano Cortés. Tailoring Plasmonic Bimetallic Nanocatalysts Toward Sunlight-Driven H₂ Production. *Advanced Functional Materials*, 32(38):2203418, sep 2022.
- [297] Wenqiang Gao, Qilu Liu, Xiaolei Zhao, Chao Cui, Shan Zhang, Weijia Zhou, Xiaoning Wang, Shuhua Wang, Hong Liu, and Yuanhua Sang. Electromagnetic induction effect induced high-efficiency hot charge generation and transfer in Pd-tipped Au nanorods to boost plasmon-enhanced formic acid dehydrogenation. *Nano Energy*, 80:105543, 2021.
- [298] Seunghoon Lee, Heeyeon Hwang, Wonseok Lee, Dmitri Schebarchov, Younhyun Wy, Johan Grand, Baptiste Auguie, Dae Han Wi, Emiliano Cortés, Sang Woo Han, Dae Han Wi, Emiliano Cortés, and Sang Woo Han. Core-Shell Bimetallic Nanoparticle Trimers for Efficient Light-to-Chemical Energy Conversion. *ACS Energy Letters*, 5(12):3881–3890, nov 2020.
- [299] Liselotte Jauffred, Akbar Samadi, Henrik Klingberg, Poul Martin Bendix, Lene B. Oddershede, Poul Martin Bendix, and Lene B. Oddershede. Plasmonic Heating of Nanostructures, 2019.
- [300] Dong Kwon Lim, Aoune Barhoumi, Ryan G. Wylie, Gally Reznor, Robert S. Langer, and Daniel S. Kohane. Enhanced photothermal effect of plasmonic nanoparticles coated with reduced graphene oxide. *Nano Letters*, 13(9):4075–4079, 2013.

- [301] M. Jazmín Penelas, Gustavo F. Arenas, Fernando Trabadelo, Galo J.A.A. Soler-Illia, Sergio E. Moya, Paula C. Angelomé, and Cristina E. Hoppe. Importance of the Structural and Physicochemical Properties of Silica Nanoshells in the Photothermal Effect of Silica-Coated Au Nanoparticles Suspensions. *Langmuir*, 38(12):3876–3886, 2022.
- [302] Rituraj Borah and Sammy W Verbruggen. Silver–Gold Bimetallic Alloy versus Core–Shell Nanoparticles: Implications for Plasmonic Enhancement and Photothermal Applications. *The Journal of Physical Chemistry C*, 124(22):12081–12094, 2020.
- [303] Gregory T. Forcherio, Behnaz Ostovar, Jonathan Boltersdorf, Yi Yu Cai, Asher C. Leff, Kyle N. Grew, Cynthia A. Lundgren, Stephan Link, and David R. Baker. Single-Particle Insights into Plasmonic Hot Carrier Separation Augmenting Photoelectrochemical Ethanol Oxidation with Photocatalytically Synthesized Pd-Au Bimetallic Nanorods. *ACS Nano*, 16(8):12377–12389, 2022.
- [304] Zhaoke Zheng, Takashi Tachikawa, and Tetsuro Majima. Single-particle study of Pt-modified Au nanorods for plasmon-enhanced hydrogen generation in visible to near-infrared region. *Journal of the American Chemical Society*, 136(19):6870–6873, may 2014.
- [305] Anneli Joplin, Seyyed Ali Hosseini Jebeli, Eric Sung, Nathan Diemler, Patrick J. Straney, Mustafa Yorulmaz, Wei Shun Chang, Jill E. Millstone, and Stephan Link. Correlated Absorption and Scattering Spectroscopy of Individual Platinum-Decorated Gold Nanorods Reveals Strong Excitation Enhancement in the Nonplasmonic Metal. *ACS Nano*, 11(12):12346–12357, 2017.
- [306] Peter Zijlstra, Pedro M R Paulo, Kuai Yu, Qing-Hua Xu, and Michel Orrit. Chemical Interface Damping in Single Gold Nanorods and Its Near Elimination by Tip-Specific Functionalization. *Angewandte Chemie International Edition*, 51(33):8352–8355, aug 2012.
- [307] Zhenbin Ge, David G. Cahill, and Paul V. Braun. Thermal conductance of hydrophilic and hydrophobic interfaces. *Physical Review Letters*, 96(18):1–4, 2006.
- [308] Jonglo Park and David G. Cahill. Plasmonic Sensing of Heat Transport at Solid-Liquid Interfaces. *Journal of Physical Chemistry C*, 120(5):2814–2821, feb 2016.
- [309] Han Hu and Ying Sun. Effect of nanopatterns on Kapitza resistance at a water-gold interface during boiling: A molecular dynamics study. *Journal of Applied Physics*, 112(5), 2012.
- [310] Hari Harikrishna, William A. Ducker, and Scott T. Huxtable. The influence of interface bonding on thermal transport through solid-liquid interfaces. *Applied Physics Letters*, 102(25), 2013.

- [311] Vera Jerry and Yildiz Bayazitoglu. Temperature and Heat Flux Dependence of Thermal Resistance of Water/Metal Nanoparticle Interfaces. *International Journal of Heat and Mass Transfer*, 86:433–442, 2015.
- [312] Young Feng Li. *Hydrogen Bronzes of WO_3 and MoO_3 as Active (Photo-) Catalyst Supports for CO_2 Reduction*. PhD thesis, University of Toronto, 2020.
- [313] E. Dulkeith, T. Niedereichholz, T. A. Klar, J. Feldmann, G. Von Plessen, D. I. Gittins, K. S. Mayya, and F. Caruso. Plasmon emission in photoexcited gold nanoparticles. *Physical Review B - Condensed Matter and Materials Physics*, 70(20):205424, nov 2004.
- [314] Frank Wackenhut, Antonio Virgilio Failla, and Alfred J. Meixner. Multicolor microscopy and spectroscopy reveals the physics of the one-photon luminescence in gold nanorods. *Journal of Physical Chemistry C*, 117(34):17870–17877, 2013.
- [315] Mustafa Yorulmaz, Saumyakanti Khatua, Peter Zijlstra, Alexander Gaiduk, and Michel Orrit. Luminescence Quantum Yield of Single Gold Nanorods. *Nano Letters*, 12(8):4385–4391, aug 2012.
- [316] Ying Fang, Wei Shun Chang, Britain Willingham, Pattanawit Swanglap, Sergio Dominguez-Medina, and Stephan Link. Plasmon emission quantum yield of single gold nanorods as a function of aspect ratio. *ACS Nano*, 6(8):7177–7184, 2012.
- [317] M. Saad Bin-Alam, Orad Reshef, Yaryna Mamchur, M. Zahirul Alam, Graham Carlow, Jeremy Upham, Brian T. Sullivan, Jean Michel Ménard, Mikko J. Huttunen, Robert W. Boyd, and Ksenia Dolgaleva. Ultra-high-Q resonances in plasmonic metasurfaces. *Nature Communications*, 12(1):1–8, dec 2021.
- [318] V. G. Kravets, A. V. Kabashin, W. L. Barnes, and A. N. Grigorenko. Plasmonic Surface Lattice Resonances: A Review of Properties and Applications, jun 2018.
- [319] Michael B. Ross, Chad A. Mirkin, and George C. Schatz. Optical Properties of One-, Two-, and Three-Dimensional Arrays of Plasmonic Nanostructures. *Journal of Physical Chemistry C*, 120(2):816–830, jan 2016.
- [320] Guillaume Baffou, Pascal Berto, Esteban Bermúdez Ureña, Romain Quidant, Serge Monneret, Julien Polleux, and Hervé Rigneault. Photoinduced heating of nanoparticle arrays. *ACS Nano*, 7(8):6478–6488, aug 2013.
- [321] Hugh H. Richardson, Michael T. Carlson, Peter J. Tandler, Pedro Hernandez, and Alexander O. Govorov. Experimental and theoretical studies of light-to-heat conversion and collective heating effects in metal nanoparticle solutions. *Nano Letters*, 9(3):1139–1146, mar 2009.
- [322] Shikai Deng, Bowei Zhang, Priscilla Choo, Paul J.M. Smeets, and Teri W. Odom. Plasmonic Photoelectrocatalysis in Copper-Platinum Core-Shell Nanoparticle Lattices. *Nano Letters*, 21(3):1523–1529, feb 2021.

- [323] Meng Ju Yu, Chih Li Chang, Hao Yu Lan, Zong Yi Chiao, Yu Chia Chen, Ho Wai Howard Lee, Yia Chung Chang, Shu Wei Chang, Takuo Tanaka, Vincent Tung, Ho Hsiu Chou, and Yu Jung Lu. Plasmon-Enhanced Solar-Driven Hydrogen Evolution Using Titanium Nitride Metasurface Broadband Absorbers. *ACS Photonics*, 8(11):3125–3132, nov 2021.
- [324] P.R. West, S. Ishii, G.V. Naik, N.K. Emani, V.M. Shalaev, and A. Boltasseva. Searching for better plasmonic materials. *Laser Photonics Reviews*, 4(6):795–808, nov 2010.
- [325] Urcan Guler, Alexandra Boltasseva, and Vladimir M. Shalaev. Refractory plasmonics, apr 2014.
- [326] Samira Khadir, Daniel Andr en, Patrick C. Chaumet, Serge Monneret, Nicolas Bonod, Mikael K all, Anne Sentenac, and Guillaume Baffou. Full optical characterization of single nanoparticles using quantitative phase imaging. *Optica*, 7(3):243, mar 2020.
- [327] Joerg Schnitzbauer, Maximilian T. Strauss, Thomas Schlichthaerle, Florian Schueder, and Ralf Jungmann. Super-resolution microscopy with DNA-PAINT. *Nature Protocols*, 12(6):1198–1228, jun 2017.
- [328] Julian Gargiulo, Thomas Brick, Ianina L. Violi, Facundo C. Herrera, Toshihiko Shibamura, Pablo Albella, F elix G. Requejo, Emiliano Cort es, Stefan A. Maier, and Fernando D. Stefani. Understanding and Reducing Photothermal Forces for the Fabrication of Au Nanoparticle Dimers by Optical Printing. *Nano Letters*, 17(9):5747–5755, sep 2017.
- [329] Yupu Liu, Dengke Shen, Gang Chen, Ahmed A. Elzatahry, Manas Pal, Hongwei Zhu, Longlong Wu, Jianjian Lin, Daifallah Al-Dahyan, Wei Li, and Dongyuan Zhao. Mesoporous Silica Thin Membranes with Large Vertical Mesochannels for Nanosize-Based Separation. *Advanced Materials*, 29(35):1702274, sep 2017.
- [330] Jin Lu, Yunshan Fan, Marco D. Howard, Joshua C. Vaughan, and Bo Zhang. Single-Molecule Electrochemistry on a Porous Silica-Coated Electrode. *Journal of the American Chemical Society*, 139(8):2964–2971, mar 2017.
- [331] Keyin Liu, Xiuqi Kong, Yanyan Ma, and Weiyin Lin. Preparation of a Nile Red–Pd-based fluorescent CO probe and its imaging applications in vitro and in vivo. *Nature Protocols*, 13(5):1020–1033, may 2018.

Acronyms

1D	one-dimensional
2D	two-dimensional
3D	three-dimensional
Ag	silver
AS	anti-Stokes
Au	gold
AuNP	gold nanoparticle
AuNR	gold nanorod
AuNS	gold nanosphere
CS	core-shell
Cu	copper
CW	continuous-wave
EBL	electron beam lithography
FDTD	Finite-Difference Time-Domain
FWHM	full-width-half-maximum
HER	hydrogen evolution reaction
IR	infrared
LSPR	localized surface plasmon resonance
MOFs	Metal-organic frameworks
NA	numerical aperture
NP	nanoparticle
NS	nanosphere
PL	photoluminescence
PMMA	polymethylmethacrylat
QLSI	quadriwave lateral shearing interferometry
Rf	resorufin
Rz	resazurin

SEM scanning-electron-microscopy

SERS surface-enhanced Raman scattering

SLR surface lattice resonance

SMLM single-molecule localization microscopy

TEM transmission-electron-microscopy

TIRF total internal reflection

TOF turnover frequency

UV ultraviolet

List of Figures

2.1	History	7
2.2	Mie theory.	11
2.3	Mie theory - calculations	12
2.4	Quasistatic approximation.	13
2.5	A small nanoparticle in an oscillating electric field.	15
2.6	Near fields.	16
2.7	Plasmon Decay.	17
2.8	Tunability of the resonances.	20
2.9	Plasmonic nanoparticles for photovoltaics.	22
2.10	Photothermal therapy	22
2.11	Plasmonic nanoparticles for CO ₂ reduction	25
2.12	Excitation mechanisms for plasmon-induced chemical reactions	27
3.1	Colloidal synthesis	31
3.2	Optical printing	32
3.3	Template-assisted self-assembly	34
3.4	Electron beam lithography	35
3.5	Darkfield scattering	37
3.6	Single particle darkfield measurements.	38
3.7	Surface enhanced Raman scattering	39
3.8	Examples of SERS for nanoantennas for energy conversion	40
3.9	Photoluminescence spectroscopy	42
3.10	Anti-Stokes photoluminescence thermometry	42
3.11	Electron microscopy	44
3.12	Example of electron microscopy for nanoantennas for energy conversion	45
3.13	Single-molecule localization microscopy	46
3.14	Examples of SMLM for nanoantennas for energy conversion	47
4.1	From optical to chemical hot spots in Plasmonics	52
4.2	Results of FDTD simulations	54
4.3	Colloidal gold nanorods	55
4.4	Assembly into arrays	56
4.5	Darkfield characterization	56
4.6	The reaction-catalyst system	57
4.7	In operando single molecule catalysis	58
4.8	Accessibility to the gold surface	58
4.9	Reaction kinetics enhanced with 561 nm illumination	60
4.10	Spatial distributions of reactivity	61
4.11	The effect of the plasmon resonance	62
4.12	Temperature profiles at different irradiances	63
4.13	Unaffected spatial distributions	63
5.1	Hybrid plasmonic photocatalysts	69
5.2	Plasmonic metal- metal hybrids	70
5.3	Plasmonic metal - semiconductor hybrids	71

5.4	Plasmonic metal-perovskite hybrids	72
5.5	Plasmonic metal - 2D hybrids	72
5.6	Plasmonic metal - MOF hybrids	73
5.7	Hybrid plasmonic nanomaterials for the generation of hydrogen	77
5.8	Hybrid plasmonic nanomaterials for CO ₂ reduction	79
5.9	Histograms of the main plasmonic component and illumination sources	81
5.10	Gold palladium core shell nanoparticles	84
5.11	Optical modelling of the interface	85
5.12	Optical cross sections of Au-Pd coreshell nanoparticles	86
5.13	Heat diffusion for a spherical core-shell nanoparticle	87
5.14	Influence of substrate calculated by COMSOL Multiphysics	88
5.15	Thermal modelling of the interface	89
5.16	Theoretically estimated photothermal properties	90
5.17	Fabricated gold palladium core shell samples	91
5.18	Optical characterization of single Au@Pd core-shell nanoparticles	92
5.19	Photothermal properties of single Au@Pd core-shell nanoparticles	93
5.20	Gold palladium nanoparticles with different geometries	94
5.21	Absorption cross section of core satellite nanoparticle	95
5.22	Comparison between core-shell and core-satellites AuPd NPs	96
5.23	Predictions for other metal-metal hybrids	97
6.1	Periodic arrangements of plasmonic resonators	100
6.2	Collective optical response	101
6.3	Collective thermal response	102
6.4	Examples of metasurfaces for photocatalysis	103
6.5	Collective anti-Stokes signals	106
6.6	Simulations of single disks	107
6.7	Setup and sample	108
6.8	Photothermal measurements	109
6.9	Quadriwave shearing interferometry	110
6.10	Verification of measured temperatures	111
7.1	Mesoporous silica coating of AuNRs	119
7.2	SEM images of assembled AuNR@mSiO ₂	120
7.3	Measured size distributions of the AuNR@mSiO ₂ nanoparticles	121
7.4	Schematic illustration of the fluorescence microscopy setup	121
7.5	Drift correction	122
7.6	Background subtraction	122
7.7	Identification and localization of events	123
7.8	Exemplary resulting characteristics the fitted events	124
7.9	Beam profiles	125
7.10	Correcting for more than 1 particle at grid position	125
7.11	Optical simulations in Lumerical FDTD	125
7.12	Determining maximum field enhancement	126
7.13	Field enhancements close to surface	127
7.14	Temperature simulations in COMSOL	128

7.15	Results of single-particle temperature simulations	128
7.16	Photostationary state of resazurin	131
7.17	Alternative fittings of different reaction orders	132
7.18	The reaction kinetics without hydroxylamine	132
7.19	AS Hyperspectral thermometry	136
7.20	2D view of the 3D simulation in COMSOL Multiphysics	137
7.21	Size Characterization of Core-shell nanoparticles	139
7.22	Size characterization of Pd satellites	140
7.23	EDX analysis of Au60-Pd satellites	140
7.24	Number of satellites using TEM images	141
7.25	Determination of gap sizes	141
7.26	Stability Test	142
7.27	Changing transmission spectra	146
7.28	Optical simulations of disks and domes	147
7.29	Influence of the distribution	148
7.30	Porous film on top of EBL structure	149
7.31	SEM of porous silica films	150
7.32	Accessibility of the porous films	151
7.33	Stability of the porous films	151
7.34	Single-molecule imaging of non-fluorescent reactions	152

Figure permissions

Figure 1.1 Refs 2-7: Creative commons

Figure 2.1 Ref 22-23: Creative commons *Figure 2.2* Ref 26: License number 5573630165941, John Wiley and Sons *Figure 2.6* Ref. 28 Creative commons *Figure 2.7* Ref 29, License number 5573630706896, Springer Nature; Ref 30, License number 5573631134401, AIP Publishing *Figure 2.8* Ref 28, as Figure 2.6 *Figure 2.9* Ref 24, License number 5573631416298, Springer Nature *Figure 2.10* Ref 35, Creative commons; Ref 36, License number 5573640233477, Springer Nature; Ref 37, permission/license is granted free of charge *Figure 2.11* Ref 68, permission/license is granted free of charge *Figure 2.12* Ref 73, 75 permission/license is granted free of charge.

Figure 3.1 Ref 80, License number 1385888-1, American Association for the Advancement of Science; Ref 81, 84 Creative commons; Ref 82, 83, 85 permission/license is granted free of charge; *Figure 3.2* Ref 86, 87, 88 permission/license is granted free of charge *Figure 3.3* Ref 93 License Number 1385897-1, Wiley-VCH; Ref 94, Ref 85 permission/license is granted free of charge *Figure 3.5* Ref 100 License Number RNP/23/AUG/069329 *Figure 3.6* Ref 102 permission/license is granted free of charge; Ref 103 License Number 5607561182132, Springer Nature *Figure 3.8* Ref 114, Ref 115 permission/license is granted free of charge; *Figure 3.10* Ref 132, permission/license is granted free of charge *Figure 3.12* Ref 150, Creative commons *Figure 3.14* Ref 151, Ref 152 permission/license is granted free of charge.

Figure 4.1 Ref 75, Ref 154, permission/license is granted free of charge.

Chapter 5 Ref 60, permission/license is granted free of charge, Ref 184, creative commons.

Figure 6.1 Ref 28, permission/license is granted free of charge, *Figure 6.2* Ref 28, permission/license is granted free of charge; Ref 317, Creative commons *Figure 6.3* Ref 320, permission/license is granted free of charge *Figure 6.4* Ref 322, permission/license is granted free of charge; Ref 323, permission/license is granted free of charge.

Acknowledgements

I had to decrease the font size to fit my acknowledgements on two pages, and still words cannot express my gratitude. During the last four years, I have had fun, but also challenges and frustration. I have learned a lot both scientifically and beyond science. The research presented in this thesis, as well as the experiences and lessons learned, would not have been possible without the help and support of numerous individuals. I am deeply grateful to everyone involved. In the following, I would like to thank a few of the people who were essential to this journey.

First and foremost, I would like to express my deep gratitude to **Prof. Dr. Emiliano Cortés**. I feel very lucky to have had such a positive and supportive supervisor. Emi, thank you for always keeping your office doors open and for always being accessible for questions and discussions. Thank you for the opportunity you gave me to lead the review that kept us busy during the pandemic. Your support for all my other commitments, such as serving as the CeNS student representative, attending conferences, and even organizing one last year, has allowed me to grow also beyond my research topic. I greatly admire your commitment to building a diverse team and your remarkable ability to foster teamwork. Once again, thank you for everything.

Dr. Julian Gargiulo for being a great colleague, teacher and friend. Juli, I am very grateful that you were there during my first year as a PhD student to guide my first steps in Optics and Plasmonics. I enjoyed the countless hours we spent in the lab and on zoom in the last four years, discussing scientific problems, careers, and life. I admire your patience, your positive attitude, and wish you all the best for your newly started research group. Anyone would be happy to have you as their colleague and supervisor and I strive to be more like you.

Prof. Dr. Stefan A. Maier thank you for being so generous with your expertise and supporting my scientific projects, INASCON and career. You are an inspiration not only in efficient communication, but also in people management.

Dr. Ana Sousa-Castillo. Ana, I do not understand the wizardry you are able to do in the chemlab but I admire both your skills and your motivation. You have taught me to deal with things going wrong and to not give up.

All other **collaborators** and co-authors. Your contributions were essential to this thesis and I became a scientist through what all of you taught me.

Dr. Nicola Kerschbaumer. Nico, I am so thankful that we both started our Physics Bachelor at the same time. I could not have asked for a better study-buddy and miss starting the day with a cup of tea, a chat and a Übungsblatt. As luck would have it, we did our Master's Thesis in the same group and then moved for our PhDs but ended up in the same building again. I am very proud of the both of us, thank you for sharing these 9 years with me.

All past and current members of the Cortés Group and Maier Chair. You made the day-to-day struggles and food at mensa enjoyable.

Martina Edenhofer, Namvar Jahanmehr, Reinhold Rath, Denise Wedemeyer: Vielen Dank für euren administrativen, technischen und persönlichen Support in den letzten Jahren. Ich bewundere eure Geduld.

Dr. Leonardo Menezes, for sharing your decades of knowledge and experience with all of us, and for your jokes.

Dr. Ludwig Hüttenhofer, Thomas Weber, Dr. Luca Sortino and **Franz Gröbmeyer** - thanks for sharing IT-admin duties of the Chair with me throughout the years.

I would especially like to thank my past and current PhD office mates **Dr. Matias Her- ran, Christoph Gruber, Lin Nan, Dr. Joong Bum Lee, Benjamin Tillman, Dr. Andrei Stefanu** and honorary office member **Dr. Andrea Mancini**. None of us had a PhD when we met, and by mid next year we all will. It was an honor to share this time with you, thank you for the distractions :).

For proofreading I want to thank Mati, Juli and Christoph again. I am also very grateful for the existence of modern technological tools. Writefull caught most of my typos as soon as I wrote them. While ChatGPT, released at the end of last year, has proven to be unreliable as a source of information in its current state, it has been a valuable language tool for me, providing feedback and suggestions that have greatly improved the quality of my writing.

Thank you, **Maximilian Maier** and **Paula Neumann** for spending a portion of your Master's in the lab with me. There is a saying "teaching is to learn twice" and I can confirm that I learned a lot from both of you.

I also want to thank e-conversion and the **Center for Nanoscience (CeNS)** for providing a scientific network for young researchers to connect, collaborate, and learn. I especially want to thank **Dr. Susanne Hennig** without whom CeNS would not be the same. I really enjoyed working with you as a CeNS student representative to organize events and conduct a supervision survey together with **Pauline Kolbeck** and **Michael Scheckenbach**.

The INASCON organization team. Thank you **Christoph Gruber, Pauline Kolbeck, Florian Binder, Jakob Blahusch, Robert Calaminus, Clara Aletsee, Kevin Bertrang, Sonia Mackewicz, Philip Petzoldt, and Tobias Hinke**. When we decided to organize the 15th International Nanoscience Student Conference in Munich, I did not anticipate how much time we would spend together. Our conference might have been the most rewarding collaboration of my PhD. Thank you all!!

All the researchers I have met and worked with before starting my PhD and who have made a lasting impact, such as **Prof. Dr. Joachim Rädler, Dr. Anita Reiser, Dr. Alexandra Murschhauser, Gerlinde Schwake, and Dr. Cornelius Schmidt-Colinet**. I want to explicitly mention also **Dr. Andreas Becker**, my high school Physics teacher, who not only shared his fascination for physics with me, but also motivated me to participate in an internship at the physics faculty of the Radboud University Nijmegen during the school holidays - this made me decide to become a Physicist.

I want to thank my **parents** for nurturing my curiosity and for always supporting me. And finally **Sebastian Klein** without whom life would not be nearly as enjoyable <3. I am grateful that you are the person I share the best and worst times with. Thank you for being so supportive. You are the best.

I apologize if I have forgotten to mention anyone who has contributed to my work. Please know that I am deeply grateful for all the support and assistance that I have received.

